

AD-A131 706

A PROGRAM OF RESEARCH ON MICROFABRICATION TECHNIQUES  
FOR VLSI MAGNETIC DEVICES(U) CARNEGIE-MELLON UNIV  
PITTSBURGH PA M H KRYDER ET AL. 01 OCT 82

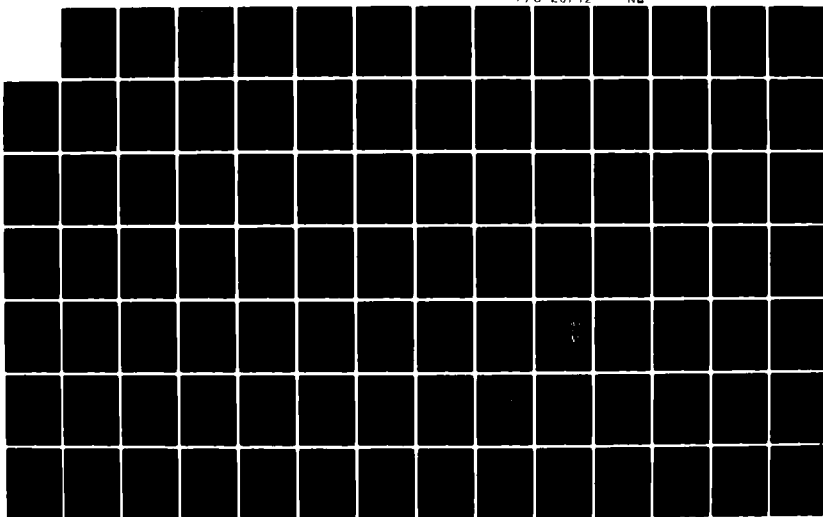
1/3

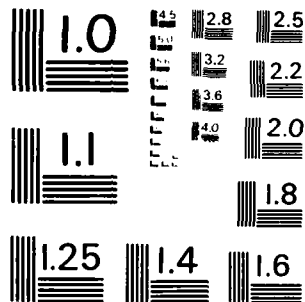
UNCLASSIFIED

AFOSR-TR-83-0685 AFOSR-80-0284

F/G 20/12

NL





MICROCOPY RESOLUTION TEST CHART  
NATIONAL BUREAU OF STANDARDS - 1963 - A

UNCLASSIFIED

4

SECURITY CLASSIFICATION OF THIS PAGE (When Data Entered)

REPORT DOCUMENTATION PAGE		READ INSTRUCTIONS BEFORE COMPLETING FORM
1. REPORT NUMBER <b>AFOSR-TR- 83-0685</b>	2. GOVT ACCESSION NO. <b>61 1137 106</b>	3. RECIPIENT'S CATALOG NUMBER
4. TITLE (and Subtitle)  <b>A Program of Research on Microfabrication Techniques for VLSI Magnetic Devices</b>		5. TYPE OF REPORT & PERIOD COVERED <b>Interim Sept. 30, 1981-Sept. 29, '82</b>
		6. PERFORMING ORG. REPORT NUMBER
7. AUTHOR(s)  <b>M. H. Kryder, C. L. Bauer, J. A. Rayne, A. Guzman</b>		8. CONTRACT OR GRANT NUMBER(s)  <b>AFOSR-80-0284</b>
9. PERFORMING ORGANIZATION NAME AND ADDRESS  <b>Carnegie-Mellon University Pittsburgh, PA 15213</b>		10. PROGRAM ELEMENT, PROJECT, TASK AREA & WORK UNIT NUMBERS  <b>2305/CI 6-1102F</b>
11. CONTROLLING OFFICE NAME AND ADDRESS <b>Air Force Office of Scientific Research Bolling Air Force Base Washington, D.C. 20332</b>		12. REPORT DATE <b>Oct. 1, 1982</b>
		13. NUMBER OF PAGES
14. MONITORING AGENCY NAME & ADDRESS (if different from Controlling Office)		15. SECURITY CLASS. (of this report)  <b>UNCLASSIFIED</b>
		15a. DECLASSIFICATION/DOWNGRADING SCHEDULE
16. DISTRIBUTION STATEMENT (of this Report)  <b>Approved for public release; distribution unlimited.</b>		
17. DISTRIBUTION STATEMENT (of the abstract entered in Block 20, if different from Report) <b>Unlimited</b>		
18. SUPPLEMENTARY NOTES		
19. KEY WORDS (Continue on reverse side if necessary and identify by block number) <b>Magnetic Bubble, Memory, Logic, Amorphous Magnetic Materials, Garnet, VLSI, Magneto-Optic, Thermo-magnetic, Recording, Charged Walls, Ion Implantation, Transmission Electron Microscopy</b>		
20. ABSTRACT (Continue on reverse side if necessary and identify by block number)  <b>Means of fabricating, selectively modifying, and characterizing single crystal epitaxial garnet and amorphous magnetic thin films are being investigated with the intention of developing new materials and processes for magnetic devices including bubble, recording, magneto-optic, and micro-wave devices.</b>  <b>Submicron ion unimplantable garnets have been developed for ion-implanted contiguous disk devices. A wideband ferromagnetic resonance spectrometer and</b>		

ADA 131706

DTIC FILE COPY

DD FORM 1 JAN 73 1473 EDITION OF 1 NOV 65 IS OBSOLETE

UNCLASSIFIED

SECURITY CLASSIFICATION OF THIS PAGE (When Data Entered)

**SECURITY CLASSIFICATION OF INFORMATION**

A number of high density bubble devices have been designed and fabricated: 2-4 $\mu$ m period ion-implanted contiguous disk devices, 4-8 $\mu$ m period current-accessed devices, and 2-6 $\mu$ m period current-accessed ion implanted devices with 4 to 16 times lower power dissipation than earlier current-accessed devices.

Accession No. X

**A**

SECURITY CLASSIFICATION OF THIS PAGE(When Data Entered)



## TABLE OF CONTENTS

1. Introduction	0
2. Garnet Bubble Materials and the Effects of Ion Implantation on Them	2
2.1. Submicron Bubble Garnets	2
2.2. Effects of Ion Implantation on The Magnetic Characteristics of Garnet Thin Films	2
2.3. Anisotropy in Ion-Implanted Layers: Investigations With the Magneto-Optic Photometer	3
2.4. Effects of Ion Implantation on Physical Characteristics of Garnet Thin Films	4
2.5. Optical Spectra of Ion Implanted Garnets	5
3. Amorphous Bubble and Magneto-Optic Materials	6
3.1. Sputtered GdCoMo Films for Bubble Devices	6
3.2. Sputtered GdCo Materials for Magneto-Optic Devices	6
3.3. Sputtered NiCoB for Bubble Devices	7
3.4. Self Bias Layers for Bubble Devices	8
4. Bubble Devices	8
4.1. Ion Implanted Contiguous Disk Devices	9
4.2. Current-Accessed Perforated-Sheet Devices	9
4.3. Current-Accessed Ion-Implanted Devices	10
5. Instrumentation and Analysis Techniques	11
5.1. Magneto-Optic Photometer	11
5.2. Wideband FMR Spectrometer	12
6. Publications Under Grant AFOSR 80-0284	12

AIR FORCE OFFICE OF SCIENTIFIC RESEARCH (AFOSR)  
 NOTICE OF CONFIDENTIALITY  
 This document contains information that is classified as CONFIDENTIAL  
 approved for release on 10/10/00 by AFOSR-100-12.  
 Distribution unlimited.  
 MATTHEW J. KESNER  
 Chief, Technical Information Division

**A PROGRAM OF RESEARCH ON  
MICRO-FABRICATION TECHNIQUES FOR  
VLSI MAGNETIC DEVICES**

**PROGRESS REPORT**

OCTOBER 1, 1982

**1. INTRODUCTION**

The Air Force Office of Scientific Research has been funding a research project entitled "A Program of Research on Microfabrication Techniques for VLSI Magnetic Devices," since September 29, 1980. This report describes the progress we have made on this research project during its second year of funding. Highlights of the progress during the second year include the development of garnet thin films supporting submicrometer diameter bubbles and which may be used in ion implanted devices. We also developed a wide band ferromagnetic resonance spectrometer with unusually high sensitivity and have used it to characterize these garnet materials and their ion-implanted layers both before and after ion implantation. We found that ion implantation produced significant reductions in the crystalline anisotropy field, but that changes in magnetostriction were proportional to changes in magnetization. We also directly determined the change in uniaxial anisotropy field produced by stress and showed that a significant portion of the anisotropy field change was produced by non-stress related mechanisms. The non-stress related anisotropy field change was shown to become more important for small bubble domain materials.

The magneto-optic photometer system was further improved so that measurements may now be carried out using transmission, rather than only reflection. Using transmission has been shown to improve the signal-to-noise ratio by an order of magnitude and greatly simplify analysis of the magneto-optic signals. In addition the purchase of a Leitz photometer unit and additional modifications have enabled us to use a pinhole aperture in the magnified image plane of the 100X objective lens to define the area on the film in which the measurement is done. With this change, the system now has  $0.5\mu\text{m}$  resolution capability. In addition, the system now has high frequency capability up to 55 MHz. Use of this system during the past year resulted in the measurement of uniaxial anisotropy components due to stress relaxation near pattern edges. In agreement with our earlier work suggesting that uniaxial anisotropy from stress relaxation was critical to formation of the charged walls, we found that uniaxial anisotropy components were measurable  $50\mu\text{m}$  from a pattern edge in a  $0.4\mu\text{m}$  thick ion-implanted layer.

Work on amorphous bubble materials has now succeeded to the point that we feel we can deposit films which will support  $0.5\mu\text{m}$  diameter bubbles and which are stable against temperature changes. Further progress will depend upon our making  $0.5\mu\text{m}$  bubble devices on these materials.

Work on amorphous materials for magneto-optic memory devices which grew out of the work on amorphous bubble material under this contract has been pursued with GE support at C-MU and has resulted in materials which appear to be adequate for building an erasable magneto-optic memory disk with a bit capacity exceeding  $10^{10}$  bits/side. GE and C-MU have jointly submitted a proposal to Rome Air Development Center for support of this work.

In the area of bubble devices the highlight of our work has been good progress on the current-access ion-implanted devices. By using a conductor sheet under the garnet we reduced power dissipation below the factor of four gain made previously and have solved edge effect problems. Furthermore, propagation patterns for these devices have been evolved. Progress on fabrication of both ion-implanted contiguous disk and current-accessed perforated-sheet devices has been made and we expect to demonstrate submicrometer device operation this year.

Since the start of this contract we have published or submitted for publication ten papers and three Master's Degree Theses.

The work being carried out under this grant is in an area of critical need to our nation. Today only Intel and Motorola are US vendors of bubble memory devices. The Bell Telephone Laboratories continue to be active in the bubble memory area, with research support from the Air Force, however, they typically do not sell components to outside users. By comparison, the Japanese are moving ahead continuously and at a great pace in their development of bubble memory devices. Hitachi has marketed more bubble memory devices than any other manufacturer and is presently producing them at a rate exceeding 25,000 memories per month. Fujitsu now reports manufacturing 5000 to 10,000 units per month.

The research effort at Carnegie-Mellon University, being funded by this grant, has attracted significant attention from industrial manufacturers and users of bubble memories. In the past, industrial firms involved in the manufacture of bubble memories have provided some support to this program in the form of equipment donations and/or support of an individual graduate student through a fellowship. Researchers involved in this program are sought out by industrial workers actively involved in bubble memory design and fabrication for consultation on future technology directions. Without the grant support provided by the AFOSR grant number 80-0284, this program would not be possible. Below are contained a progress summary by area and detailed reports from selected areas, as well as appended publications.

## 2. GARNET BUBBLE MATERIALS AND THE EFFECTS OF ION IMPLANTATION ON THEM

### 2.1. SUBMICRON BUBBLE GARNETS

In our last progress report (10-1-81), we described the implementation of the LPE growth facility and the development of characterization techniques to measure film properties. We gave results for numerous 1  $\mu\text{m}$  diameter bubble films and some submicron films. We report here on further progress on the development of garnet epitaxial films which are suitable for submicron diameter bubble devices.

Garnet materials of  $(\text{YSmTmGd})_3(\text{FeGaAl})_5\text{O}_{12}$  and  $(\text{YSmTmGdLu})_3(\text{FeAl})_5\text{O}_{12}$  compositions were investigated for as 1.0  $\mu\text{m}$  and 0.5  $\mu\text{m}$  diameter ion-implantable bubble materials, respectively. The results of this investigation were reported at the Intermag-Magnetism and Magnetic Materials Conference held in July, 1982 and are to be published in an upcoming issue of the IEEE Transactions on Magnetics (7). The particular compositions used were evolved from compositions typically used for larger bubble diameter materials. These compositions are well suited for ion-implanted devices because they have relatively large magnetostriction constants ( $\lambda_{111} = -3.3 \times 10^{-6}$  for the 1  $\mu\text{m}$  materials and  $\lambda_{111} = -3.8 \times 10^{-6}$  for the 0.5  $\mu\text{m}$  materials) and sufficient anisotropy for device applications. For the 1  $\mu\text{m}$  composition the temperature dependence of collapse field from room temperature to 100°C was nearly constant. On the other hand for the 0.5  $\mu\text{m}$  compositions the temperature coefficient of the collapse field in this range was about -0.2%/°C, providing a good match to barium-ferrite permanent magnets. The 1  $\mu\text{m}$  bubble materials were in fact tested in ion implanted contiguous disk devices and demonstrated to give good propagation margins. The 0.5  $\mu\text{m}$  bubble materials were implanted and measurements of the anisotropy field change produced by the implantation indicate that the materials should work well in implanted devices. We are now fabricating 2  $\mu\text{m}$  period propagation structures on these materials and expect to demonstrate 0.5  $\mu\text{m}$  bubble propagation in the near future.

A copy of the paper entitled "Investigations of Ion Implantable Submicron Bubble Material" is attached to this report and explains in more detail the results of these investigations.

### 2.2. EFFECTS OF ION IMPLANTATION ON THE MAGNETIC CHARACTERISTICS OF GARNET THIN FILMS

The wideband ferromagnetic resonance spectrometer described below in section 5.2 was used to measure the changes in magnetostriction constant  $\lambda_{111}$ , magnetocrystalline anisotropy field  $H_1$ , and the effective uniaxial anisotropy field  $H_K - 4\pi M_s$ , when a garnet thin film is implanted with deuterium and oxygen ions. These results were described in detail at a paper presented at the International Colloquium on Magnetic Thin Films and Surfaces in Yokohama, Sept. 1982 (9), and

in a paper presented at the Conference on Ion-Beam Modification of Materials, Grenoble, France, Sept., 1982 (8). These measurements enabled us to determine the contribution to the anisotropy field change which was produced by stress and compare that with the total change. Direct measurements indicated that stress alone cannot account for the total change in anisotropy field. The additional change, which is believed to be related to disordering of the crystal lattice, is nearly the same for  $1\mu\text{m}$  and  $0.5\mu\text{m}$  bubble materials. On the other hand the stress induced anisotropy field change is inversely proportional to  $4\pi M_s$ , and therefore smaller in the  $0.5\mu\text{m}$  materials which have large  $4\pi M_s$ . These results therefore indicate that, as bubble size is reduced, the non-stress related mechanism increases in relative importance. It was also found that  $\lambda_{111}/M_s$  remained constant in the films we investigated so long as implant energies and doses were kept to moderate levels. A substantial reduction in the crystalline anisotropy field from  $-160\text{ Oe}$  to  $-40\text{ Oe}$  and from  $-115\text{ Oe}$  to  $-25\text{ Oe}$  was observed in the  $1\mu\text{m}$  and  $0.5\mu\text{m}$  bubble materials described above in section 2.1 when they were implanted with  $5 \times 10^{15}/\text{cm}^2$  molecular deuterium ions at  $60\text{ keV}$  and  $9.5 \times 10^{13}/\text{cm}^2$  atomic oxygen ions at  $110\text{ keV}$ . The reduction of  $H_i$  with implantation agrees with the trend of the crystal structure becoming increasingly disordered after implantation.

Copies of the papers "Investigation of Implantation Induced Changes in Surface Layers of Epitaxial Garnet Thin Films" and the "Effect of Ion Implantation on Epitaxial Magnetic Garnet Thin Films" are attached to this report and provide considerably more detail about the investigations conducted.

### 2.3. ANISOTROPY IN ION-IMPLANTED LAYERS: INVESTIGATIONS WITH THE MAGNETO-OPTIC PHOTOMETER

In the last progress report (10/1/81) we described the magneto-optic photometer system and its use to characterize the crystalline anisotropy constant  $K_i$  in ion implanted layers of garnets (1). During this past year we have been using this system to characterize the anisotropy in ion implanted layers of garnet thin films having their  $[111]$  axis slightly misaligned from the film normal. Theoretical models for the behavior of magnetization in such tilted films are being developed. Such tilted films have different anisotropic behavior than non-tilted films and may produce superior device margins. Furthermore, in order to specify the tolerance on tilt of the  $[111]$  axis, it is necessary to have an understanding of the effects of the variation in tilt on the ion implanted device behavior.

Following the theoretical models, some experiments have been devised to measure the anisotropies of the ion implanted films using the magneto-optic photometer. These experiments are currently underway on the tilted films and indicate large variations in planar anisotropy for relatively small, (less than  $5^\circ$ ) tilt angles. Further magneto-optic measurements are being made on the tilted samples to test the validity of the theoretical model. If the model is shown to be

valid, it will be used to predict charged wall behavior in a tilted contiguous disk device.

With the magneto-optic photometer, we have successfully measured for the first time, the stress induced anisotropy near ion implanted pattern edges. This was done by using the small spot size capability of the magneto-optic photometer and measuring the anisotropy as a function of distance from a non-implanted pattern edge. Confirming our previous finding, that stress relaxation at the pattern edge was responsible for the uniaxial anisotropy parallel to the pattern edge which caused a charged wall to form, we measured a significant uniaxial anisotropy, a distance of  $10\mu\text{m}$  away from the boundary edge. This uniaxial anisotropy was found to increase in magnitude as the pattern edge was approached.

In our work with uniaxial and tri-directional anisotropies we have also evolved some experiments which allow us to characterize the nature of the anisotropy in a magnetic material whose general properties are not known.

A more detailed report on the investigations of the magneto-optic photometer system is attached to this brief summary.

## 2.4. EFFECTS OF ION IMPLANTATION ON PHYSICAL CHARACTERISTICS OF GARNET THIN FILMS

Our previous investigations of ion implanted garnet (described in last year's 10-1-81 progress report) and in reference (4) with 60keV deuterium to a dosage of  $0.5 \times 10^{16}/\text{cm}^2$  and 110 keV Oxygen to a dosage of  $0.95 \times 10^{14}/\text{cm}^2$ , using the techniques of electron microscopy, showed that no change occurs in structure and that only strain distortions at ion implanted boundaries can be observed. During this past year the structure change of ion implanted garnet with increasing implantation dosage was investigated. Amorphization of garnet crystals was observed with 60 keV deuterium to a dosage of  $3.0 \times 10^{16}/\text{cm}^2$  and 110 keV Oxygen to a dosage of  $5.7 \times 10^{14}/\text{cm}^2$ . In order to study profiles of implanted oxygen and deuterium layers, a cross sectional TEM technique was developed. Preparation procedures of cross sectional samples, irradiation profiles and amorphization of garnet with oxygen and deuterium implantation and annealing behavior of amorphous garnet were studied.

Cross sectional transmission electron microscopy clearly shows the formation kinetics of an amorphous layer on the surface of garnet. At low dosage (less than  $0.5 \times 10^{16}$  deuterium/ $\text{cm}^2$  and  $0.95 \times 10^{14}$  Oxygen/ $\text{cm}^2$ ), no change was observed without strain profiles at ion implanted boundaries. As the implantation dose increases (less than  $1.0 \times 10^{16}$  deuterium/ $\text{cm}^2$  and  $1.9 \times 10^{14}$  Oxygen/ $\text{cm}^2$ ), isolated amorphous regions are formed. These isolated amorphous regions increase and finally a continuous amorphous layer is formed by further ion implantation. The critical

dosage of amorphization is below  $3 \times 10^{16}$  deuterium/cm<sup>2</sup> and  $5.7 \times 10^{14}$  Oxygen/cm<sup>2</sup>.

No evidence of small crystallite formation was observed by cross sectional transmission electron microscopy. However, by observing the ion implanted surface, small crystallites were observed; both Debye rings and dark field images show evidence for this. These facts lead to the conclusion that small crystallites exist only in the very thin surface region. The surface receives a relatively small amount of damage, even after heavy ion implantation, since implanted ions do not exist in the shallow surface layer. Recovery of damage may occur easily in this shallow surface.

Oxygen implantation was found to play a dominant role for the crystalline to amorphous transformation, since no drastic change was observed to be caused by deuterium implantation. Two types of amorphization processes by ion implantation have been proposed (J. Bourgoin, Solid State Communications, 34, 25 (1980)). One type is amorphization with heavy ion implantation where the concentration of defects in the cascade can be large enough to induce the transformation and isolated amorphous regions are directly formed. The other type is amorphization with light ions where the critical concentration of defects is reached only after several ions have come to rest at the same region. In this case an abrupt transformation of an implanted layer is expected. In our experiment the former type of amorphization process has been observed. It is due to the fact that oxygen atoms are relatively heavy.

More details of these studies may be found in the report entitled "Direct Observation of Heavily Implanted Layers in Garnets" attached to this summary and in the digest entitled "Characterization of Microstructure in Ion-Implanted Garnet by Transmission Electron Microscopy," submitted to the Intermag Conference to be held April 5-8, 1983 in Philadelphia (12).

## 2.5. OPTICAL SPECTRA OF ION IMPLANTED GARNETS

Optical Investigations of ion implanted garnet epilayers were discussed in our last progress report (10-1-81). Since then considerable progress has been made in coupling a cryomagneto-optical dewar to a spectro photometer. The dewar support structure and the mating spectrophotometer cart have been finished. The transmission probe, nitrogen purging system, wafer cooling system, vacuum pump station and other accessories have been completed. To give the proper magnetic and thermal properties, most materials used were either aluminum, stainless steel or copper. Considerable machining time was required to meet the design flexibility and precision necessary for alignment of the dewar with the spectrophotometer optics. Currently we are trying to correct a persistent leak in the cryomagneto-optic dewar.

Once the leak has been fixed and a successful cool-down demonstrated, the first  $\text{Er}^{3+}$  doped epilayer will be run. The amount of new machining should be minimal and confined to new sample holders and probes. We have now grown our first set of  $\text{Er}^{3+}$  doped epilayers, but we anticipate that some experimentation will be required to optimize the amount of doping to obtain adequate sensitivity. The first samples will be run in transmission, perpendicular to the epilayer, as this is the easiest mode. Based upon the sensitivity of these early runs, doping concentrations may be changed or the samples may be looked at in one or both of two other modes. The samples can be placed in the reflection mode or the epilayer can be used as a waveguide (transmission parallel to the epilayer). The last mode is most sensitive to weak absorptions since the path length and the material of interest is substantially longer and the background absorption in the GGG substrate is reduced. The interest in using  $\text{Er}^{3+}$  doped epilayers revolves around the N-center satellites. As explained in the previous report, these satellites (called P and I-centers) should give insight into stoichiometric and crystal field deviations caused by ion implantation. The objective of this investigation is to explain the microscopic behavior of ion implanted garnet epilayers in terms of microscopic effects manifested through these deviations.

### 3. AMORPHOUS BUBBLE AND MAGNETO-OPTIC MATERIALS

#### 3.1. SPUTTERED $\text{GdCoMo}$ FILMS FOR BUBBLE DEVICES

Amorphous  $\text{GdCoMo}$  bubble materials supporting  $0.5 \mu\text{m}$  diameter bubbles are now routinely fabricated by r.f. sputtering at C-MU. These materials have been shown to have adequately insensitive temperature characteristics in the  $0$  to  $100^\circ\text{C}$  range, that they could be used for device applications. A master's degree thesis written by P. Nittoli and entitled "The Fabrication and Characterization of Amorphous Magnetic Films in the Gadolinium Cobalt Molybdenum Argon System," describes the deposition and characterization of these amorphous bubble materials and is attached to this summary report. Having satisfied ourselves that we can deposit amorphous films which will support  $0.5 \mu\text{m}$  diameter bubbles, and which are stable against changes in temperature, we now need to fabricate device structures on these films in order to further establish their viability as a bubble domain material.

#### 3.2. SPUTTERED $\text{GdCo}$ MATERIALS FOR MAGNETO-OPTIC DEVICES

The work on  $\text{GdCo}$  and  $\text{GdCoMo}$  materials for bubble device applications, begun under AFOSR grant 80-0284, lead to interest in using such amorphous materials for erasable magneto-optic memory disk applications. Accordingly, the General Electric Company has supported two graduate students doing work in this area under Professor Kryder's direction. This research resulted in the demonstration of the feasibility of a magneto-optical disk system having a bit density of  $10^4$  bits per centimeter along the track and a track density of  $5 \times 10^3$  tracks per centimeter, for a total



areal bit density of  $5 \times 10^7$  bits/cm<sup>2</sup>. One micrometer diameter domains were written with a focused AlGaAs laser diode and shown to be stable against temperature changes from 0 to 100°C and against applied fields ranging from -100 Oe to +100 Oe. The erasability of individual bits was also demonstrated.

This cooperative program between GE and C-MU has now resulted in a proposal to the Rome Air Development Center request for Proposal No. I-3-4158 for investigations of "Reusable Optical Disk Techniques."

### 3.3. SPUTTERED NiCoB FOR BUBBLE DEVICES

In an attempt to replace the ion implanted drive layer in contiguous disk bubble devices with a sputter deposited amorphous thin film, we have been investigating metal-metalloid films. These films can be grown with a wide range of magnetization axes, very low anisotropy and a low coercive force. Initial studies by M. H. Kryder using ferrofluid indicated that by etching patterns into the surface of NiCoB films, it was possible to form weakly charged domain walls which could be used to move bubble domains around pattern boundaries. Bubble propagation margins were, however, quite small and we hoped that a thorough investigation of NiCoB films would yield drive layers which would provide strongly charged walls and good propagation margins. During the first year of the grant, we deposited a large number of NiCoB films and studied the influence of r.f. sputtering conditions on the magnetic parameters of the films. Thus far we have, however, been unsuccessful in obtaining strongly charged walls.

Investigations carried out under this contract showed the importance of magnetostriction and stress relaxation at the boundary between the unimplanted and implanted material in forming the charged wall in implanted garnets. Since vacuum deposited films typically have built-in planar stress, we felt it might be possible to achieve stress relaxation at boundaries of etched holes in a suitable amorphous drive layer. However, to create the desired magnetic anisotropy at the boundary, it is also necessary that the material have suitably large magnetostriction constants. We therefore began to search for high magnetostriction magnetic materials with low coercivity, low anisotropy and magnetization values of a few hundred to a few thousand gauss, similar to that of the ion implanted layer of garnets. NiCoB films do not provide adequate magnetostriction. High magnetostriction constant amorphous materials do exist, however. We believe that Tb or Dy doped metal-metalloid amorphous films would have relatively high magnetostriction. Whether we can simultaneously achieve low coercivity and low anisotropy in these materials is unknown at the present, however.

A copy of a thesis by Robert G. DeCesaris and entitled "Fabrication and Characterization of Amorphous and Polycrystalline NiCoB Ferromagnetic Thin Films," provides more details on the

deposition and characterization of the NiCoB amorphous materials and is attached as an appendix to this summary report (8).

### 3.4. SELF BIAS LAYERS FOR BUBBLE DEVICES

Liu *et al.* (J. Appl. Phys. 42, 1360 (1971)), showed that bubble domains could be stabilized by the energy of a domain wall separating a high coercive force layer magnetized anti-parallel to the bubble domain itself. Devices using such bias layers would require no external bias magnets and therefore would be significantly lighter and more compact than presently manufactured devices. In our previous report (10-1-81) it was pointed out that we had investigated CoCr materials as a potential self-bias layer but found that the CoCr films did not remain saturated when the field was removed. Thus, self biasing could not be obtained. We, therefore, proposed using Sm additions to CoCr to obtain a higher coercive force and hopefully a single domain layer of permanent magnet material. Thus far, we have been unsuccessful in obtaining films with sufficient anisotropy perpendicular to the plane of the film so that the magnetization stays saturated in that direction.

In addition to CoCrSm, we have investigated the use of high coercive force GdCoX compositions as a self bias layer. It is well known that GdCo alloys have very high coercive force near the compensation point. During the past year we made some two layer GdCo film structures which exhibited stable bubble diameters of about  $5\mu\text{m}$  with zero applied bias field. The structures consisted of a high coercive force compensation point layer with a typical low coercive force bubble layer on top. These layered structures proved to be temperature sensitive because the magnetic parameters of GdCo change rapidly near the compensation temperature. To circumvent this problem, we are now interested in examining impurity additions to raise the coercivity. An attempt to use oxygen to raise the coercivity was only partially successful. The coercivity did increase, but by an amount far too little to prevent the GdCo films from breaking up into domains. At the International Conference on Magnetism held in Kyoto, Japan in September, 1982, Dr. Y. Togami presented a paper in which he showed that GdTbCo films exhibited high coercivity. Accordingly, we have recently added some terbium to our GdCo target and have begun sputtering these materials. Assuming that we are able to get the same properties as Togami has reported, we will then deposit the GdTbCo films on top of a bubble material to demonstrate the self bias effect.

## 4. BUBBLE DEVICES

#### 4.1. ION IMPLANTED CONTIGUOUS DISK DEVICES

During the course of this grant, we have successfully propagated  $1\mu\text{m}$  diameter bubbles in  $4\mu\text{m}$  period patterns; however, we have been frustrated in attempts to propagate  $0.5\mu\text{m}$  diameter bubbles because of fabrication difficulties associated with very narrow linewidth lithography. Until recently we were trying to fabricate the submicron bubble devices using a Cobilt mask aligner and electron beam generated masks fabricated at the National Research and Resource Facility for Submicron Structures at Cornell University. The Cobilt mask aligner did not have adequate resolution to faithfully reproduce the narrow line width mask patterns. An attempt to fabricate devices using direct-write on-wafer with electron beam lithography also failed because resist residue was left in the exposed areas of the pattern. Now, however, we have acquired a new deep-ultraviolet Karl Suss mask aligner with  $0.2\mu\text{m}$  resolution and  $\pm 0.1\mu\text{m}$  alignment tolerance. We expect to have masks generated early in December and fabricate the  $0.5\mu\text{m}$  devices shortly thereafter.

In spite of the difficulties in fabricating  $0.5\mu\text{m}$  diameter bubble devices, we made good progress in obtaining control of our processing techniques. We significantly improved our control over the plating process used to form the gold pattern which serves as the ion implantation mask for the ion implanted contiguous disk devices.

We also made good progress on device design. We now have designs for full function bubble memory chips for  $0.5\mu\text{m}$ ,  $1\mu\text{m}$  and  $2\mu\text{m}$  diameter bubbles. The layouts of the chips for various bubble diameters are designed to be identical except for the scale factors. We intend to study the scaling behavior of these devices and verify our earlier projections. Also contained on this chip are designs for a novel replicate transfer gate utilizing bubble-bubble interaction. We expect to fabricate this mask set during the month of November at the National Research and Resource Facility for Submicron Structures at Cornell University and to fabricate the actual devices shortly thereafter using our new deep U.V. mask aligner.

A report entitled "Fabrication of Contiguous Disk Magnetic Bubble Devices," which is attached to this summary report, provides more details on these investigations.

#### 4.2. CURRENT-ACCESSED PERFORATED-SHEET DEVICES

Current-accessed perforated-sheet devices are being studied in spite of power dissipation problems (M. H. Kryder, IEEE Trans. Magnet. MAG-17, 2392 (1981)) because they offer high performance and because they are especially amenable to design of bubble logic. We plan to use a limited amount of current-access technology on an otherwise field field accessed chip in order to improve performance and functionality of bubble devices. By using only a small amount of current-access technology on a chip, total power dissipation will be held to a tolerably low level.

During the past year, we designed and fabricated chips with both contiguous disk and current-access perforated-sheet technologies on the wafer. The devices fabricated had a number of logic gates employing bubble-bubble interaction on them. These chips are now being tested.

#### 4.3. CURRENT-ACCESSED ION-IMPLANTED DEVICES

A novel current-accessed ion implanted device which combines the ultra high density of ion implanted contiguous disk devices with the performance and simpler packaging (no rotating field coils) of current-access devices, was invented at C-MU and has been pursued under AFOSR contract AFOSR-80-0284. This new device uses currents in apertured conductor sheets to access charged walls in ion implanted layers of garnet. Data taken on early device structures indicated that the device required about one-fourth the power of current-access perforated sheet devices without the ion implanted structure. Since that time additional progress has been made. First of all, a design employing a ground plane conductor sheet, was developed to eliminate the large perpendicular component of field near the edge of the conductor pattern. It had been recognized by Bobeck *et al.* (Bell Sys. Tech. J., 58, 1453 (1979)) in their apertured sheet devices, that this large perpendicular field made one sacrifice a large amount of chip area near the edges of the conductor sheet. In our device structure, as opposed to Bobeck's, however, it was not possible to use a return conductor above the apertured conductor sheet, because doing so would eliminate the in-plane field components below the apertured sheet which access the charged walls. Instead, our design calls for the return conductor sheet below the garnet so that the in-plane field in the garnet is effectively doubled in comparison to a single sheet without the ground plane return. Doubling the in-plane field component will further reduce the drive current and hence the power requirements. With the ground plane return, edge effects are kept to tolerably low levels over 80% of a  $1\text{cm}^2$  chip area. Realizing that some fraction of the chip area must be devoted to space for lead connection etc., this is believed to be an acceptably small amount to sacrifice. It is noted that the ground plane return need not be actually fabricated on the garnet substrate, but can be on the surface of the chip carrier, to which the chip is bonded.

In addition to the above described solution to the edge effect problem and the accompanying further reduction in power dissipation, designs for bubble propagation patterns have been evolved since the original publication of this device structure. In most of these designs, a conventional contiguous disk propagation pattern is used with a apertured conductor sheet placed above it. Currents in the apertured sheet will access the charged walls and drive bubbles around the contiguous disk pattern. Two layer conductor patterns may be used and overcome the tendency for the current to flow around the edges of the central perforated area to the area to where the orthogonal current connection is made. Bobeck *et al.* pointed out that this effect caused power dissipation in single conductor sheets to be higher than when two layers are used to carry orthogonal currents. These new propagation structures have been laid out on a CAD system and

will be fabricated into mask patterns early in January at the National Research and Resource Facility for Submicron Structures at Cornell University. Shortly thereafter they will be reproduced using our deep U.V. contact aligner, fabricated into bubble devices and tested.

## 5. INSTRUMENTATION AND ANALYSIS TECHNIQUES

### 5.1. MAGNETO-OPTIC PHOTOMETER

The magneto-optic photometer system (1) was improved significantly since our last progress report (10/1/81). Since that time it has been modified to allow the use of transmitted light in measuring the magnetic properties of transparent magnetic material such as bubble garnets. A lens and polarizer assembly was designed to fit underneath the microscope stage. The assembly focuses and directs the laser beam through the magnetic sample and into the usual optics of the microscope. As the polarized light passes through the sample, it undergoes Faraday rotation, and this rotation is detected in the same way as in the past for reflected light. Using transmitted light instead of reflected light, significantly increases the system's sensitivity and significantly simplifies interpretation of the recorded magneto-optic information. Measurements indicate that signals are an order of magnitude larger in transmission than in reflection. These modifications have made possible the measurement of the stress relaxation at pattern boundaries described in section 2.3 of this report.

Also since the last progress report (10-1-81), we have significantly improved the resolution and spot size of the magneto-optic photometer system. With use of a Leitz photometer unit, we have been able to put a pin hole aperture in the magnified image plane of the 100 objective typically used with the magneto-optic photometer. Thus, a  $50\mu\text{m}$  diameter pin hole corresponds to  $0.5\mu\text{m}$  on the sample. Hence, we can now measure with  $0.5\mu\text{m}$  resolution on the sample surface and near device structures. This improvement is also responsible for our ability to detect the stress relaxation near pattern boundaries of ion implanted contiguous disk devices.

The frequency response of the system has also significantly improved. The system will now operate at frequencies of up to 55 megahertz so the dynamic properties of charged walls and also of normal domain walls may be measured. Work on magneto-resistive and thin film recording heads which is being funded by Magnetic Peripherals Inc. and the IBM Corporation, is being carried out by using the high frequency characteristics of the magneto-optic photometer system.

## 5.2. WIDEBAND FMR SPECTROMETER

A wideband ferromagnetic resonance spectrometer system (6) was assembled since the last progress report (10-1-81). This system uses a non-resonant microstrip transmission line instead of a tuned microwave cavity for applying microwave fields to the garnet material. Using this apparatus, we developed techniques to measure the magnetostriction constant  $\lambda_{111}$  in both submicrometer diameter bubble material and in ion implanted layers of full wafer garnets. In addition, we develop techniques for measuring the magneto-crystalline anisotropy field using this apparatus. Accuracy of the anisotropy measurement is believed to be better than  $\pm 10$  Oe. Our apparatus offers higher sensitivity than previously reported microstrip structures and no problems with coupled resonances in magneto-striction measurements, as previously found (G. P. Vella-Coleiro, Rev. Sci. Instrum., 50, 1130 (1979)) when using a shorted wave guide. A paper describing this apparatus in more detail and entitled "Measurement of Magneto-Crystalline Anisotropy Field and Magneto-Striction Coefficient in Garnet Films," was presented at the Joint Intermag-Magnetism and Magnetic Materials Conference in Montreal in July 1982 and is attached to this summary report.

## 6. PUBLICATIONS UNDER GRANT AFOSR 80-0284

1. J. J. Fernandez de Castro and M. H. Kryder, "Magneto-Optic Measurements of the Effects of Crystalline Anisotropy in Ion-Implanted Layers of Garnet," IEEE Trans. Magnet., MAG-18, (1982).
2. H. Ohta and M. H. Kryder, "Current-Access Ion-Implanted Bubble Device Structure," J. Appl. Phys., 53, 2531 (1982).
3. T. Omi, C. L. Bauer and M. H. Kryder, "Strain Profiles in Ion Implanted Bubble Devices Investigated by Transmission Electron Diffraction," J. Appl. Phys., 53, (1982).
4. T. Omi, M. H. Kryder and C. L. Bauer, "Measurement of Strain Profiles in Ion-Implanted Bubble Devices by Transmission Electron Microscopy," presented at International Congress on Electron Microscopy, Hamburg, Aug. 17-14, 1982.
5. M. Alex, "The Fabrication of Dual Conductor Current Access Magnetic Bubble Devices," Master's Degree Thesis, Carnegie-Mellon University, April, 1981.
6. X. Wang, C. S. Krafft and M. H. Kryder, "Measurement of Magnetocrystalline Anisotropy Field and Magnetostriction Coefficient in Garnet Films," presented at INTERMAG-Magnetism and Magnetic Materials Conf., Montreal (July, 1982), to be published in IEEE Trans. Magnet.
7. C. S. Krafft, X. Wang and M. H. Kryder, "Investigations of Ion Implantable Submicron Bubble Material," presented at INTERMAG-Magnetism and Magnetic Materials Conference, Montreal, to be published in IEEE Trans. on Magnet.
8. A. M. Guzman, C. S. Krafft, X. Wang and M. H. Kryder, "The Effect of Ion Implantation on Epitaxial Magnetic Garnet Thin Films," presented at the Conference

on Ion-Beam Modification of Materials, Grenoble, France, Sept. 3-6, 1982.

9. M. H. Kryder, X. Wang, C. S. Krafft and A. M. Guzman, "Investigation of Implantation Induced Changes in Surface Layers of Epitaxial Garnet Thin Films," presented at International Colloquium on Magnetic Films and Surfaces, Yokohama, Japan, Sept. 1982, to be published in *Journal of Magnetism and Magnetic Materials*.
10. P. Nittoli, "The Fabrication and Characterization of Amorphous Magnetic Films in the Gadolinium Cobalt Molybdenum Argon System," Master's Degree Thesis, Carnegie-Mellon University, August, 1982.
11. R. G. DeCesaris, "Fabrication and Characterization of Amorphous and Polycrystalline Ni-Co-B Ferromagnetic Thin Films," Master's Degree Thesis, Carnegie-Mellon University, November 1982.
12. T. Yoshiie, C. L. Bauer and M. H. Kryder, "Characterization of Microstructure in Ion-Implanted Garnet by Transmission Electron Microscopy," submitted to the Intermag Conference, Philadelphia, April 5-8, 1983.
13. M. H. Kryder and D. A. Saunders, "The Effects of Stress Relaxation and Anisotropic Magnetostriction on Charged Walls in Ion Implanted Garnets," Invited paper at Intermag Conference, Philadelphia, April 5-8, 1983.

# INVESTIGATIONS OF ION-IMPLANTABLE SUBMICRON BUBBLE MATERIAL

C. S. Krafft, X. Wang, M. H. Kryder

## ABSTRACT

We have investigated (Y Sm Tm Gd) (Fe Ga Al) garnets and (Y Sm Tm Gd Lu) (Fe Al) garnets for use as 1.0  $\mu\text{m}$  and 0.5  $\mu\text{m}$  diameter ion-implantable bubble materials, respectively. The selection of garnet composition is based on bubble size, Q factor, temperature dependence of magnetization and anisotropy field, FMR linewidth, and magnetostriction coefficient. Measurements of these parameters, as well as the crystalline anisotropy field are given for different film compositions. Effects of samarium and lutetium addition to achieve 0.5  $\mu\text{m}$  bubbles are discussed. Both film compositions were implanted with deuterium and oxygen and the implantation induced strain and uniaxial anisotropy field change were measured. Margins for 1  $\mu\text{m}$  diameter bubble propagation patterns are given.

## INTRODUCTION

The success of submicron diameter ion-implanted bubble devices depends, in part, on the development of suitable garnet film compositions. Although a wide range of compositions have been investigated, an optimal submicron garnet has yet to be reported. We report here on the development of two ion-implantable epitaxial garnet film compositions which support 1.0  $\mu\text{m}$  and 0.5  $\mu\text{m}$  diameter bubbles.

## EXPERIMENTAL DETAILS

Films were grown by the standard LPE [1] method on 2.54 cm diameter, [111] oriented, GGG substrates. Typical melt compositions are listed in Table I. The growth process was automated. During growth, rotation speed was 100 rpm with direction reversal typically set at 5 seconds. Melt saturation temperature ranged from 865°C to 880°C, depending on melt composition. Temperature drift was controlled to within 1°C for a 10 minute film growth. Film uniformity was typically better than one fringe over 80% of the wafer. The reproducibility of material parameters for films grown under identical conditions was comparable with characterization uncertainty limit.

Routine characterization included thickness, stripwidth, collapse field, effective anisotropy field, and lattice mismatch. On selected samples, the temperature coefficient of collapse field  $\Delta H_0/\text{°C}$ , was measured. This was obtained by measuring collapse field at a low and a high temperature, normalizing to  $H_0$  at 30°C, multiplying by 100, and dividing by the temperature range. Typically, we measured  $H_0$  between 20°C and 100°C. The thickness was measured precisely on samples of each garnet system with a scanning electron microscope. The measurement uncertainty in thickness is  $\pm 5\%$  absolute. Relative uncertainty on films of similar composition is  $\pm 3\%$ . Measurements of the effective anisotropy field,  $H_K = H_K - 4\pi M$ , crystalline anisotropy field  $H_1$ , and magnetostriction coefficient  $\lambda_{111}$ , were made on full wafer garnets using a wide band resonance spectrometer with microstrip transmission line [2].  $H_K$  and the gyromagnetic ratio  $\gamma$ , were determined from the frequency dependence of resonance field.  $H_1$  was determined from the angular dependence of resonance field at a fixed frequency.

Manuscript received 6/11/82.

This work was supported by the Air Force Office of Scientific Research, under grant AFOSR 80-0284, and by the National Science Foundation under grant ECS-7912677.

The authors are with Carnegie-Mellon University, Pittsburgh, Pennsylvania 15213.

Table I: Melt Composition

Oxides	0.5 $\mu\text{m}$ (Melt H2)	1.0 $\mu\text{m}$ (Melt Q2)
PbO	182.2 (moles $\times 10^{-2}$ )	175.2 (moles $\times 10^{-2}$ )
B <sub>2</sub> O <sub>3</sub>	11.8	13.8
Fe <sub>2</sub> O <sub>3</sub>	20.6	23.0
Al <sub>2</sub> O <sub>3</sub>	0.2784	0.5767
Ga <sub>2</sub> O <sub>3</sub>	-	0.7752
Y <sub>2</sub> O <sub>3</sub>	0.2274	0.1927
Gd <sub>2</sub> O <sub>3</sub>	0.0650	0.0749
Tm <sub>2</sub> O <sub>3</sub>	0.2817	0.2569
Sm <sub>2</sub> O <sub>3</sub>	0.0758	0.0749

Uncertainty in  $H_K$ , attributed to uncertainty in field and frequency measurement and temperature drift is  $\pm 25$  Oe. Uncertainty in magnetization  $4\pi M$ , which is determined from thickness, stripwidth, and collapse field measurement [3] is approximately 5%. Lattice mismatch  $\Delta a_0$  was measured with an (888) plane double crystal x-ray diffractometer.

Propagation patterns were fabricated on a 1  $\mu\text{m}$  diameter bubble garnet. A 6200 Å gold mask defined the patterns. Beneath the gold was a 500 Å chromium reflecting layer and a 400 Å SiO<sub>2</sub> passivation layer. Patterns were 6  $\mu\text{m}$  period contiguous diamonds and 5  $\mu\text{m}$  period contiguous triangles. Tracks were aligned parallel to [112] direction.

## EXPERIMENTAL RESULTS

Nominal compositions based on unity segregation coefficients for the rare-earth oxides, and the material parameters for 1  $\mu\text{m}$  bubble films are given in Table II. In Fig. 1, material parameters are plotted versus growth temperature. Temperature dependences of  $H_1$  and  $H_K$  are given in Table III. Ion implantation conditions and propagation pattern margins are given in Table IV. Implant thickness was estimated to be 4000 Å as determined from x-ray diffraction data [4].

For typical 1  $\mu\text{m}$  films, the resonance linewidth is 125 Oe at 6 GHz and the gyromagnetic ratio is 2.4 MHz/Oe. The linewidth is measured on derivative absorption curve as peak to peak separation. Magnetostriction coefficient was measured to be  $-3.3 \times 10^{-6}$ .  $H_1$  is -155 Oe.  $H_1$  and  $\lambda_{111}$  are not expected to change significantly for different 1  $\mu\text{m}$  film compositions.

Nominal compositions, based on unity segregation coefficients for the rare-earth oxides, and the material parameters for 0.5  $\mu\text{m}$  diameter bubble films are given in Table V. In Fig. 2, plots of the uniaxial anisotropy energy  $K_u$ , growth induced anisotropy energy  $K_g$ , lattice mismatch  $\Delta a_0$ , and Q versus Sm content and versus Lu content are given. Growth temperature dependent parameters  $l$ ,  $Q$ ,  $4\pi M$ ,  $H_K = H_K - 4\pi M$ ,  $67H_1$ , and  $\Delta a_0$  are plotted versus growth temperature in Fig. 3. General trends of increasing  $l$  and  $\Delta a_0$ , and decreasing  $4\pi M$ , are attributed to the increase in Al incorporation at higher growth temperatures. Saturation temperature for this melt is 868°C. Films grown at temperatures between 858°C and 840 °C have reasonable growth rates, 0.2 to 0.35  $\mu\text{m}/\text{min}$ .

Table II: One Micron Compositions and Material Parameters

Melt	Film Composition				
O1	Y <sub>0.90</sub> Sm <sub>0.20</sub> Gd <sub>0.60</sub> Tm <sub>1.3</sub> Fe <sub>4.60</sub> Ga <sub>0.40</sub> O <sub>12</sub>				
O2	Y <sub>0.80</sub> Sm <sub>0.30</sub> Gd <sub>0.60</sub> Tm <sub>1.3</sub> Fe <sub>4.65</sub> (Ga Al) <sub>0.35</sub> O <sub>12</sub>				

Melt	l ( $\mu\text{m}$ )	t ( $\mu\text{m}$ )	$4\pi M_s$ (G)	$H_K$ (Oe)	$\Delta a_0$ (Å)
O1	.103	.95	856	490	-.006
O2	.111	.85	774	960	-.003

Melt	$H_1$ (Oe)	$\Delta H_0$ (%/°C)	Rate ( $\mu\text{m}/\text{min}$ )	$T_G$ (°C)
O1	-150	-.04	.34	838
O2	-155	-.06	.31	840



Table III: Temperature Dependence of  $H_1$ ,  $H_{KE}$ , and  $4\pi M$

Melt	Temp ( $^{\circ}\text{C}$ )	$H_1$ (Oe)	$H_{KE}$ (Oe)	$4\pi M$ (G)
O1	27	-155	782	774
	84	-95	426	715
H3	25	-115	884	1292
	84	-85	372	1120

Table IV: Implant Conditions and Margins for 1  $\mu\text{m}$  Garnet

Energy		Deuterium 80 keV		Oxygen 110 keV	
Implant	Ion	Dose ( $/\text{cm}^2$ )	Ion	Dose ( $/\text{cm}^2$ )	
1	Oxygen	$8.5 \times 10^{13}$	Deuterium	$5 \times 10^{15}$	
2	Oxygen	$1.5 \times 10^{14}$	Deuterium	$8 \times 10^{15}$	
Implant	Pattern	Margin	Pattern	Margin	
1	Diamond	16%	Triangle	14%	
2	Diamond	11%	Triangle	11%	

Margins at 50 Oe Drive Field

Table V: 0.5  $\mu\text{m}$  Compositions and Material Parameters

Melt Film Compositions			
H1	$\text{Y}_{0.90}\text{Sm}_{0.35}\text{Gd}_{0.45}\text{Ti}_{1.30}$	$\text{Fe}_{4.7}\text{Al}_{0.3}\text{O}_{12}$	
H2	$\text{Y}_{1.05}\text{Sm}_{0.35}\text{Gd}_{0.30}\text{Ti}_{1.30}$	$\text{Fe}_{4.8}\text{Al}_{0.2}\text{O}_{12}$	
H3	$\text{Y}_{0.82}\text{Sm}_{0.65}\text{Gd}_{0.24}\text{Ti}_{1.02}\text{Lu}_{0.27}\text{Fe}_{4.8}\text{Al}_{0.2}\text{O}_{12}$		

Melt	$l$ ( $\mu\text{m}$ )	$t$ ( $\mu\text{m}$ )	$4\pi M_s$ (G)	$H_K$ (Oe)	$\Delta H_a$ (A)
H1	.078	.90	1000	904	-.006
H2	.059	.70	1287	481	-.006
H3	.057	.75	1292	790	-.004

Melt	$H_1$ (Oe)	$\Delta H_a$ (%/°C)	Rate ( $\mu\text{m}/\text{min}$ )	$T_g$ (°C)
H1		-.16	.27 ( $\mu\text{m}/\text{min}$ )	840
H2	-100	-.19	.22	840
H3	-115	-.20	.43	850

Magnetostriction coefficient was determined on a film with 0.54 Sm ion content and no Lu to be  $-3.8 \times 10^{-6}$ .  $H_1$  was determined to be  $-115 \text{ Oe} \pm 10 \text{ Oe}$ . FMR linewidth,  $\Delta H$  is 150 Oe at 6 GHz for films from melt H2 and 200 Oe for films from melt H3.  $\Delta H$  increased linearly with samarium addition at a rate of 240 Oe per samarium ion. Frequency dependence of  $\Delta H$  was typically 20 Oe/GHz. Gyromagnetic ratio on all 0.5  $\mu\text{m}$  films was approximately 2.6 MHz/Oe.

Implantation induced shift in anisotropy field  $\Delta H_K$  is plotted against the average strain  $\langle \epsilon \rangle$  in Fig. 4 for both 1.0 and 0.5  $\mu\text{m}$  garnets.

## DISCUSSION

The goal of the 1  $\mu\text{m}$  garnet development program was to produce films with an  $l$  of 0.11  $\mu\text{m}$ , a  $Q$  of 2.5, and a relatively small lattice mismatch. Starting from the single layer composition reported by Ju et al. [5] we added Fe to decrease  $l$  from 0.137  $\mu\text{m}$  to 0.111  $\mu\text{m}$  and increased Sm content to maintain  $Q$  near 2.5. Aluminum was used to help improve lattice matching due to increased Sm content. Aluminum is also more effective than gallium in reducing exchange constant due to a slightly higher octahedral preference [6]. We found no significant difference in slopes of  $H_K$  and  $4\pi M$  versus growth temperature curves for Ga and Ga-Al containing melts as shown in Fig. 1. This is partially attributed to the small amount of Al used. We measured the same growth temperature dependence of lattice parameter for every melt, including the 0.5  $\mu\text{m}$ , 0.00025  $\mu\text{m}^2/\text{C}$ .

The goal of 0.5  $\mu\text{m}$  bubble material development was to grow films with an  $l$  of 0.056  $\mu\text{m}$  and a  $Q$  greater than 1.5 at room temperature [7]. The first composition listed in Table V is suitable for 0.75  $\mu\text{m}$  diameter bubbles. Films from melt H2 support half micron diameter bubbles, but the  $Q$  is too low. Additions of samarium and lutetium were made in order to increase  $Q$ . Temperature dependence of  $H_1$ ,  $H_{KE}$ , and  $4\pi M$ , are given in Table III for a film grown from melt H3. The  $Q$  ( $= 1 + H_{KE}/4\pi M$ ) for this film is 1.55 at  $25^{\circ}\text{C}$  and 1.32 at  $84^{\circ}\text{C}$ .

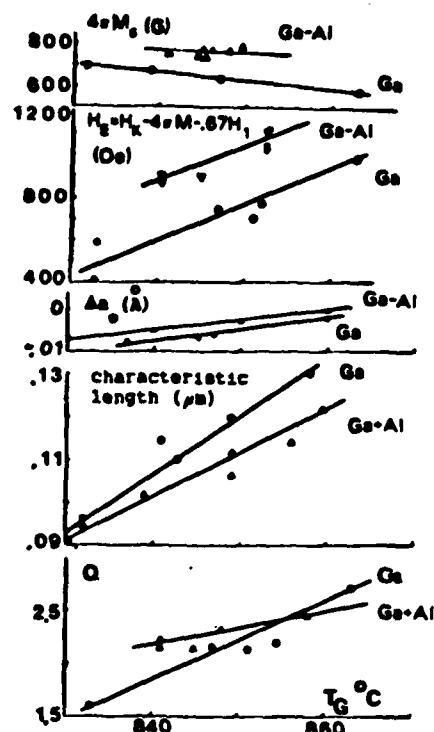


Fig. 1: Material Parameters Versus Growth Temperature for 1.0  $\mu\text{m}$  Films using Ga and Ga-Al based Compositions

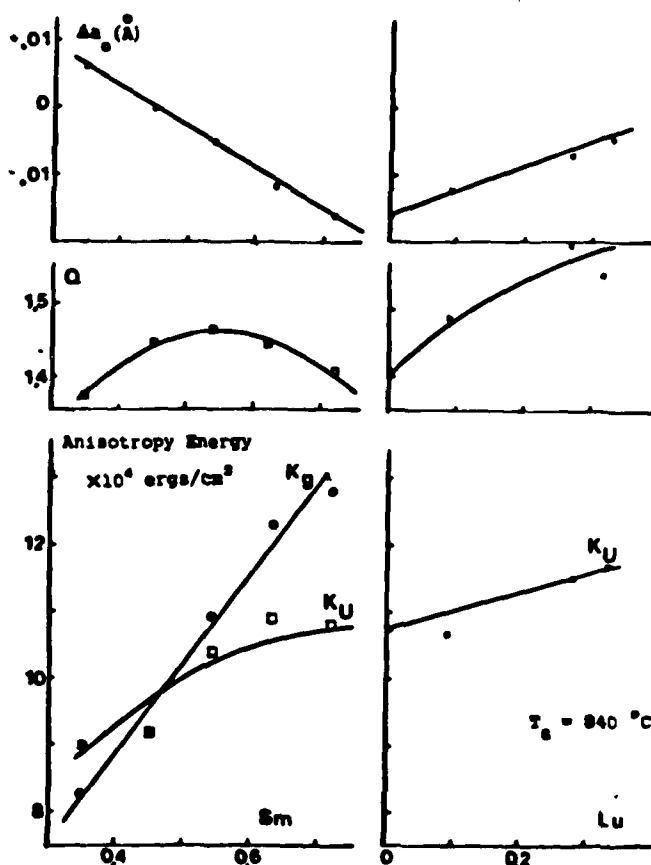


Fig. 2:  $K_t$ ,  $K_u$ ,  $Q$ , and  $\Delta H_a$  Versus Sm and Lu Content

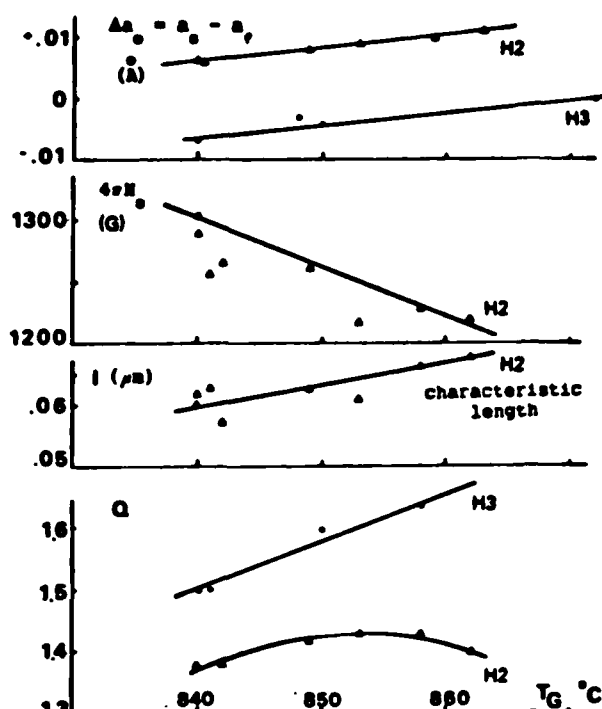


Fig. 3: 0.5  $\mu$ m Material Parameters Versus Growth Temperature

Samarium additions increased the uniaxial anisotropy energy  $K_u$ , as shown in Fig. 2. However, increasingly unfavorable lattice mismatch at high Sm concentrations limited its effectiveness.  $K_u$  is also plotted versus Sm content in Fig. 2.  $K_u$  was calculated from  $K_u = K_s - K_e$ , where  $K_s$  is the stress induced anisotropy energy,  $K_s = 1.5\sigma\lambda_{111}$ , where  $\sigma$  is the mismatch induced stress.  $K_e$  is negative for negative mismatch. Lutetium additions were effective in increasing  $K_u$  and decreasing negative effect of  $K_e$  due to its small ionic radius, thus increasing Q.  $4\pi M_s$  remains nearly constant, increasing slightly with Sm addition and decreasing slightly with Lu addition.

We measured the lattice mismatch on films from each melt which were grown at 840°C. As shown in Fig. 2, Sm addition increases the lattice parameter 0.061 Å/Sm ion in the garnet formula. This is comparable to 0.051 Å/Sm ion predicted for Sm substitution into YIG [8]. We note that YIG has the same lattice parameter, 12.376 Å, as the film grown from melt H2. The Lu addition resulted in a -0.036 Å/Lu ion decrease in lattice parameter which is comparable to -0.039 Å/Lu predicted for Lu substitution into a film with a 12.399 Å lattice parameter, which is the lattice parameter of the film containing 0.72 Sm ions. Lutetium is expected to substitute octahedrally as well as dodecahedrally resulting in a smaller decrease in lattice parameter. Linearity of mismatch versus Sm content, provides evidence that Sm increase in the film is proportional to the amount added to the melt.

As noted above,  $H_1$  decreases from -155 Oe to -110 Oe as bubble size is reduced from 1  $\mu$ m to 0.5  $\mu$ m. This decrease is attributed to the increase in  $4\pi M_s$ . The crystalline anisotropy energy  $K_1$  increases slightly for the smaller bubble material. The temperature dependence of  $H_1$  and  $H_K$ , given in Table III, is in agreement with expected decrease in exchange effects with increasing temperature. The increase in  $\lambda_{111}$  for the 0.5  $\mu$ m garnet is attributed to the higher iron and samarium content.

Device margins are given in Table IV. Direct comparison of results is not possible due to difference in period size. Margins were measured at quasi-static

frequencies. The ion-implantation energy and dose were selected to give a uniform damage level with a thickness approximately 30% of the total film thickness using data provided by Gallagher [9]. Ion dose is chosen so that the change in the uniaxial anisotropy field,  $\Delta H_K$ , will exceed  $H_K$  of the non-implanted material. However, too high a dose is undesirable, as it will destroy the magnetization. We found no saturation of  $\Delta H_K$ , due to the use deuterium as the primary implant species. The higher strain required to obtain the same anisotropy field change in the 0.5  $\mu$ m as in the 1  $\mu$ m material is attributed to the higher  $4\pi M_s$ .

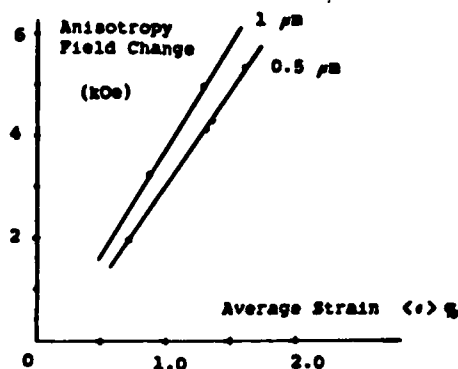


Fig. 4: Implantation Induced Change in  $H_K$  Versus Strain

#### CONCLUSION

The (Y Sm Gd Tm) (Fe Al Ga) garnets are well suited for 1.0  $\mu$ m material use. They have good temperature properties and can be grown with good reproducibility. Lattice parameter is easily matched to GGG substrate.

The (Y Sm Tm Gd Lu) (Fe Al) garnet system is suitable as 0.5  $\mu$ m diameter bubble, ion-implantable material. The temperature coefficient of collapse field closely matches the temperature coefficient of magnetization for the standard barium ferrite bias magnets. The temperature dependence of the anisotropy field appears to be sufficient to prevent low Q related problems at temperatures up to 100°C. Use of Lu is important both to reduce lattice parameter and to increase growth induced anisotropy.

Both garnet systems have a relatively high  $\lambda_{111}$ , which makes them suitable for ion-implanted bubble devices. Ion implantation with deuterium and oxygen provides adequate change in uniaxial anisotropy field without turning the material amorphous. Use of Al instead of Ga, or in addition to Ga, is helpful in achieving a lattice match and in decreasing the exchange constant.

#### ACKNOWLEDGEMENTS

The authors would like to thank Dr. A. Guzman and J. Tabacchi for ion implantation and S. Jo for device fabrication and testing.

#### REFERENCES

1. H. J. Levinstein, R. W. Landorf, S. J. Licht, S. L. Blank, Appl. Phys. Lett., **19**, 486, (1971).
2. X. Wang, C. S. Krafft, M. H. Kryder, Paper No. CB-07, presented this conference
3. D. C. Fowles, J. A. Copeland, AIP Conf. Proc., **5**, 240, (1972).
4. W. T. Stacy, M. M. Janssen, J. Cryst. Growth, **27**, 282, (1974)
5. K. Ju, H. L. Hu, R. G. Hirko, E. B. Moore, D. Y. Seiki, R. D. Schwenker, IBM J. Res. Develop., **25**, 295, (1981).
6. J. W. Nielsen, IEEE Trans. on Magn., **MAG-12**, 327, (1976).
7. M. H. Kryder, IEEE Trans. on Magn., **MAG-17**, 8, 2385, (1981).
8. A. H. Eschenfelder, *Magnetic Bubble Technology*, Springer-Verlag, New York, (1980).
9. T. Gallagher, private communication.

343

# INVESTIGATIONS OF IMPLANTATION-INDUCED CHANGES IN SURFACE LAYERS OF EPITAXIAL GARNET THIN FILMS

M.H. Kryder, X. Wang, C.S. Krafft, A.M. Guzman

The authors are with Carnegie-Mellon University, Pittsburgh,  
Pa. 15213 USA.

## ABSTRACT

Using newly improved FMR characterization techniques, we have established that mechanisms other than the implantation-induced stress are responsible for uniaxial anisotropy field change. We have measured  $\lambda_{111}/M_s$  and the crystalline anisotropy field  $H_1$  in the implanted layer.  $H_1$  is shown to decrease after implantation.

## INTRODUCTION

The mechanisms responsible for ion implantation-induced changes in the magnetic parameters of garnet films are not completely understood. Early investigators attributed the in-plane anisotropy in the implanted layer to compressive stress and magnetostrictive effects [1, 2]. More recent measurements have led to the suggestion that implantation reduces the magnetization [3] and the growth-induced anisotropy [4]. Here, we report on implantation-induced changes in the effective uniaxial anisotropy field  $H_E = H_K - 4\pi M_s - 2/3 H_1$ , the magnetocrystalline anisotropy  $H_1$ , and the magnetostriction coefficient  $\lambda_{111}$ . By measuring the change in uniaxial anisotropy field due to pressure-induced strain, and the implantation created strain, we are able to determine the stress-induced anisotropy contribution to the total uniaxial anisotropy field change. Results are presented for 1  $\mu\text{m}$  and 0.5  $\mu\text{m}$  diameter bubble garnets.

## EXPERIMENTAL DETAILS

Investigations were carried out on films which were grown by standard LPE method [5] on 1 inch diameter GGG substrates. Nominal compositions, based on unity segregation coefficients for the rare-earth oxides, and material parameters are given in Table 1. Measurements of anisotropy fields and magnetostriction coefficient were carried out on full wafer garnets in a wide band resonance spectrometer with microstrip transmission line [6]. The wideband system eliminates inaccuracies caused by cavity detuning and coupled resonances while making it possible to measure resonance at low fields thereby improving the accuracy of anisotropy field measurements. The high sensitivity of the microbox structure, attributed to the use of a long, serpentine-shaped conductor, placement of the sample between the conductor and the ground plane, and use of an inner/outer DC block, enables us to make measurements on thin ion-implanted layers.

$H_E$  and the gyromagnetic ratio  $\gamma$ , are determined from the frequency dependence of the resonance field.  $H_1$  is calculated from the angular dependence of the resonance field at a fixed frequency.  $\lambda_{111}$  is determined from the resonance field shift which is caused by applying a vacuum pressure to one side of the wafer. Strain due to implantation is measured from x-ray rocking curves using the method of Speriosu [7]. Saturation magnetization in the bulk film is determined from thickness, stripwidth, and collapse field measurements [8].

Accuracy of resonance field shift measurement is  $\pm 10$  Oe. To determine  $H_1$  to an accuracy of  $\pm 10$  Oe in the implanted layer, thin films were implanted so that they had a negligible bulk layer. Problems with mode overlap make measurement difficult on films which have thick bulk layers with low anisotropy field values.

## THEORY

The total change in uniaxial anisotropy field  $\Delta H_K$  may be attributed to magnetostriction due to implantation-induced strain which creates a stress, and mechanisms independent of stress. The strain in the implanted film is measured directly from x-ray rocking curves. Applying a pressure to the sample, we are able to measure an additional stress-induced change in anisotropy field,  $\delta H_{111}$ . The additional strain in the implanted layer is the same as the additional strain in the outermost layer of the GGG substrate. The calculation of this strain is reported in the literature [9, 10]. If we assume that the stress-induced change in anisotropy field is linearly proportional to the strain, we can separate the implantation-induced stress effect from non-stress related change in anisotropy field.

The average additional strain in the outermost layer of the GGG substrate, obtained by integration over the conductor line pattern is given by [6]:

$$\delta \epsilon_s = (1-\nu)/2 \times 1.526 \times a^2/T^2 \times q/E \quad (1)$$

where  $\nu$  is Poisson's ratio, 0.29 for GGG,  $a$  is the o-ring inner radius,  $q$  is the applied pressure,  $T$  is the wafer thickness, and  $E$  is Young's modulus. The ion implantation-induced strain can be found from x-ray diffraction data using the following equation:

$$\Delta \epsilon_i = \Delta d_i/d_i \times (1-\nu_i)/(1+\nu_i) \quad (2)$$

where  $\nu_i$  is Poisson's ratio in the implanted layer and  $\Delta d_i/d_i$  is the fractional change in lattice parameter in the direction normal to the film plane, determined from Bragg condition and given by

$$\Delta d/d = \Delta \theta / \tan \theta_B \quad (3)$$

where  $\Delta \theta$  is the angular separation between the film and implanted layer peak and  $\theta_B$  is the Bragg angle. The average strain in the direction normal to the film plane is given by [7]:

$$\langle \epsilon \rangle = -\Delta\theta \left( |\gamma_H| (1-\gamma_H^2)^{1/2} + \gamma_H^2 \tan\theta_B \right)^{-1} \quad (4)$$

where  $\gamma_H$  is the direction cosine for the diffracted wavevector. Equation (4) includes a correction which accounts for changes in the direction and magnitude of the reciprocal lattice vector. We can find the stress-induced anisotropy field change  $\Delta H_{K\text{stress}}$  from:

$$\Delta H_{K\text{stress}} = \Delta\epsilon / \delta\epsilon_s \times \delta H_{111} \quad (5)$$

To determine  $\lambda_{111}$ , we used the equation given by Wang et al. [6]:

$$\lambda_{111} = 4\pi M_s T^2 \delta H_{111} / 28.76 a^2 q \quad (6)$$

where  $T$  is the wafer thickness,  $\delta H_{111}$  is the measured resonance field shift due to the additional pressure-induced strain,  $q$  is the applied pressure, and  $a$  is the inner radius of the supporting ring which forms the vacuum seal between the microbox and the wafer.

The calculation of  $H_1$  is described elsewhere [6].

## RESULTS

The material parameters are given in Table I. These include the magnetization  $4\pi M_s$ , characteristic length  $l$ , effective anisotropy field  $H_E = H_K - 4\pi M_s - 2/3 H_1$ , lattice mismatch  $\Delta a_0 = a_s - a_f$ , crystalline anisotropy field  $H_1$ , and epitaxial film thickness  $t$ .  $4\pi M_s$  and  $l$  were determined from collapse field, zero-field stripwidth, and film thickness measurements [8]. Films 1 and 3 are  $1\mu\text{m}$  diameter bubble material, whereas films 2 and 4 are  $0.5\mu\text{m}$  diameter bubble material.

All of the films were implanted with  $5 \times 10^{15}/\text{cm}^2$  molecular deuterium ions at 60 keV and  $9.5 \times 10^{13}/\text{cm}^2$  atomic oxygen ions at 110 keV. Film 1 was implanted twice with this dose. The results of FMR and X-ray measurements are given in Table II. The average strain for films 2, 3, and 4 is the same. Difference in

strain for film 1 is unexplained, but may be due to some unknown difference in implant conditions. Implant thickness, determined from Pendellosung interference [11], is  $3500 \text{ \AA}$ . Implant dose was selected to give a  $1.5 \text{ eV/\AA}^3$  damage level [12]. Fine tuning of implant conditions to optimize the damage profile was not done.

In Fig. 1 experimental resonance field measurements for film 2 are plotted for bulk and ion implanted layer. Solid curves are for calculated  $H_1$  values,  $-115 \text{ Oe}$  in the bulk layer and  $-40 \text{ Oe}$  in the implanted layer. Note that fit of experimental data to theoretical curves is quite good.

The results for the implanted films are given in Table II.  $\Delta H_K$  is the total anisotropy field change, as determined by separation of bulk and main implanted layer mode resonance fields.  $\Delta H_{K \text{ stress}}$  is determined from resonance field shift of implanted layer mode.  $\langle \epsilon \rangle$  is the average stress normal to the film plane. In Fig. 2  $\Delta H_K$  and  $\Delta H_{K \text{ stress}}$  are plotted versus average strain for film 1.

The linewidth and gyromagnetic ratio of the implanted layer was not appreciably different from that in the bulk film for the implant doses we investigated. Several resonance modes associated with the implanted layer were observed, but only the main mode was used for  $H_K$ ,  $H_1$ , and  $\lambda_{111}$  measurements.

The magnetostriction coefficient was determined to be  $-3.3 \times 10^{-6}$  for the non-implanted layer on film 1 and  $-3.8 \times 10^{-6}$  on film 2.  $\lambda_{111}/M_s$  was determined to be  $-6.14 \times 10^{-6} \text{ G}^{-1}$  on film 1 and  $-3.48 \times 10^{-6} \text{ G}^{-1}$  on film 2, after implantation but  $4\pi M_s$  was not measured.

Straining the films caused approximately the same resonance field shift for bulk and implanted layers for the same applied pressure. For film 1, at 635 mm Hg pressure, we measured 85, 80

and 79 Oe field shifts for the non-implanted, singly, and doubly implanted films, respectively. The resonance field shift for film 2 was 38 Oe for both non-implanted and implanted layers. This implies that  $\lambda_{111}/M_s$  is a constant so if  $M_s$  is reduced by this implant dose, then  $\lambda_{111}$  must also be reduced proportionately.

#### DISCUSSION

The measurement of the implantation-induced stress contribution to anisotropy field change is based on the assumption that the stress-induced anisotropy field change is linearly proportional to the strain. By measuring the resonance field shift due to the additional strain in the implanted layer, measuring implant strain, and calculating the pressure-induced strain, we are able to determine  $\Delta H_K$  due to implant strain. With this technique, we do not need to know  $E$ ,  $\nu$ ,  $\lambda_{111}$ , or  $M_s$  in the implanted layer. We expect that  $E$  and  $\nu$  will not change appreciably, while  $M_s$  is expected to decrease.

The anisotropy field change  $\Delta H_E$  does not saturate due to use of deuterium as primary implant species [13]. The deuterium implant is used to create the deep level damage, and is the major source of the measured anisotropy field change. The oxygen implant is designed to make the strain near the surface of the implanted layer match the strain in the deep layer caused by the deuterium implant.

The anisotropy energy density due to stress is nearly the same for both materials, but differences in  $M_s$  cause the stress-induced anisotropy field to be higher for the 1  $\mu\text{m}$  material. For identical amounts of strain,  $\Delta H_K$  is 3200 Oe for film 3 and 1800 Oe for film 4. The anisotropy energy change is  $97.5 \times 10^3$  ergs/cm<sup>3</sup> for film 3 and  $90.7 \times 10^3$  ergs/cm<sup>3</sup> for film 4. Thus



within experimental uncertainty in  $4\pi M_s$  and  $\Delta H_K$  measurement, we obtain the same change in energy density for different size bubble materials implanted under identical conditions.

The contribution due to stress is related to  $\lambda_{111}/M_s$ . The most significant difference between 1  $\mu\text{m}$  and 0.5  $\mu\text{m}$  materials is in  $M_s$ , as  $\lambda_{111}$  does not differ appreciably. The  $\Delta H_K$  stress contributes approximately 2/3 of the total  $\Delta H_K$  for the 1  $\mu\text{m}$  material, and 1/2 for the 0.5  $\mu\text{m}$  material. The remaining portion, not attributed to  $\Delta H_{K\text{stress}}$ , does increase with strain, from 810 Oe for 0.86% strain to 1742 Oe for 1.27% strain for film 1. However, this increase is more likely due to increased damage and disorder created by heavier implant dose at higher strain levels, than due to pure magnetostrictive effects.

$H_i$  decreases with implantation, from -155 Oe to -40 Oe for film 1, from -115 Oe to -40 Oe for film 2, and from -115 Oe to -25 Oe for film 4. The larger change in the 1  $\mu\text{m}$  material is believed to be due in part to a lower exchange constant. We suggest that the same mechanism which is responsible for change in  $\Delta H_K$  not related to stress, is acting to reduce  $H_i$  in the implanted layer. The reduction of  $H_i$  is indicative of disorder being introduced into the crystalline material by the implantation.

### CONCLUSION

Direct measurements of stress-induced changes in the anisotropy field of ion-implanted magnetic garnet films has shown that stress alone can not account for the total change in anisotropy field. The additional change, which is believed to be related to disordering of the crystal lattice, is nearly the same for 1  $\mu\text{m}$  and 0.5  $\mu\text{m}$  diameter bubble materials. A significant difference in total anisotropy field change for the different size

bubble materials was found and is attributed to difference in stress-induced anisotropy field change which is inversely proportional to  $4\pi M_s$ . It was found that  $\lambda_{111}/M_s$  remained constant in implanted layers of films investigated, indicating that any change in  $\lambda_{111}$  is proportional to a change in  $4\pi M_s$ . Finally, a substantial reduction of  $H_i$  with implantation was found which is in agreement with the trend of the crystal structure becoming disordered by the implantation.

#### ACKNOWLEDGEMENTS

The authors would like to thank Dr. J. O. Artman for use of his FMR equipment, J. Tabacchi for ion implantation, and V. Speriosu for help with x-ray analysis.

This work was supported by the Air Force Office of Scientific Research under grant number AFOSR-80-0284 and by the National Science Foundation under grant number ECS-7912677.

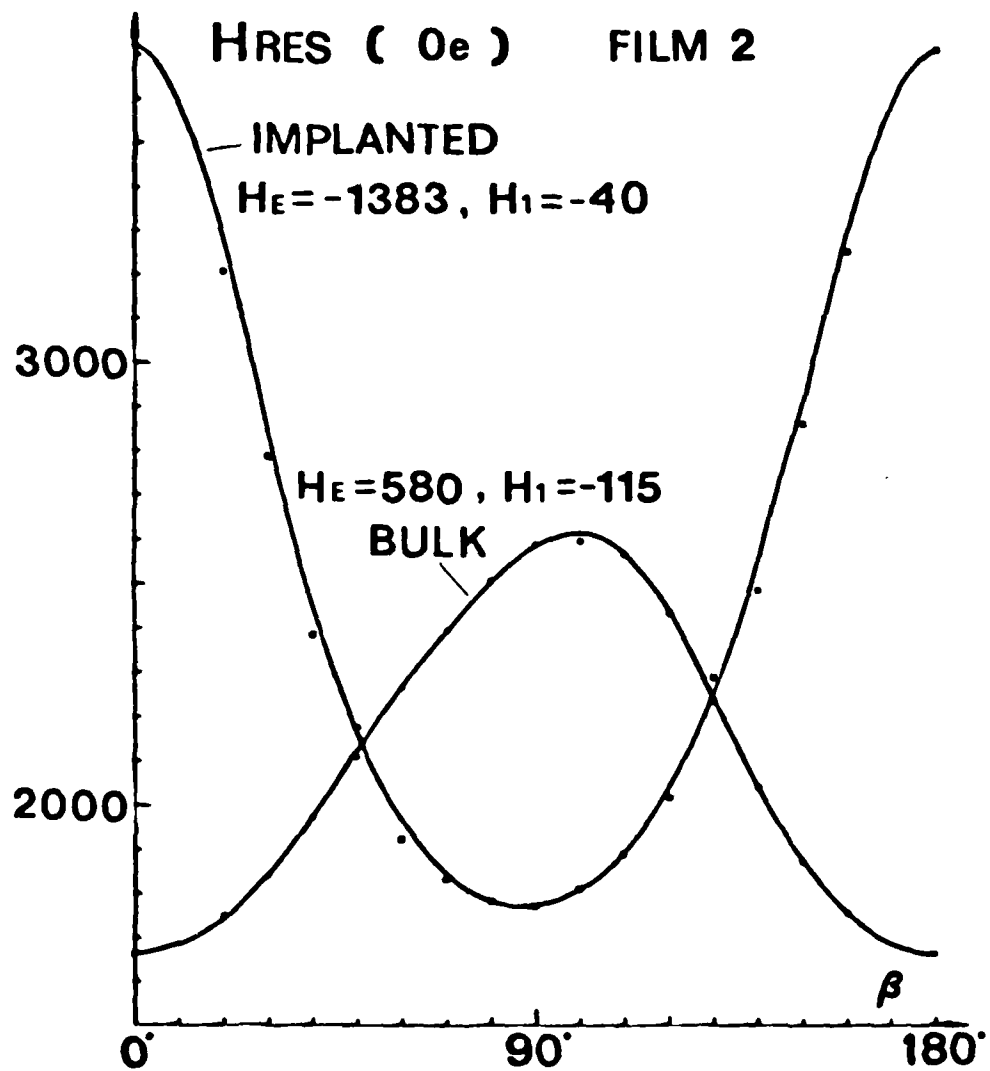
Table I: Material Parameters

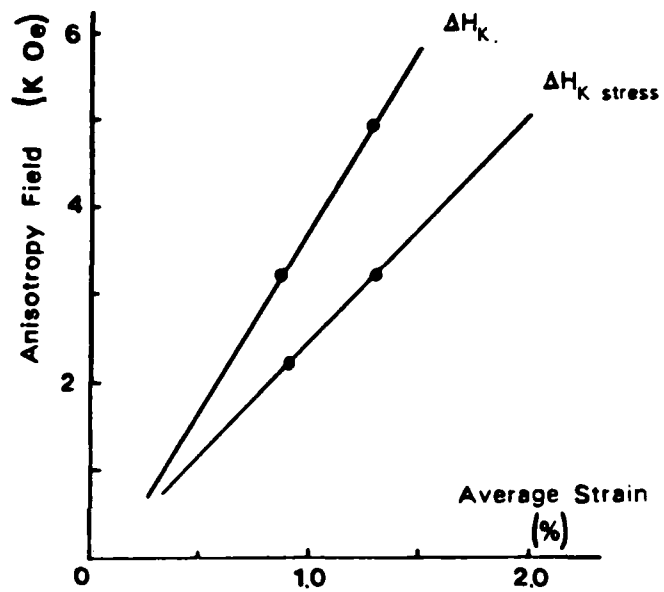
Film	$4\pi M_s$	$l$	$H_E$	$\Delta a_0$	$H_1$	$t$
1	636 (G)	.136 ( $\mu\text{m}$ )	1060 (Oe)	+0.002 ( $\text{\AA}$ )	-160 (Oe)	1.26 ( $\mu\text{m}$ )
2	1370	.057	580	-.012	-115	0.5
3	766	.113	1009	-.003	-155	.39
4	1266	.059	558	0.000	-115	.85

Film	Compositions						
1,3	$\text{Y}_{0.8}$	$\text{Sm}_{0.3}$	$\text{Gd}_{0.6}$	$\text{Tm}_{1.3}$	$\text{Fe}_{4.65}$	$(\text{Al Ga})_{0.35}$	$\text{O}_{12}$
2,4	$\text{Y}_{1.0}$	$\text{Sm}_{0.45}$	$\text{Gd}_{0.3}$	$\text{Tm}_{1.25}$	$\text{Fe}_{4.8}$	$\text{Al}_{0.2}$	$\text{O}_{12}$

Table II: Implanted Film Results

Film-Implant	$\langle \epsilon \rangle$	$\Delta H_K$	$\Delta H_{K \text{ stress}}$	$H_1$
1-1	0.86 (%)	3033 (Oe)	2223 (Oe)	-40 (Oe)
1-2	1.27	4950	3208	
2	0.70	1963	870	-40
3	0.71	3200		
4	0.70	1760		-25





## References

1. Y.S. Lin, G.S. Almasi, G.E. Keefe, IEEE Trans. on Magn., MAG-13, 1744, 1977 .
2. R. Wolfe, J.C. North, R.L. Barns, M. Robinson, and H.J. Levinstein, Appl. Phys. Lett., 19, 298, 1971 .
3. C.H. Wilts and S. Prasad, IEEE Trans. on Magn., MAG-17, 2405, 1981 .
4. G.P. Vella-Coleiro, R. Wolfe, S.L. Blank, R. Caruso, T.J. Nelson, and V.V.S. Rana, J. Appl. Phys., 52, 2355, 1981 .
5. H. J. Levinstein, R. W. Landorf, S. J. Licht, S. L. Blank, Appl. Phys. Lett., 19, 486, 1971 .
6. X. Wang, C. S. Krafft, M. H. Kryder, Paper No.CB-07, Joint Intermag- Magnetism and Magnetic Materials Conference, Montreal July 20-23, 1982, to be published in IEEE Trans. on Magn.
7. V.S. Speriosu, J. Appl. Phys., 52, 10, 6094, 1981 .
8. D. C. Fowles, J. A. Copeland, AIP Conf. Proc., 5, 240, 1972 .
9. S. Timoshenko, S. Woinowsky-Krieger, *Theory of Plates and Shells*, McGraw-Hill, New York, (1959).
10. G. P. Vella-Coleiro, Rev. Sci. Instrum., 50, 9, 1130, 1979 .
11. W.T. Stacy, M.M. Janssen, J. Cryst. Growth, 27, 282, 1974 .
12. T. Gallagher, private communication.
13. C. S. Krafft, X. Wang, M. H. Kryder, Paper No.CB-07, Joint Intermag- Magnetism and Magnetic Materials Conference, Montreal July 20-23, 1982, to be published in IEEE Trans. on Magn.

**LIST OF FIGURES**

- Fig. 1:** Experimental Resonant Field Data and Theoretical Resonant Field Curves Versus Applied Field Angle for Calculated  $H_1$  Values 10
- Fig. 2:** Total and Stress-Related Anisotropy Field Change versus Average Strain for Film 1 11



# THE EFFECT OF ION IMPLANTATION ON EPITAXIAL MAGNETIC GARNET THIN FILMS

Alberto M. Guzman, Charles S. Krafft, Xubin Wang, Mark H. Kryder  
Carnegie-Mellon University, Pittsburgh, Pennsylvania 15213, USA

## ABSTRACT

Recently investigators have reported that ion implantation of magnetic garnet films causes magnetostrictive effects related to stress as well as effects not directly related to stress, such as the suppression of growth-induced anisotropy [1]. This suppression occurs especially in the case of heavy dose implantations, such as  $2 \times 10^{14}$  at/cm<sup>2</sup> Ne for example. We report here on the measurement of the stress contribution to implantation-induced anisotropy field change and the total anisotropy field change in films which have compositions suitable for 1  $\mu$ m and 0.5  $\mu$ m diameter bubbles. We also report on the measurement of the crystalline anisotropy field in the implanted layer. Films were implanted with deuterium and oxygen ions. Motivation for this choice is discussed.

## INTRODUCTION

Ion implantation of magnetic garnet epitaxial thin films has received considerable attention since its use in altering the magnetic anisotropy of garnet crystals was first reported in 1971 [2]. Implantation has been used for hard bubble suppression and in the fabrication process for contiguous disk bubble devices [3]. The effects of implantation have recently been the subject of numerous investigations [4, 5, 6, 7]. Selection of ions and of implantation conditions has been based to a large extent on experimental results. The understanding of the implant mechanisms has lagged behind its application due in part to the complex nature of these mechanisms and difficulties in characterizing implanted layers.

As techniques are developed and applied to characterization of implanted garnet films, more of the uncertainties regarding the implant mechanisms are being revealed. One goal of these investigations is to reach a better understanding of the implantation process so that implant conditions and ion

species may be selected to provide optimal properties for submicron diameter ion-implanted bubble devices.

We report on the use of newly improved ferromagnetic resonance characterization techniques to determine the crystalline anisotropy field  $H_1$  in the implanted layer, and to determine the stress contribution to the implantation-induced uniaxial anisotropy field change.

### BACKGROUND

Magnetic garnet films are grown by liquid phase epitaxy (LPE) on non-magnetic garnet substrates, such as (111) oriented  $\text{Gd}_3\text{Ga}_5\text{O}_{12}$  (GGG) [8]. By choosing the appropriate rare earth ions in the  $[\text{R.E.}]_3\text{Fe}_5\text{O}_{12}$  garnet formula and the growth conditions, one can produce a film which has a uniaxial anisotropy energy density of the form

$$E_K = K_U \sin^2 \theta \quad (1)$$

where  $\theta$  is the angle between the magnetization  $M$  and film normal and  $K_U$  is the uniaxial anisotropy parameter. If  $E_K$  exceeds the demagnetizing energy density of the film  $2\pi M_s^2$ , where  $4\pi M_s$  is the saturation magnetization, the magnetization will be oriented perpendicular to the film. The predominant factor contributing to the uniaxial anisotropy energy is believed to be the preferential ordering of the large and small rare-earth ions during growth [9]. In addition to the growth-induced anisotropy energy, there is a stress-induced anisotropy energy which is attributed to magnetostrictive effects. For films with a negative magnetostriction coefficient ( $\lambda_{111}$ ), which is typical for most of the commonly used bubble compositions, a compressive stress will create a negative stress-induced uniaxial anisotropy energy which opposes  $E_K$ .

Instead of discussing changes in anisotropy energy density, one often speaks in terms of the anisotropy field  $H_K = 2K_U/M_s$ . In an otherwise isotropic material, so long as  $H_K > 4\pi M_s$ , the demagnetizing field of the film, the magnetization will lie perpendicular to the film plane. Garnet films, being cubic crystals, also exhibit a cubic crystalline anisotropy field  $H_1$ , which adds to the

uniaxial anisotropy and demagnetizing fields in such a manner that the total effective anisotropy field of a garnet film is

$$H_E = H_K - 4\pi M_s - (2/3)H_1 \quad (2)$$

The effects of ion implantation include displacement of oxygen cations and other garnet ions from their regular lattice sites and the formation of dislocations before thermal annealing [10]. The strain in the implanted layer is attributed to the displacement of the atoms in the lattice due to nuclear stopping of the implanted ions [11] and the presence of the implanted species. Since the film is constrained laterally by the substrate, it deforms by expanding slightly in a direction perpendicular to the film plane. The compressive stress in the plane is given by:

$$\sigma = E/(1-\nu) \times \Delta d/d \quad (3)$$

where  $E$  is Young's modulus,  $\nu$  is Poisson's ratio, and  $\Delta d/d$  is the fractional change in lattice parameter in the direction normal to the film plane.  $\Delta a/a = (1-\nu)/(1+\nu) \times \Delta d/d$  is the corrected strain, which accounts for the film being constrained laterally by the substrate. We assumed that  $E$  and  $\nu$  in the LPE film were equal to  $E$  and  $\nu$  in the GGG substrate. The stress gives rise to an energy:

$$E_{K_s} = (3/2)\sigma\lambda_{111}\sin^2\theta = K_s\sin^2\theta \quad (4)$$

which describes an anisotropy with hard axis perpendicular to the film plane since  $\lambda_{111} < 0$  and  $\sigma > 0$  perpendicular to the plane. The total anisotropy energy density is given by:

$$E = E_K + E_{K_s} \quad (5)$$

With sufficient implant dose,  $E_{K_s} + E_K$  will be less than  $2\pi M_s^2$ , causing the magnetization to lie in the plane of the film. The in-plane magnetization layer provides flux closure, preventing the formation of hard bubbles [3], and will support charged walls, which are the basis for contiguous disk (C.D.) bubble device propagation [12]. The ion-implanted garnet is shown schematically in Fig. 1. The gold or photoresist pattern on the surface serves as an implantation mask.

In the implanted regions there is an in-plane magnetization  $M$ . As there is a discontinuity in  $M$  at the implanted-nonimplanted boundary, magnetically charged walls are formed, as shown in Fig. 1. Bubbles are attracted to the edge of the implanted pattern and to the charged walls. When a rotating in-plane field is applied, the charged walls move around the implanted patterns, and thus propagate the underlying bubbles. The thicknesses given in Fig. 1 are for a 1  $\mu\text{m}$  diameter bubble device.

The implant dose for C.D. devices must be enough so that the change in anisotropy field exceeds the effective uniaxial anisotropy field  $H_E$ . Typically, a higher implant dose is used than that required to make  $H_E$  zero in the implanted layer. The optimal anisotropy field change is determined by experimentally finding the maximum range in bias fields over which a device will operate. The optimum dose for hard bubble suppression is generally in the range which is sufficient to create a layer with in-plane magnetization. Too high a dose will cause the garnet to become paramagnetic, resulting in a lower collapse field due to a shortening effect on the bubble height, and the reappearance of hard bubbles [13].

Hydrogen and deuterium have been found to exhibit a linear dependence of the implantation-induced anisotropy field change on implant dose. All other ions exhibit a linear dependence at low to moderate doses, but the anisotropy field change is found to saturate at high doses [14]. Hydrogen and deuterium ions lose their energy predominantly through electron interactions, whereas all other ion species have a significant nuclear energy loss. In Table I, we list values for mean projected range, projected standard deviation, and nuclear and electronic energy loss for deuterium at 60 keV and oxygen at 110 keV [15].

The choice of deuterium and oxygen as implant species in our investigations was based on several factors. The main advantage of the deuterium implant is the non-saturation of the change in anisotropy field with implant dose. The necessary anisotropy field change increases as bubble diameter decreases, making

deuterium a preferred ion species for submicron diameter bubble devices [14]. A disadvantage of the deuterium implant is the diffusion of implanted ions out of the film upon annealing. This can be prevented by depositing a  $\text{SiO}_2$  layer on top of the implanted layer [16]. Compared to hydrogen, deuterium requires 1/2 the dose and thus 1/2 the implantation time, which can be considerable at low current levels necessary to prevent self annealing. Molecular deuterium ions, with mass 4, are used instead of atomic deuterium ions, reducing the required dose by another factor of two. Oxygen implant is used to make the strain at the surface of the garnet equal to that due to the deep level deuterium implant. Oxygen implant time is considerably shorter than deuterium due to the lower dose required. The combination of ion species is more efficient than using different energies with the same species to achieve a uniform strain profile.

Recently, it has been suggested that the stress-induced contribution to the uniaxial anisotropy field change is linear with implant dose, while the intrinsic growth-induced anisotropy is suppressed at typical device dose levels,  $\text{Ne } 2 \times 10^{14}/\text{cm}^2$ , regardless of its initial value [1]. This implies that a significant reduction in the anisotropy field is due to *non-stress related mechanisms* in films with a large growth-induced anisotropy. Thus the anisotropy field change necessary for submicron diameter bubble devices will be realized by a combination of effects.

#### EXPERIMENTAL TECHNIQUES

Garnet films were implanted with molecular deuterium and atomic oxygen ions. Current density ranged from  $0.3 \mu\text{A}/\text{cm}^2$  to  $1.0 \mu\text{A}/\text{cm}^2$ . The ion beam is scanned at frequencies of 4000 Hz vertical and 300 Hz horizontal over a 7.6 cm diameter area. Beam diameter is approximately 1.3 cm. Samples are attached to a silicon substrate with bees wax. The Si wafer is then placed on the wafer chuck. There is no cooling system on the chuck.

Measurements of anisotropy fields and the magnetostriction coefficient ( $\lambda_{111}$ ) were carried out on full wafer, one inch diameter garnets in a wide band

resonance spectrometer with a microstrip transmission line [17]. A block diagram for the spectrometer system is shown in Fig. 2. The microbox structure and serpentine conductor pattern are shown schematically in Fig. 3. The high sensitivity of the microbox structure, attributed to the use of a long, serpentine-shaped conductor, placement of the sample between the conductor and the ground plane, and use of an inner/outer DC block, enables us to make measurements on thin ion-implanted layers.

The ferromagnetic resonance (FMR) condition for the field applied along the [111] direction, normal to the film plane is given by:

$$\omega = \gamma(H + H_E) \quad (6)$$

where  $\omega$  is the angular velocity of spin precession, which is equivalent to the microwave frequency,  $\gamma$  is the ratio of the magnetic moment to the angular momentum, and  $H$  is the external field. The zero-field intercept of the resonance field versus frequency plot divided by the slope  $\gamma$  gives the effective anisotropy field  $H_E = H_K - 4\pi M_s - (2/3)H_1$ .  $H_1$  is calculated from the angular dependence of the resonance field at a fixed frequency [18].

The magnetostriction coefficient  $\lambda_{111}$  is determined from the resonance field shift  $\delta H_{111}$ , which is caused by applying a vacuum pressure to one side of the wafer [17]. The resonance field shift is related to  $\lambda_{111}$  divided by the saturation magnetization by the following expression which we derived to determine  $\lambda_{111}$  in non-implanted films:

$$\lambda_{111}/4\pi M_s = \delta H_{111} T^2 / 28.76 a^2 q \quad (7)$$

where  $T$  is the wafer thickness,  $a$  is the inner radius of the supporting o-ring which forms a vacuum seal with the wafer, and  $q$  is the applied pressure.  $\delta H_{111}$  is linear with strain, as shown in Fig. 4. Saturation magnetization  $4\pi M_s$  in the bulk film is determined from thickness, stripwidth, and collapse field measurements [19].

Film thickness  $t$ , is measured with a reflectance spectrometer by the interference method. Strain due to implantation and lattice mismatch  $\Delta a_0 =$

$a_{\text{substrate}} - a_{\text{film}}$  are measured with a double crystal x-ray diffractometer using (888) reflection with  $\text{Cu-K}_{\alpha 1}$  radiation. The stress is determined from the measured strain [20].

The uniaxial anisotropy field change  $\Delta H_E = H_{E \text{ bulk}} - H_{E \text{ implanted}}$  is determined from the resonance field separation of main implanted layer mode and bulk mode measured at the same frequency. The total  $\Delta H_E$  may be attributed to magnetostriction due to implantation-induced stress and mechanisms independent of stress. From the resonant field shift measurement we determined the stress-induced change in anisotropy field due to ion implantation. By comparing the total anisotropy field shift due to implantation with the anisotropy field shift in the implanted layer produced by applying tension to the wafer, it is possible to determine the portion of the total anisotropy field shift which is due to stress-magnetostrictive effects.

The determination of the stress-induced contribution to the anisotropy field change is made from the following equation:

$$\Delta H_{K\text{stress}} = \Delta \epsilon_i / \delta \epsilon_s \times \delta H_{111} \quad (8)$$

where  $\delta \epsilon_s$  is the average additional strain in the outermost layer of the GGG substrate and is given by [17]:

$$\delta \epsilon_s = (1-\nu)/2 \times 1.526 \times a^2/T^2 \times q/E \quad (9)$$

where  $T$ ,  $a$ , and  $q$  are the same variables as those used in Eq.(7). The ion implantation-induced strain  $\Delta \epsilon_i$ , determined from x-ray diffraction measurements, is given by:

$$\Delta \epsilon_i = \Delta d_i/d \times (1-\nu_i)/(1+\nu_i) \quad (10)$$

where  $\nu_i$  is Poisson's ratio in the implanted layer, which we assume does not change from that in the bulk film.  $\Delta d_i/d$  is determined from angular separation between film peak and the location in the peaks due to the implanted layer corresponding to the average strain. Equation (10) accounts for the fact that the film is constrained laterally by the substrate.

## RESULTS

The material parameters and compositions for the films we investigated are given in Table II. Film compositions are estimated from the melt composition using the assumption of unity segregation coefficients for the rare-earth oxides. The composition of films 1 and 3 is suitable as  $1\text{ }\mu\text{m}$  diameter bubble material, whereas that of films 2 and 4 is suitable as  $0.5\text{ }\mu\text{m}$  diameter bubble material. All of the films were implanted with  $5 \times 10^{15}/\text{cm}^2$  molecular deuterium ions at 60 keV and  $9.5 \times 10^{13}/\text{cm}^2$  atomic oxygen ions at 110 keV. Film 1 was implanted two times with this dose. Implant dose was selected to give a  $1.5\text{ eV}/\text{\AA}^3$  damage level [15]. Fine tuning of implant conditions to optimize the damage profile was not done. No profile of  $4\pi M_s$  or  $H_K$  was obtained. These are most likely not uniform through the implanted layer thickness. The results of FMR and x-ray measurements are given in Table III. The average strain  $\langle \epsilon \rangle$ , for films 2, 3, and 4 is the same. Difference in strain for film 1 is unexplained, but may be due to a difference in implant conditions or annealing. Implant thickness, determined from Pendellosung interference [21] is  $3500\text{ }\text{\AA}$ .

The FMR linewidth and gyromagnetic ratio of the implanted layer was not appreciably different from that in the bulk film for the implant doses we investigated. Several resonance modes associated with the implanted layer were observed, but only the main mode was used for  $\Delta H_E$ ,  $H_1$ , and  $\lambda_{111}$  measurements. We did not attempt to estimate the uniformity or change in  $4\pi M_s$  from the resonance spectrum.

To establish the effect of annealing during implantation on film properties, we implanted two identical films with the same dose and energy ( $5 \times 10^{15}\text{ D}_2^+/\text{cm}^2$  @40 keV) at different current densities. The results are given in Table IV. The current density for film 6 was three times that for film 5. The  $4\pi M_s$  for both films is 1350 G. Film thickness is approximately  $0.4\text{ }\mu\text{m}$ , as estimated from growth time and rate. Projected implant range is  $3500\text{ }\text{\AA}$  [15]. The annealing effect is seen in difference in  $\Delta H_E$ , and in the average and maximum strain. For



film 6, which has the higher implant current, the change in anisotropy field is about 200 Oe less than that for film 5. Furthermore, the range in the maximum strain, determined from the angle at which x-ray rocking curve rises up from zero on the low angle side, to the angle at which the maximum in the first peak on the low angle side occurs, referenced to the LPE film peak, or substrate if there is no separate film peak, is smaller on film 6, indicating that some annealing is occurring. The error margin on the determination of maximum strain is typically 10% as determined by S/N ratio of x-ray detector and diffraction conditions as governed by sample alignment parallel to the plane of x-ray beam.

Stress applied to the films caused approximately the same resonance field shift  $\delta H_{111}$  for non-implanted and implanted layers. This implies that  $\lambda_{111}/M_s$  is nearly constant for implant doses used here. For film 1, at 635 mm Hg applied pressure, we measured  $\delta H_{111}$  of 82 Oe for the non-implanted, singly, and doubly implanted films.  $\delta H_{111}$  for film 2 was 38 Oe for the non-implanted and implanted layers. The magnetostriction coefficient was determined to be  $-3.3 \times 10^{-6}$  for the non-implanted layer on film 1 and  $-3.8 \times 10^{-6}$  on film 2. In the implanted layer,  $\lambda_{111}/M_s$  was determined to be  $-6.14 \times 10^{-8} \text{ G}^{-1}$  on film 1 and  $-3.48 \times 10^{-8} \text{ G}^{-1}$  on film 2, but  $4\pi M_s$  was not measured. Thus if  $M_s$  is reduced by this implantation dose, then  $\lambda_{111}$  must also be reduced proportionately. The accuracy for  $\delta H_{111}$  measurement is  $\pm 5$  Oe.

Evidence for the linearity of the stress-induced anisotropy field shift is shown in Fig. 5. As the total anisotropy field change is linear with strain, we expect its components to also be linear with strain.

The anisotropy energy density due to stress is nearly the same for both 1  $\mu\text{m}$  and 0.5  $\mu\text{m}$  materials, but differences in  $M_s$  cause the stress-induced anisotropy field to be higher for the 1  $\mu\text{m}$  material. For identical amounts of strain,  $\Delta H_E$  is 3200 Oe for film 3 and 1800 Oe for film 4. The anisotropy energy change  $\Delta K_U = \frac{1}{2} M_s \times \Delta H_E$  is  $97.5 \times 10^3 \text{ ergs/cm}^3$  for film 3 and  $90.7 \times 10^3 \text{ ergs/cm}^3$  for film 4, assuming  $M_s$  is the same in the bulk and implanted layer.

Thus within the experimental uncertainty in  $4\pi M_s$  and  $\Delta H_E$  measurement, we observed the same change in energy density for different size bubble materials implanted under identical conditions.

The portion of the total anisotropy field shift due to stress is proportional to  $\lambda_{111}/M_s$ . As can be seen in Fig. 6 the total  $\Delta H_E$  for the 1  $\mu\text{m}$  material (Film 1) is higher for the same amount of strain than the 0.5  $\mu\text{m}$  material (Films 2,4), due to a lower  $4\pi M_s$  for the 1  $\mu\text{m}$  material.  $\lambda_{111}$  is nearly the same for both materials. The  $\Delta H_{K\text{stress}}$  contributes approximately 2/3 of the total  $\Delta H_E$  for the 1  $\mu\text{m}$  material, and 1/2 for the 0.5  $\mu\text{m}$  material. The remaining portion, not attributed to  $\Delta H_{K\text{stress}}$ , increases with strain, from 810 Oe for 0.86% strain to 1742 Oe for 1.27% strain in film 1. This increase is attributed to increased damage and disorder created by heavier implant dose. Apparently the change in anisotropy created by this mechanism is also linear with strain. The uncertainty in determining  $\Delta H_{K\text{stress}}$  is approximately  $\pm 100$  Oe.

Results for  $H_1$  measurement are given in Table II for the bulk layer and Table III for the implanted layer. In Fig. 7 experimental resonance field measurements for film 2 are plotted for bulk and ion implanted layer. Solid curves are for calculated  $H_1$  values. The fit of the experimental data to the theoretical curves is quite good.  $H_1$  decreases with implantation, from -155 Oe to -40 Oe for bubble film 1, from -115 Oe to -40 Oe for film 2 and from -115 Oe to -25 Oe for film 4. The larger change in the 1  $\mu\text{m}$  material is believed to be due in part to a lower exchange constant. The reduction of  $H_1$  is indicative of disorder being introduced into the crystalline material by the implantation. We suggest that the same mechanism which is responsible for the change in  $\Delta H_E$  not related to stress, is acting to reduce  $H_1$  in the implanted layer.

### CONCLUSION

Direct measurement of stress-induced changes in the anisotropy field of ion implanted magnetic garnet films has shown that stress alone can not account for the total change in anisotropy field. The additional change, which is believed to

be related to disordering of the crystal lattice, is nearly the same for 1  $\mu\text{m}$  and 0.5  $\mu\text{m}$  diameter bubble materials. A significant difference in total anisotropy field change for the different size bubble materials was found and is attributed to differences in stress-induced anisotropy field change which is inversely proportional to  $4\pi M_s$ . For any given film composition, it was found that  $\lambda_{111}/M_s$  remained constant in the implanted layers, indicating that any change in  $\lambda_{111}$  is proportional to a change in  $4\pi M_s$ . Finally a substantial reduction of  $H_1$  with implantation was found, in agreement with the trend of the crystal structure becoming disordered by implantation.

#### ACKNOWLEDGEMENTS

This work was supported by the Air Force Office of Scientific Research, under grant AFOSR 80-0284, and by the National Science Foundation under grant number ECS-7912677. The authors would like to thank Dr. J. O. Artman for use of his FMR equipment, J. Tabacchi for ion implantation, and V. Speriosu for help with x-ray analysis.

**Fig. 1: Ion Implantation of a Magnetic Garnet Epitaxial Thin Film**

**Fig. 2: Schematic Diagram of the Wideband Resonance Spectrometer for FMR Measurement**

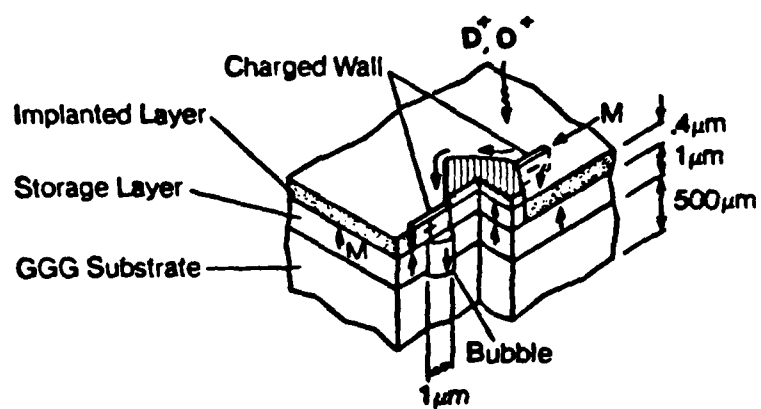
**Fig. 3: Microbox Structure and Serpentine Conductor**

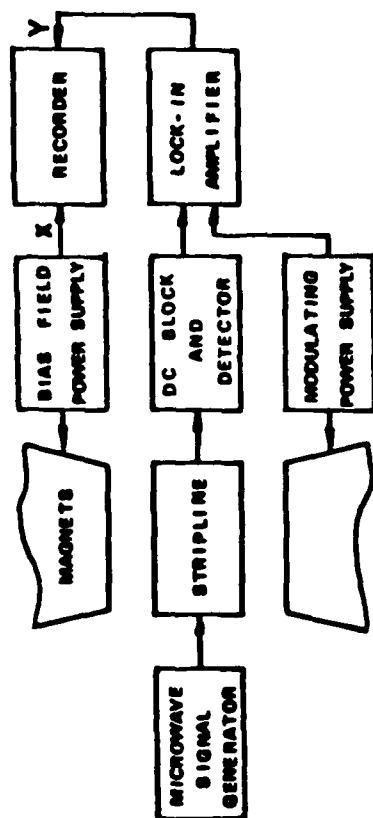
**Fig. 4: Resonance Field Shift  $\delta H_{111}$  Versus Applied Pressure  $q$  for a Non-Implanted Film**

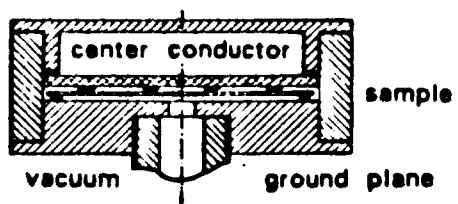
**Fig. 5: Total and Stress-Related Anisotropy Field Change versus Average Strain for Film 1**

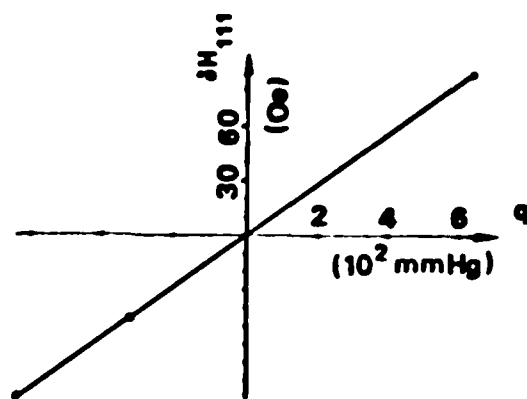
**Fig. 6: Anisotropy Field Change versus Average Strain for 1.0  $\mu\text{m}$  and 0.5  $\mu\text{m}$  Diameter Bubble Materials**

**Fig. 7: Experimental Resonant Field Data and Theoretical Resonant Field Curves Versus Applied Field Angle for Calculated  $H_1$  Values**

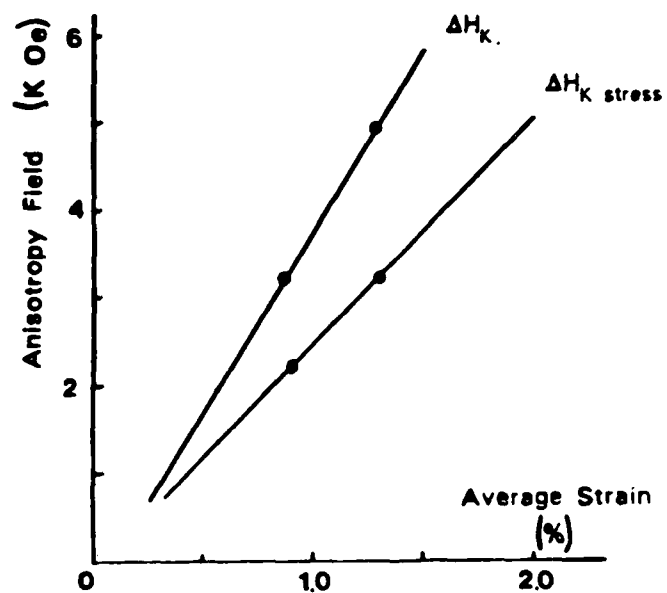


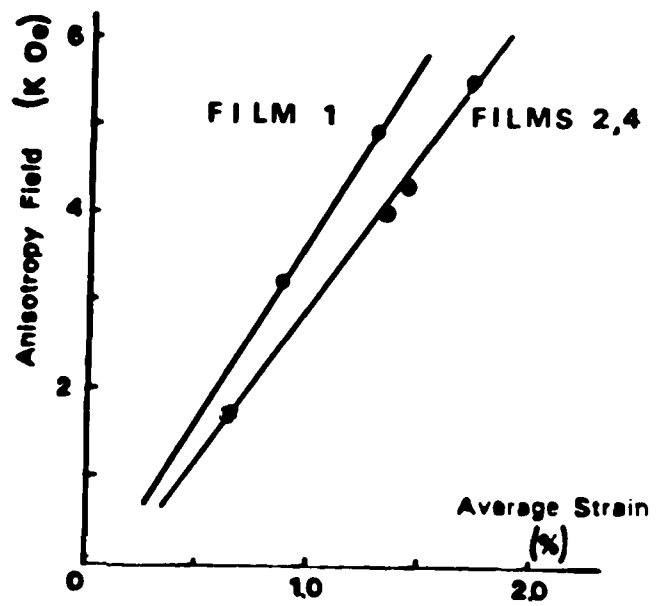












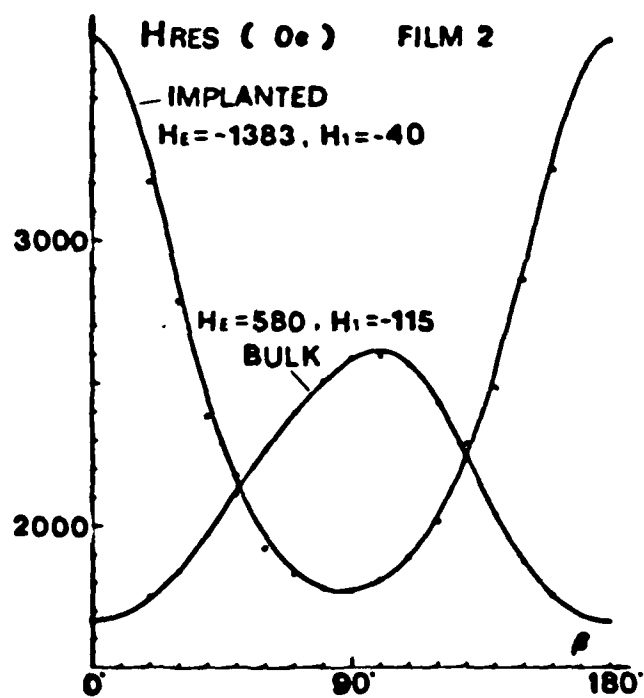


Table I: Parameters for Deuterium and Oxygen Ions in Garnet [15]

Ion	Energy keV	Projected Range	Standard Deviation	Nuclear Energy Loss	Electronic Energy Loss
		$R_p$ ( $\mu\text{m}$ )	$\Delta R_p$ ( $\mu\text{m}$ )	keV/ $\mu\text{m}$	keV/ $\mu\text{m}$
Deuterium	60	.492	.102	1.09	137.1
Oxygen	110	.136	.081	194.4	440.1

Electronic Cross Sections of Lindhard, Scharff. Schiott

Table II: Material Parameters

Film	$4\pi M_s$	$l$	$H_E$	$\Delta a_0$	$H_1$	$t$
1	636 (G)	.136 ( $\mu m$ )	1060 (Oe)	+0.02 ( $\text{\AA}$ )	-160 (Oe)	1.26 ( $\mu m$ )
2	1370	.057	580	-.012	-115	0.5
3	766	.113	1009	-.003	-155	.39
4	1266	.059	558	0.000	-115	.85

Film	Nominal Diameter	Compositions
1,3	1 $\mu m$	$Y_{0.8} Sm_{0.3} Gd_{0.6} Tm_{1.3} Fe_{4.65} (Al Ga)_{0.35} O_{12}$
2,4	0.5 $\mu m$	$Y_{1.0} Sm_{0.45} Gd_{0.3} Tm_{1.25} Fe_{4.8} Al_{0.2} O_{12}$

Table III: Implanted Film Results

Film-Implant	Average Strain < $\epsilon$ >	$\Delta H_K$	$\Delta H_{K \text{ stress}}$	$H_1$
1-1	0.86 (%)	3033 (Oe)	2223 (Oe)	-40 (Oe)
1-2	1.27	4950	3208	
2	0.70	1963	870	-40
3	0.71	3200		
4	0.70	1760		-25

Table IV: Effects of Current Density on Film Parameters for  $5 \times 10^{15}$   
Deuterium ions/cm<sup>2</sup> Implanted at 40 keV

Parameter	Film 5	Film 6
Current Density	0.33 $\mu\text{A}/\text{cm}^2$	1.0 $\mu\text{A}/\text{cm}^2$
$H_E$ bulk	752 Oe	793 Oe
$\Delta H_E$	2382 Oe	2110 Oe
$\epsilon_{\text{max}}$	.75% - .89%	.73% - .82%
$\langle \epsilon \rangle$	0.67%	0.64%

## REFERENCES

1. G.P. Vella-Coleiro, R. Wolfe, S.L. Blank, R. Caruso, T.J. Nelson, and V.V.S. Rana, J. Appl. Phys., 52, 2355, 1981 .
2. R. Wolfe, J.C. North, R.L. Barns, M. Robinson, and H.J. Levinstein, Appl. Phys. Lett., 19, 298, 1971 .
3. J.C. North, R. Wolfe, in *Ion Implantation in Semiconductors and Other Materials*, B.L. Crowder, ed., Plenum, New York, 1973, pp. 505.
4. K. Komenou, I. Hirai, K. Asami, and M. Sakai, J. Appl. Phys., 49, 5816, 1978 .
5. K. Komenou, J. Zebrowski, C.H. Wilts, J. Appl. Phys., 50, 5442, 1979 .
6. H. Jouve, J. Appl. Phys., 50, 3, 2246, 1979 .
7. Y. Satoh, M. Ohashi, T. Miyashita, K. Komenou, J. Appl. Phys., 53, 3740, 1982 .
8. H. J. Levinstein, R. W. Landorf, S. J. Licht, S. L. Blank, Appl. Phys. Lett., 19, 486, 1971 .
9. A. H. Eschenfelder, *Magnetic Bubble Technology*, Springer-Verlag, New York, (1980).
10. W.H. deRoode, H.A. Algra, J. Appl. Phys., 53, 3, 2507, 1982 .
11. Y.S. Lin, G.S. Almasi, G.E. Keefe, IEEE Trans. on Magn., MAG-13, 1744, 1977 .
12. G.S. Almasi, E.A. Giess, R.J. Hendel, G.E. Keefe, Y.S. Lin, M. Slusarczyk, AIP Conf. Proc., 24, 6300, 1974 .
13. H.A. Washburn, G. Galli, J. Appl. Phys., 50, 3, 2267, 1979 .
14. K. Ju, H. L. Hu, R. G. Hirko, E. B. Moore, D. Y. Saiki, R. D. Schwenker, IBM J. Res. Develop., 25, 295, 1981 .
15. T. Gallagher, private communication.
16. P. Gerard, private communication.
17. X. Wang, C. S. Krafft, M. H. Kryder, Paper No. CB-07, Joint Intermag- Magnetism and Magnetic Materials Conference, Montreal July 20-23, 1982, to be published in IEEE Trans. on Magn.
18. H. Makino, Y. Hidaka, Mat. Res. Bull., 16, 957, 1981 .
19. D. C. Fowles, J. A. Copeland, AIP Conf. Proc., 5, 240, 1972 .
20. V.S. Speriosu, J. Appl. Phys., 52, 10, 6094, 1981 .
21. W.T. Stacy, M.M. Janssen, J. Cryst. Growth, 27, 282, 1974 .



## MAGNETO-OPTIC PHOTOMETER

The Magneto-Optic Photometer (MOP) is an instrument used to measure the local magnetic properties of small areas in magnetic films. Employing an argon laser as a light source and a photomultiplier as a detector, the MOP utilizes the Faraday or Kerr effect (when polarized light passes through or is reflected off a magnetic material the polarization rotates depending upon the magnetization direction in the material) to detect the magnetic response of a material to applied magnetic fields. The MOP employs a microscope to focus the polarized laser beam to a very small spot on an experimental sample while magnetic fields are applied to the sample. A change in the rotation of the light polarization due to a change in the direction of magnetization in the sample causes an intensity change in the light after it passes through an analyzer (a polarizer set at about 90 degrees to the original polarization.) The photomultiplier (PMT) converts the intensity into a voltage. The variation of the voltage with applied fields gives information about the materials magnetic characteristics - anisotropy, coercivity, etc. To enhance sensitivity, ac fields are usually used to excite the magnetization at a set frequency and a lock-in amplifier is used to extract the signal from the photomultiplier. A more complete description can be found in the report of one year ago.

### MODIFICATIONS

The magneto-optic photometer system has been upgraded by the acquisition of a Leitz MPV photometric microscope system. This system has the capability of doing small spot measurements with the use of an apertured measuring diaphragm inserted into the image plane of the microscope (Fig. 1). The diaphragm allows the photomultiplier (PMT) to see only that portion of the image that is revealed by the aperture. By using a pinhole aperture of  $70\mu\text{m}$  in the image plane and a 100X objective lens along with a tube factor of 1.6X, the measuring area (the effective spot size) is reduced to a diameter of  $70\mu\text{m} / (100 \times 1.6) = 0.44\mu\text{m}$ . Being able to make measurements on such a small area allows us to accurately map magnetic parameters as a function of position in devices such as ion-implanted contiguous-disk bubble memories or magnetic recording heads.

The magneto-optic photometer system has also been expanded to allow measurements to be made on transparent magnetic media such as ion-implanted bubble garnets using transmitted light. Before this modification, measurements on the planar magnetization of ion-implanted garnets were made using light reflected at an angle off the ion-implanted surface of the garnets. However, the magneto-optic effect in garnets using reflected light is complex in analysis and is not as strong as the effect with transmitted light. The modification which allows the use of transmitted light consists of a substage assembly (Fig. 2) which holds and positions a polarizing prism and a microscope objective under the standard microscope stage supporting the coil assembly and sample. The laser beam is transmitted up through the polarizer and the lens to the sample, where it undergoes Faraday rotation. After the light passes up through the sample, it is received by the usual microscope optics and is analyzed and detected. The substage assembly is capable of translation in any of the three principle directions and allows rotation of the polarizing prism about the optical axis. In order to give the light beam the angle necessary to detect planar magnetization, the beam is moved off of the substage assembly's optical axis so that the transmitting lens causes the beam to pass through the sample at an angle. Compared to the use

of reflected light, the use of transmitted light has given an order of magnitude increase in the signal-to-noise ratio. The substage assembly was designed to allow the quick and easy conversion from transmission photometry to reflection photometry and vice versa.

The high frequency dynamics of magnetic materials may also be investigated with the magneto-optic photometer. High frequency magnetic fields (up to 50 MHz) can now be applied to a sample by a coplanar waveguide powered by an RF amplifier and an oscillator. The coplanar waveguide provides a high frequency in-plane magnetic field along the incident plane of the light (reflection photometry must be used). The magnetic response (the Faraday rotation) to the high frequency field is measured using the usual microscope optics and the PMT. However, the resistive load of the PMT output is decreased for high frequency measurements so that the PMT can react to the quickly changing light intensity. A lock-in amplifier is used to detect the magnitude and phase of the magnetic response at the applied field frequency. Since it is usually desirable that memory devices be operated at as high of a frequency as possible to minimize access time, knowledge of the dynamic characteristics is essential. This high frequency capability has been used to make dynamic measurements on permalloy thin films with good success.

## CURRENT RESEARCH

### 1. Effect of crystalline alignment in ion-implanted bubble devices:

The garnet films typically used in ion-implanted devices have cubic crystalline symmetry and are oriented with a  $\langle 111 \rangle$  crystal axis perpendicular to the film. When a perpendicular bias field is applied to the film so as to stabilize bubble domains, the in-plane magnetization of the drive layer is subject to the forces of the crystalline anisotropy which result in three equally favorable directions for the magnetization - a threefold symmetry. Misalignment of the film so that the  $[111]$  axis is at some angle to the film normal will cause deviations from the threefold symmetry. The effects of these deviations upon device operation are not known; the effects could be detrimental or they could even be beneficial. In cooperation with the Laboratoire d'Electronique et de Technologie de l'Informatique in Grenoble, France, we have obtained a number of ion-implanted garnet films which have their  $[111]$  axes tilted at some known angles from the film normal. We have developed a theoretical model for the magnetic anisotropy that should have formed as a result of the tilt and we are doing magneto-optic experiments to measure the character and magnitude of the anisotropy.

The theory is based on general symmetry considerations of the cubic crystalline structure and the direction of film growth. For a film grown with its normal at a small angle,  $\gamma$ , from the  $[111]$  direction and toward the  $[112]$  direction, the in-plane anisotropy energy is approximated by

$$\begin{aligned}
 E(\phi) = & \quad \gamma \sin\theta \cos\theta \quad 4/3 \quad K_A \quad \cos\phi \\
 & + \quad \gamma \sin^2\theta \quad 2/3 \quad K_A \quad \cos 2\phi \\
 & - \quad \sin^3\theta \cos\theta \quad 2/3 \quad K_1 \quad \cos 3\phi \\
 & - \quad \gamma \sin^4\theta \quad 2/6 \quad K_1 \quad \cos 4\phi
 \end{aligned}$$

where  $K_1$  is the crystalline anisotropy and  $KA$  is an anisotropy due to growth conditions and ion-implantation.  $\theta$  is the polar angle of the magnetization from the film normal and  $\phi$  is the azimuthal magnetization angle from the  $[112]$  projection into the film plane. When there is no tilt ( $\gamma = 0$ ) notice that only the threefold term of the azimuthal angle ( $\cos 3\phi$ ) remains. However, as the tilt is increased the other terms become increasingly important. Because  $KA$  is likely to be significantly larger than  $K_1$ , it may not require a large tilt,  $\gamma$ , before the  $KA$  terms become important in determining the behavior of the magnetization in the ion-implanted layer.

Figure 4 presents the results of an experiment used to determine the characteristics of the in-plane anisotropy. In this experiment a small oscillating field is applied in the film plane along the direction of the light beam (i.e. along the  $y$ -axis of our laboratory system). A larger field,  $H_y$ , is applied also along the  $y$ -axis and is slowly varied (ramped). The MOP output is plotted as a function of the larger field,  $H_y$ . A DC in-plane field,  $H_x$ , applied perpendicular to the other fields (along the  $x$ -axis) is changed in steps and a plot is made for each step. The compilation of plots gives the output versus in-plane fields  $H_x$ ,  $H_y$ . The data in Fig. 4 is arranged to give a three-dimensional effect. The peaks in the plots correspond to the magnetization switching between a pair of easy directions.

The data in Fig. 4 is for a film grown without tilt,  $\gamma = 0$ . Therefore, the dominant anisotropy is the  $K_1 \cos 3\phi$  term, giving rise to three easy directions. Notice that in Fig. 4 there are three "ridges" of peaks. Each of these ridges corresponds to switching between a specific pair of the three easy directions. There are three such pairs, so there are three ridges.

In Fig. 5 the same kind of data is presented except that the sample was grown with a tilt of  $\gamma = 5.1^\circ$ . Instead of three ridges there is only one ridge. Preliminary considerations suggest that this may be due to the dominance of the  $KA \cos 2\phi$  term, which gives only two easy magnetization directions and hence only one pair between which there may be switching. Further measurements will be made to determine the values of  $K_1$  and  $KA$  and to ascertain the effect of crystal orientation on device operation.

#### 11. Effect of Stress Relaxation of Ion-Implanted Propagation Pattern Edges

Ion-implantation of contiguous-disk drive layers serves to convert perpendicular magnetization to planar magnetization through magnetostriction. The ion-implantation causes planar compressive stress which results in a negative uniaxial anisotropy perpendicular to the film. However, at a boundary between implanted areas and non-implanted areas, (such as at the edge of a propagation pattern) there is stress relief perpendicular to the boundary. The resultant stress at the boundary is no longer a planar compression, but becomes effectively a uniaxial compression parallel to the boundary. The magnetic anisotropy which results is a uniaxial anisotropy with the easy axis along the boundary plus a unidirectional anisotropy - the direction of which depends upon the orientation of the boundary with respect to the crystal. The energy equation describing these anisotropies is:

$$E(\phi) = -\sigma(\lambda_{111} + \frac{1}{2}\lambda_{100}) \sin^2 \theta \cos^2(\phi - \psi) \\ - \sigma(\frac{2}{3}\lambda_{111} - \frac{2}{3}\lambda_{100}) \sin \theta \cos \theta \cos(\phi + 2\psi)$$

where  $\sigma$  is the uniaxial stress along the boundary,  $\lambda_{100}$  and  $\lambda_{111}$  are the magnetostriction constants of the garnet,  $\theta$  and  $\phi$  are the polar angle and the azimuthal angle (from  $[11\bar{2}]$ ) of the magnetization, and  $\psi$  is the angle of the boundary from the  $[11\bar{2}]$  direction (see Fig. 7).

The uniaxial anisotropy at the boundary is very important to the formation of the charged walls used to propagate the bubbles in the underlying storage film. The anisotropy stabilizes the charged walls by overcoming the demagnetizing field emanated by the wall. With distance from the boundary, the uniaxial stress gradates to become the planar stress in the "bulk" of the film. Because of this, the in-plane uniaxial anisotropy decreases with increasing distance from the boundary, and hence results in the charged wall extending only a short distance from the boundary before it bends to become uncharged. We have been using the MOP to measure anisotropies as a function of distance from non-implanted areas. We intend to detect the presence of this stress anisotropy, and determine how it varies with distance from the boundary and around propagation patterns.

The plots in Fig. 6 illustrate how the anisotropy changes as a function of distance from a straight boundary. These plots are similar to those in Figs. 4 and 5 (though the experimental sample is different) and were taken on an area far from the boundary (Fig. 6a), 12.5  $\mu\text{m}$  away from the boundary (Fig. 6b), and on an area right at the edge of the boundary (Fig. 6c). The data in Fig. 6a is similar to that in Fig. 4 in that, far from a boundary, the threefold magnetocrystalline anisotropy is the dominant force. Here again there are three ridges: two coming toward the viewer and one receding. Near to the boundary, stress relief and demagnetizing effects give rise to a uniaxial anisotropy. The uniaxial anisotropy increases with proximity to the boundary and becomes dominant over the threefold crystalline anisotropy. For the data in Fig. 6, the uniaxial anisotropy is such that it favors the pair of magnetization directions whose switching causes the receding ridge in 6a. As a result, as one nears the boundary (i.e. as the uniaxial anisotropy increases), the receding ridge is seen to grow at the expense of the other two ridges. The peaks at  $H_x = +4$  in Fig. 6b are closer together than the peaks at  $H_x = +4$  in Fig. 6a. This is because the receding ridge extends further along the  $H_x$  direction in Fig. 6b. A line has been drawn at the base of each ridge to show that the ridges intersect at about  $H_x = 2.5$  Oe in Fig. 6b, whereas they intersected at  $H_x = 0$  in Fig. 6a. As measurements are taken closer to the boundary, this intersection point is found to move further out along  $H_x$ . In addition, the angle between the two unfavored ridges decreases as the two ridges merge into one. In Fig. 6c, the uniaxial anisotropy has become completely dominant and only one ridge is present.

These experiments show that there is a uniaxial anisotropy along the boundary; however, it is yet to be determined by experimentation what the cause of the anisotropy is - demagnetizing effects alone or demagnetizing effects plus stress relief effects. This will be ascertained by measurement of the magnitude of the anisotropy which will be compared to theoretical estimates made for both effects.

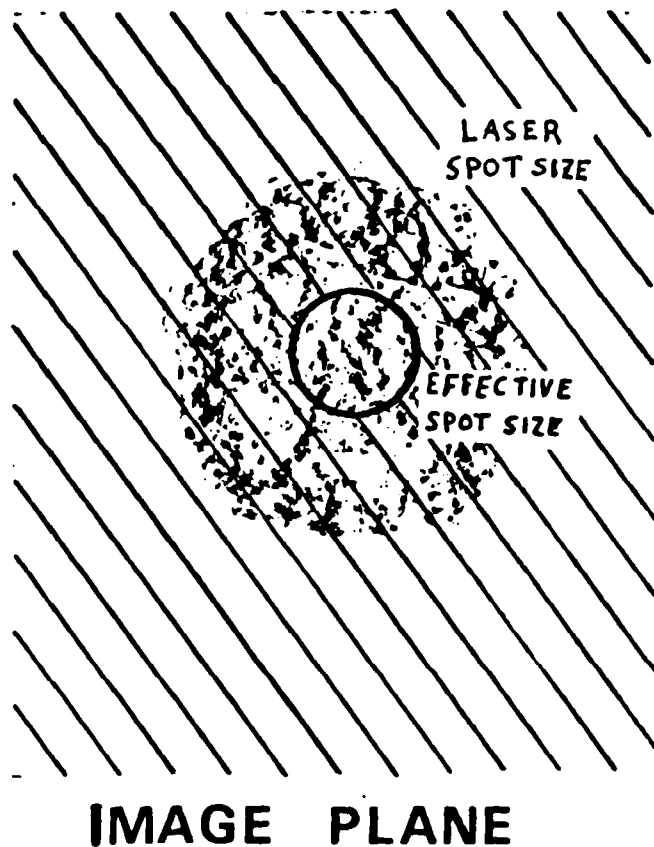
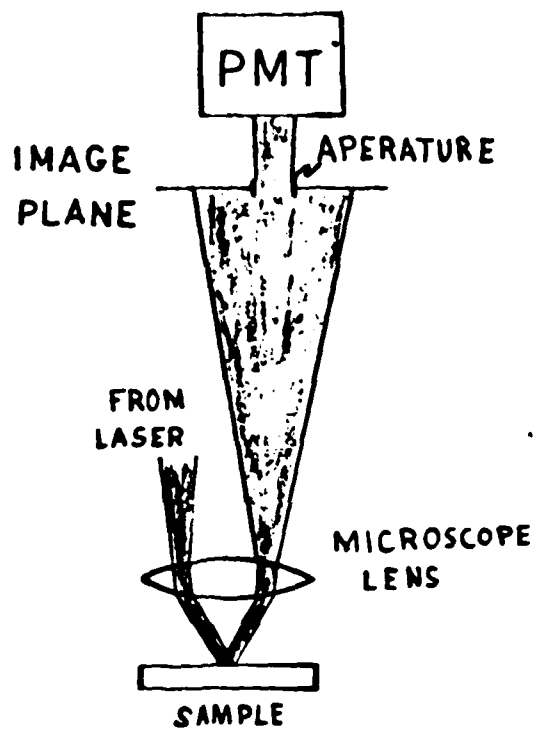


FIGURE 1

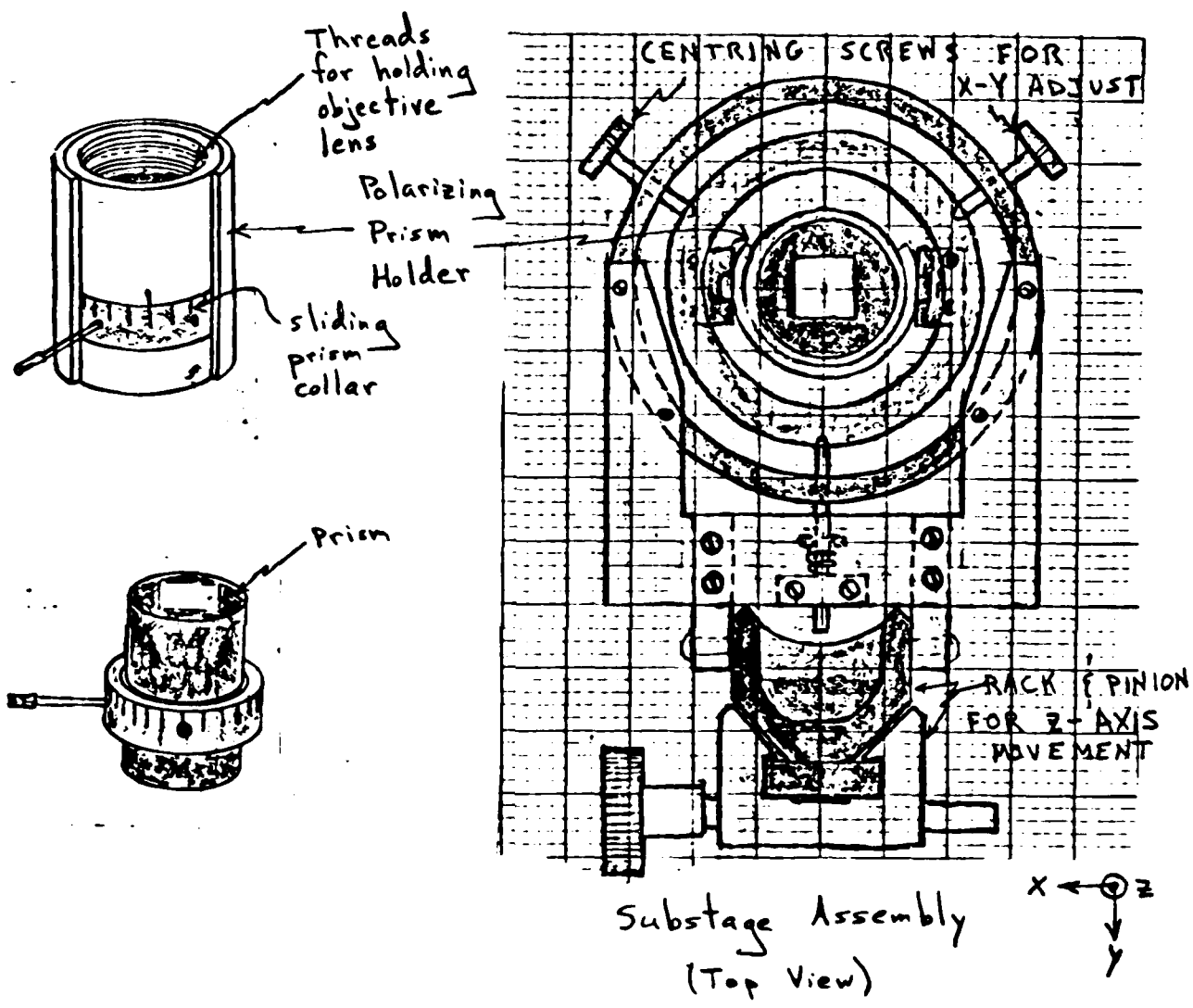


FIGURE 2

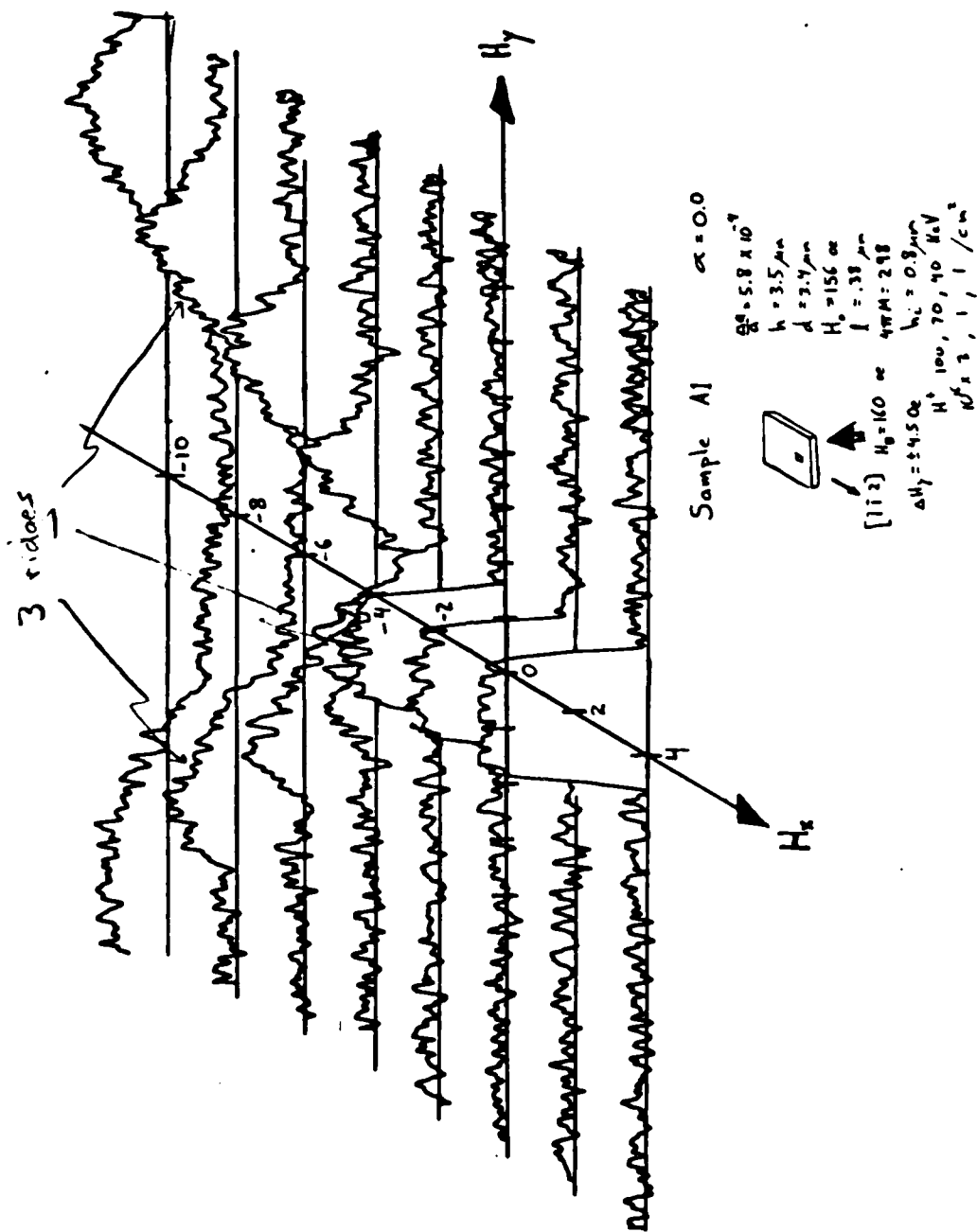
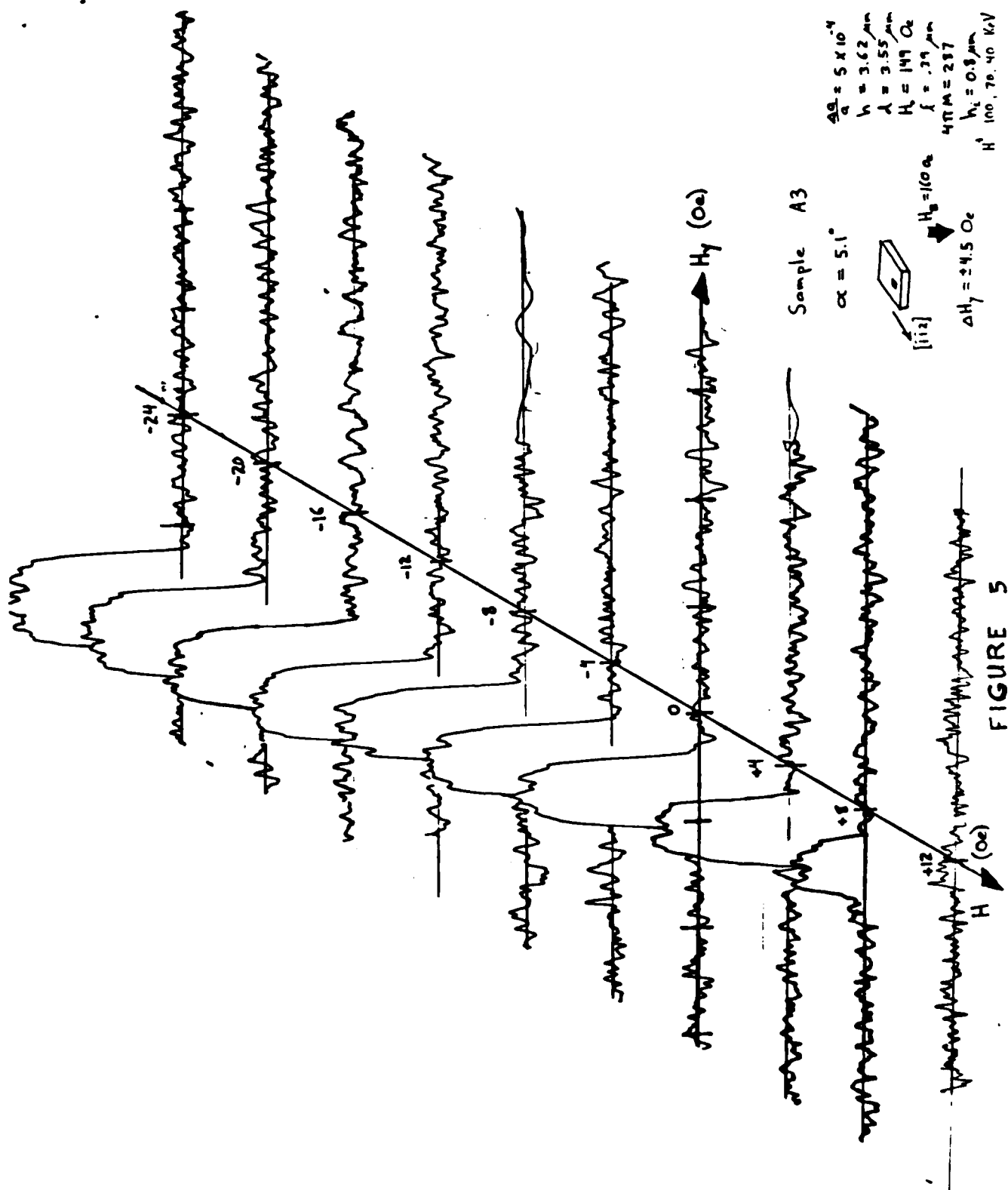


Figure 4





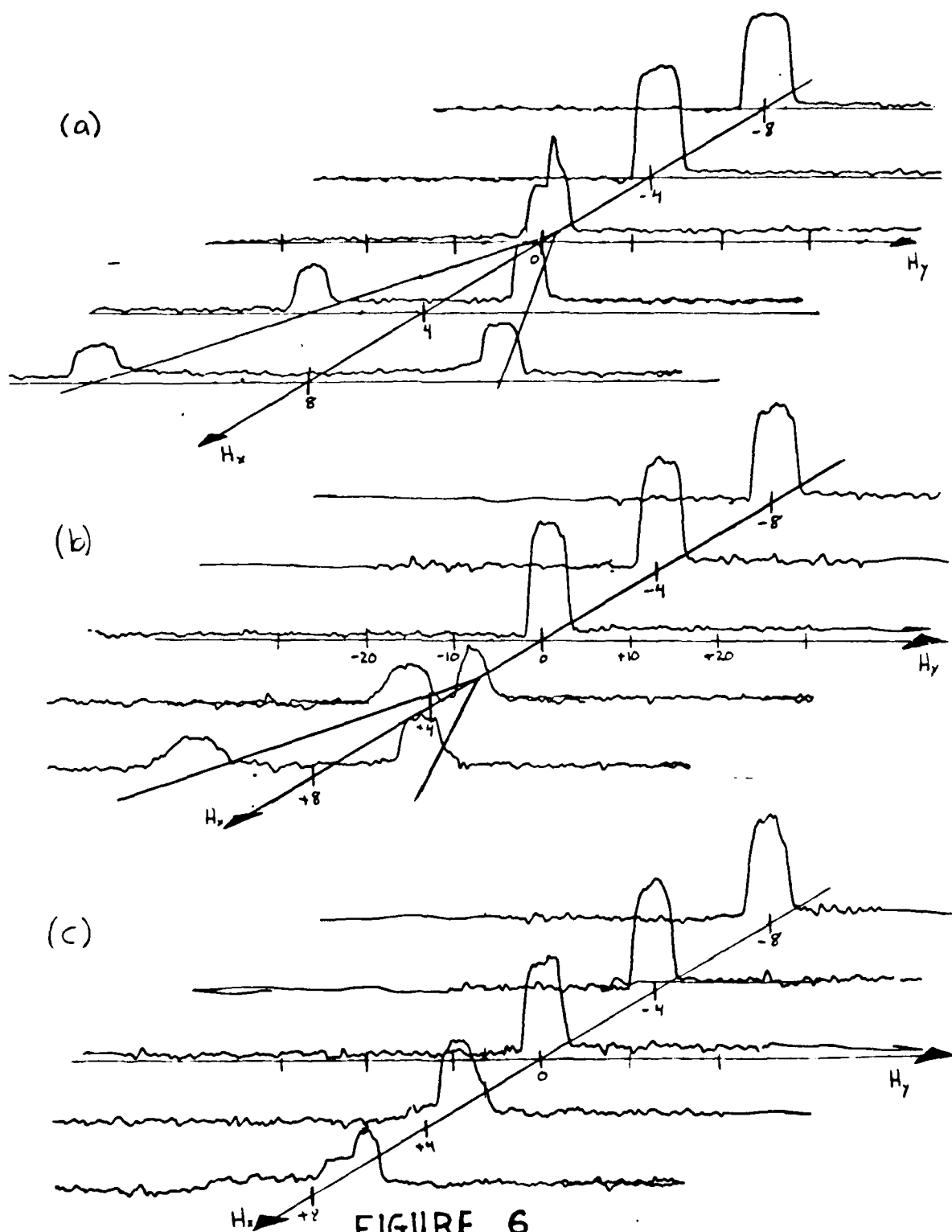


FIGURE 6

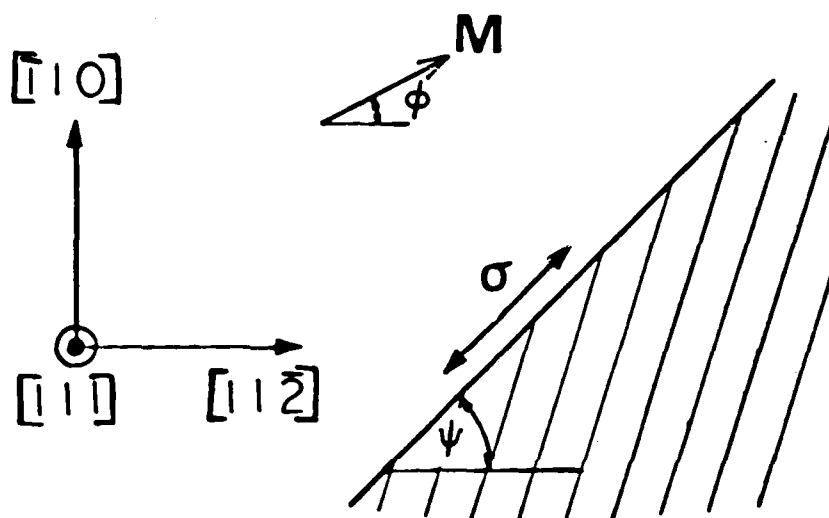


FIGURE 7

THE EFFECTS OF STRESS RELAXATION AND ANISOTROPIC  
MAGNETOSTRICTION ON CHARGED WALLS IN  
ION IMPLANTED GARNETS\*

M. H. Kryder and D. A. Saunders  
Electrical Engineering Department, Carnegie-Mellon  
University, Pittsburgh, PA 15213

Introduction

This paper reviews present understanding and presents new data on the effects of ion implantation on garnet materials and on the mechanisms giving rise to charged walls at boundaries between implanted and unimplanted regions. Data strongly indicate that uniaxial anisotropy parallel to pattern boundaries and due to stress relaxation near pattern edges is necessary for the formation of charged walls<sup>1</sup>. Furthermore, it is shown that, whereas early researchers ascribed the 3-fold symmetric behavior of charged walls in the ion implanted layers of (111) oriented garnets to magnetocrystalline anisotropy, anisotropic magnetostriction is dominant in determining the anisotropic behavior of charged walls<sup>2,3</sup>.

Measurement Techniques

Transmission electron diffraction (TED), Ferrofluid observation of charged walls, measurements of crystalline anisotropy in ion implanted layers of garnet with ferromagnetic resonance (FMR), and measurements with a small spot (0.5 $\mu$ m) magneto-optic photometer all were used to gather data on the behavior of the magnetization and of charged walls in the ion implanted layers of garnets.

The small spot magneto-optic photometer uses the Faraday magneto-optic effect to measure the response of the inplane magnetization in the ion implanted layer to applied fields. A focussed plane-polarized laser beam transmitted through the substrate and film at an angle of about 20 degrees to the film normal is used as the light source for a polarized light microscope. A pin-hole aperture in the magnified image plane of the microscope makes possible measurements in areas as small as 0.5 $\mu$ m. The magnetization in the film is modulated by the application of an inplane field at a set frequency. The resultant modulation of the light polarity is detected using an analyzer, a photomultiplier and a lock-in amplifier.

Stress Relaxation at Pattern Boundaries

Data supporting recent models<sup>1</sup>, which suggest that uniaxial anisotropy resulting from stress relaxation perpendicular to boundaries between implanted and unimplanted regions is necessary for the formation of charged walls, are presented. Transmission electron diffraction data confirm the stress relaxation. Observations of charged walls using Ferrofluid show that charged walls form only when the sign of the magnetostriction constant is appropriate to produce an easy axis of magnetization parallel to the boundary<sup>2</sup>. Furthermore, measurements of the anisotropic behavior of the magnetization as a function of distance from a pattern boundary with the magneto-optic photometer show that,

Category 1

M. H. Kryder  
Carnegie-Mellon University  
Electrical Engineering Dept.  
Pittsburgh, PA 15213

as the boundary is approached, the anisotropy changes from 3-fold symmetric to 2-fold symmetric with an easy axis parallel to the boundary. A uniaxial anisotropy component may be detected as far as 50 $\mu$ m away from a long straight boundary; however, it dominates over the tri-directional anisotropy only within a few microns of the boundary.

#### Anisotropic Magnetostriction

Contrary to early suppositions, it has been found that magneto-crystalline anisotropy plays a relatively minor role in determining the 3-fold symmetric behavior of charged walls. Instead, the effects of anisotropic magnetostriction are much more important. Stress relaxation near a pattern edge produces, in addition to uniaxial anisotropy, an anisotropy which varies as

$$\sigma(\lambda_{100} - \lambda_{111})\cos 3\phi$$

where  $\sigma$  is the uniaxial stress,  $\lambda_{100}$  and  $\lambda_{111}$  are magnetostriction constants and  $\phi$  is the angle which the normal to the boundary edge makes with respect to a  $[11\bar{2}]$  direction. The dominance of anisotropic magnetostriction over magnetocrystalline anisotropy was found to be increased by ion implantation. Using FMR it was found that whereas  $2K_1/M$  decreased by a factor of three during implantation,  $\lambda_{111}/M$  remained constant.

#### Conclusion

This new understanding of the role of magnetostriction in the formation and behavior of charged walls suggests that more attention should be paid to the magnetostriction constants of materials used for ion implanted devices. For example, with the proper choice of  $\lambda_{111} - \lambda_{100}$  nearly isotropic charged wall behavior is expected. Problems in device design associated with the anisotropic behavior of charged walls would then be reduced.

#### References

1. Y. Hidaka and H. Matsutera, J. Appl. Phys., 53, 5815 (1982).
2. D. A. Saunders and M. H. Kryder, to be published in IEEE Trans. Magnet.
3. A. Hubert to be published in IEEE Trans. Magnet.

\*This work was supported by AFOSR Grant 80-0284 and NSF Grant ECS-7912677.

Invited paper at Intermag Conference,  
Philadelphia, April, 1983

**FABRICATION AND CHARACTERIZATION OF AMORPHOUS AND  
POLYCRYSTALLINE NI-CO-B FERROMAGNETIC THIN FILMS**

Robert G. De Cesaris

M.S. Thesis  
Department of Electrical Engineering  
Carnegie-Mellon University

November 1982

## ABSTRACT

In this project, thin films of NiCoB were fabricated by RF sputtering employing two decoupled plasmas. Thicknesses from 500 Å to 11,000 Å were obtained by sputtering at 100 to 600 watts for 35 to 600 minutes.

The composition of the sputtered films was determined by spectrochemical analysis using the electron microprobe. Accuracy on all elements was on the order of 1%. In addition, energy dispersive spectra were obtained to detect impurities in the films.

Measurements of the saturation magnetization were made with a force-balance magnetometer and were found to vary between 0 and 5300 Gauss and to be a very strong function of the boron content of the film. Anisotropy was determined by ferromagnetic resonance where a uniform mode resonance was distinguishable.

In addition, various spin-wave spectra were observed for both unannealed and annealed films and the behavior of the most interesting spectra are compared to the simple theory.

## TABLE OF CONTENTS

<b>1. Introduction</b>	<b>1</b>
1.1 Magnetic Bubbles and Bubble Devices--An Overview	1
1.2 Magnetic Amorphous and Polycrystalline Alloys: NiCoB Ferromagnetic Thin Films	8
1.2.1 Introduction	8
1.2.2 Survey of Amorphous Magnetic Alloys	8
<b>2. Fabrication of the Ni-Co-B Films</b>	<b>11</b>
2.1 The Sputtering Process	11
2.2 Sputtering With Decoupled Plasmas	13
2.2.1 Preparation of the NiCoB Films	13
2.2.2 Discussion	18
<b>3. Characterization of the Ni-Co-B Films</b>	<b>20</b>
3.1 Electron Microprobe Analysis	20
3.1.1 Physical Principles of Microprobe Analysis	20
3.1.2 Experimental Procedure	21
3.2 Ferromagnetic Resonance	25
3.3 Force-Balance Magnetometer	29
<b>4. Results and Discussion</b>	<b>32</b>
4.1 Composition Results with the Electron Microprobe	32
4.2 Saturation Magnetization	36
4.3 Measured Anisotropy by Ferromagnetic Resonance	39
4.4 Effects of the Sputtering Conditions	43
4.5 Ferrofluid Investigations (Bitter Pattern Method)	52
4.6 Annealing of the NiCoB Films	53
4.7 Conclusions	54
<b>A. Observed Spin-Wave Resonances in the Ferromagnetic Ni-Co-B Thin Films</b>	<b>56</b>
A.1 Brief Theoretical Discussion	56
A.2 Experimental Spectra for the NiCoB Films and Comparison to the Simple Theory	60
<b>References</b>	<b>74</b>

## LIST OF FIGURES

Figure 1-1:	The formation of stable magnetic bubble domains under the influence of an externally applied bias field.	2
Figure 1-2:	Bubble propagation due to interaction between bubble domain and externally magnetized permalloy overlay.	4
Figure 1-3:	Schematic representation of a contiguous-disk device.	6
Figure 1-4:	Comparison of properties of present crystalline ion-implanted contiguous-disk drive layer with that of a proposed NiCoB amorphous film drive layer.	7
Figure 2-1:	Manually-fabricated cobalt-nickel target used for sputtering.	14
Figure 2-2:	Manually-fabricated cobalt-boron target used for sputtering.	15
Figure 2-3:	Relative positions of the targets and the substrate table.	17
Figure 3-1:	Schematic diagram of the electron microprobe. <sup>35</sup>	22
Figure 3-2:	Position of the sample in the FMR apparatus.	28
Figure 3-3:	Schematic construction of a force-balance magnetometer.	29
Figure 3-4:	MV vs. applied H for paramagnetic, diamagnetic, and ferromagnetic materials.	31
Figure 4-1:	Qualitative observation of boron X-ray line at 67.6 Å and 5 kV accelerating voltage.	32
Figure 4-2:	Energy dispersive spectra for various NiCoB films at different beam voltages.	34
Figure 4-3:	Room temperature $4\pi M_s$ (normalized) vs. applied H-field for various NiCoB thin film samples.	38
Figure 4-4:	Dependence of $K_u - 2\pi M_s^2$ on $4\pi M_s$ for NiCoB ferromagnetic thin films.	43
Figure 4-5:	Saturation magnetization vs. boron content in NiCoB ferromagnetic thin films.	47
Figure 4-6:	Dependence of film thickness on sputtering time.	52
Figure A-1:	Diagram of expected spin-wave behavior under assumption of perfect pinning in a <u>magnetically uniform</u> film.	57
Figure A-2:	Typical spin-wave resonance modes observed for different unannealed samples of the NiCoB ferromagnetic film 4-25-80A.	62
Figure A-3:	Resonance spectra obtained for film 3-17-80A (annealed).	63
Figure A-4:	Resonance spectra obtained for film 8-20-80A.	64
Figure A-5:	Other types of distinct spectra obtained for the NiCoB ferromagnetic thin films.	65
Figure A-6:	Log-log plot of the magnetic field separation from the first-order mode (mode #1) vs. the assigned mode number n.	67
Figure A-7:	Observed spectra for varying angles of inclination of the applied static H-field.	72



## LIST OF TABLES

Table 2-1:	Sputtering yields in atoms per ion of $\text{Ar}^+$ for different bombarding energies of the Ar ions. <sup>22,23</sup>	13
Table 3-1:	X-ray lines analyzed and crystals used with the microprobe.	24
Table 4-1:	Characteristic lines evident in the energy dispersive spectra.	35
Table 4-2:	Strong unambiguous FMR absorption peaks for some ferromagnetic NiCoB films.	40
Table 4-3:	Magnetic parameters for some ferromagnetic NiCoB films.	42
Table 4-4:	Observed target voltage fluctuations with sputtering time.	46
Table 4-5:	Sputtering parameters, thickness, and composition of various ferromagnetic and paramagnetic NiCoB thin films.	48
Table 4-6:	Composition reproducibility for fixed sputtering conditions.	50
Table A-1:	Sputtering conditions and composition of ferromagnetic NiCoB thin films for which spin-wave spectra are presented.	60
Table A-2:	H-field values and intensities of the observed resonances for films 4-25-80A, both unannealed and annealed samples.	68
Table A-3:	Experimentally determined mode separation and mode intensity for film 4-25-80A, both unannealed and annealed samples.	69
Table A-4:	Comparison of mode separation of various samples of film 4-25-80A to theory.	70
Table A-5:	Comparison of mode intensities of various samples of film 4-25-80A to theory.	71

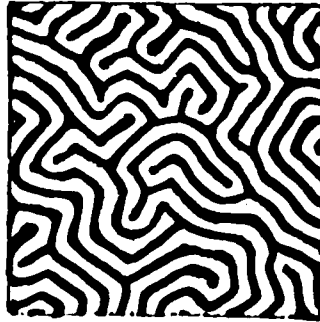
## 1. INTRODUCTION

### 1.1 Magnetic Bubbles and Bubble Devices--An Overview

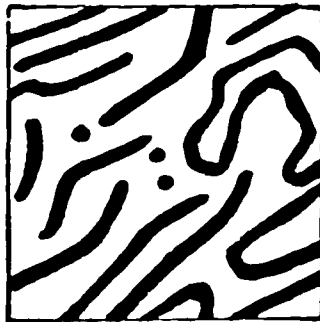
Much attention has been given to the subject of speed and capacity of memory systems since present-day data-processing systems are generally limited in performance by memory systems considerations. A recent memory device, first proposed by Bobeck<sup>1</sup> in 1967, involves the use of data bits stored in the form of magnetic bubbles-- tiny cylindrical magnetic domains whose magnetization is opposite to that of the ferromagnetic thin film in which they are located. Some of the major advantages of magnetic bubble memory systems include a very high potential bit density, non-volatility, and the fact that one can perform many logical operations on the stored data without reading the data out of memory and then writing it back in again. The materials commonly used for bubble devices are ferromagnetic garnet films grown on a single crystal, non-magnetic garnet substrate by the liquid phase epitaxy (LPE) method. These thin films, usually one to three microns in thickness, can be tailored by the melt composition, and hence the desired physical and magnetic properties required of these epitaxially grown films can be obtained. Although the garnet substrate, typically a 10 to 20 mil thick substrate of Gadolinium Gallium Garnet (GGG), has a cubic crystal structure, the epitaxial films exhibit a uniaxial anisotropy with the easy axis of magnetization perpendicular to the film. This epitaxial layer is the actual bubble storage layer, that is, it contains the cylindrical magnetic domains under proper external bias conditions. Desired characteristics of this layer include: small bubbles for high storage densities, high bubble domain mobility, perpendicular uniaxial anisotropy, low number of film defects, and stability over a large temperature range.

In order to further understand the mechanisms by which various bubble devices function and thereby motivate the research that is being done in NiCoB thin films, it is necessary that we briefly review the present bubble device technology.

Assume that the ferromagnetic thin garnet film shown in Fig. 1-1 has been grown so that the easy axis of magnetization is perpendicular to the surface. Then, in the absence of an external magnetic field, the film reaches a minimum energy state by forming domains of alternating magnetization in the form of serpentine patterns (Fig. 1-1a). By applying an external magnetic field, the total energy of the system is affected in such a way that domains with a magnetization opposite to that of the applied field shrink until only cylindrical domains remain (Fig. 1-1c).

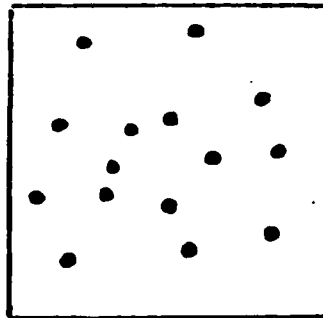


(a) No external magnetic field.



⊗  $H_{ext}$

(b) Small external magnetic field.



⊗  $H_{ext}$

(c) Large external magnetic field.

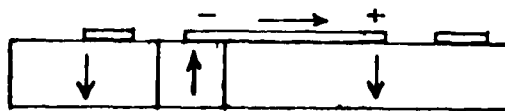
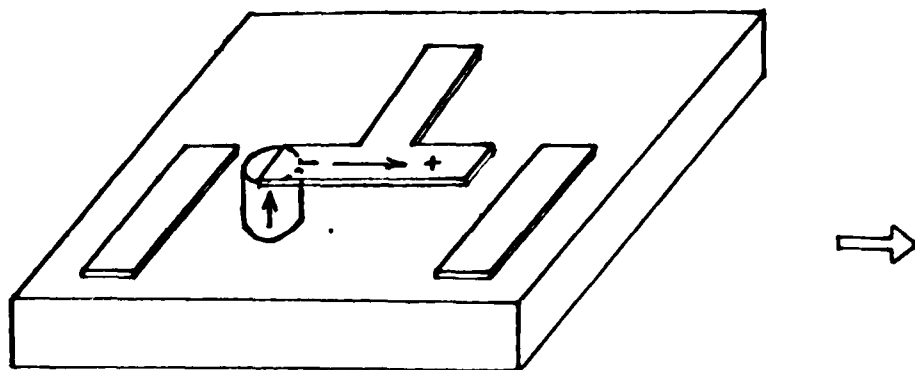
Figure 1-1: The formation of stable magnetic bubble domains under the influence of an externally applied bias field.

Manipulation of the cylindrical domains, or bubbles, is achieved indirectly by applying an in-plane magnetic field. By the use of appropriately placed patterns of thin films of permalloy (.79 Ni - .21 Fe) on the surface of the garnet film, the gradient of the magnetic field perpendicular to the plane can be controlled. The permalloy acts to convert the applied in-plane field into field gradients perpendicular to the film plane, thereby creating positions where the bubble has low energy (stable positions). The presence or absence of a bubble at such a position represents the binary one or zero, respectively. By laying down permalloy with a specific pattern, bubbles can be propagated along the pattern by an in-plane rotating field. As depicted in Fig. 1-2, the applied in-plane magnetic field orients the magnetization in the permalloy so that a magnetic bubble of the polarity shown is attracted to the "negative" end of the permalloy bar. By rotating the in-plane field counter-clockwise, as shown, the bubble domain moves to the new position (Fig. 1-2b). As one can easily see, by applying a continuously rotating in-plane H field, bubbles may be propagated along a path defined by the permalloy pattern. Devices which employ an applied rotating in-plane H field to induce bubble domain motion are termed field access devices. The actual shape of the permalloy need not be restricted to T-I bars and in fact, other shapes, such as the asymmetric chevron, are successfully being employed as propagation patterns with higher bit densities than is permitted by T-I bars.<sup>2</sup>

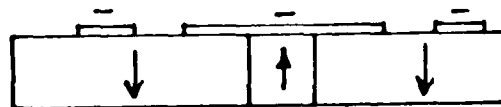
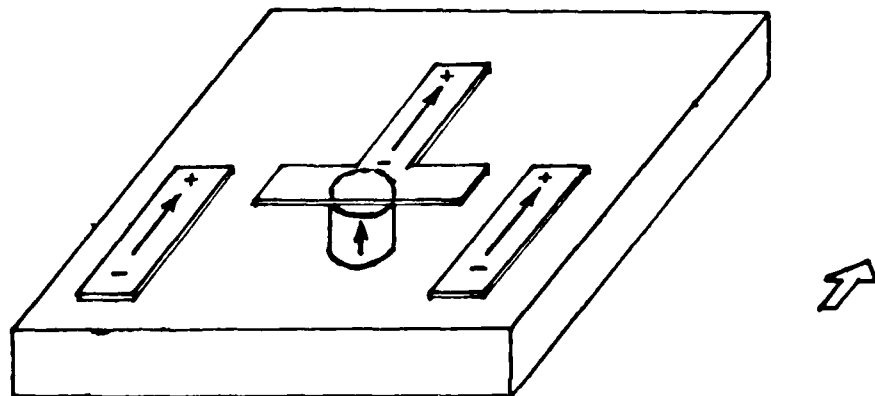
Conventional magnetic bubble memory devices presently use the field-access method for bubble propagation, that is, permalloy patterns are used for propagation, as described above. However, any method that creates magnetic drive fields, i.e., field gradients perpendicular to the plane of the bubble layer, will permit manipulation of the bubble domains and therefore represents a potential magnetic bubble memory device.

One way of modulating the magnetic field gradients is by means of currents through conductors that have been deposited on the garnet film. This current-driven propagation method (also known as a conductor-access device) avoids the drive-field coils that are necessary in the field-access method, thereby facilitating higher bit rates.<sup>3</sup>

Yet another possibility that has been investigated involves the use of continuous tracks in the form of contiguous disks (contiguous-disk devices). These devices, which can to some extent be considered as a refinement of conventional field-access technology, contain patterns of disks which are continuously joined to one another



(a) Bubble attracted to the "negative" end of the permalloy.



(b) Applied in-plane field rotated  $90^\circ$  counterclockwise as compared to (a).

Figure 1-2: Bubble propagation due to interaction between bubble domain and externally magnetized permalloy overlay.

rather than separated by gaps as with permalloy patterns. Since the lithographic limit in conventional bubble circuits is set by the gaps between pattern elements, contiguous-disk devices allow for much greater bubble densities given the same lithographic limit.

The bubble motion in contiguous-disk devices is controlled by domain boundaries, or "charged walls". A rotating in-plane magnetic field coupled with the in-plane magnetization due to the magnetostriction resulting from ion-implanting the surface of the garnet film (originally with easy axis perpendicular to the plane of the film) produces attractive and repulsive charged walls that circulate around each disk and more or less "drag" the bubble with them, thereby passing the bubbles from one disk to another.<sup>4,5</sup> Referring to Fig. 1-3, one can understand more specifically the basis of operation of a contiguous-disk device. An epitaxially grown film with magnetic anisotropy perpendicular to the film plane is implanted with ions outside the disk pattern, thereby inducing stress in the ion-implanted areas; this induced stress causes the magnetization in these regions to lie parallel to the plane of the film while the magnetization in the unimplanted regions (inside the disks) remains perpendicular to the plane as before. The in-plane magnetization of the implanted regions can now be oriented by the application of an in-plane magnetic field. Note however, that near the boundaries between the implanted and unimplanted regions, the in-plane magnetization is forced to "diverge" around the unimplanted region thereby causing a local accumulation of "magnetic charge" at opposite sides of the unimplanted disk. These charged walls, one negative where the magnetization diverges and one positive where it converges, will rotate along with the in-plane magnetization as the applied in-plane field is rotated. By placing a continuous series of these disks adjacent to one another (hence the name contiguous-disk device), a bubble propagation path is defined.

One of the disadvantages of contiguous-disk devices, however, lies in the fact that the actual propagation of a bubble on a track is complicated by the crystalline anisotropy of the implanted drive layer. This directly influences the device behavior, and hence, the device design.<sup>5</sup> Due to the magnetocrystalline anisotropy of this drive layer, certain tracks have depressed collapse margins, and bubble propagation speed varies by a considerable amount when the applied field moves through  $0^\circ$ ,  $120^\circ$ , and  $240^\circ$ , leading to a lower frequency margin than would otherwise be possible. Although one can avoid "bad" tracks in a device by orienting all of the propagation patterns in specific directions, this naturally leads to inefficient use of the chip area.

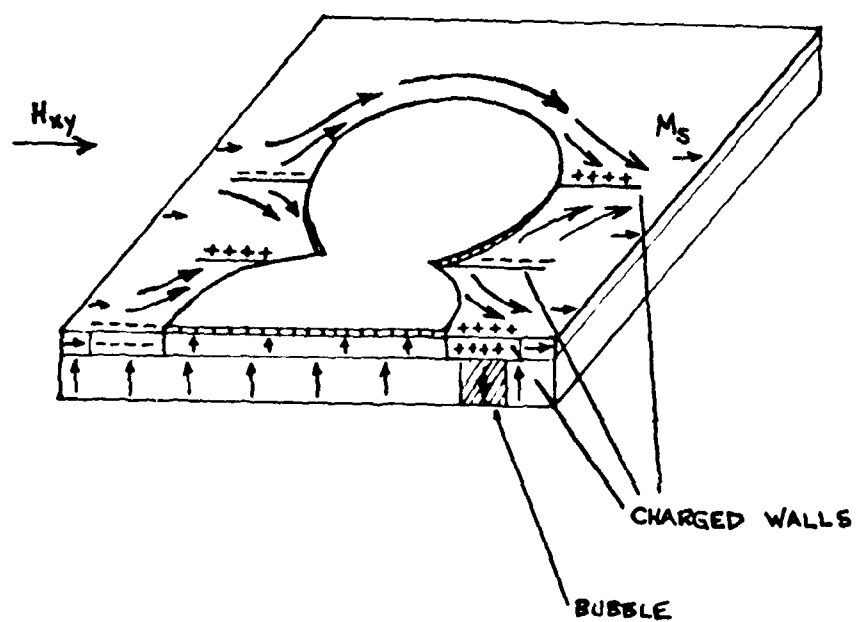


Figure 1-3: Schematic representation of a contiguous-disk device.  
Adopted from Eschenfelder<sup>5</sup>

By using a NiCoB ferromagnetic thin film as the drive layer (refer to Fig. 1-4), this problem is avoided since the drive layer is now basically amorphous and therefore isotropic. As can be seen in Fig. 1-4, desirable properties of such a layer would include  $K_u \text{ PERP} < 0$  (hard axis perpendicular to the film plane) and no preferred direction in the plane of the film.

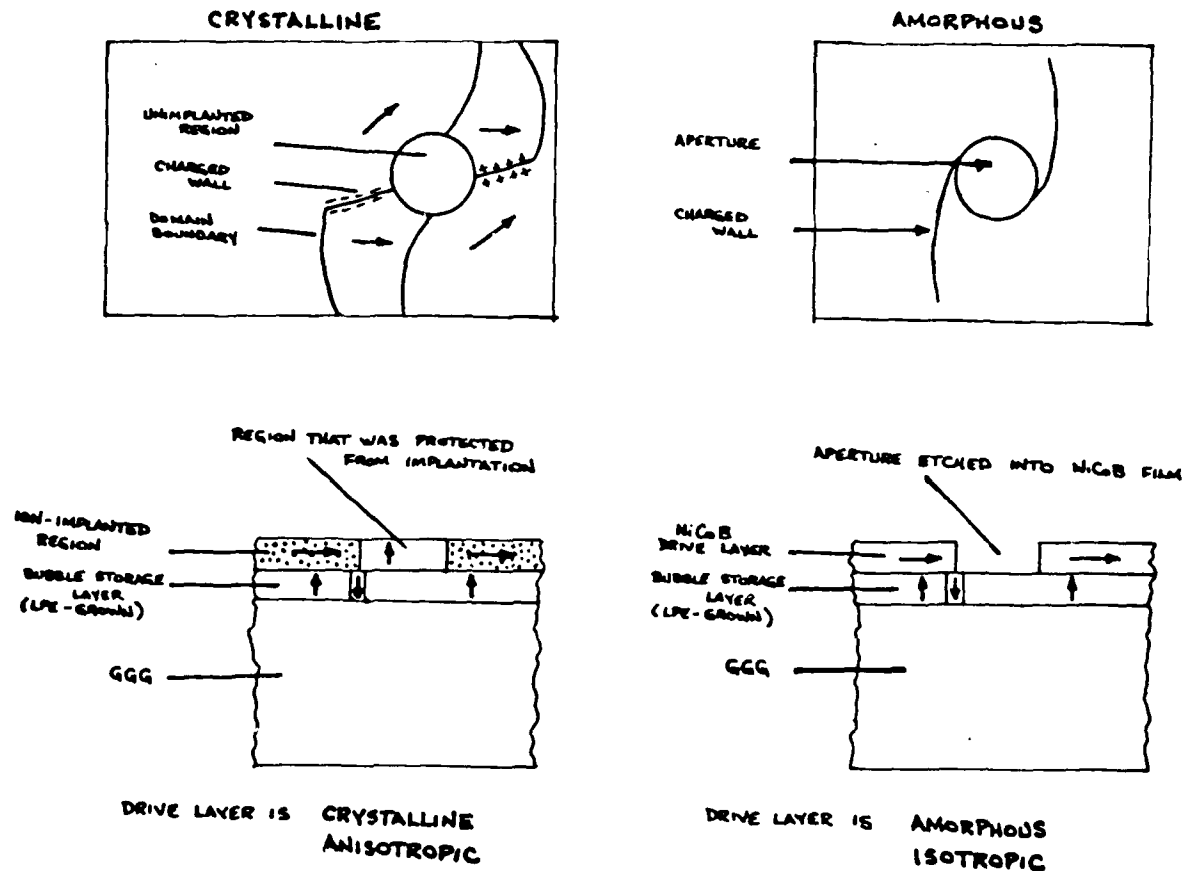


Figure 1-4: Comparison of properties of present crystalline ion-implanted contiguous-disk drive layer with that of a proposed NiCoB amorphous film drive layer.

Therefore, the principal task becomes that of thorough magnetic characterization of a variety of potential NiCoB film compositions in order to determine the feasibility of using these films as the drive layer of a contiguous-disk device. By varying the



composition, the important magnetic film properties  $4\pi M_s$ ,  $H_{k \text{ PERP}}$  (or equivalently,  $K_{u \text{ PERP}}$ ), and  $H_{k \text{ PAR}}$  ( $K_{u \text{ PAR}}$ ) are directly influenced; these can then be measured using a force-balance magnetometer and a ferromagnetic resonance system and the suitability of a particular composition can be determined.

Other possible potential advantages of such an amorphous-film device include simpler fabrication steps, and hence, lower manufacturing costs. Other considerations, which have become evident during the course of this work, such as additional anisotropy and coercivity requirements are discussed in Section 4.7.

For a more complete and detailed description of magnetic bubble domains, materials, and devices, the reader is referred to any of the several fine texts and articles on the subject.<sup>5-9</sup>

## 1.2 Magnetic Amorphous and Polycrystalline Alloys: NiCoB Ferromagnetic Thin Films

### 1.2.1 Introduction

The enormous amount of progress that has been made in magnetic bubble devices is due in large part to advances that have occurred in the fabrication of magnetic materials. The unending quest for higher bit density, lower power consumption, and lower cost has fueled great interest in the search for new magnetic bubble devices, with some emphasis based on new magnetic materials. In particular, work has been done in the field of fabrication of amorphous ferromagnetic thin films, both with and without an anisotropy perpendicular to the plane of the film.<sup>10-14</sup>

In some amorphous films, charged walls, such as those described above in conjunction with contiguous disk devices have been observed.<sup>12,15</sup> From previous work that has been done on films of this nature, in particular NiCoB films, various properties of the charged walls have been found to depend on the composition of the film, the thickness ( $t$ ) of the film, and the value of the saturation magnetization ( $4\pi M_s$ ).<sup>15</sup>

### 1.2.2 Survey of Amorphous Magnetic Alloys

Since the NiCoB films under investigation fall under the general category of amorphous magnetism, it is instructive to briefly review the basic properties of these materials.

Amorphous magnetism generally encompasses the study of the magnetic properties of dilute random substitutional alloys, amorphous metallic alloys, amorphous magnetic semiconductors and the conventional glasses, including chalcogenide, organic, and inorganic glasses. Although thought to be quite different at one time due to differences in atomic structure, it is now generally recognized that these materials exhibit certain basic similarities. Three categories of amorphous metals and alloys thus far experimentally obtained emerge, each division closely reflecting the method of preparation:

1. amorphous pure metals and alloys which can be obtained by evaporating on a cooled substrate. In this case, the amorphous state is stable only at low temperatures and is sustained by the substrate.
2. metal-metal alloys prepared by evaporation, sputtering, or by rapid quenching from the liquid state. Typical of this category are the various rare earth-transition metal combinations.
3. metal-metalloid alloys obtained by rapid quenching, chemical deposition from aqueous solutions, electrodeposition, or by sputtering. The NiCoB films investigated in this report fall into this category.

It appears that in a majority of the cases that have thus far been carefully examined, the structure of the amorphous state can be described reasonably well as a random dense packing of hard spheres.<sup>16</sup> Apparently, the stability of the state is due to a mixture of appropriately different-sized atoms and also by a combination of metallic and covalent bonding. Typical experimental studies of ferromagnetism in amorphous metal-metalloid solids use alloys of 3d transition metals (esp Fe, Co, Ni, Cr, and Mn) with about 15 to 30 atomic percent of light metalloid elements of groups IIIA, IVA, and VA (B, C, Si, P). It is believed that these small metalloid atoms are supposed to occupy relatively larger holes in the dense random packing structure of the metal atoms, transferring electrons to the unfilled d band of the transition metal(s).<sup>16</sup> This neatly accounts for the reduction of magnetization of these amorphous alloys when compared to the corresponding metallic crystalline alloys without the metalloid component. Of particular interest to this project is the investigation of Aboaf, et.al.,<sup>10</sup> where various amorphous transition metal--metalloid ferromagnetic films were deposited by RF sputtering for metalloid content from 0 to 40 atom percent. Here, it was reported that for the binary systems FeSi, FeB, FeAl, CoB, CoSi, and NiB, only FeSi, FeB, and CoB form films which are magnetic at room temperature for the sputtering conditions that were used. In addition, the formation of the amorphous phase in these three magnetic systems occurs respectively for metalloid content of over 26, 16, and 14 atom percent; films are still magnetic for

the highest concentration of metalloid studied, respectively 42 and 36 atom percent for FeSi and FeB.

## 2. FABRICATION OF THE NI-CO-B FILMS

### 2.1 The Sputtering Process

Sputtering is a process in which atoms from a cathode, or target, are driven off, or sputtered, by bombarding ions due to a transfer of momentum from the ions to the target atoms. In this process, the momentum of the bombarding ions is more important than the amount of energy transferred. An atom of hydrogen or helium accelerated to 500 eV will cause very little sputtering compared, say, to a heavier ion such as (chemically inert) argon with the same 500 eV energy because the smaller amount of momentum within the much lighter hydrogen or helium ion simply has much less effect. Ions, rather than neutral atoms, are used for bombardment because one can accelerate these to any desired kinetic energy by the use of electric fields.

Sputtered atoms travel until they impinge upon a substrate, where they deposit to form the desired layer. Since they travel as individual atoms, they can be chemically active and form compounds with the ions and atoms of the bombarding gas. For this reason, the noble gas argon, which is chemically inert, is generally used as the source of bombarding ions.

*When ions of argon strike the target, their electrical charge is neutralized and they return to the process as atoms. Note, however, that as a result, a net positive charge results at the target surface due to this form of sputtering, called DC sputtering. If the target is an electrical conductor, this poses no problem since the charge is instantly cancelled by a free electron; however, if the target is an insulator, the result is a positive charge build-up at the target surface. This charge may grow large enough that the ions of bombarding gas are repelled causing the sputtering process to stop. To continue the process, the anode-cathode polarity must be reversed to attract electrons from the discharge to eliminate the target surface charge. By applying an RF voltage to the target assembly, the polarity is automatically reversed periodically and the problem is eliminated. Also, note that due to the vast differences in the mobilities of the ions and electrons, the much faster electrons are attracted in much greater numbers to the target during the positive half-cycle of the RF voltage than are the ions during the alternate half-cycle. The applied RF voltage is what distinguishes this type of sputtering from simple DC sputtering.*

Sputtering is a function of many variables-- parameters which determine yields

(atoms per ion), thresholds (minimum kinetic energy of ions for sputtering to become noticeable), and angular distribution of ejected atoms (atoms, ions, or clusters) are primarily the masses of the ion and the target atom, the outer electronic configuration of the collision partners, the angle of incidence and the kinetic energy of the impinging ions, the crystal structure and crystal orientation of the target material, the target temperature, and the ion flux (or current density).<sup>17,18</sup> The measured sputtered yield will also be a function of the background sputtering gas pressure, the previous history of the solid (including the concentration of implanted ions), and electrical fields existing at the surface of the target. In addition, if the mean free path of the sputtered atoms is small in comparison to the distance between the target and substrate, which is usually the case at pressures above several microns, many additional effects resulting from collisions between gas atoms, ions, sputtered particles, and electrons become important.

Usually, for technological applications, one may use the empirical values of the sputtering yields, provided that the target materials are relatively featureless and nearly isotropic.

Also, it should be noted that the main disadvantage of sputtering is the fact that the deposition rates are relatively low; typically, deposition rates are in the range of 50 to 3000 Å/min.<sup>19</sup>

In some instances, a bias voltage applied between the target and substrate is used to alter the sputtered film composition and structure. When the substrate is deliberately given a negative potential with respect to the plasma, the resulting technique is referred to as bias sputtering. Although generally bias sputtering leads to films of higher purity since during resputtering most impurities are preferentially removed relative to the atoms of the main film, the amount of sputtering gas trapped in a sputtered film is experimentally found to increase above a given bias voltage. This leads to the final significant consideration that must be addressed--that of the amount of trapped sputtering gas atoms within the deposited film. It is expected that any such inert atoms would serve as a dilutant to the magnetization and not affect film properties significantly in any other way. At bias voltages of less than 200 volts, which is the only region of interest for the purpose of this discussion since all of the NiCoB films were sputtered at zero-bias voltage, no significant amount of argon was found in the nickel-argon system studied by Winters and Kay.<sup>20</sup> Also, although 1 atomic percent argon was reported in sputtered GdCo and GdCoMo films at 60 volts bias voltage, with a rapid increase for higher bias

voltages, no significant amounts of argon were found at zero-bias voltage in these films, either.<sup>21</sup> This was also the case found experimentally for the NiCoB films in this report; this will be discussed further in Chapter 4.

When sputtering under conditions of identical system geometry and current density, it is expected that deposition rates for different materials would correlate well with their theoretical sputtering yields. The values given in Table 2-1<sup>22</sup> are the sputtering yields in atoms per ion of  $\text{Ar}^+$  for different bombarding energies of the argon ions. The error here may be as high as 20 percent for some values since much of the published data fails to make corrections due to secondary-electron emission.<sup>22,23</sup>

TARGET MATERIAL	200	600	1000	(VOLTS)
<hr/>				
	Sputtering Yields (Atoms/ion)			
Co	0.6	1.4	---	
Ni	0.7	1.5	2.1	
B	---	0.4	---	
<hr/>				

Table 2-1: Sputtering yields in atoms per ion of  $\text{Ar}^+$  for different bombarding energies of the Ar ions.<sup>22,23</sup>

## 2.2 Sputtering With Decoupled Plasmas

### 2.2.1 Preparation of the NiCoB Films

Amorphous and polycrystalline ferromagnetic NiCoB films were fabricated by RF sputtering in order to permit characterization as to various magnetic properties according to the methods described in Chapter 3 of this report. The films were deposited by sputtering using argon gas from hand-made targets containing foils (nickel and cobalt) and slices (boron) of the desired elements. Figs. 2-1 and 2-2 show the precise geometries for the cobalt-nickel and the cobalt-boron targets, respectively.

Each of the 15 cm (6 inch) diameter cathode targets was made of copper plate on

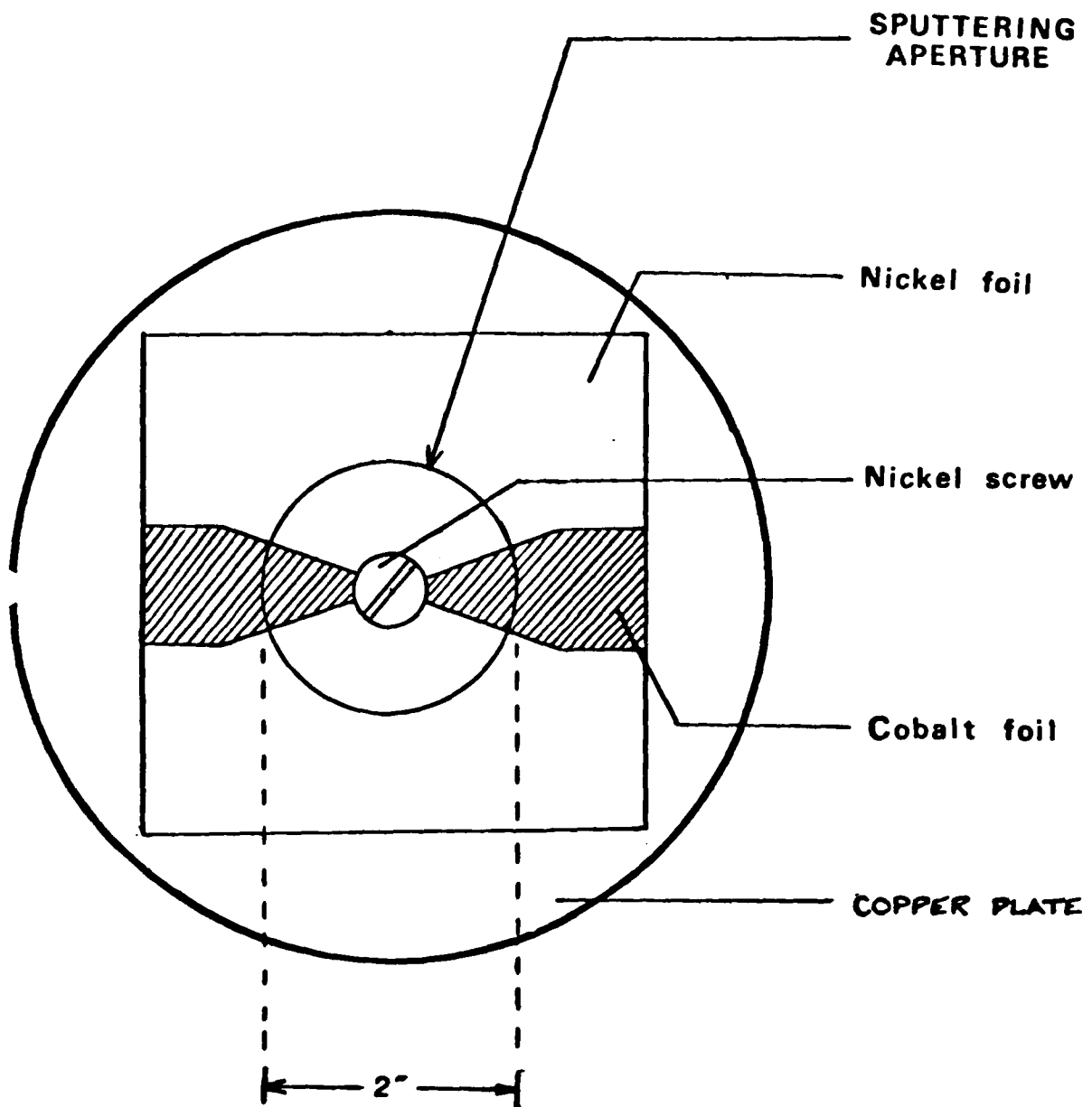


Figure 2-1: Manually-fabricated cobalt-nickel target used for sputtering.

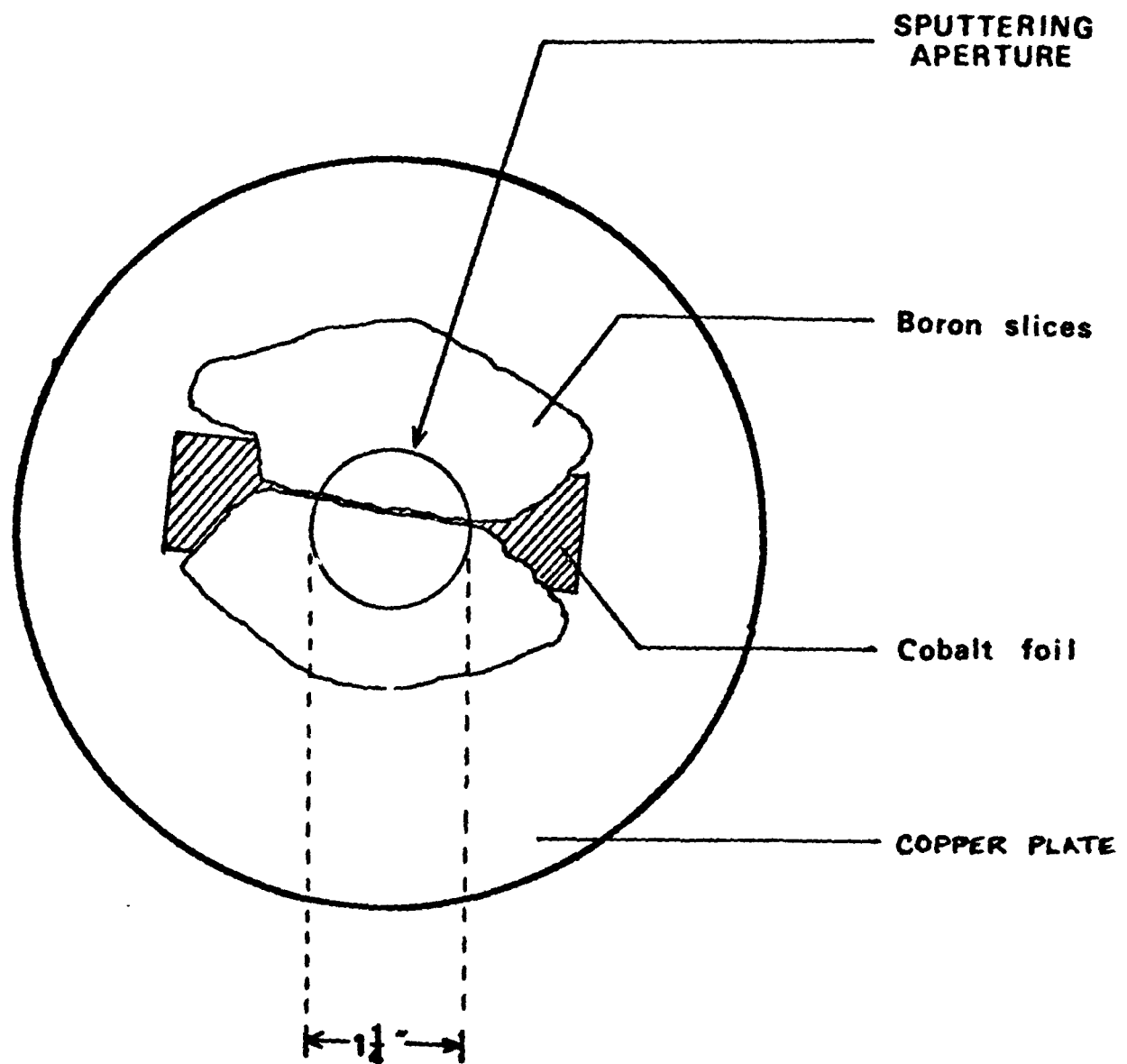


Figure 2-2: Manually-fabricated cobalt-boron target used for sputtering.



which the desired foils and slices were mounted by clamps located near the periphery of the plate. The plate was then attached by screws located equidistantly at the perimeter to the water-cooled copper cathode assembly. A grounded dark shield located approximately 12 mm below each target surface effectively defined an area on the target from which the deposited films were sputtered. Silicone vacuum grease was used between the foils and slices and the copper plate to increase the thermal coupling. For the cobalt-nickel target, the nickel foil, a .5 mm thick plate of 99.997% purity (Alfa Products<sup>24</sup>) was used as a base upon which carefully-measured pie-shaped segments of .25 mm thick, 99.9% pure cobalt (Materials Research Corporation VP grade<sup>25</sup>) were attached. The base of these triangular cobalt segments along with the nickel backing were held by the aforementioned clamps while the inner tips of the cobalt foils were fixed under the wide head of a nickel screw mounted in the center; this screw was fashioned from a .5 inch diameter nickel rod (99.995% pure, Materials Research Corporation Marz grade<sup>25</sup>). The boron slices used in the cobalt-boron target were cut from large boron chunks of 99.9% purity and these ranged from 5 to 10 mm in thickness over the bulk of a single slice. The somewhat awkward shapes of the boron pieces were due to difficulties encountered in cutting that material. This was due in part to the large surface area that was being cut and also to the hardness of the boron which, being 9.5, approaches that of diamond (10.0). The Micromatic wafering machine used in cutting the boron employed a Norton diamond wheel blade; attempting to achieve thinner slices resulted in numerous unusably small fractured pieces so that pieces of greater thickness than originally intended were used out of necessity.

The RF sputtering apparatus used was a Perkin-Elmer Sputtering System Model 2400-6J.<sup>26</sup> The vacuum system employed a helium cryogenic vacuum pump<sup>27</sup> with a conventional carbon filtering system. The argon pressure during sputtering was maintained at a constant value by monitoring an Ultek digital gauge control and manually adjusting a gas-bleed needle valve as required. The vacuum chamber consisted of a 66 cm-diameter stainless steel cylinder containing three 15 cm-diameter, water-cooled target electrodes arranged 90 degrees apart on a 15 cm-radius circle; since only two target assemblies were used, the cobalt-nickel and cobalt-boron targets were mounted 180 degrees apart. The 15 cm-diameter, water-cooled substrate table was mounted on a "J-arm" configuration and was supported on a double O-ring rotary vacuum seal so that the J-arm could be rotated up to a maximum of 10 rpm, thereby sequentially exposing the substrate to each of the target electrodes. The relative arrangement of the targets and substrate table is shown in Fig. 2-3.

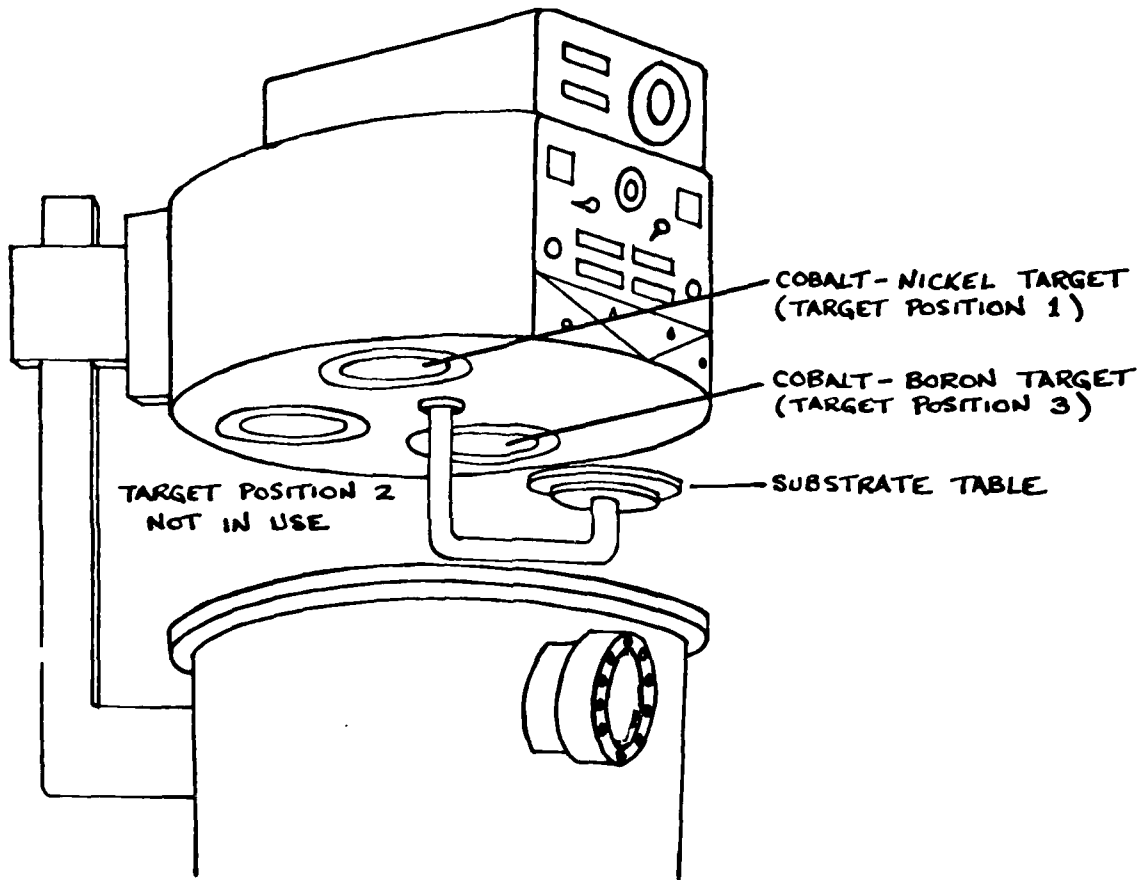


Figure 2-3: Relative positions of the targets and the substrate table.  
The dark shields and sputtering table shield have been omitted for clarity.

Each target was individually powered from a single Randex 1 kW RF power supply. Meters which provided a separate reading of each target voltage were used as a guide in adjusting the power division between the two targets and for resetting a previously established set of conditions. The best impedance match to the generator was adjusted automatically by the Randex servo-match control in the system; during a successful sputtering run, it was relatively easy to keep the reflected power to less than 5 watts (on the order of 1%).

The amorphous and polycrystalline NiCoB films were deposited onto 1 inch-diameter Corning 0211 glass substrates<sup>28</sup> and 25 mm by 25 mm pieces of VWR Scientific microscope slides.<sup>29</sup> Before each sputtering run, the vacuum chamber was evacuated to a pressure of less than  $7 \times 10^{-7}$  torr before permitting the ultra-high purity argon into the chamber. During deposition the argon pressure was held constant at 25 millitorr  $\pm$  4% by manual control. The distance between the target surface and the substrate table was generally held at 45 mm (1.25 inches from dark shield to substrate table) as measured when the substrate was directly beneath any given target. The substrate table rotation rate was kept near 3 rpm although this tended to increase by as much as 25% during the course of a long sputtering run. Both targets were "sputter-cleaned" for 15 to 45 minutes prior to each run, the amount of time depending on the condition of the target surface before the run. The substrates were cleaned ultrasonically in boiling solutions of trichloroethylene, acetone, and methanol, in that order, and then any remaining organic residue was removed by use of a plasma asher for 30 seconds. The total input sputtering power was on the order of 300 to 600 watts. A typical sputtering run of 2 hours duration yielded films on the order of 3000 Å in thickness. By changing the fraction of the total power that was applied to each target, the voltage applied to each target was varied and hence the final deposited film composition was altered. In addition, by changing the number of pie-shaped foils of cobalt on the cobalt-nickel target, the nickel-to-cobalt ratio in the films was varied.

### 2.2.2 Discussion

The chemical composition of a sputtered film will often be the same as that of the target from which it was sputtered even though the individual components of the system may have relative sputtering rates which are quite different from one another. This can be explained by noting that, although it is true that the component with the highest sputtering rate will come off faster the very first time that sputtering is performed on a multi-component (homogeneously mixed) target, a compositionally

"altered" region forms quite readily at the target surface. Subsequent deposits have the same composition as the target since the sputtering surface is depleted of the higher sputtering yield component by an amount just adequate to compensate for its greater rate of removal from the target surface. For this reason, one can sputter-deposit films of complicated materials such as permalloy or even stainless steel directly from targets made of that material without composition changes even though the sputtering rates of the individual elements are quite different.

Of course, this will not be true if a significant amount of resputtering occurs as, for example, during bias sputtering. If this is the case, then material with the highest sputtering yield will be preferentially removed from the film-- exactly the principle of bias sputtering. Since the surface of the growing film is being constantly replenished with material of the target composition, an altered layer cannot form so that the sputtered film composition will contain less of the materials with the higher sputtering yields as compared to the target.

When one is not using "pre-alloyed" targets, but instead separate elements placed individually on the cathode(s), one must take into consideration the amount of mixing of the atoms which will occur. As early as in 1962, an experimental arrangement utilizing separate cathodes was described by Sinclair and Peters.<sup>30</sup> A fair degree of intermingling of the components sputtered from the two interleaving cathodes was found; the method depended on the fact that not all of the sputtered material is deposited on the substrate directly beneath its point of origin on the target but instead may travel a small distance laterally as well. Various alloy compositions were obtained by suitably adjusting the relative voltages to the targets. This and other evidence from the literature<sup>31,32,33</sup> indicate that a fair degree of mixing will occur due to the collisions of the target atoms with each other and the argon gas atoms as they travel from the target to the substrate. In other words, when the mean free path of the sputtered atoms is small when compared to the distance between the target and substrate, one can expect the sputtered films to be a homogeneous mixture of the separate target elements. Electron microprobe analysis done on the NiCoB films lend further credence to the above; the film compositions were found to be very homogeneous. Again, this will be discussed further in Chapter 4.

### 3. CHARACTERIZATION OF THE NI-CO-B FILMS

Average film composition was determined by electron microprobe analysis and saturation magnetization by force-balance magnetometer. Investigation of the magnetic anisotropy of the films was carried out using ferromagnetic resonance and the torque magnetometer. In addition, in an attempt to observe domain walls in the films with hard axis perpendicular to the film plane, a ferrofluid investigation was performed. Details of these methods of characterization appear in this and the following chapter.

Film thickness was measured using a Sloan Dektak<sup>34</sup> film profile monitor.

#### 3.1 Electron Microprobe Analysis

The method of electron microprobe analysis was used to determine the composition of the NiCoB thin films. A very brief and basic discussion of this technique follows; any one of several good textbooks on microprobe analysis will provide a more detailed description of the subject.<sup>35,36,37</sup>

##### 3.1.1 Physical Principles of Microprobe Analysis

In the electron microprobe, electrons, emitted from a hot filament, are accelerated and focused onto a sample surface. Inelastic scattering in the sample material leads to ionization and then to the emission of X-rays, characteristic of the elemental composition. The X-rays thus emerging from the sample are then analyzed in appropriate spectrometers and differentiated according to wavelength and intensity, thereby providing qualitative (identifying the elements present) and quantitative (determining the amount of each element present) chemical analyses, respectively. The use of a finely focused electron beam gives this technique the particular advantage of enabling X-ray spectrochemical analyses to be obtained on volumes of specimen as small as one cubic micron.

At present, all elements heavier than beryllium can, theoretically at least, be studied with the probe. However, as the probe is sensitive to the weight percentage of an element present in the sample, light elements with atomic numbers less than 13 are difficult to measure accurately. In general use, limits of detectability in solid solution approximate 0.005% to 0.05% depending upon the elements themselves and the corresponding sample matrices. Since local concentrations may vary largely from average composition, true limits of detectability are generally difficult to define.

By recording the spectrum by means of an X-ray spectrometer over the range of wavelengths within which relevant lines may be present, the wavelength corresponding to a particular characteristic line and hence the corresponding element, may be identified. In quantitative analysis, the intensities of the X-ray lines from the sample are compared with those from standard samples of known composition. These measured intensities require correction for background, the chief source of which is the continuous X-ray spectrum, as well as certain instrumental correction dependent on the characteristics of the measuring system. Once the corrected intensities have been determined, the composition at the analyzed point is calculated by applying matrix corrections which take account of various factors governing the relationship between intensity and composition. These factors include absorption of characteristic X-rays from the specimen, enhancement due to fluorescence by other lines, electron backscattering, and an atomic-number-dependent "stopping power" of the specimen which creates a variation in the efficiency of X-ray production.

Typically, the electrons have a kinetic energy of 10 to 30 keV, and penetrate the sample to a depth of the order of  $1\text{ }\mu\text{m}$ , spreading out laterally to a similar distance. Although in theory the spatial resolution can be further improved by reducing the electron energy, this is generally impractical because the electrons must have sufficient energy for efficient X-ray excitation.

The microprobe instrument itself has the general configuration as shown schematically in Fig. 3-1.<sup>35</sup> The source of electrons is usually an electron gun in which a tungsten "hairpin" filament is heated to over  $2500^{\circ}\text{K}$  in order to create thermionic emission. This filament is kept at a negative potential (10 to 30 kV) which therefore causes acceleration of the electrons through an aperture in the grounded anode plate. Magnetic lenses (condenser and final lens in the figure) are used to focus the beam into a fine probe incident on the surface of the specimen. In order to prevent scattering of the electrons, oxidation of the hot tungsten filament, and absorption of the resulting X-rays in air, the electron path, the sample, and the spectrometers are all maintained at a high vacuum.

### 3.1.2 Experimental Procedure

The diffracting crystal which comprises the Bragg spectrometer (which is generally used to analyze the X-ray spectrum) acts as a monochromator, selecting one wavelength at a time. Covering the full range of interest of X-ray wavelengths (from 1 to about 100 Å) requires the use of several crystals. Equipping the instrument with

AD-A131 706

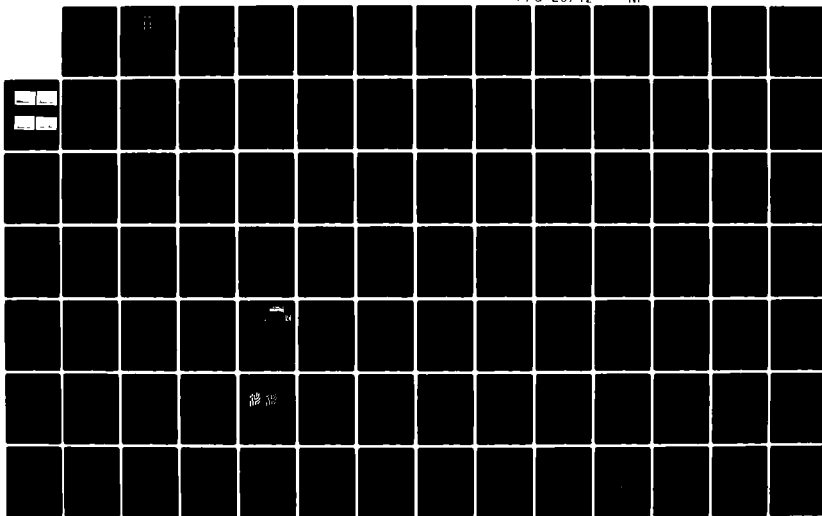
A PROGRAM OF RESEARCH ON MICROFABRICATION TECHNIQUES  
FOR VLSI MAGNETIC DEVICES(U) CARNEGIE-MELLON UNIV  
PITTSBURGH PA M H KRYDER ET AL. 01 OCT 82  
AFOSR-TR-83-0685 AFOSR-80-0284

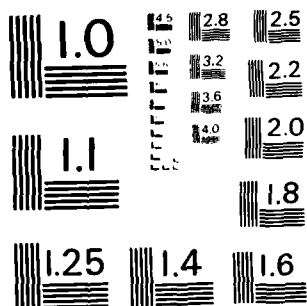
2/3

UNCLASSIFIED

F/G 20/12

NI





MICROCOPY RESOLUTION TEST CHART  
NATIONAL BUREAU OF STANDARDS-1963-A



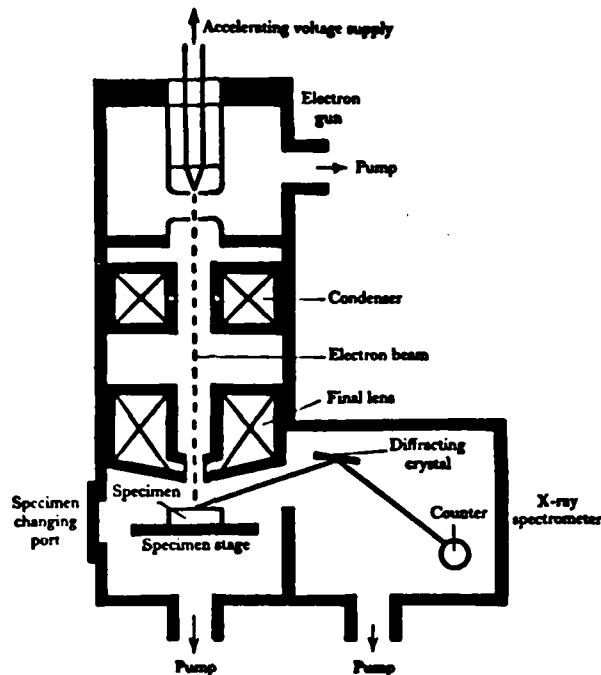


Figure 3-1: Schematic diagram of the electron microprobe.<sup>35</sup>

more than one spectrometer permits the simultaneous analysis of more than one element. The microprobe<sup>38</sup> at Carnegie-Mellon University has three spectrometers equipped with LiF/ADP, LiF/ADP, and KAP/PbSD crystal couples (crystals could be interchanged) giving a wavelength coverage from 1 to 90 Å [LiF: 1.07--3.77 Å, ADP: 2.88--10 Å, KAP: 7--25 Å, PbSD: 29--93 Å]. Proportional counters were used as X-ray detectors in the desired regions; in these counters, the pulse amplitude generated by the X-ray photon depends on the photon energy. Then, by using pulse height analyzers which were adjusted so that only pulses of a selected amplitude are admitted to the counting circuitry, interference of spectral lines due to order overlapping was eliminated.

The composition of the NiCoB film was determined by comparison of X-ray intensities from the sample to those from suitable standards, typical of microprobe quantitative analyses. The standards chosen, namely pure nickel, cobalt, and boron, were made from the same high purity foils and pieces, respectively, that were used to fabricate the sputtering targets. Since the take-off angle and intensity of the X-rays is directly affected by a very small change in surface inclination, it was

essential that the surface of all analyzed areas (standards and samples) be flat, smooth, and parallel to one another. To minimize cross-contamination, each standard was prepared individually; after being mounted by epoxy on the flattened tip of a #4-40 stainless steel set screw, each standard was polished mechanically in a polishing block first using increasingly fine-grained sandpaper down through 600 grit and then polishing with 0.3  $\mu\text{m}$  and 0.05  $\mu\text{m}$  alumina polishing powder. The sputtered samples to be analyzed were prepared by dicing small pieces compatible with the screw tip from a sputtered film using a diamond saw and then mounting this film-on-glass to a #4-40 screw with epoxy.

In order to prevent beam instability when using the microprobe, it is important that the incident electron beam be able to pass to ground without building up charge at the region which is under analysis. This posed no problem in the case of the pure metal and metalloid standards since although non-conducting epoxy was used to attach the standards to the metal screws, enough actual contact between the standard and screw was achieved to provide a path for the beam current. However, in the case of the sputtered-films-on-glass, a very small dab of conducting silver paint, applied at the very edge of the sample between the conducting film and the screws, was required to provide a beam current path. Using this method obviated the need to coat both samples and standards with a thin film of a conducting material, since then one must become concerned with the absorption effects of the coating film. The elements and lines analyzed can be found in Table 3-1.

ELEMENT	Z	LINE	WAVELENGTH(A)	ENERGY(keV)	CRYSTAL USED
Ni	28	K <sub>α</sub>	1.659	7.471	LiF
Co	27	K <sub>α</sub>	1.790	6.924	LiF
B	5	K <sub>α</sub>	67.6	0.183	PbSD

Table 3-1: X-ray lines analyzed and crystals used with the microprobe.

In actual use, the samples- and standards-on-screws were mounted in a brass sample holder, which consisted of a 1.25-inch diameter concentric set of 24 equally-spaced tapped holes into which the #4-40 screws could be inserted. The fact that the standards and samples are mounted on screws not only allows one to easily change samples, but also permits one to set the screws in such a way that the entire holder, including samples and standards, is in focus in the same horizontal plane. In this way, only very minor adjustments need be made when traveling from sample to sample on the holder. The #4-40 screw thread size was chosen for its large number of threads per inch, which reduces the variation of sample surface angle. Along with the sample and standard, it was also necessary to include a magnesium oxide (MgO) crystal; since this material is cathodoluminescent (i.e., the electron beam impinging on this material causes a visible fluorescence effect which allows one to visually observe the beam), it was used to visually focus the electron beam.

In making a typical measurement, the X-ray counting rate is recorded for both the unknown and the standard by averaging many trials for each case. Likewise, the background levels are recorded for both the unknown and the standard. After making corrections on the measured counting rates for instrument dead-time, the concentration of the measured element may be computed from:

$$C = [N_U - N_U^B] / [N_S - N_S^B]$$

where  $N_U$  is the averaged number of counts per some unit time interval for the unknown,  $N_U^B$  the background for the unknown,  $N_S$  the number of counts for the

standard, and  $N_S^B$  the background for the standard. For complicated element matrices, this ratio must then be subjected to matrix corrections using a computer program. In the case of the simple Ni-Co-B matrix, it was assumed that the substrate factor was the same for all elements so that the only correction required was due to the thinness of the films (most less than 5000 Å). To be sure that each of the samples had been mounted parallel with respect to the standards, measurements were made on each sample at rotations of both  $0^\circ$  and  $180^\circ$ ; if the measured count rate differed by more than the standard deviation due to the counting statistics, then the sample was removed and reattached properly. Although measurements of the Ni and Co compositions appeared reliable, severe difficulty was encountered in working with the light element boron. Although a PbSD crystal was available, a special-purpose X-ray detector with satisfactory efficiency for long wavelengths was not. Since absorption of the X-rays is especially serious for those with long wavelengths, proportional counters are fitted with extremely thin entrance windows and a gas filling of low density is used. Various methods of enhancing the number of these long-wavelength X-rays was attempted including the use of a significant increase in beam current, but all netted only limited success. Since these measurements could not be made at the facility located at CMU, quantitative values for boron content were obtained by Malcolm McConnel at General Electric on an automated Cameca Electron Microprobe equipped with the necessary apparatus. A discussion of these results can be found in Section 4.1.

### 3.2 Ferromagnetic Resonance

The magnetization vector of a ferromagnetic material can precess about its equilibrium position, this being due to the gyroscopic properties of the magnetic moment. In a typical ferromagnetic resonance experiment, a sample of ferromagnetic material is placed in a uniform field large enough to magnetize the sample in the direction of the applied field. When the magnetization is disturbed slightly from this equilibrium position, it does not return directly, but precesses about the field direction. Eventually, however, energy loss associated with the magnetization motion causes the precession to be damped, ending in alignment along the applied field direction. To maintain this precessional motion for an actual atomic moment in a material, energy must be fed into the system from without. One of the means available for doing this is to apply a small sinusoidal magnetic field perpendicular to the axis of precession. This sinusoidal field excites precessional motion, but unless the frequency  $\omega$  is nearly equal to the precessional frequency, or resonant frequency,

$\omega_{res}$ , the energy coupled from the sinusoidal field to the precessing magnetization will be small. On the other hand, if  $\omega \approx \omega_{res}$ , the coupling is very large and is limited only by the damping of the system.

A universal relationship between the resonant frequency and the effective external field is readily found to be:

$$\omega_{res} = \gamma H_{eff}$$

where  $\gamma = g (e/2mc)$ ,  $\gamma$  being the gyromagnetic constant,  $g$  the gyromagnetic ratio or "g factor", and  $c$ ,  $e$ , and  $m$  being the speed of light and the electron charge and mass, respectively.<sup>39</sup> Also,  $H_{eff}$  represents the effective static H-field within the sample and in the simplest case is just  $H$ , the static applied field. Upon evaluation of  $\omega$  for typical values of  $\gamma$  and  $H$  (where  $\gamma/2\pi = 2.8$  Mhz/Oe in cgs or  $2.2 \times 10^5$  m/A-sec in mks and  $H$  is several thousand oersteds), we find that the frequency  $\omega_{res}$  corresponds to the microwave region. Since the precession frequency may be changed by changing the static applied field,  $H$ , one observes that by measuring the absorption of the microwave H-field as a function of the applied static H-field, the strongest absorption occurs at that value of the static field where the precession frequency coincides with the microwave frequency.

Note, however, that the equation above does not account for demagnetizing effects which reduce the effect of the applied static field within samples of finite dimension. Here,  $H_{eff}$  depends on the demagnetizing effects present and hence on the shape of the sample. In the case of isotropic thin films, one finds:<sup>40,41</sup>

$$\omega_{PERP} = \gamma [H_{DC PERP} - 4\pi M_s]$$

$$\omega_{PAR} = \gamma \left\{ H_{DC PAR} [H_{DC PAR} + 4\pi M_s] \right\}^{1/2}$$

where  $H_{DC PERP}$  and  $H_{DC PAR}$  represent the applied static H-fields applied perpendicular and parallel to the film plane at resonance, respectively, and  $\omega_{PERP}$ ,  $\omega_{PAR}$  represent the resulting resonant frequencies. For the slightly more complicated case of a thin film with a uniaxial crystalline anisotropy,  $K_u$ , favoring alignment normal to the plane, and no anisotropy in the plane of the film, we find:

$$\omega_{\text{PERP}} = \gamma [H_{\text{DC PERP}} - 4\pi M_s + H_k]$$

$$\omega_{\text{PAR}} = \gamma \left\{ H_{\text{DC PAR}} [H_{\text{DC PAR}} + 4\pi M_s - H_k] \right\}^{1/2}$$

where all of the parameters are as before and, in addition,

$$H_k \equiv 2K_u / M_s$$

In actual practice,  $\omega$  is usually fixed by the resonant frequency of the microwave cavity, so that absorption is plotted as a function of  $H_{\text{DC}}$ . If this procedure is followed for one sample for  $H_{\text{DC}}$  in both the perpendicular and parallel directions, then one obtains two simultaneous equations in two unknowns, namely,  $\gamma$  and  $H_k - 4\pi M_s$ , which can then be determined once  $\omega_{\text{PERP}}$ ,  $\omega_{\text{PAR}}$ ,  $H_{\text{DC PERP}}$ , and  $H_{\text{DC PAR}}$  are known experimentally. Of course, this procedure assumes a unique resonance in either direction (uniform precessional mode) and hence a single value for  $H_{\text{DC PERP}}$  and for  $H_{\text{DC PAR}}$ . Note that the individual values of  $H_k$  and  $4\pi M_s$  can not be separated with this technique since the angular dependence of the anisotropy energy is identical in both cases.

NiCoB amorphous film samples were prepared for FMR by cutting a 7 mm x 7 mm (approx.) square from a 1-inch sputtered film circle. Upon insertion into a microwave cavity of circular cross-section ( $\text{TE}_{011}$  mode at a frequency of 9.60 GHz), a measurement of the absorption perpendicular and one parallel to the plane of the film as a function of  $H_{\text{DC}}$  was made. Although the film could only be rotated about one specific axis in the plane of the film (the x-axis in Fig. 3-2), the magnet itself could be rotated by  $\pm 20^\circ$  about the z-axis thereby permitting measurements at various positions with an applied  $H_{\text{DC PAR}}$  and allowing verification that no significant anisotropy within the plane of the film existed.

A significant problem encountered in making these measurements in many of the films was the presence of many resonances for applied field both perpendicular to and in the plane of the film. It is believed that a set of such resonances is associated with the spin-wave modes which can be excited in such films, as is discussed in Appendix A.

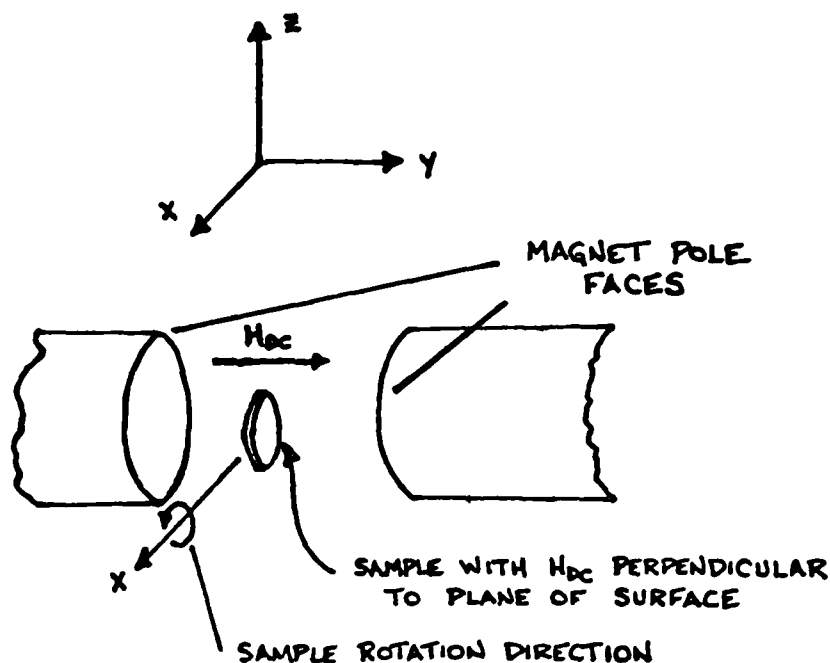


Figure 3-2: Position of the sample in the FMR apparatus.

In many instances, one resonance was significantly larger than the others; here, it was assumed that this was the uniform mode resonance and hence that it was valid to use this value of  $H_{DC}$  in subsequent calculations. In cases where all of the resonances are comparable, each value of  $H_{DC}$  at resonance was used in subsequent calculations and the final results using all possible combinations of resonances were compared. Since such a set of comparable resonances suggests a profile variation of  $H_k$ , the comparison method did not permit an exact value to be calculated, but provided for a mean value estimate of  $H_k - 4\pi M_s$ . Experimental results and further discussion can be found in the following chapter.

When the physical dimensions of the sample are such that boundary effects cannot be neglected, as is the case with thin films, spin wave modes for which the directions of the spins vary with the sample depth become significant. Macroscopically, one may expand the magnetization in the form of a Fourier series of spin wave modes. If one is interested in determining the magnetic parameter profiling in the more complicated cases, it is necessary to use numerical analysis,

presumably on a computer. For example, a recent theoretical determination of spin wave profiles for ion-implanted garnet films has been reported by Wilts and Prasad<sup>42</sup> where a computer program employing depth-varying magnetic parameters and established surface boundary conditions was used.

### 3.3 Force-Balance Magnetometer

The saturation magnetization of the NiCoB films was determined by using a force-balance magnetometer,<sup>43</sup> a schematic representation of which is shown in Fig. 3-3.

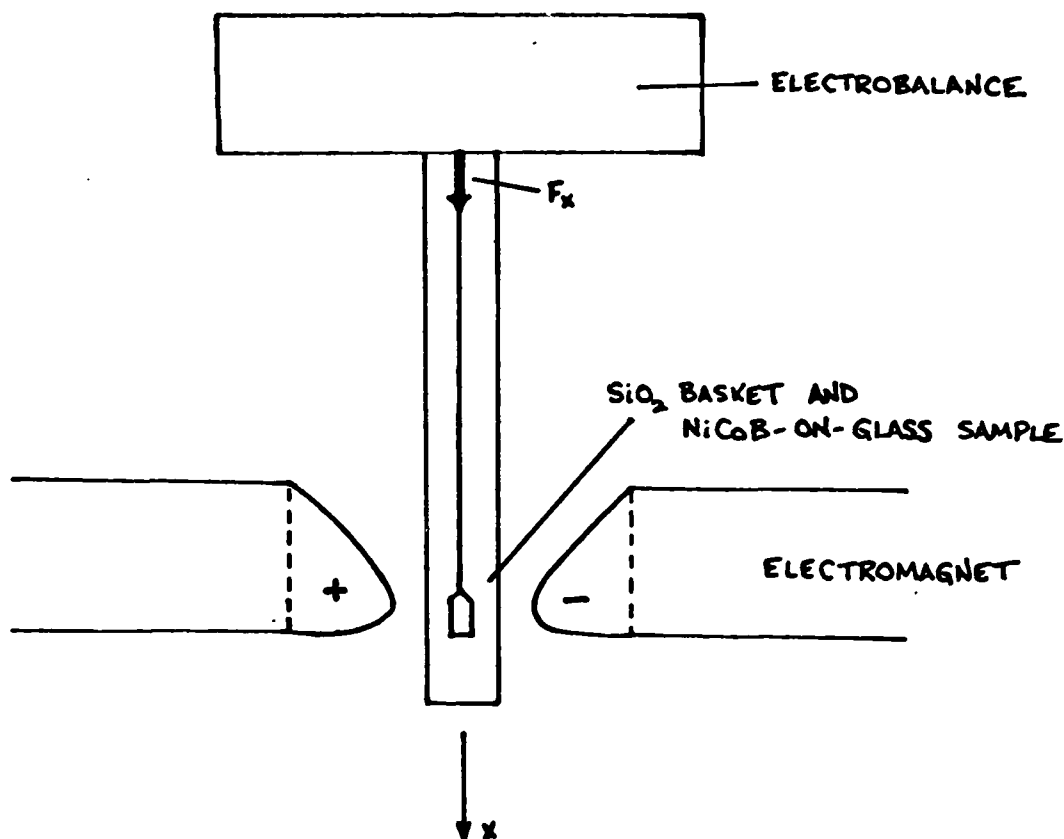


Figure 3-3: Schematic construction of a force-balance magnetometer.

Note that the pole faces of the electromagnet are shaped in such a way that a magnetic field gradient ( $dH/dx$ ) is present in the direction of operation of the balance. The force  $F_x$  (measured in dynes) exerted on the entire sample which consists of the



NiCoB film, glass substrate, and  $\text{SiO}_2$  basket by the field gradient  $dH/dx$  (measured in Oe/cm) is proportional to the magnetic moment  $MV$  of the sample ( $M$  measured in emu, and therefore  $4\pi M_s$  in gauss, and  $V$  in  $\text{cm}^3$ ). Therefore, one obtains

$$F_x = MV(dH/dx)$$

Note that the force  $F_x$  represents the force on the entire sample only, that is, after corrections have been made due to the force on the  $\text{SiO}_2$  rod. The field gradient acting on the sample is a function of the current through the magnet, the distance between the poles, and the position in the  $x$ -direction of the sample between the poles. For a limited range of  $x$ -values,  $(dH/dx)$  is found to be independent of  $x$ ; the sample to be measured is positioned within this range. By dividing  $F_x$  by  $(dH/dx)$ , the moment of the entire sample is found, that is:

$$(MV)_{\text{TOTAL}} = (MV)_{\text{FILM}} + (MV)_{\text{SUBSTRATE}} + (MV)_{\text{BASKET}}$$

The relationship between the magnetization and the applied  $H$ -field depends on the magnetic nature of the material. As can be seen in Fig. 3-4, for ferromagnetic films,  $M$  increases very rapidly with  $H$  and becomes constant with a value  $M = M_s$ , the saturation magnetization. For diamagnetic (such as the  $\text{SiO}_2$  basket and rod and the glass substrate) and paramagnetic materials, we have  $M = \chi H$ , where  $\chi$  is the susceptibility which is negative for diamagnetic and positive for paramagnetic materials. When  $(MV)_{\text{TOTAL}}$  is plotted against  $H$ , straight lines should be obtained and  $(M_s V)_{\text{FILM}}$  can be determined by extrapolation towards zero magnetic field strength. Although generally diamagnetic and paramagnetic magnetizations are small compared to ferromagnetic magnetizations, the dia- and paramagnetic moments can become competitive or even overshadow the ferromagnetic film moment. This is especially true in cases where very thin films with low  $M_s$  are deposited onto dia- or paramagnetic substrates that are many orders of magnitude thicker, since the volume of the substrate is much larger than that of the film.

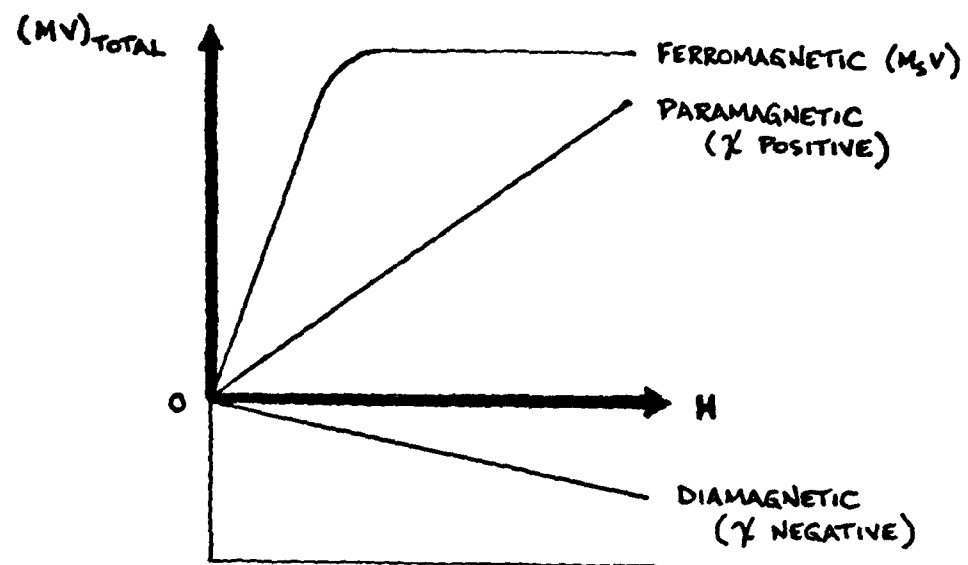


Figure 3-4: MV vs. applied H for paramagnetic, diamagnetic, and ferromagnetic materials.

## 4. RESULTS AND DISCUSSION

### 4.1 Composition Results with the Electron Microprobe

The compositions found in Table 4-5 were measured by electron microprobe as described in Section 3.1.2. The Applied Research Laboratory instrument at CMU and a Cameca Electron Microprobe<sup>44</sup> located at General Electric, in Schenectady, NY, were used to analyze the NiCoB films on glass substrates. The cobalt-to-nickel ratios were typically obtained at 20 kV accelerating voltages with both probes. Due to the lack of a special-purpose long wavelength X-ray detector, it was not possible to analyze the extremely long boron wavelengths quantitatively at CMU, although, using the PbSD crystal, a very broad and weak X-ray peak was observed at a wavelength of 67.6 Å (setting of 2.7650 on the PbSD crystal) as can be seen in Fig. 4-1.

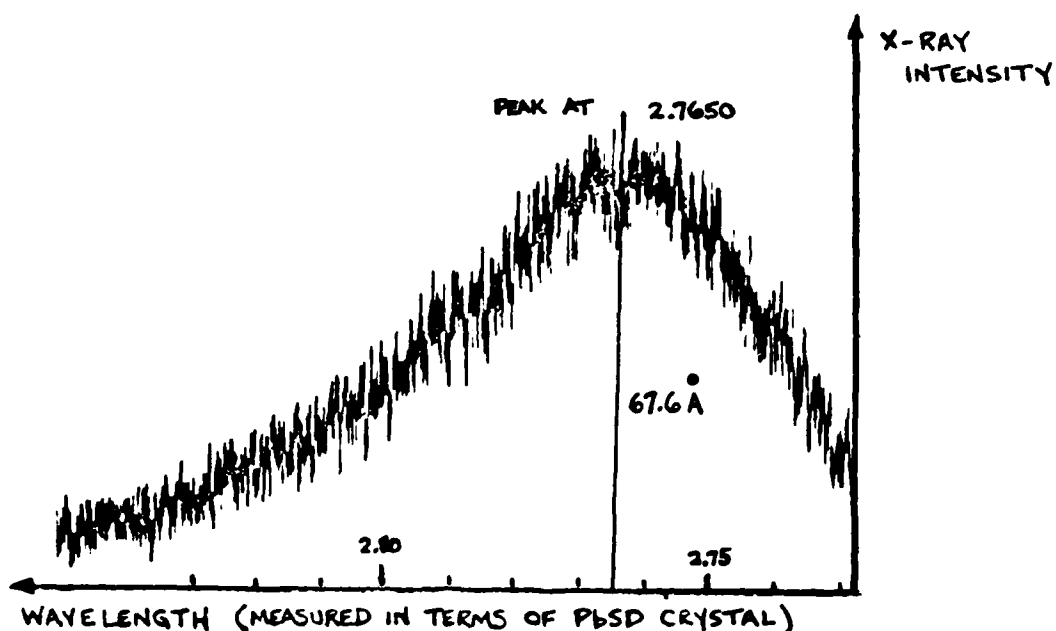
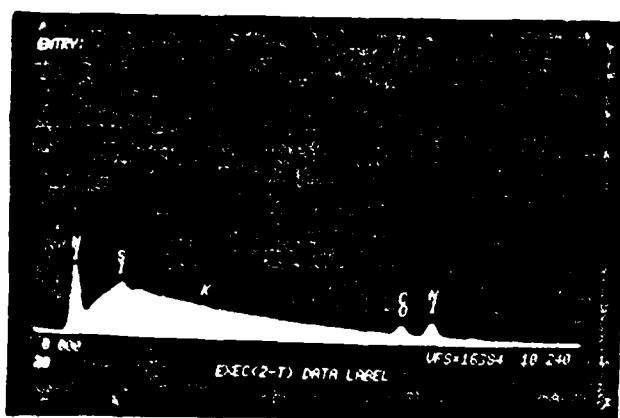


Figure 4-1: Qualitative observation of boron X-ray line at 67.6 Å and 5 kV accelerating voltage.

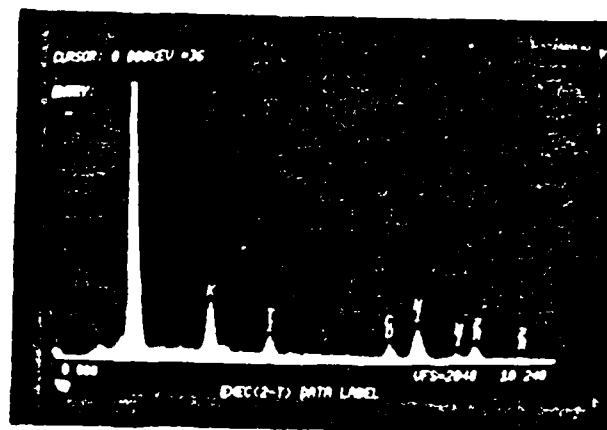
The quantitative values for boron content were obtained by Malcolm McConnel at General Electric on the automated Cameca probe using a PbSD crystal where 3 kV and 5 kV accelerating voltages were used since the critical excitation energy of the

boron  $K_{\alpha}$  line is 192 eV (as compared to 7.708 and 8.330 keV for Co and Ni, respectively). The boron values obtained in this manner are accurate to within 15% relative. In addition, in order to get a complete qualitative picture of each sample (including any significant amounts of impurities), energy dispersive spectra, taken at various voltages, were also measured. Some of these are included in Fig. 4-2. Note that X-rays from the glass substrate are very prominent in the thinner films. Also, the penetration of higher voltage electron beams into the substrate can be seen by comparing 8-20-80A and 6-30-81A, both films of 2100 Å, but measured at different electron beam voltages. Since the potassium peak is clearly evident only when beam penetration into the substrate is great, we can safely assume the potassium to be a component of the glass substrate. However, iron, copper, zinc, and titanium can also be seen in the dispersive spectra and are obviously impurities in the films themselves. Evidently, the dark shield is effective but not completely so in preventing atoms from the copper backing plate and brass attachment screws from entering. Also, since the dark shields, sputtering table, and chamber are made of stainless steel, a minute amount of iron also found its way into the films. The presence of the titanium is somewhat more mysterious; occasional use of the sputtering system for a different project which employed a sintered powder titanium-tungsten target apparently is the source. The target, being sintered powder, crumbled and flaked severely upon sputtering and although great lengths were taken by all parties to assure that none of the titanium-tungsten remained in the system, a small amount of residue apparently did at times. Generally, it is felt that the presence of these impurities, all being in small amounts, is not significant; the iron, although magnetic, appears in extremely small quantities (always less than 1%) and the others, being non-magnetic in nature, should not affect the magnetic properties of the films in any way.

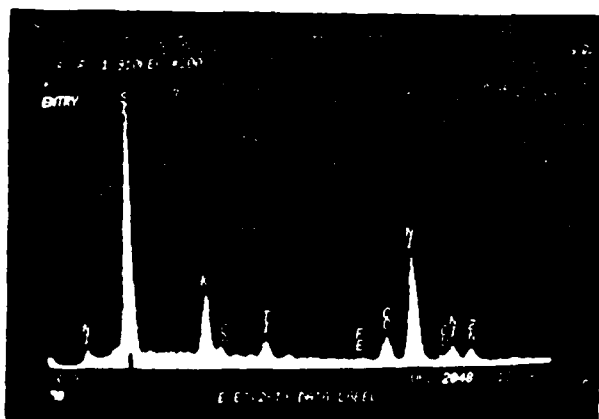
As expected (see page 12), no argon lines are evident in the spectra implying that the films contain no significant amounts of that element. This agrees with previous studies reported in the literature<sup>20</sup> since no target bias voltage was used in sputtering any of the NiCoB films. Listed in Table 4-1 are all of the characteristic lines evident from the energy dispersive spectra. In addition to the principal  $K_{\alpha}$  lines observed, note also the existence of the typically weaker  $K_{\beta_1}$  and  $L_{\alpha_1}$  lines for the elements cobalt and nickel, this apparently being due to their dominating presence in the samples.



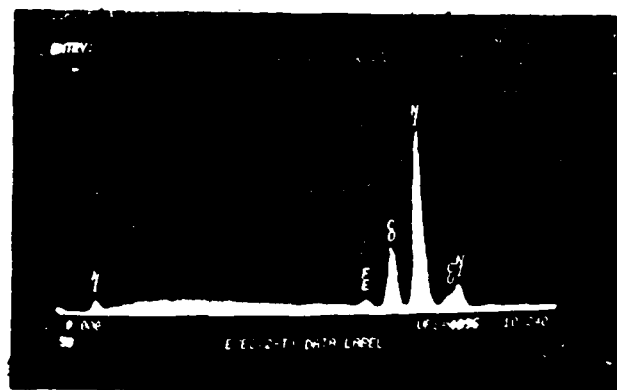
Film 8-20-80A Thickness 2100 Å  
Beam 9 kV



Film 2-15-81B Thickness 920 Å  
Beam 20 kV



Film 6-30-81A Thickness 2100 Å  
Beam 20 kV



Film 3-21-81A Thickness 10900 Å  
Beam 25 kV

Figure 4-2: Energy dispersive spectra for various NiCoB films at different beam voltages.

ELEMENT	Z	LINE	WAVELENGTH(A)	ENERGY(keV)
Ni	28	$L_{\alpha 1}$	14.595	0.85
Si	14	$K_{\alpha}$	7.126	1.739
K	19	$K_{\alpha}$	3.742	3.312
Ti	22	$K_{\alpha}$	2.750	4.508
Fe	26	$K_{\alpha}$	1.937	6.398
Co	27	$K_{\alpha}$	1.790	6.924
Ni	28	$K_{\alpha}$	1.659	7.471
Co	27	$K_{\beta 1}$	1.621	7.648
Cu	29	$K_{\alpha}$	1.542	8.040
Ni	28	$K_{\beta 1}$	1.500	8.263
Zn	30	$K_{\alpha}$	1.436	8.630

Table 4-1: Characteristic lines evident in the energy dispersive spectra.

As was previously described in Section 3.1.2, the concentrations of nickel and cobalt in the thicker films were determined using 20 kV accelerating voltages and then comparing the resulting X-ray intensities with those from pure element standards to obtain the intensity ratio,  $C_T$ , or k-ratio. For thinner films, a ratio of the cobalt-to-nickel k-ratio was determined at 20 and 10 kV (to reduce penetration of the beam into the glass substrate). Since the matrix corrections for adjacent elements are very similar, these "uncorrected" ratios are particularly accurate and hence were used to determine the absolute film composition.

One important consideration must be emphasized here. Since absolute percentage concentrations of nickel or cobalt could not be determined for the thinner films (that is, for those less than 4000 Å), the ratio of the cobalt-to-nickel concentration obtained was used to estimate the absolute concentrations in these films. Based on the impurity concentrations that were directly measureable for the "thicker" films

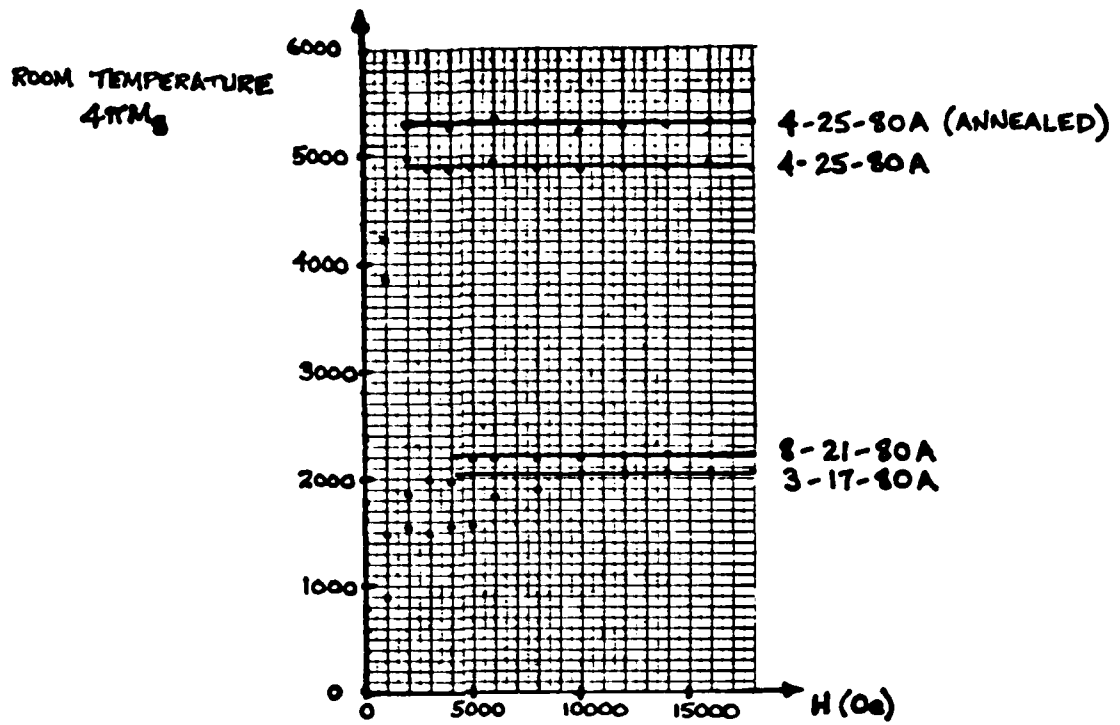
(4000 to 11,000 A), a total impurity concentration of 5% was assumed for these thin films. This is considered to be a very reasonable approximation since the thicker films exhibited measured impurity concentrations which ranged from 3.9 to 5.5%, the composition of which consisted mostly of copper (typically 4%) with traces of iron and zinc (<1% combined). Although the amount of impurities is significant, it being comparable to the boron concentration in the films, none of them are expected to affect the film properties significantly since the copper and zinc only act to slightly dilute the magnetization in the films and the trace amount of iron will influence the films in much the same way as the nickel and cobalt.

#### 4.2 Saturation Magnetization

Shown in Fig. 4-3 are results obtained with a force-balance magnetometer as described in Section 3.3 which were subsequently normalized and graphed. The measurements of room temperature  $4\pi M_s$  were made assuming a standard film area of  $1 \text{ cm}^2$  with a thickness of 1000 A. To obtain the true (normalized) value of  $4\pi M_s$  from the direct magnetometer measurement, one needs to merely multiply by the ratio of the assumed (standardized) film volume to the actual film volume since:

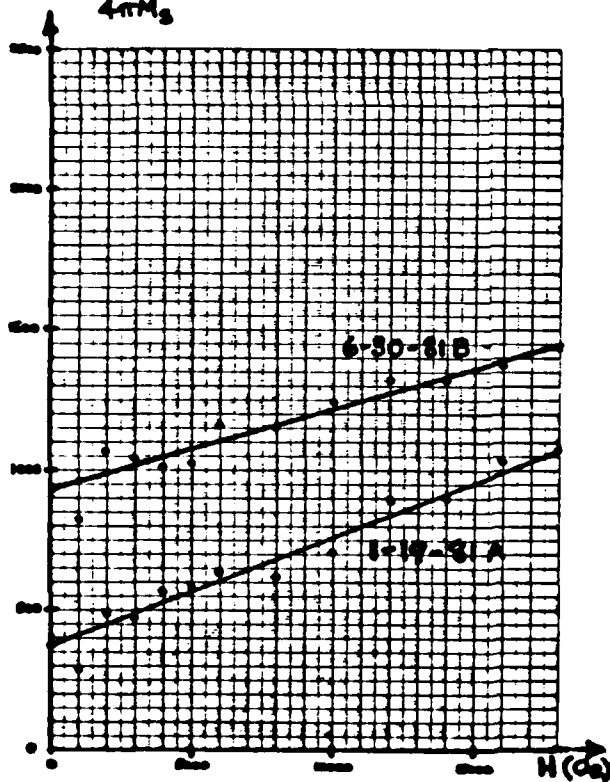
$$4\pi M_s \propto \frac{\text{FORCE}}{\text{VOLUME (dH/dx)}}$$

Normalized values of room temperature  $4\pi M_s$  for these films are contained in Table 4-3. In cases where the films were weakly ferromagnetic so that the paramagnetic component was significant, the value of  $4\pi M_s$  for H projected to zero was used. Evidentially, the paramagnetic magnetization of the much thicker substrate has become competitive in size with the low  $M_s$  thin films since the volume of the substrate is orders of magnitude larger than that of the deposited thin film.

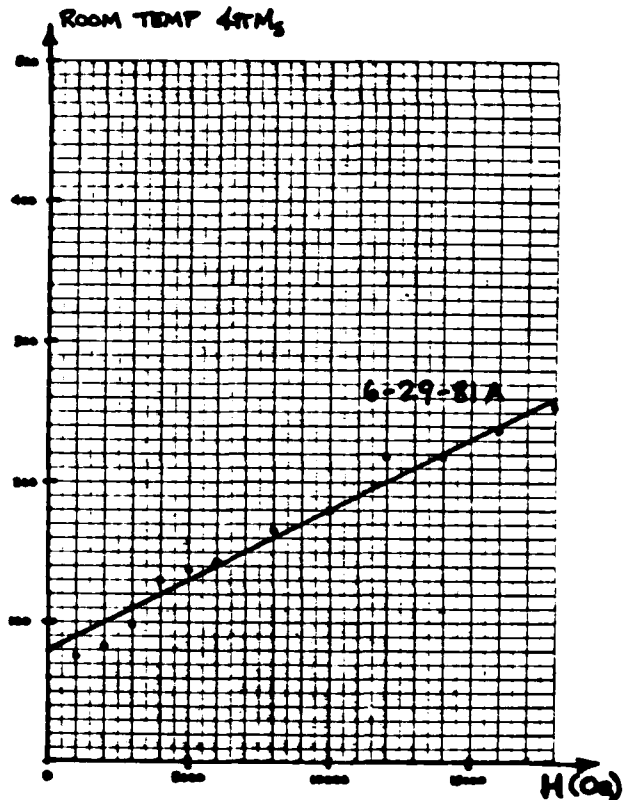


ROOM TEMPERATURE  
 $4\pi M_s$

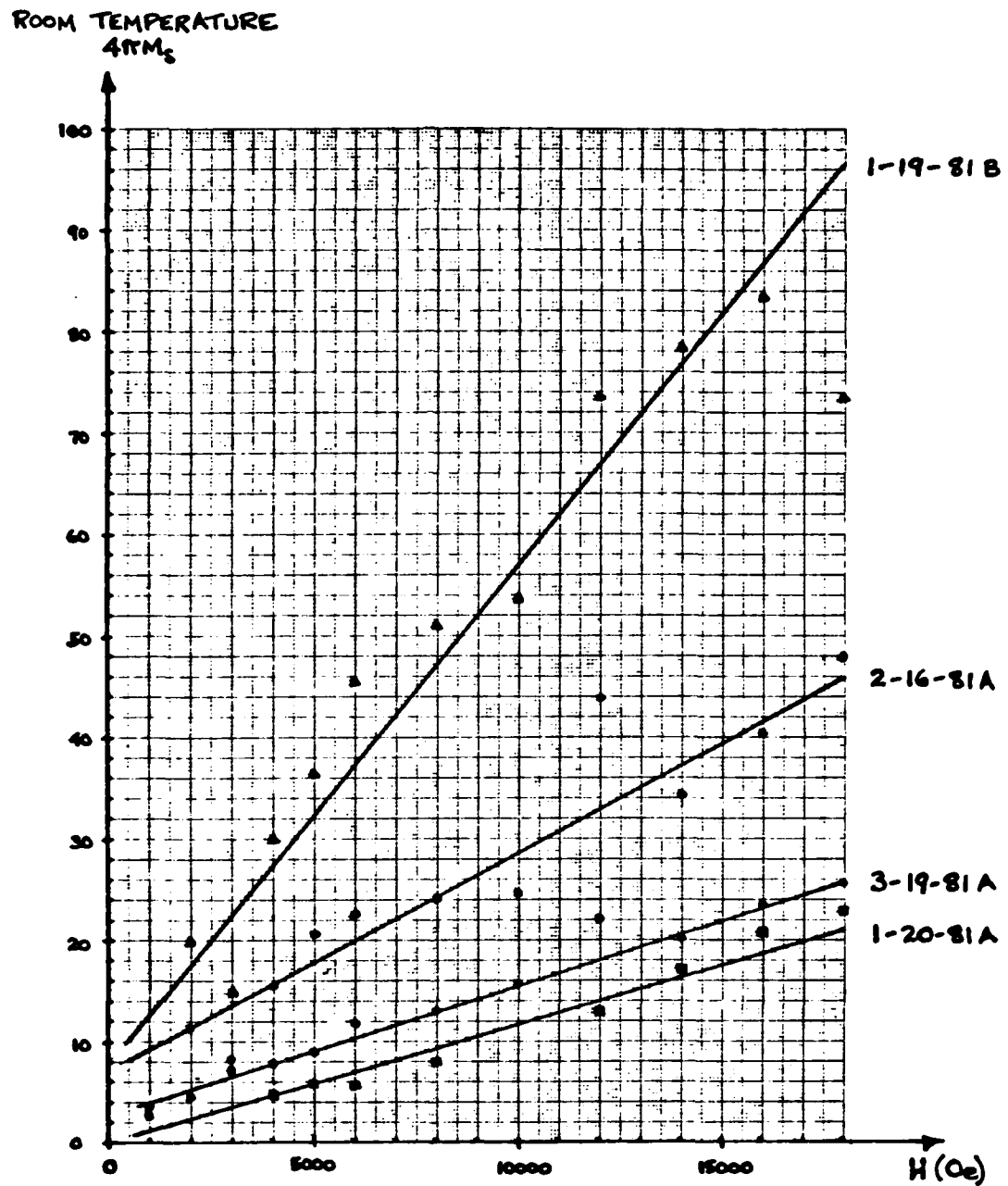
(a) NiCoB ferromagnetic thin films



(b) Weakly ferromagnetic films







(c) Paramagnetic films

Figure 4-3: Room temperature  $4\pi M_z$  (normalized) vs. applied H-field for various NiCoB thin film samples.

#### 4.3 Measured Anisotropy by Ferromagnetic Resonance

As described in Section 3.2, by finding the value of  $H_{DC\ PAR}$  and  $H_{DC\ PERP}$  at which resonance occurs, one may find a value for  $H_k - 4\pi M_s$ . For the microwave resonance studies, the film was placed inside a resonant cavity which was fed through a waveguide with radiation originating from a klystron. The microwave cavity resonant frequency (TE<sub>011</sub> circular cylindrical mode), determined primarily by the cavity dimensions with small corrections due to the nature of the sample, was always found to be in the vicinity of 9.36 GHz. The cavity set-up was such that the film was placed in the center, so that the RF H-field is at a maximum and the E-field, a minimum. Then, since the RF frequency was fixed, resonance was found by varying the DC H-field (Refer to Fig. 3-2). At resonance, the energy absorbed by the film is a maximum, so that the resonance condition may be detected by monitoring the electromagnetic energy reflected back from the cavity.

Although usually many resonances in sequence were obtained for H applied both parallel and perpendicular to the film plane, in most instances, one resonance was markedly larger than the rest so that it was assumed to be the uniform mode resonance and this H-field value was used as the value of  $H_{DC}$ . Table 4-2 contains the values of these distinct and unambiguous absorption peaks along with the corresponding microwave cavity resonant frequency from which subsequent values of  $H_k - 4\pi M_s$  and g were calculated. No values could be determined for those films with values of  $4\pi M_s$  of less than 500 G since the observed absorption peaks were extremely weak.

SAMPLE	$H_{\text{PERP DC}}$ (kG)	$H_{\text{PAR DC}}$ (kG)	$\nu$ (GHz.)
3-17-80A	5.5	2.0	9.360
3-17-80A (annealed)	5.1	1.3	9.359
4-25-80A	6.6	1.6	9.360
8-20-80A	6.9	1.7	9.359
8-21-80A	6.1	1.8	9.358
6-29-81C	3.2	2.4	9.357
6-30-81B	4.0	2.6	9.357

Table 4-2: Strong unambiguous FMR absorption peaks for some ferromagnetic NiCoB films.

Table 4-3 gives the values that were obtained for  $H_k - 4\pi M_s$  for those films for which this measurement was possible, normalized  $4\pi M_s$  from the force-balance magnetometer, the resulting value of  $H_k$ , and the value of  $g$ . As can be seen here, the amount of boron in the film very strongly influences  $4\pi M_s$ . Also included is Fig. 4-4 which gives a general idea of the dependence of  $(K_u - 2\pi M_s^2)$  on  $4\pi M_s$  obtained from the values of those films which were ferromagnetic or weakly ferromagnetic.

The anisotropy observed in the NiCoB films is not uncommon in amorphous ferromagnetic materials. Although occurrence of magnetic anisotropy has received somewhat less attention for amorphous ferromagnetic materials (in contrast to the extensive literature available for the ferrimagnetic RE TM films), recently it was reported by Cargill et al.<sup>45</sup> that amorphous electrodeposited CoP and CoNiP alloy films have a weak perpendicular easy-axis anisotropy with  $H_k/4\pi M_s$  equal to values from 0.01 to 0.1. Sherwood et al.<sup>46</sup> found long-range magnetic anisotropy in amorphous ferromagnetic metal-metalloid alloys of the type  $(\text{FeCoNi})_{0.75}(\text{PBAI})_{0.25}$ , quenched from the liquid state by the roller quenching technique. Work on the composition dependence of the anisotropy of evaporated and electrodeposited NiCo films was done somewhat earlier by Wolf<sup>47</sup> and Prutton,<sup>48</sup> this being of some

importance since studies compiled by Luborsky<sup>49</sup> show that the trend with transition metal content is the same as for the corresponding crystalline alloy. More recently, Taylor<sup>12</sup> studied approximately 100 films representing three groups of amorphous materials: evaporated  $\text{Gd}_x\text{Co}_{1-x}$  ( $x = 0.1$  to  $0.3$ ), evaporated  $\text{Gd}_x(\text{Co}_y\text{Ni}_{1-y})_{1-x}$  ( $x = 0.15$  to  $0.3$ ,  $y = 0.25$  to  $0.5$ ), and sputtered  $(\text{Gd}_x\text{Fe}_{1-x})_{0.9}\text{B}_{0.1}$  ( $x = 0.16$  to  $0.39$ ). It was observed that all of these films displayed a hard perpendicular axis of magnetization. The evaporated films also exhibited an in-plane uniaxial anisotropy undoubtedly due to the directionality of the vapor streams in the evaporation process since the direction could be altered by substrate rotation during evaporation. The magnitude of the anisotropy in the direction of the plane was on the order of 10 times less than the anisotropy perpendicular to the plane. In the sputtered films, planar uniaxial anisotropy was only encountered when the substrates were thermally backed during the deposition.

In the case of the NiCoB ferromagnetic films, although an anisotropy perpendicular to the film plane was noted, no anisotropy in the plane of the film was ever observed (see page 27), this being determined by noting that the points of maximum resonance absorption did not shift when the magnet, and hence the applied parallel H-field, was rotated around the sample.

SAMPLE	$H_k - 4\pi M_s$	$4\pi M$ (25°C) <sup>s</sup>	$H_k$	g	COMPOSITION (weight %)		
					Ni	Co	B
3-17-80A	-1450	2050	600	2.35	71.4*	22.1*	1.5
4-25-80A	-4200	4900	700	2.27	72.2*	22.8*	0.0
8-20-80A	-4550	----	----	2.32	75.2*	17.4*	2.4
8-21-80A	-3300	2200	-1100	2.29	70.1*	22.4*	2.5
1-19-81A	not enough sensitivity	375	----	----	69.0*	21.4*	4.6
6-29-81C	-575	650	-495	2.55	76.8*	13.7*	4.5
6-30-81B	-950	935	-15	2.54	77.9*	12.9*	4.2

Table 4-3: Magnetic parameters for some ferromagnetic NiCoB films.

(All samples before annealing.)

\*Absolute percentages for Ni and Co are values based on the measured boron content and an estimated value of 5% impurities. However, the ratio of Ni-to-Co percentages is correct to three places.

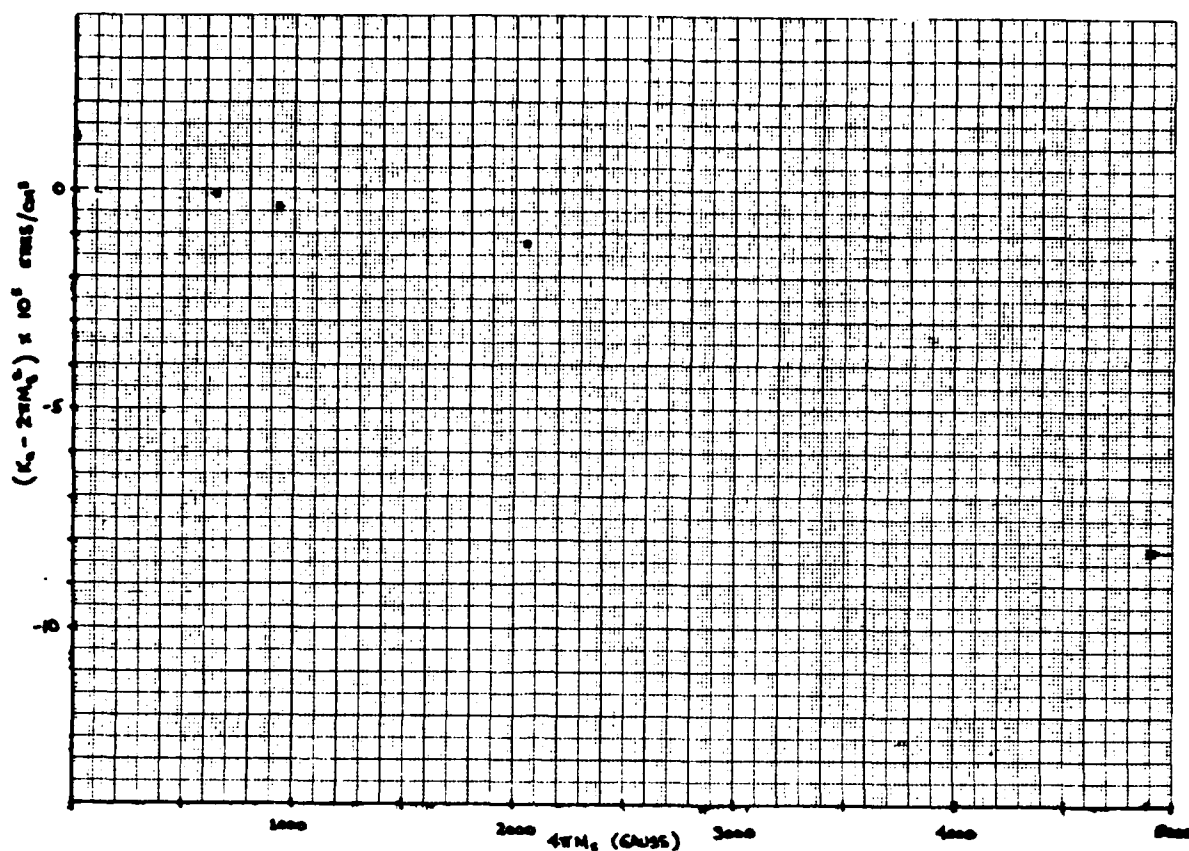


Figure 4-4: Dependence of  $K_u - 2\pi M_s^2$  on  $4\pi M_s$  for NiCoB ferromagnetic thin films.  
(All samples before annealing.)

As noted previously, many spin-wave resonance modes with the DC H-field applied either perpendicular or parallel to the film plane were observed in the NiCoB ferromagnetic thin film samples that were investigated. A comprehensive summary of these experimental results and a comparison to the simple theory can be found in Appendix A.

#### 4.4 Effects of the Sputtering Conditions

As mentioned previously, the NiCoB films were fabricated by RF sputtering using two decoupled plasmas from targets containing foils and slices of the desired elements. In order to obtain an estimate of the composition beforehand, sputtering yield rates of 1.5 Ni to 1.4 Co to .4 B were assumed,<sup>22,23</sup> although theoretically, the

published results are strictly valid only provided that the target materials are relatively featureless. From this information and the desired composition, the Ni to Co foil area ratio on the NiCo target was set and the NiCo to CoB target voltage ratio was determined. Initially, the assumption was made that the contribution of cobalt to the films from the CoB target would be negligible since the cobalt foil in this arrangement (see Fig. 2-2) was basically being used only as a backing to prevent copper impurities (from the backing plate) from being sputtered into the film. After electron microprobe composition results were obtained, it was found that this was not precisely true; hence a small correction factor, depending on the CoB target voltage (typically 5 % additional cobalt) was used in addition to the above. This method worked relatively well in estimating the Ni and Co percentages to within 5% but was relatively poor for the boron composition, part of this being due to the much smaller amount of boron desired in the film.

It was found that due to the long sputtering times required to produce a film of reasonable thickness (e.g., 2 hours, 30 minutes at 600 watts for a particular film of 2700 Å), it was very difficult to keep all of the parameters steady for the necessary amount of time. Due to the moving geometry, the target voltages and power to the system were fluctuating constantly by 3 to 5 %, but it was felt that this effect would be averaged out over the course of a sputtering run. To insure that the films were homogeneous (that is, to make sure that the film was not layer upon layer of alternating target material), the amount of material deposited per table revolution was always kept below 8 Å. On numerous occasions, the plasma would simply extinguish and refuse to ignite thereafter; this was traced to a build-up of sputtered material on the dark shield (due to the long sputtering times) which would eventually begin flaking causing a short to ground. At times, this effect was very temporary, causing only a momentary flicker of the plasma and resulting surge in reflected power; however, equally as common were cases where runs would have to be curtailed and sometimes aborted. Even more common was the sporadic (and therefore difficult to pin-point) problem of not being able to ignite the plasma on the boron target only; evidently, the small dark shield aperture required (1.25 inches), along with the thickness of the target, hindered plasma ignition; this was finally traced to arcing between target and dark shield and appropriate adjustments to the target were made. Substrates which were sputtered during the time these problems occurred were not characterized.

A problem which developed somewhat later, after the J-arm had been removed

several times due to other uses of the sputtering system, resulted in the substrate table occasionally "jerking" as it rotated around causing substrates to move considerably out of position, thereby resulting in uneven films of questionable composition uniformity, and therefore, not useable. Although using silicon grease for adhesion gave better results, the jerking motion was still often so abrupt that the substrates were still displaced. A stainless steel metal holder with holes punched through completely to insure thermal contact with the table was also made but after a few uses, the surface of the holder began to buckle slightly, undoubtedly due to the heat build-up from the sputtering, allowing the substrates to shift and make their way under the holder. Any substrate which had become displaced in the course of a sputtering run was not characterized since the composition was certain to be varying within the film.

Overall, these problems did severely limit the number of samples from which useful data could be obtained. All of the data presented in this paper represents only those runs in which the above problems were not encountered.

It was also observed that, as the system became hotter, the table revolution speed increased by as much as 10% during a typical run; this was not considered to be a problem of any consequence.

Independent of the problems above, it was observed that, although the power to the system was kept constant, the voltages on each target very gradually changed over the course of a long sputtering run. As can be seen in Table 4-4, these changes were a function of the duration of the run and could be as much as 10%.



TIME (hrs.)	FORWARD POWER (watts)	TARGET VOLTAGE [targets 1 and 3 (volts)]					
		(4-8-81A)		(6-23-81A)		(6-30-81B)	
		1	3	1	3	1	3
0.0	600	810	1240	780	1280	900	1450
0.5	600	810	1240	790	1300	900	1450
1.0	600	820	1250	780	1290	850	1410
1.5	600	820	1250	780	1290	800	1300
2.0	600	820	1250	790	1310	800	1300
2.5	600	820	1250				
3.0	600	820	1260				
4.0	600	820	1250				
5.0	600	820	1250				

Table 4-4: Observed target voltage fluctuations with sputtering time.

As can be seen from the table, during certain runs the voltages seemed particularly unsteady for no apparent reason. Runs 4-8-81A and 6-23-81A are representative of a typically steady run whereas 6-30-81B represents the opposite extreme. Since this change in the target voltages directly affects the sputtering yields of each element differently (especially that of boron as compared to the rest), reproducibility of film composition using the method of decoupled plasmas was not exact. Above the threshold the sputtering yield rises first exponentially, then linearly, then less than linearly until it approaches a flat maximum indicating that the composition of the sputtered film will certainly depend to some extent on the values of the target voltages throughout the sputtering run. Evidently, the unpredictable fluctuations of the target voltages make exact reproducibility of the film composition impossible. This becomes a major problem in light of the fact that magnetic parameters such as the saturation magnetization were found to depend very strongly on the precise amount of boron in the film as can be seen in Fig. 4-5. From this figure, it is evident that the saturation magnetization becomes zero near 4.8 weight percent boron, this value corresponding to 22 atomic percent boron. An extensive review of various properties of amorphous alloys including saturation magnetization by Luborsky<sup>49</sup> shows a similar type of dependence reported in the literature for other metal-metalloid amorphous films.

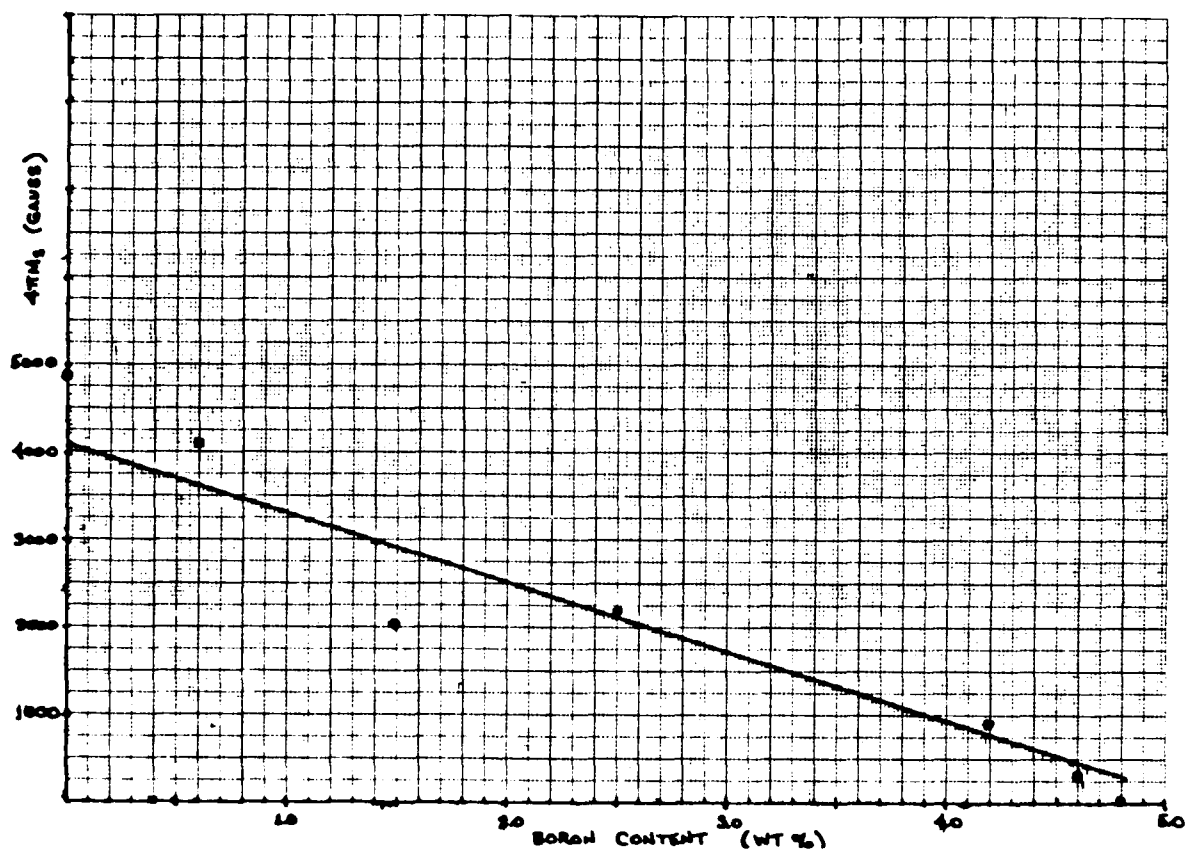


Figure 4-5: Saturation magnetization vs. boron content in NiCoB ferromagnetic thin films.

SAMPLE	AVG SPUTTERING POWER(watts)	SPUTTERING TIME(hours)	INITIAL VOLTAGE		POWER SPLITTING RATIO	THICK- NESS (A)	COMPOSITION (weight %)		
			(1)	(3)			Ni	Co	B
3-17-80A	560	4.00	820	1250	.39-.61	1650	71.4*	22.1*	1.5
4-25-80A	470	4.00	1570	420	.81-.19	2700	72.2*	22.8*	0.0
8-20-80A	400	3.50	1000	720	.60-.40	2100	75.2*	17.4*	2.4
8-21-80A	400	3.10	650	1000	.39-.61	3200	70.1*	22.4*	2.5
8-22-80B	400	3.50	300	1160	.20-.80	1600	38.8*	43.7*	12.5
12-6-80A	600	2.50	760	1380	.35-.65	2350	67.6*	21.6*	5.8
12-6-80C	600	2.50	610	1420	.30-.70	2300	60.5*	27.2*	7.3
12-7-80A	600	2.50	790	1350	.37-.63	2700	68.6*	21.2*	5.2
1-19-81A	600	2.50	820	1260	.39-.61	3200	69.0*	21.4*	4.6
1-19-81B	600	2.50	780	1310	.37-.63	3200	70.3*	20.1*	4.6
1-20-81A	600	2.50	740	1380	.35-.65	2750	64.7*	21.8*	8.5
2-15-81A	600	1.25	810	1240	.39-.61	1800	68.3*	20.5*	6.2
2-15-81B	600	.63	820	1280	.39-.61	920	68.8*	21.0*	5.2
2-16-81A	600	1.88	810	1230	.39-.61	2700	66.5*	22.0*	6.5
3-19-81A	600	10.00	810	1240	.39-.61	10800	70.8	19.5	4.8
3-21-81A	600	10.00	780	1320	.37-.63	10900	70.2	19.0	5.5
6-29-81C	600	2.00	760	1240	.38-.62	2600	76.8*	13.7*	4.5
6-30-81A	600	1.38	760	1240	.38-.62	2100	76.8*	13.5*	4.7
6-30-81B	600	2.07	900	1450	.38-.62	2950	77.9*	12.9*	4.2
6-30-81C	600	.68	880	1420	.38-.62	970	78.9*	12.6*	3.5

Table 4-5: Sputtering parameters, thickness, and composition of various ferromagnetic and paramagnetic NiCoB thin films.

\*Absolute percentages for Ni and Co are values based on the measured boron content and an estimated value of 5% impurities. However, the ratio of Ni-to-Co percentages is correct to three places.

Referring again to 4-5, one can see that boron content reproducibility to within  $\pm 0.3\%$  is a minimum requirement to obtain  $4\pi M_s$  to within 500 Gauss of a desired value. Using decoupled plasmas, with the changing target voltages, it was only possible to obtain reproducibility on the order of 1 to 2 % (weight percent) for the exact same directly controllable initial sputtering conditions.

From Table 4-5, one may obtain a general idea of the range of compositions and thicknesses considered. Note that composition percentages do not add to 100% due to non-magnetic impurities in the films. These impurities were taken into account explicitly in determining the composition percentages given in this table. As discussed in detail in Section 4.1 (see page 35), the impurities consist primarily of copper with traces of zinc and iron; these metals in the amounts encountered are not expected to affect the film properties significantly.

While sputtering, the parameters under direct control are the sputtering power, the argon gas pressure, and the ratio of power being directed to each individual target. Since mixing of the elements increases with argon gas pressure due to more collisions between target and substrate, the argon pressure was kept at 25 mT for all of the sputtering runs. Also, it was not possible to ignite nor sustain a plasma on the CoB target at lower pressures approaching 10 mT. The sputtering power, which fluctuated by  $\pm 5\%$  during each table revolution, was usually kept as close to 600 watts as possible via manual monitoring. Higher sputtering powers would have yielded the desired thickness in less time, but this was not feasible as the system was heating considerably at 600 watts forward power even after the cooling water flow rate had been maximized. The initial temperature of the cooling water could not be changed since filtered cold tap water was being used.

Although the individual target voltages could not be controlled directly, they could be manipulated by changing either the sputtering power, the argon sputtering pressure, or the power splitting ratio. Also the voltage labeled (1) represents that of target position 1, the NiCo target, and (3) that of the CoB target. Now with all of these facts in mind, one may refer to Table 4-6 where only those films for which the power splitting ratio of NiCo to CoB of .39-.61 and .38-.62 and 600 watts average sputtering power appear. It should be noted here that the Ni-to-Co foil ratio (on the NiCo target) is different in going from the .39-.61 to the .38-.62 data so that direct comparison of the Ni and Co compositions between the two sets of data is not meaningful.

SAMPLE	SPUTTERING TIME(hours)	INITIAL VOLTAGE		POWER SPLITTING RATIO	THICK- NESS (A)	COMPOSITION (weight %)		
		(1)	(3)			Ni	Co	B
1-19-81A	2.50	820	1260	.39-.61	3200	69.0*	21.4*	4.6
2-15-81A	1.25	810	1240	.39-.61	1800	68.3*	20.5*	6.2
2-15-81B	.63	820	1280	.39-.61	920	68.8*	21.0*	5.2
2-16-81A	1.88	810	1230	.39-.61	2700	66.5*	22.0*	6.5
3-19-81A	10.00	810	1240	.39-.61	10800	70.8	19.5	4.8
MAXIMUM ABSOLUTE DIFFERENCE						4.3	2.5	1.9
MAXIMUM % DIFFERENCE						6.5%	13.0%	41.0%
6-29-81C	2.00	760	1240	.38-.62	2600	76.8*	13.7*	4.5
6-30-81A	1.38	760	1240	.38-.62	2100	76.8*	13.5*	4.7
6-30-81B	2.07	900	1450	.38-.62	2950	77.9*	12.9*	4.2
6-30-81C	.68	880	1420	.38-.62	970	78.9*	12.6*	3.5
MAXIMUM ABSOLUTE DIFFERENCE						2.1	1.1	1.2
MAXIMUM % DIFFERENCE						2.7%	8.7%	34.0%

**Table 4-6:** Composition reproducibility for fixed sputtering conditions.  
Average sputtering power of 600 watts and argon pressure of 25 mT  
for all samples listed in this table.

\*See footnote on page 48.

Let us now focus on the reproducibility of a desired composition and hence on the reproducibility of the magnetic properties. Although all controllable parameters were held fixed, the initial voltage (which could not be directly controlled) varies slightly

in some cases (for example, compare 2-16-81A and 3-19-81A or 6-29-81C and 6-30-81A) and more markedly in others (e.g., 1-19-81A and 2-16-81A or 6-30-81A and 6-30-81B). In addition, as was shown in Table 4-4, the target voltages also fluctuated with time. This, naturally, makes precise reproducibility difficult as can be seen from the microprobe composition data in Table 4-6. The absolute weight percent of the nickel, cobalt, and boron varied by 4.3, 2.5, and 1.9, respectively, for the films sputtered at 600 watts forward power and at a power splitting ratio of .39-.61, and by 2.1, 1.1, and 1.2, respectively, for those with a power splitting ratio of .38-.62. Although this magnitude of composition deviation would probably be acceptable in many applications (hence sputtering by decoupled plasmas is used successfully elsewhere), the amount of boron composition deviation in the NiCoB films from run to run is simply too great to make films with reproducible magnetic properties. In fact, the previously mentioned requirement of  $\pm 0.3\%$  boron composition deviation (absolute weight percent) evidently cannot be obtained by this method of sputtering. Besides direct control of the total sputtering power and of the ratio being directed to each individual target, one also apparently requires that the target voltages remain fixed throughout the run in order to eliminate the unacceptable boron composition deviations. Note that the boron composition percent differences are clearly above the level of microprobe measurement error (within 15% relative or on the order of  $\pm 7.5\%$ ).

Fig. 4-6 shows how the sputtering rate decreased with time by exhibiting the dependence of film thickness on sputtering time holding all other parameters fixed. This effect is evidently due to the increase in substrate temperature which increased with the length of the sputtering run. Although one can see that for the range 0 to 3000 A the relationship appears nearly linear, likewise, a careful inspection in the area of 2000 to 3000 A shows a slight decrease in thickness for a given sputtering time. This trend is confirmed by the films 3-19-81A and 3-21-81A, both of which yielded roughly 11,000 A for 10.0 hours of sputtering. It should be noted that these are the only two films which were not sputtered as one continuous run-- both were sputtered in two 5-hour shifts with one hour of system cooling between. This, however, should only serve to increase the overall film thickness for the given amount of sputtering time. A strictly linear dependence of thickness on sputtering time would have yielded a thickness in the vicinity of 14,000 A for 10.0 hours of sputtering. A strong dependence of the deposition rate on the substrate temperature has been reported for a number of sputtered materials, including  $\text{SiO}_2$ ,<sup>50</sup> gallium arsenide,<sup>51</sup> and germanium.<sup>52</sup> In all of these cases, a marked decrease in the deposition rate was noted with increasing substrate temperature.

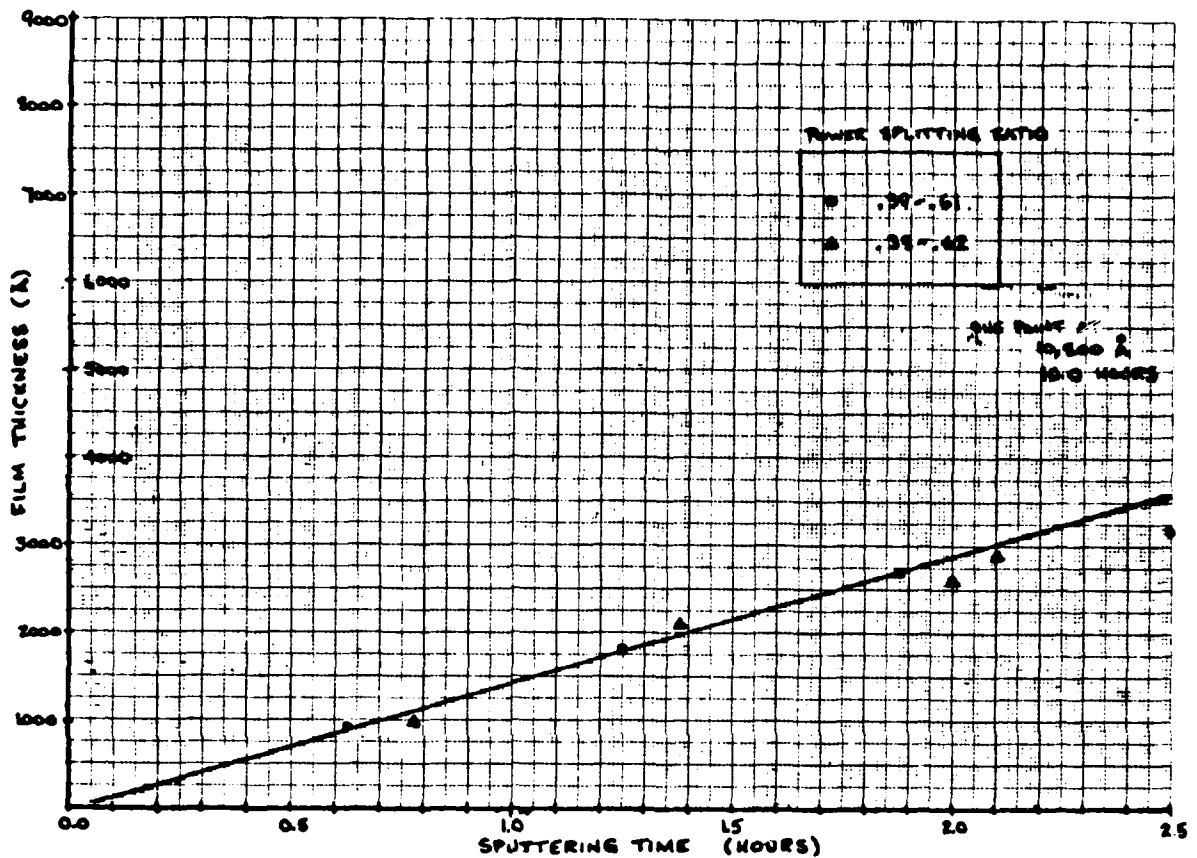


Figure 4-6: Dependence of film thickness on sputtering time.

#### 4.5 Ferrofluid Investigations (Bitter Pattern Method)

By depositing a drop of colloidal suspension of very fine magnetic particles ( $\text{Fe}_3\text{O}_4$ ) on the surface of a magnetic specimen, the configuration of the ferromagnetic domains at the surface can generally be observed. The very fine particles of magnetite tend to congregate in the region of the domain walls due to the very strong local magnetic fields in the vicinity of the boundary between domains which are magnetized in different directions. In order to induce the formation of domain walls in the sputtered NiCoB thin films, small elliptical holes were etched into the surface of the films via standard photolithography techniques.

Of the various acid etches that were used, best results were obtained with a water ( $\text{H}_2\text{O}$ ) to nitric acid ( $\text{HNO}_3$ ) mixture of 1:1. Adding any sulfuric acid ( $\text{H}_2\text{SO}_4$ ) to water or water and nitric acid mixtures always caused the films to crack and pit to some degree and seriously decreased the adhesion of the film to the glass substrate. Water-to-nitric acid mixtures of 2:1 to 5:1 resulted in poor detail-- the time required for etching through to the glass in these cases was too long so that overetching occurred near the top surface of the film; mixtures of 1:2 to 1:5 resulted in excellent detail but excessive cracking of the film. Also films with a significantly higher boron content etched somewhat more slowly than the others.

To observe the films using ferrofluid, a "sandwich" consisting of a small piece of microscope slide, NiCoB film-on-substrate, and microscope cover glass were epoxied together in such a way that the NiCoB/ferrofluid was effectively sealed within the two pieces of glass. Studies were made at a magnification of 200x with a field of 0 to 30 Oe applied perpendicular to the film in order to magnetically orient the magnetite particles. An in-plane field of 0 to 300 Oe was applied which could be rotated manually or at a fixed frequency. No distinct domain walls (charged walls) were observed in these films. As discussed in Section 4.7, it is felt that a higher magnetostriction is required in the amorphous alloy in order to induce the charged walls.

#### 4.6 Annealing of the NiCoB Films

Since measurements made on the films sputtered initially suggested that  $H_k$  was positive, an investigation of the effect of annealing the films to bring the anisotropy into the plane of the film ( $H_k < 0$ ) was performed. Films were annealed at 300°, 350°, and 400°C for 2 to 4 hours under a vacuum of less than  $3 \times 10^{-7}$  torr. The temperature was controlled with a TECO<sup>53</sup> TP-2000 temperature programmer employing an iron constantan thermocouple and was accurate to within  $\pm 5^\circ$ . After annealing, the system was allowed to cool to room temperature before the samples were removed. Those films annealed at 400°C showed considerable grain formation while the physical appearance of those annealed at the other temperatures did not change at all; therefore, subsequent annealing was done exclusively at 300° and 350°C. Since the spin-wave spectra changed radically upon annealing for each sample, it was not possible to compare  $H_k - 4\pi M_s$  for the cases pre-anneal and post-anneal to determine how the anisotropy had changed. Some of the ferromagnetic resonance spectra that were obtained with these annealed samples is presented in Appendix A.



#### 4.7 Conclusions

Using sputtering with decoupled plasmas has both its advantages and disadvantages. The composition of the sputtered film could be easily modified by simply changing the power ratio between targets, thereby obviating the need for many expensive, specially-prepared, pre-alloyed targets of different composition. This is especially useful when it is not certain which composition is required so that a broad-based study of different compositions can be performed easily and inexpensively. However, since the composition reproducibility is only generally within 2 atomic percent due to the fluctuating target voltages and unstable system geometry, this method is only feasible if such a restriction is acceptable. For this project, the very strong dependence of the magnetic properties on the amount of boron in the films made this method difficult to use. Although one might modify the present sputtering system so that the target voltages could be controlled directly, it is felt that based on the observed fluctuations of the forward power (which is being directly controlled) during the course of a table revolution, especially as the substrate passes beneath each target, that it would not be possible to achieve the required reproducibility using decoupled plasmas. Instead sputtering from a single target containing all three elements should be implemented. The subsequent shorter sputtering run times (30 minutes or less) and unchanging target-to-substrate geometry will result in better reproducibility than obtained by using two-target power-splitting techniques. Also, based on the evidence that the changing target voltages significantly influenced the sputtering rate of the boron as compared to the nickel and cobalt, the method of power-splitting appears useful only with sets of materials having a similar sputtering yield dependence on target voltage. For groups of materials such as these, small fluctuations in the different target voltages could be tolerated with little effect on the final composition of the sputtered film.

No distinct charged walls were ever observed in the NiCoB ferromagnetic films. Based on evidence that the charged walls form only where there is a stress-induced uniaxial anisotropy with an easy axis parallel to the implanted/unimplanted boundary in a garnet film,<sup>54</sup> it appears necessary to use amorphous alloys that include some highly magnetostrictive elements, if the desired charged walls are to be obtained. The most likely candidates to be used to induce this high magnetostriction appear to be the rare earths terbium and/or dysprosium-- both demonstrating extremely high basal plane magnetostriction at low temperatures<sup>55</sup>. Although both of these rare earths possess very low-temperature Curie points, various combinations of these two rare earths with the magnetic transition metals Co and Fe are found to exhibit

moderate magnetostrictions at room temperature.<sup>55</sup> The inclusion of these other elements will increase the in-plane stress and hence augment the charged walls in the film. An excellent review of magnetostriction in amorphous alloys is provided by Luborsky<sup>49</sup> for the interested reader.

With the composition modifications considered above, the eventual fabrication of a magnetic bubble device, utilizing an amorphous film which includes highly magnetostrictive rare earths as the drive layer (and thereby using stress-induced anisotropy through magnetostriction to augment the charged walls), may become possible in analogy with the present contiguous disk technology.

## A. OBSERVED SPIN-WAVE RESONANCES IN THE FERROMAGNETIC NI-CO-B THIN FILMS

### A.1 Brief Theoretical Discussion

Frequently, when performing FMR in thin films, standing spin-wave resonance modes are observed in addition to or in place of the uniform mode. In some cases, these spin-waves are associated primarily with pinning of the magnetization at the surfaces of a uniform film; in others, they correspond to an inhomogeneous distribution of the magnetization and/or magnetic anisotropy throughout the film depth. Attention is now focused on the spin-wave excitations rather than on the dynamics of the uniform mode resonance. The analysis is simplest for perpendicular resonances, that is,  $H_{DC}$  applied normal to the plane of the film. Let us initially consider the case where there is no profiling of magnetic parameters.

The dispersion relation between the frequency  $\omega$  and the propagation vector  $k$  of a traveling spin wave can be shown to be of the form:<sup>40,56</sup>

$$\omega = \gamma H_{\text{eff}} + Dk^2 + \dots$$

where  $D = 2\gamma A/M$  and  $H_{\text{eff}}$  includes applied, demagnetizing, and anisotropy fields, exactly as described previously in Section 3.2. This condition is possible if the spin waves can be represented as standing waves set up by reflections at the film boundaries. If the magnetic anisotropy at these interfaces is strong enough to pin the spins there, the problem becomes analogous to that of the vibrating string fixed in position at both ends. These boundary conditions require a standing wave solution of the form  $\sin kx$  where  $k = n\pi/d$  ( $d$  being the film thickness) and  $n$ , the mode number, is an integer. If the RF H-field is uniform within the film, as is the case when using the microwave cavity system,  $n$  must be an odd integer in order to excite a spin wave, since, when  $n$  is even, the transverse component of the magnetization averages out to zero when taken over the entire film thickness. Hence, for  $n$  even, no coupling occurs between the RF field and the magnetization. Then, in theory, under the assumption of perfect pinning in a magnetically uniform film, one would expect a spin-wave spectrum as shown in Fig. A-1. Note that the uniform-mode resonance does not appear in this spectrum due to the imposed boundary conditions.

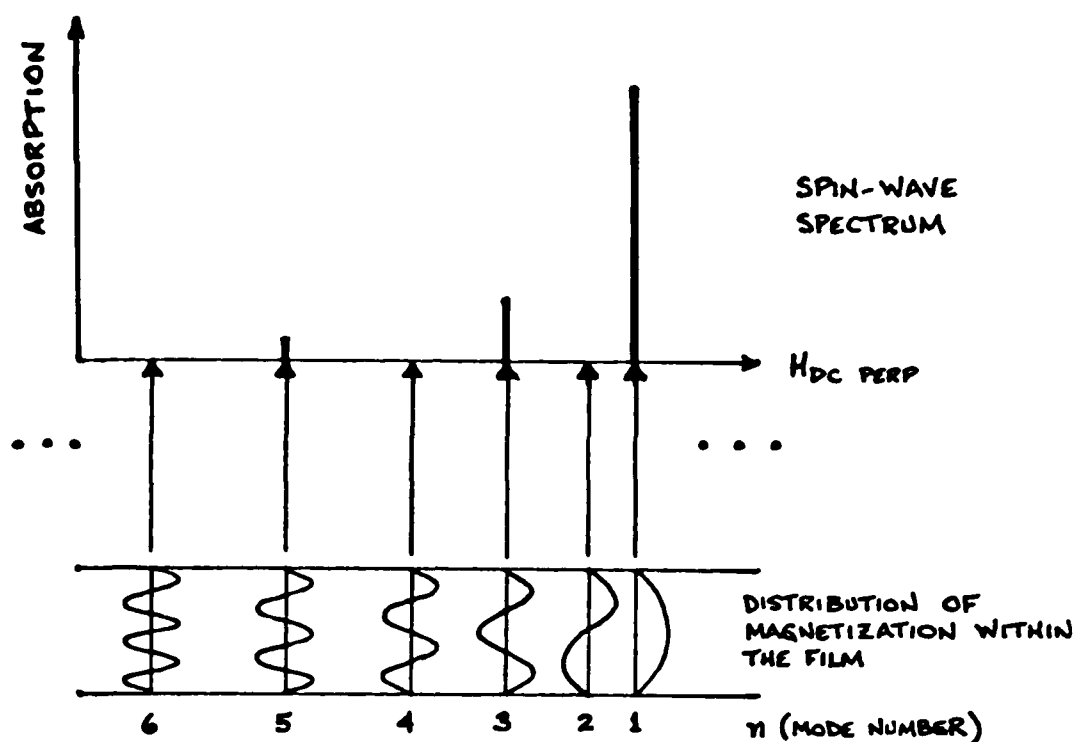


Figure A-1: Diagram of expected spin-wave behavior under assumption of perfect pinning in a magnetically uniform film.

Note that all of the even-numbered modes are absent and that since the coupling decreases as the mode number increases, one expects the amplitudes of each resonance to decrease with mode number as shown.

Theoretically, then, due to the nature of the dispersion relation

$$\omega = \gamma H_{\text{eff}} + DK^2 + \dots,$$

it is expected that if  $\omega$  is kept fixed and  $H_{DC}$  varied, that  $H_{DC}$  would depend linearly on  $n^2$  (recall  $k = n\pi/d$ ). This predicted  $n^2$  dependence can be experimentally confirmed by making log-log plots of the field separation from the first-order mode vs. the mode number<sup>57</sup> and noting that the slope of the resulting straight line is 2. From such plots, it is possible to find the exchange constant  $A$  if  $d$ ,  $\gamma$ , and  $M$  are known.

Kittel<sup>58</sup> first showed theoretically that it should be possible to excite standing spin-wave modes in thin films which would absorb energy from a uniform time-varying field. He suggested that the discontinuity of the boundary at the surface, that is, the lowered local symmetry of the spin at the surface as compared to the interior, might produce spin pinning. However, subsequent calculations have shown that such a surface anisotropy would not be large enough to be effective.<sup>59</sup> Since then, other possibilities, many relevant to this discussion, have also been proposed. For example, the NiCoB films may contain a thin antiferromagnetic surface layer, say NiO or CoO, both being antiferromagnetic; then pinning may be caused by the ferromagnetic-antiferromagnetic exchange interaction at this interface. Or perhaps the magnetization of a film's surface layer may differ from the value in the body of the film, again possibly due to differences in chemical composition. In this case, the spins in the surface layers will resonate at a slightly different frequency compared to the spins in the bulk of the film, thereby causing the surface spins to pin the bulk spins by exchange coupling.<sup>60</sup> In fact, it is possible that both of these mechanisms are at work in these films.

Large deviations from the quadratic  $n$  dependence have also been reported,<sup>61,62,63,64</sup> particularly at low  $n$  values where linear  $n$  dependences have sometimes been found. The interface pinning model discussed above is no longer adequate to explain the spin-wave resonance spectrum of these films. Instead, an effective variation of  $M$ , or  $2K_u/M$ , through the thickness of the film in either a linear or parabolic fashion, or some other relationship, must be assumed.<sup>65</sup> In addition, the effect may be produced by a variation of  $K_u$  in the film caused, for example, by a variation of strain through the film thickness. Furthermore, the spin-wave spectrum is expected to collapse when the static field makes some critical angle lying between the extreme  $H_{DC \text{ PAR}}$  and  $H_{DC \text{ PERP}}$  orientations.

Portis<sup>65</sup> has assumed that the saturation magnetization varies parabolically, with the smallest values occurring at the film surfaces. When the static field is applied perpendicular to the plane of the film, the alternating component of the magnetization, if the parabolic potential is extended to infinity, then satisfies a harmonic oscillator equation; this leads naturally to mode positions which depend linearly on  $n$ , rather than quadratically. In this way, one is lead to a spectrum which is uniformly spaced for the lowest modes and approaches the expected quadratic dependence only for the higher modes in which the finite extent of the parabolic potential becomes important. Also, in this composite model, it should be noted that

the intensities drop off very slowly at first, falling finally as  $1/p^2$  in the region of the quadratic spacing.

The parallel spin-wave resonances observed in the NiCoB films, that is, with  $H_{DC}$  applied parallel to the plane of the film, will be seen to be weaker than the perpendicular resonances, typical of results reported in the literature. Since parallel spin-wave resonances are observed only when inhomogeneities in the film permit the RF field to couple to the magnetization, they are observed less frequently than the perpendicular resonances.

In the more complicated case of changing magnetization (or magnetic anisotropy) profile throughout the film depth, a method of numerical analysis must be employed. Considerable research has been carried out on multilayer films consisting of two or more layers of ferromagnetic material<sup>66,67,68</sup> and in modelling ferromagnetic thin films as consisting of different layers with depth-varying magnetic parameters.<sup>42</sup> Various kinds of magnetic interactions between these layers are possible, depending on the magnetic properties of the different ferromagnetic layers and the properties of non-magnetic intermediate layers, if any, which separate the ferromagnetic layers, thereby resulting in characteristic perpendicular and parallel spin-wave resonance spectra.<sup>42</sup>

This type of theoretical analysis, applied to the NiCoB spin-wave resonance spectra presented here, may aid in understanding the mechanisms by which these distinct spectra are produced. In particular, it would be useful to explain the peculiar spin-wave spectrum of a film such as 4-25-80A which appears to follow the composite model of Portis<sup>65</sup> to some extent (uniformly spaced for the lowest modes, tending towards quadratic at the higher modes) with the additional property that pairs of adjacent modes appear to be equal in intensity. Although the theoretical analysis of Wilts and Prasad<sup>42</sup> was developed for implanted garnets, by modifying it to accept possible boundary conditions and magnetic profiles of the NiCoB films, it should be possible to use this type of approach to explain and understand the experimentally observed spin-wave spectra. Also, films of varying thicknesses and with known boundary conditions (e.g. sputtering a thin layer of  $SiO_2$  or iron on both sides of a sample film) could be fabricated and the experimental spectra determined and compared to the spectra predicted from the theoretical model.

## A.2 Experimental Spectra for the NiCoB Films and Comparison to the Simple Theory

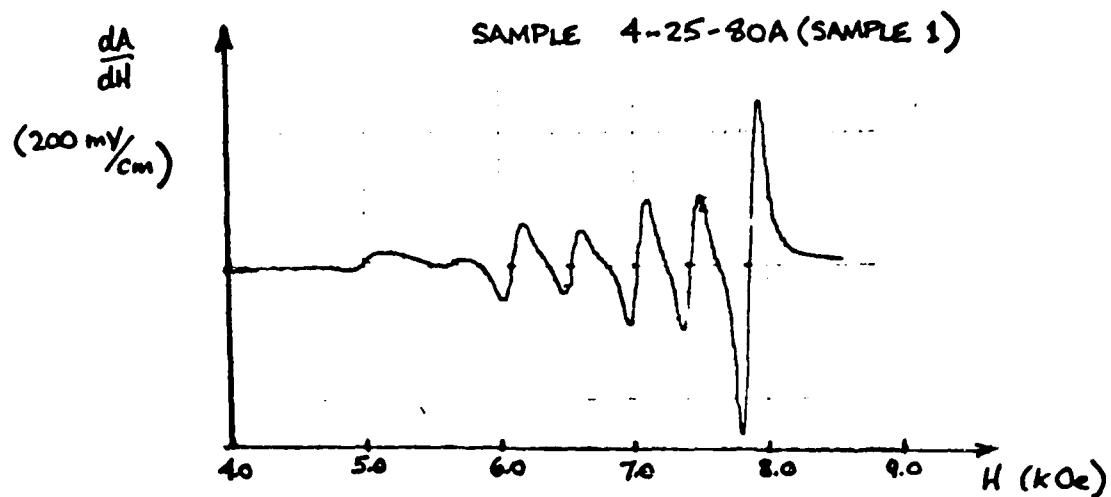
Many spin-wave resonance modes with the DC H-field applied either perpendicular or parallel to the film plane, were observed in the NiCoB ferromagnetic thin film samples that were investigated. In Figs. A-2, A-3, A-4, and A-5 are examples of observed resonances. Since these plots represent the derivative of the absorption with respect to the DC H-field vs. the DC H-field, the points of resonance, or of maximum absorption, occur where the plot passes through the baseline. Table A-1 compares the conditions under which these films were sputtered and the measured compositions. Films which have been annealed can be identified by the added suffix (annealed), i.e., film 8-20-80A is not annealed but 3-17-80A(annealed) is. Also, 4-25-80A(1) and 4-25-80A(2) represent two different unannealed pieces of film 4-25-80A.

SAMPLE	AVG SPUTTERING POWER(watts)	SPUTTERING TIME(hours)	INITIAL VOLTAGE		POWER SPLITTING RATIO	THICK- NESS (Å)	COMPOSITION (weight %)		
			(1)	(3)			Ni	Co	B
3-17-80A (annealed)	560	4.00	820	1250	.39-.61	1650	71.4*	22.1*	1.5
4-25-80A(1)	470	4.00	1570	420	.81-.19	2700	72.2*	22.8*	0.0
4-25-80A(2)	470	4.00	1570	420	.81-.19	2700	72.2*	22.8*	0.0
4-25-80A(1) (annealed)	470	4.00	1570	420	.81-.19	2700	72.2*	22.8*	0.0
8-20-80A	400	3.50	1000	720	.60-.40	2100	75.2*	17.4*	2.4
6-30-81B	600	2.07	900	1450	.38-.62	2950	77.9*	12.9*	4.2

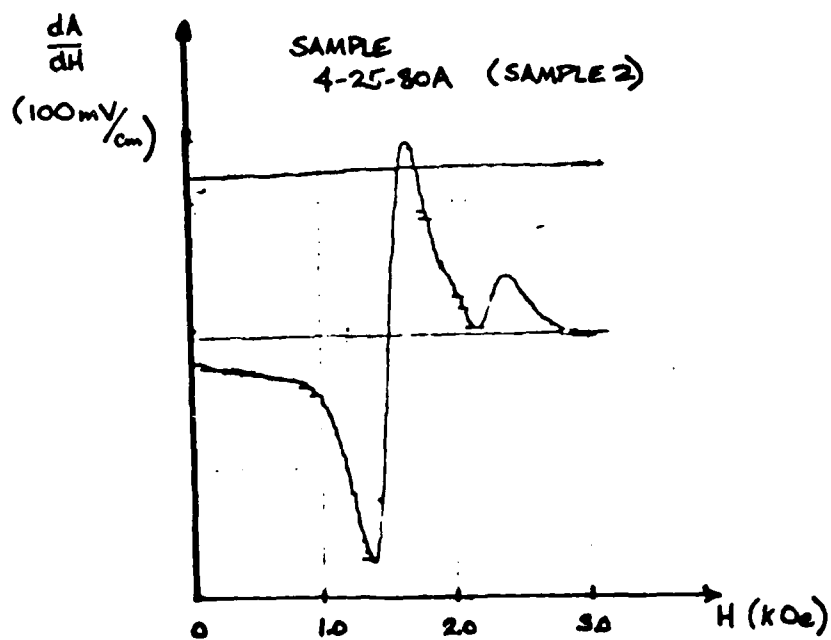
**Table A-1:** Sputtering conditions and composition of ferromagnetic NiCoB thin films for which spin-wave spectra are presented.

All films sputtered at 25 mT argon pressure.

\*See footnote on page 48.

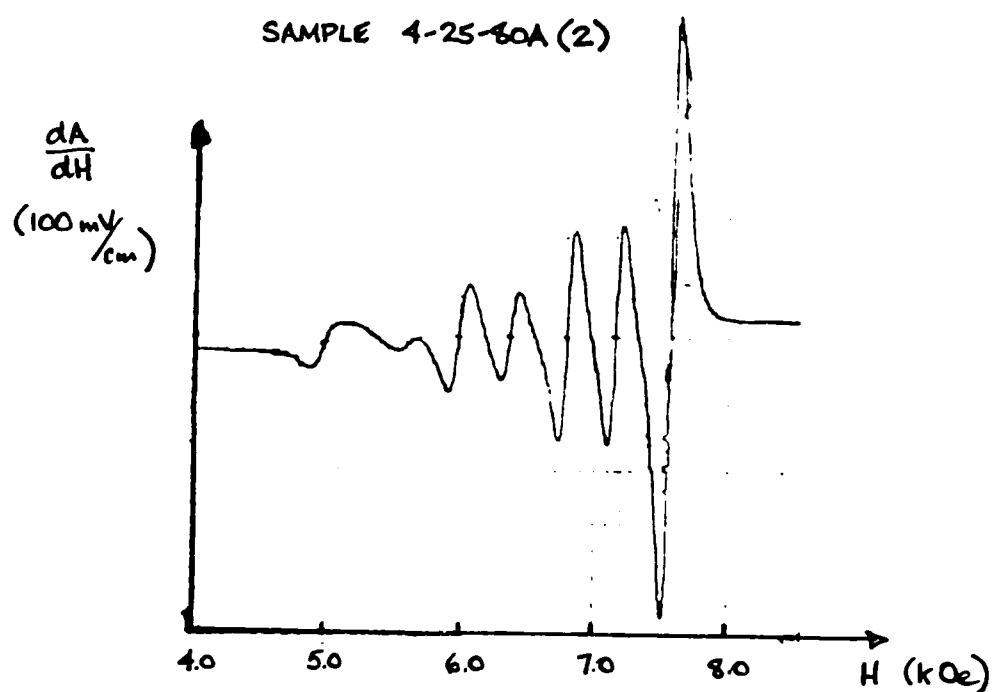


(a)  $dA/dH$  vs. applied perpendicular H-field for film 4-25-80A(1).



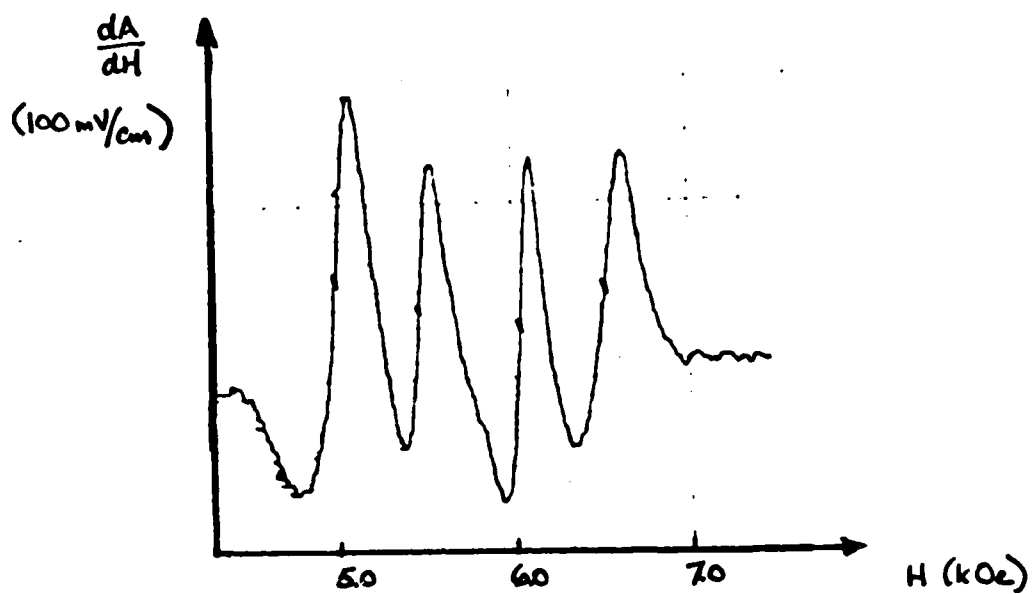
(b)  $dA/dH$  vs. applied parallel H-field for film 4-25-80A(2).



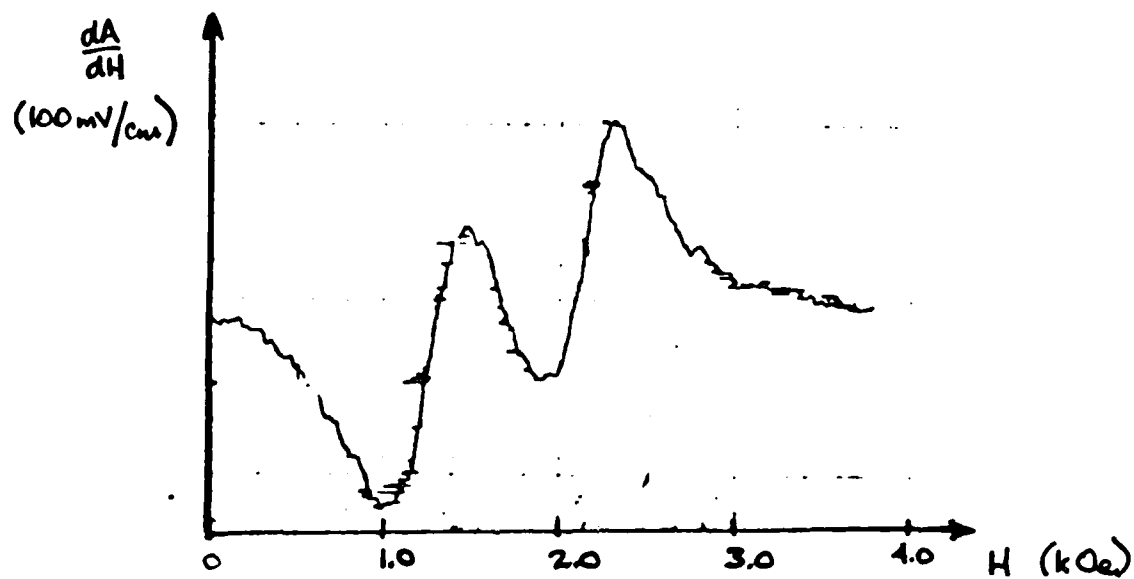


(c)  $dA/dH$  vs. applied perpendicular H-field for film 4-25-80A(2).

Figure A-2: Typical spin-wave resonance modes observed for different unannealed samples of the NiCoB ferromagnetic film 4-25-80A.

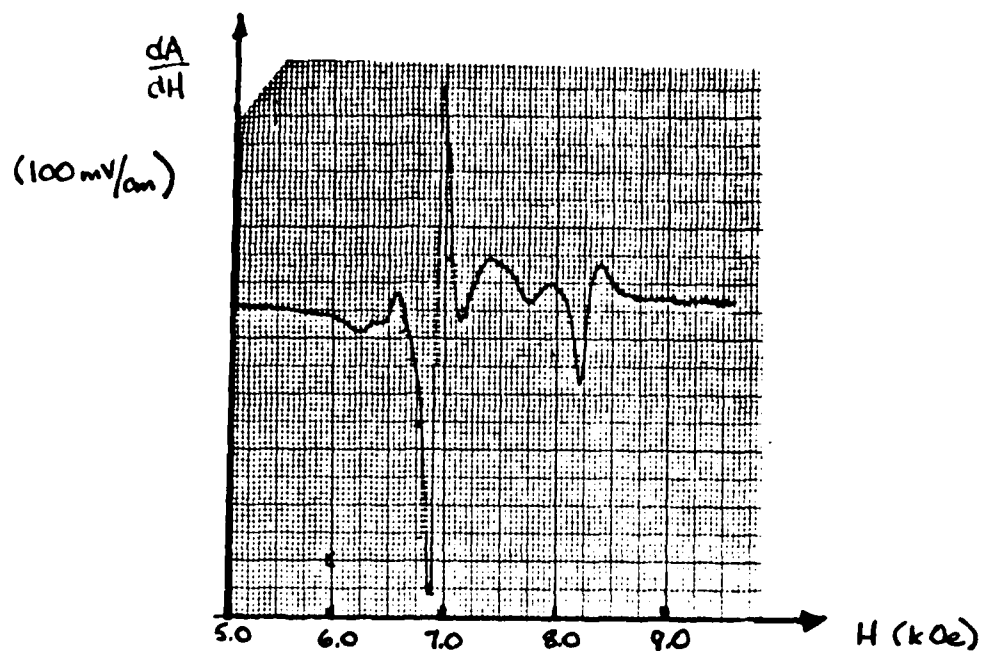


(a)  $dA/dH$  vs. applied perpendicular H-field for film 3-17-80A(annealed).

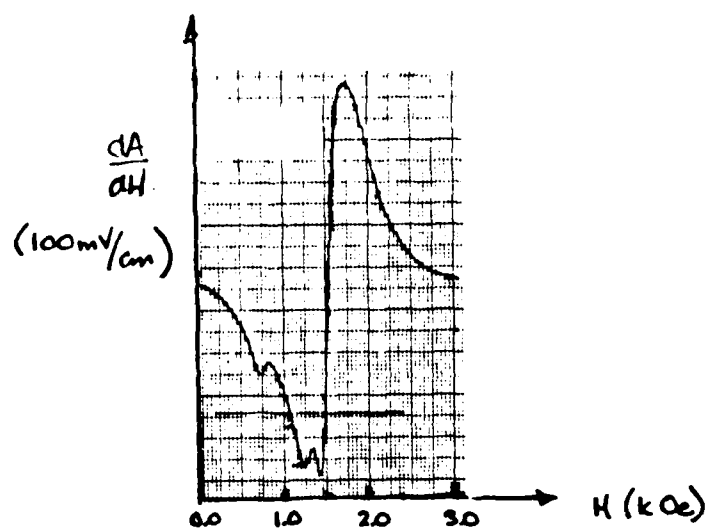


(a)  $dA/dH$  vs. applied parallel H-field for film 3-17-80A(annealed).

Figure A-3: Resonance spectra obtained for film 3-17-80A(annealed).



(a)  $dA/dH$  vs. applied perpendicular H-field for film 8-20-80A.



(b)  $dA/dH$  vs. applied parallel H-field for film 8-20-80A

Figure A-4: Resonance spectra obtained for film 8-20-80A.

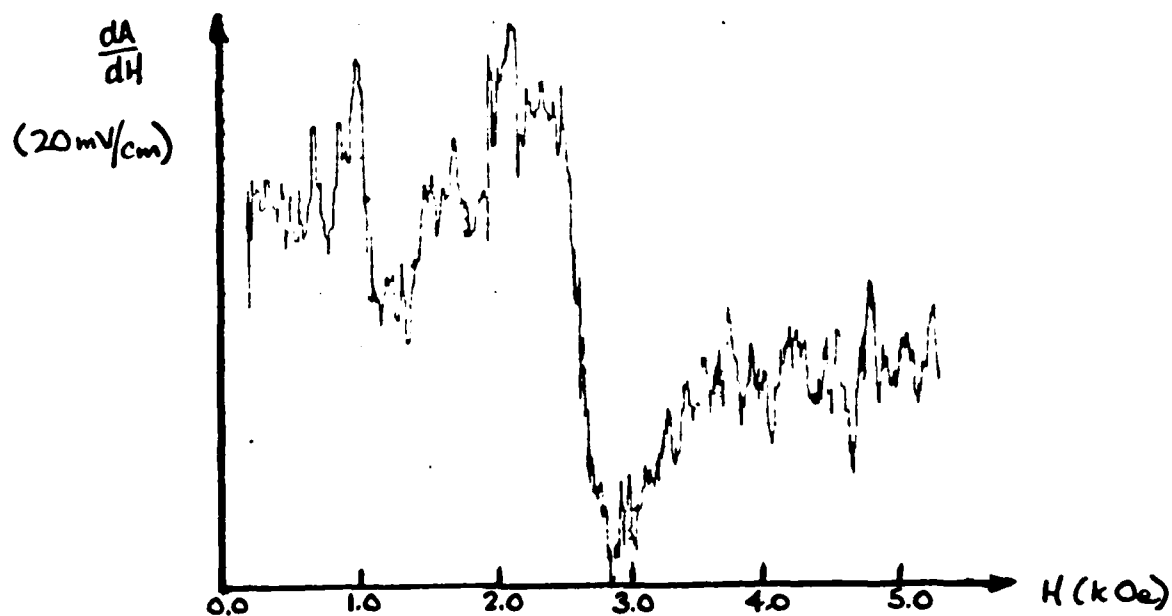
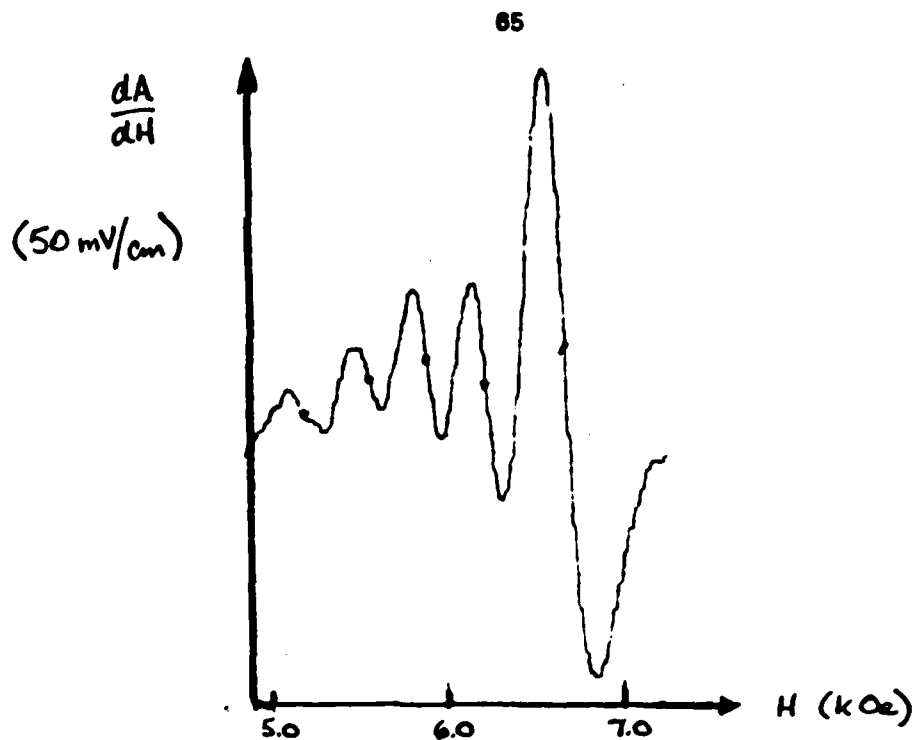


Figure A-5: Other types of distinct spectra obtained for the NiCoB ferromagnetic thin films.

As can be seen in Figs. A-2, A-3, A-4, and A-5, the perpendicular spin-wave resonances were generally much more pronounced in amplitude than the parallel modes. The experimentally observed cases which are most amenable to analysis are those cases for which four or more resonances were observed in sequence. A log-log plot of the magnetic field separation from the first-order mode vs. the assigned mode number  $n$  for some of the films can be found in Fig. A-6. From this plot, we can see that for the two samples 4-25-80A,  $\Delta H_{DC \text{ PERP}}$ , the magnetic field separation of each mode from the first-order mode (i.e., mode #1), depends linearly on  $n$  at low  $n$  values [e.g. 4-25-80A(2) follows  $\Delta H = 175n - 175$  for  $n = 3, 5, 7$ ] and then deviates from this behavior at higher mode numbers. At mode numbers greater than 9, the slope becomes greater than one, implying that the expected quadratic behavior is being approached for the higher modes. A better signal-to-noise ratio at high sensitivity would have been required to confirm this by enabling observation of the weak modes above mode number 13. The difference in the exact positioning of the two plots for samples 4-25-80A(1) and 4-25-80A(2) is due to a small difference in the thickness of each sample<sup>57</sup> since when measuring sample thicknesses it was observed that the thickness of the films tended to decrease by 10 to 15 % near the edge of the sample wafer as compared to the center. For sample 4-25-80A(1)(annealed) [annealed at 300°C for 3 hours under vacuum], an  $n^{0.8}$  dependence can be observed from the plot (the equation which describes this line well is  $\Delta H = 265n^{0.8} - 175$ ). Since four peaks of nearly the same amplitude were observed for the sample 3-17-80A(annealed) [annealed at 300°C, 3 hours], the mode located at the highest value of H-field was arbitrarily chosen as the first-order mode in order to compare this case to the others on a log-log plot.

One may also compare the mode separation and intensities of the NiCoB samples to those expected from theory<sup>65</sup> for the case of a linear or a quadratic dependence. Table A-2 gives the H-field values at which resonance occurred along with their intensities for those films which appear in Fig. A-6.

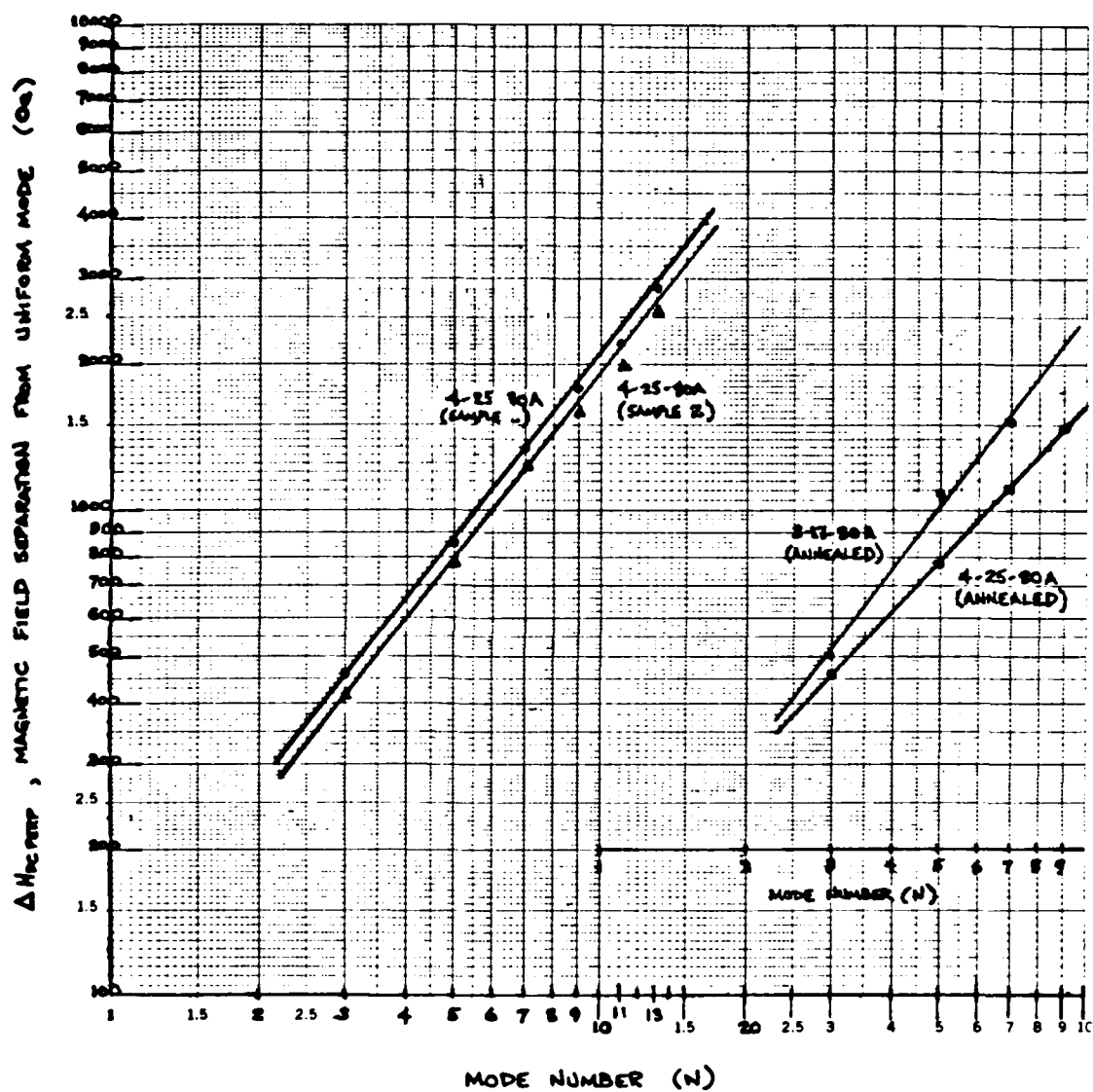


Figure A-6: Log-log plot of the magnetic field separation from the first-order mode (mode #1) vs. the assigned mode number n.

SAMPLE	MODE NUMBER						
	1	3	5	7	9	11	13
<b>4-25-80A(1)</b>							
H-field (Oe)	7880	7420	7020	6530	6100	5670	5010
Intensity (arbitrary units)	8.75	3.50	3.40	1.85	2.30	0.30	0.60
<b>4-25-80A(2)</b>							
H-field (Oe)	7580	7160	6800	6380	6000	5610	4990
Intensity (arbitrary units)	8.70	3.30	3.20	1.30	1.60	0.20	0.70
<b>4-25-80A(1)(annealed)</b>							
H-field (Oe)	6660	6200	5880	5550	5180	----	----
Intensity (arbitrary units)	7.00	2.50	1.60	0.70	0.50	----	----

Table A-2: H-field values and intensities of the observed resonances for films 4-25-80A, both unannealed and annealed samples.

Table A-3, derived directly from Table A-2, shows the mode separation and mode intensity for the same films normalized to the spacing between the first two modes and to the intensity of the first-order mode, respectively.

SAMPLE	MODE NUMBER						
	1	3	5	7	9	11	13
<hr/>							
4-25-80A(1)							
$\Delta H_{DC \text{ PERP}}^{(Oe)}$ (normalized)	1.00	0.87	1.07	0.93	0.93	1.43	
Intensity (normalized)	1.00	0.40	0.39	0.21	0.26	0.034	0.069
<hr/>							
4-25-80A(2)							
$\Delta H_{DC \text{ PERP}}^{(Oe)}$ (normalized)	1.00	0.86	1.00	0.90	0.93	1.48	
Intensity (normalized)	1.00	0.38	0.37	0.15	0.18	0.023	0.080
<hr/>							
4-25-80A(1)(annealed)							
$\Delta H_{DC \text{ PERP}}^{(Oe)}$ (normalized)	1.00	0.70	0.72	0.80	----	----	
Intensity (normalized)	1.00	0.36	0.23	0.10	0.071	----	----
<hr/>							

Table A-3: Experimentally determined mode separation and mode intensity for film 4-25-80A, both unannealed and annealed samples.

Now we may compare these values to those predicted from theory assuming either linear or quadratic modes. In Table A-4 is shown the observed normalized mode separation of the three NiCoB samples as compared to the expected normalized separation for both the linear and quadratic case.



n	LINEAR	QUADRATIC	4-25-80A(1)	4-25-80A(2)	4-25-80A(1)(annealed)
1	1.00	1.00	1.00	1.00	1.00
3	1.00	2.00	0.87	0.86	0.70
5	1.00	3.00	1.07	1.00	0.72
7	1.00	4.00	0.93	0.90	0.80
9	1.00	5.00	0.93	0.93	----
11	1.00	6.00	1.43	1.48	----
13					

Table A-4: Comparison of mode separation of various samples of film 4-25-80A to theory.

It is seen here that the first 5 modes appear linearly spaced for the unannealed films but that the  $n = 11$  mode is more widely spaced. Also, one can clearly see the smaller spacing of the annealed film for which it was determined that the mode separation went as  $n^{0.8}$  instead of depending linearly on  $n$ . In Table A-5 is shown the experimentally observed normalized mode intensities as compared to that which is theoretically predicted for the linear and quadratic cases.

n	LINEAR	QUADRATIC	4-25-80A (1)	4-25-80A (2)	4-25-80A(annealed)
1	1.00	1.00	1.00	1.00	1.00
3	.50	.11	.40	.38	.36
5	.38	.040	.39	.37	.23
7	.31	.020	.21	.15	.10
9	.27	.012	.26	.18	.071
11	.25	.0083	.034	.023	----

Table A-5: Comparison of mode intensities of various samples of film 4-25-80A to theory.

The first 5 modes for the films 4-25-80A(1) and 4-25-80A(2) tend to roughly follow the linear intensities but the  $n = 11$  mode is much weaker. One peculiarity for these two films is exhibited by the fact that the intensities for modes 3 and 5, and again for 7 and 9, are nearly equal, unlike anything expected from the simple theory. By increasing the sensitivity of the FMR system, higher order resonances can be observed and one will be able to determine if, in fact, the mode behavior does become quadratic at higher modes as the results above seem to indicate.

It was also observed that the spin-wave spectrum collapsed when the static field made an angle of  $14^\circ$  from the film normal for sample 4-25-80A(1). The observed spectra for varying angles of inclination of the applied static field (with  $0^\circ$  defined as  $H_{DC}$  applied normal to the film plane) can be seen in Fig. A-7. As can be seen here, at angles of  $14^\circ$  and greater, only the first-order mode remained.

Continued study of the distinct spin wave spectra which were obtained appears to be a viable avenue for further research. A very thorough analysis will yield experimental spectra which can then be compared to theoretically generated spectra based on the boundary conditions and magnetic profiles of the NiCoB films similar to the method employed by Wilts and Prasad<sup>42</sup> to implanted garnets. Also, it would be possible to sputter films with established boundary conditions by sputtering a thin layer of the appropriate material (e.g., Fe,  $SiO_2$ , etc.) on one or both sides of the

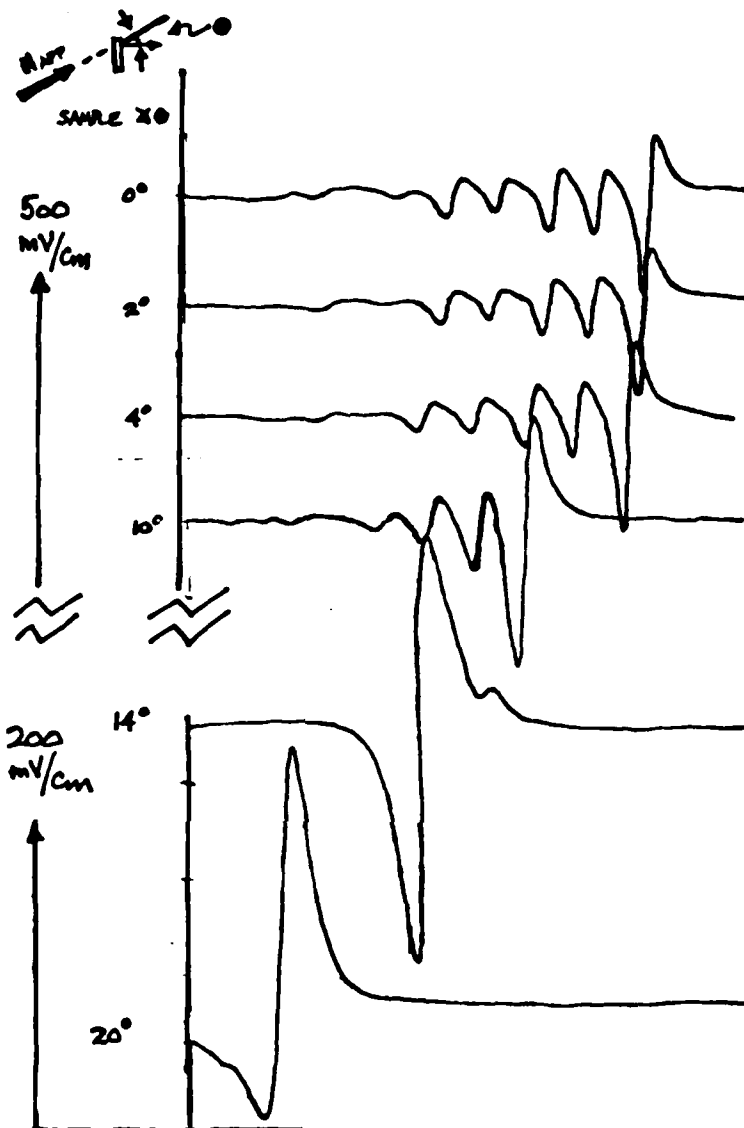


Figure A-7: Observed spectra for varying angles of inclination of the applied static H-field.

NiCoB film and then studying the resulting spectra. In addition, the present samples could be reduced in thickness by sputter-etching in 200 to 300 Å steps and the spectra obtained for each thickness and compared to one another. In particular, spectra of the kind exhibited by sample 4-25-80A appear especially suited for further analysis. This type of work will aid in explaining, for example, whether the interface pinning model is valid for these films, how the value of  $M$  varies throughout the

thickness of the film, and whether a variation of the strain through the film might be producing a variation of  $K_u$  through the film thickness.

In addition to the FMR analysis using the X-band microwave cavity, a potentially more useful system employing a stripline is available. Although the resulting RF H-field across the sample when employing the stripline is less uniform than that obtained by the cavity, thereby perhaps causing higher order weak modes to be excited more strongly than in a uniform RF field, it may be possible to check the spacing and intensities of order 15 and greater to confirm that a quadratic ( $1/n^2$ ) intensity dependence and a quadratic mode separation dependence is indeed observed. An added advantage of the stripline lies in the fact that the frequency need not remain fixed; in fact, besides sweeping the DC H-field at different values of fixed frequency, it is also possible to sweep the frequency while maintaining the H-field at a constant value.

Further, a ferromagnetic resonance system in the Department of Physics operating at K-band (24 GHz) could also be used to obtain spectra with a uniform RF field and at a much different frequency than with the X-band system. Spin-wave spectra obtained at this frequency could then be compared with those from the X-band system.

## REFERENCES

1. Bobeck, A.H., "Properties and Device Applications of Magnetic Domains in Orthoferrites," *Bell Sys. Tech. J.*, 46, 1901 (1967).
2. Eschenfelder, A.H., Magnetic Bubble Technology, Springer-Verlag, Berlin, 1980, Chapter 4.
3. Bobeck, A.H., S.L. Blank, A.D. Butherus, F.J. Ciak, and W. Strauss, "Current-Access Magnetic Bubble Circuits," *Bell Sys. Tech. J.*, 58, 1453 (1979).
4. Lin, Y.S., G.S. Almasi, "Self-Aligned Contiguous-Disk Chip Using  $1\mu\text{m}$  Bubbles and Charged-Wall Function", *IEEE Trans. Mag. Mag-14*, 494 (1978).
5. Eschenfelder, A.H., Magnetic Bubble Technology, Springer-Verlag, Berlin, 1980.
6. Bobeck, A.H., and H.E.D. Scovil, "Magnetic Bubbles," *Sci. Amer.*, 224, 78 (1971).
7. George, P.K., and G. Reyling, Jr., "Bubble Memories Come to the Boil," *Electronics*, 52, 99 (1979).
8. O'Dell, T.H., Magnetic Bubbles, John Wiley and Sons, New York, 1974.
9. Chang, H., Magnetic Bubble Technology: Integrated-Circuit Magnetics for Digital Storage and Processing, IEEE Press, New York, 1975.
10. Aboaf, J.A., R.J. Kobliska, and E. Klokholm, "Properties of Transition Metal-Metalloid Ferromagnetic Thin Films," *IEEE Trans. Mag.*, MAG-14, 941 (1978).
11. Chaudhari, P., C.H. Bajorek, and M.H. Kryder, "Amorphous Gd-Co Alloys for Magnetic Bubble Applications," unpublished.
12. Taylor, R.C., "Charged Walls in Amorphous Magnetic Films," *IEEE Trans. Mag.*, MAG-16, 902 (1980).
13. Esho, Sotaro, "Perpendicular Magnetic Anisotropy in Sputtered GdCo Films," *J. Appl. Phys.*, 50, 1006 (1979).
14. Shimada, Yutaka, and Hiroshi Kojima, "Magnetic Properties of Amorphous Fe-Si Thin Films," *J. Appl. Phys.*, 47, 4156 (1976).

15. Aboaf, J.A., personal communication.
16. Cargill, G.S., Solid State Physics (F. Seitz, D. Turnbull, and H. Ehrenreich, editors), Academic Press, New York, Vol. 30, 1975.
17. Luborsky, F.E., Ferromagnetic Materials, Vol. I (E.P. Wohlfarth, editor), North-Holland Publishing Company, Amsterdam, 1980, Chapter 6.
18. Weijsenfeld, C.H., "Yield, Energy, and Angular Distributions of Sputtered Atoms," *Philips Res. Repts.*, No. 2, Supplement (1967).
19. Maissel, L.I., and R. Glang, Handbook of Thin Film Technology, McGraw-Hill, New York, 1970, Chapter 3.
20. Winters, H.F., and E. Kay, "Gas Incorporation into Sputtered Films", *J. Appl. Phys.*, 38, 3928 (1967).
21. Bajorek, C.H. and R.J. Kobliska, "Amorphous Materials for Micrometer and Submicrometer Bubble Domain Technology", *IBM J. Res. Dev.*, 20, 271 (1976).
22. Maissel, L.I., and R. Glang, Handbook of Thin Film Technology, McGraw-Hill, New York, 1970, Chapter 4.
23. Aboaf, J.A., personal communication.
24. Alfa Products, Thiokol/Ventron Division, P.O. Box 299, 152 Andover St., Danvers, MA.
25. Materials Research Corporation, Orangeburg, NY 10962.
26. Perkin Elmer Ultek, P.O. Box 10920, Palo Alto, CA 94303.
27. Air Products and Chemicals, Inc., Advanced Products Department, 1919 Vultee St., Allentown, PA 18103.
28. Corning Glass Works, Science Products Division, Corning, NY 14830.
29. VWR Scientific, 147 Delta Drive, Pittsburgh, PA 15238.
30. Sinclair, W.R., and F.G. Peters, "Method for Controlled Multicomponent Sputtering", *Rev. Sci. Inst.*, 33, 744 (1962).

31. Bickley, W.P., and D.S. Campbell, *Vide*, 99, 214 (1962).
32. Corsi, Carlo, "Pb<sub>x</sub>Sn<sub>1-x</sub>Te Layers by RF Multicathode Sputtering", *J. Appl. Phys.*, 45, 3467 (1974).
33. Burilla, C.T., W.R. Bekebrede, and A.B. Smith, "The Multiple-Target Method for Sputtering Amorphous Films for Bubble-Domain Devices", *AIP Conf. Proc.*, 34, 340 (1976).
34. Sloan Technology Corporation, Santa Barbara, CA.
35. Reed, S.J.B., *Electron Microprobe Analysis*, Cambridge University Press, Cambridge, 1975.
36. Birks, L.S., *Electron Probe Microanalysis*, John Wiley and Sons, Interscience Publishers, New York, 1963.
37. Salter, W.J.M., *A Manual for Quantitative Electron Probe Microanalysis*, Structural Publications, Ltd., London, 1970.
38. Manufactured by Applied Research Laboratory.
39. Vonsovskii, S.V., *Ferromagnetic Resonance*, Israel Program for Scientific Translations, Jerusalem, 1964, p. 2.
40. Soohoo, R.F., *Magnetic Thin Films*, Harper and Row Publishers, New York, 1965, chapter 10.
41. Chikazumi, S. and S.H. Charap, *Physics of Magnetism*, Robert F. Krieger Publishing Co., Huntington, NY, 1978, chapter 3.
42. Wilts, C.H. and S. Prasad, "Determination of Magnetic Profiles in Implanted Garnets Using Ferromagnetic Resonance", *IEEE Trans. Mag.*, MAG-17, 2405 (1981).
43. The measurements were done by T. McGuire and H. Lilienthal at the IBM T.J. Watson Research Center. A description of their measurement technique is included here for clarity.
44. Measurements at G.E. were done by Malcolm McConnel.

45. Cargill, G.S., R.J. Gambino, and J.J. Cuomo, "Stripe and Cylindrical Domains in Amorphous Co-P and Co-Ni-P Films", *IEEE Trans. Mag.*, MAG-10, 33 (1974).
46. Sherwood, R.C., E.M. Gyorgy, H.S. Chen, S.D. Ferris, G. Norman, and H.J. Leamy, "Ferromagnetic Behavior of Metallic Glasses", *AIP Conf. Proc.*, 24, 745 (1974).
47. Wolf, I.W., *J. Appl. Phys.*, "Electrodeposition of Magnetic Materials", 33, 1152S (1962).
48. Prutton, M., Thin Ferromagnetic Films, Butterworth and Co., Washington, D.C., 1964.
49. Townsend, P.D., J.C. Kelly, and N.E.W. Hartley, Ion Implantation, Sputtering, and their Applications, Academic Press, New York, 1976, Chapter 6.
50. Davidse, P.D. and L.I. Maissel, "Dielectric Thin Films through RF Sputtering", *J. Appl. Phys.*, 37, 574 (1966).
51. Evans, P. and A.J. Noreika, "Effect of Gaseous Environment on the Structure of Sputtered GaAs Films on NaCl Substrates", *Phil. Mag.*, 13, 717 (1966).
52. Krikorian, E. and R.J. Sneed, "Epitaxial Deposition of Germanium by Both Sputtering and Evaporation", *J. Appl. Phys.*, 37, 3665 (1966).
53. Theall Engineering Company, Box 336, Oxford, PA.
54. Saunders, D. and M.H. Kryder, "The Influence of Stress Relaxation in Charged Walls in a (100)-Oriented Garnet Field", (unpublished).
55. Clark, A., Ferromagnetic Materials, Vol. I (E.P. Wohlfarth, editor), North-Holland Publishing Company, Amsterdam, 1980, Chapter 7.
56. Akhiezer, A.I., V.G. Bar'yakhtar, S.V. Peletminskii, Spin Waves, North Holland Publishing Co. (Interscience Publishers Division), Amsterdam, 1968.
57. Weber, R., "Spin-Wave Resonance", *IEEE Trans. Mag.*, MAG-4, 28 (1968).
58. Kittel, C., "Excitation of Spin-Waves in a Ferromagnet by a Uniform RF Field", *Phys. Rev.*, 110, 1295 (1958).
59. Soohoo, R.F., "Excitation and Boundary Effects in Spin-Wave Resonance", *J. Appl. Phys.*, 32, 148S (1961).



60. Wigen, P.E., C.F. Kooi, and M.R. Shanabarger, "Dynamic Pinning in Thin-Film Spin-Wave Resonance", *Phys. Rev. Lett.*, 9, 206 (1962).
61. Seavey, M.H. and P.E. Tannenwald, "Direct Observation of Spin-Wave Resonance", *Phys. Rev. Lett.*, 1, 168 (1958).
62. Tannenwald, P.E., *J. Phys. Soc. Japan, Supplement B-1*, 17, 592 (1962).
63. Soohoo, R.F., "General Exchange Boundary Condition and Surface Anisotropy Energy of a Ferromagnet", *Phys. Rev.*, 131, 594 (1963).
64. Nisenoff, M., and R.W. Terhune, "Experimental Studies of Standing Spin-Wave Modes in Ferromagnetic Films", *J. Appl. Phys.*, 35, 806 (1964).
65. Portis, A.M., "Low-Lying Spin-Wave Modes in Ferromagnetic Films", *Appl. Phys. Lett.*, 2, 69 (1963).
66. Middelhoek, S., "Domain-Wall Structures in Magnetic Double Films", *J. Appl. Phys.*, 37, 1276 (1966).
67. Feldtkeller, E., "Coupled Walls in Multilayer Films", *J. Appl. Phys.*, 39, 1181 (1968).
68. Chen, D. and A.H. Morrish, "Ferromagnetic Resonances in Thin Films", *J. Appl. Phys.*, 33, 1146S (1962).

## CHARACTERIZATION OF MICROSTRUCTURE IN ION-IMPLANTED GARNET

### BY TRANSMISSION ELECTRON MICROSCOPY\*

T. Yoshie, C. L. Bauer and M. H. Kryder, Carnegie-Mellon University,  
Pittsburgh, PA 15213

#### Introduction

Ion implantation is commonly used to modify magnetic properties of garnet for bubble device applications. Although changes in magnetic properties with implantation dose have been investigated in detail, corresponding changes in microstructure have received relatively little attention. The purpose of this investigation is to characterize the evolution of microstructure in garnet as a function of implantation dose by transmission electron microscopy.

#### Experimental Procedures

Films of  $(\text{SmY}\text{Gd}\text{Tm})_3\text{Ga}_{0.4}\text{Fe}_{4.6}\text{O}_{12}$  garnet were grown by liquid phase epitaxy (LPE) on gadolinium-gallium garnet (GGG) substrates and subsequently implanted with ions of deuterium at 60 keV and doses ranging from  $1.0$  to  $5.0 \times 10^{16} \text{D}_2^+/\text{cm}^2$  and with ions of oxygen at 110 keV and doses ranging from  $1.9$  to  $9.5 \times 10^{14} \text{O}^+/\text{cm}^2$ . Specimens were then thinned in directions both parallel and perpendicular to the implanted surfaces and examined in a JEOL 120CX electron microscope.

#### Experimental Results

Typical results are presented in Fig. 1, wherein bright field images and selected micro-microdiffraction patterns of specimens implanted with (a)  $4.5 \times 10^{16} \text{D}_2^+/\text{cm}^2$  and (b)  $3.0 \times 10^{16} \text{D}_2^+/\text{cm}^2$  and  $5.8 \times 10^{14} \text{O}^+/\text{cm}^2$  and subsequently thinned perpendicular to the implanted surface are pictured. In general, the implanted surface, the LPE/GGG interface, and distinct bands, aligned parallel to the implanted surface, are observed.

The band pictured in Fig. 1(a) terminates at about 450 nm below the implanted surface, corresponding to the penetration depth of deuterium. The microstructure within this band was investigated by selected-area diffraction, but neither Debye rings nor halo rings, associated with polycrystalline or amorphous structure, respectively, could be observed. Therefore, it is concluded that this band is delineated by the difference in strain between the implanted and unimplanted regions.

Implantation with both deuterium and oxygen changes the structure more drastically. For example, a dose of  $3.0 \times 10^{16} \text{D}_2^+/\text{cm}^2$  and  $5.8 \times 10^{14} \text{O}^+/\text{cm}^2$  produces two distinct bands, associated with implantation of both deuterium and oxygen (Band A) and implantation of deuterium (Band B), as pictured in Fig. 1(b). Micro-microdiffraction patterns from these bands indicate that Band A is amorphous whereas Band B is crystalline, since halo rings and sharp

\*Supported by the Air Force Office of Scientific Research under Grant 80-0284.

Category 1

C. L. Bauer (412) 578-2676  
Dept. of MEMS  
Carnegie-Mellon University  
Pittsburgh, PA 15213

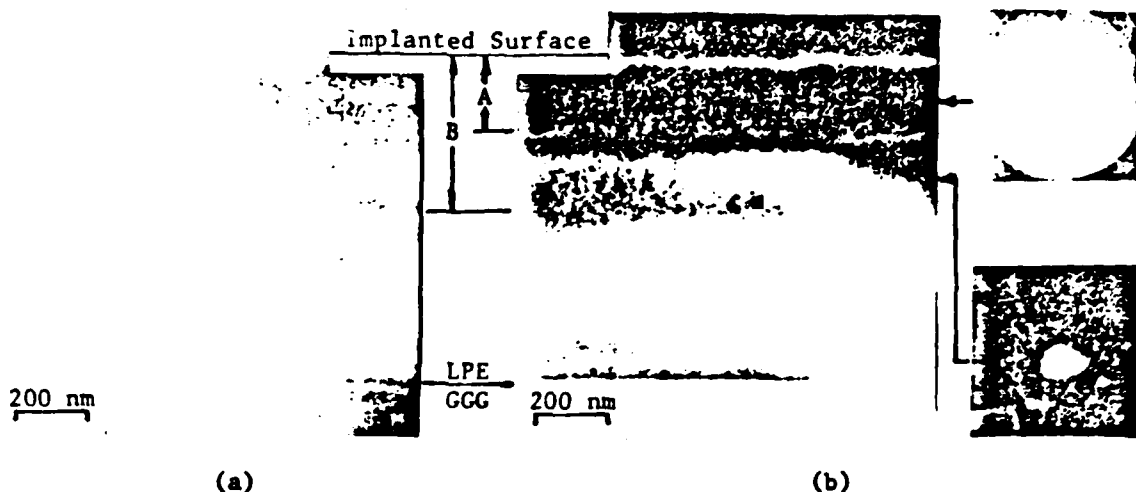


Fig. 1. Bright-field images and selected micro-microdiffraction patterns in garnet implanted with (a)  $4.5 \times 10^{16} \text{D}_2^+/\text{cm}^2$  and (b)  $3.0 \times 10^{16} \text{D}_2^+/\text{cm}^2$  and  $5.8 \times 10^{14} \text{O}^+/\text{cm}^2$  and subsequently thinned perpendicular to the implanted surface. The implanted surface, LPE/GGG interface, and distinct bands, aligned parallel to this surface, are evident.

diffraction patterns are observed, respectively. Moreover, Band A terminates at about 180 nm below the implanted surface, corresponding to the penetration depth of oxygen, whereas Band B terminates at about 450 nm below the surface, as previously noted in reference to Fig. 1(a). Similar results were obtained with doses ranging from  $1.0 \times 10^{16} \text{D}_2^+/\text{cm}^2$  and  $1.9 \times 10^{14} \text{O}^+/\text{cm}^2$  to the maximum values reported. Again, Debye rings, associated with polycrystalline structure, could not be observed. The amorphous structure, however, can be transformed to the original (crystalline) structure by annealing at or above  $200^\circ\text{C}$ .

#### Discussion and Summary

Results indicate that, for the energies and doses reported herein, implantation with oxygen produces highly strained regions, which, upon further implantation, expand and rearrange to form a metastable amorphous layer, whereas implantation with deuterium only produces strained regions. The resulting microstructure is envisioned to evolve in three stages: First an implanted band, delineated by the strain profile, is formed; then isolated amorphous regions are formed below the implanted surface; finally, the amorphous regions expand to form a continuous band extending to the implanted surface. The critical dose for this last stage is about  $3 \times 10^{16} \text{D}_2^+/\text{cm}^2$  and  $5.7 \times 10^{14} \text{O}^+/\text{cm}^2$ .

#### Acknowledgement

The films characterized in this research were produced by C. S. Krafft and implanted by A. Guzman and J. Tabacchi.

Submitted to Intermag Conference,  
Philadelphia, April, 1983

**THE FABRICATION AND CHARACTERIZATION  
OF AMORPHOUS MAGNETIC FILMS IN THE  
GADOLINIUM COBALT MOLYBDENUM ARGON SYSTEM**

August 1982

Paul J. Nittoli

M.S. Thesis

Carnegie-Mellon University

## TABLE OF CONTENTS

<b>ABSTRACT</b>	<b>1</b>
<b>INTRODUCTION</b>	<b>2</b>
<b>1. BUBBLE MATERIAL PHYSICS</b>	<b>4</b>
<b>2. BACKGROUND INFORMATION</b>	<b>12</b>
2.1 FILM STRUCTURE	12
2.2 FILM CONSTITUENTS	12
2.3 POTENTIAL FILM ADDITIVES	17
<b>3. THE SPUTTERING PROCESS</b>	<b>18</b>
3.1 ADVANTAGES OF SPUTTERING	18
3.2 AN OVERVIEW OF THE PROCESS	19
<b>4. SPUTTERING THE AMORPHOUS FILMS</b>	<b>25</b>
4.1 FABRICATION FACILITIES	25
4.2 TARGET FABRICATION	28
4.3 GdCoMoAr FILM FABRICATION	30
<b>5. CHARACTERIZING THE AMORPHOUS FILM</b>	<b>34</b>
5.1 DETERMINATION OF FILM COMPOSITION	34
5.2 THICKNESS MEASUREMENT	34
5.3 MAGNETIC MEASUREMENTS	35
5.3.1 DETERMINATION OF MAGNETIZATION, CHARACTERISTIC LENGTH AND DOMINANT SUBLATTICE	35
5.3.2 DETERMINATION OF THE UNIAXIAL ANISOTROPY CONSTANT	36
<b>6. RESULTS AND DISCUSSION</b>	<b>39</b>
6.1 COMPOSITION DATA	39
6.2 SPUTTER ETCH RATE CALIBRATION	45
6.3 MAGNETIZATION, CHARACTERISTIC LENGTH AND ANISOTROPY DATA	49
<b>CONCLUSION</b>	<b>63</b>
<b>ACKNOWLEDGEMENTS</b>	<b>64</b>

## LIST OF FIGURES

Figure 1-1:	Electron Spins Within a Portion of a Bloch Wall <sup>7</sup>	7
Figure 1-2:	The Formation of Magnetic Bubbles Through the Application of a Magnetic Field to a Demagnetized Film <sup>8</sup>	9
Figure 1-3:	Coercive Force as a Function of Temperature for a GdCo Film <sup>3</sup>	10
Figure 2-1:	Typical Relationship Between Magnetization and Temperature for GdCoMoAr Films	14
Figure 2-2:	Critical Temperatures as a Function of $(\text{Gd}_{1-x}\text{Co}_x)_{1-y}\text{Mo}_y$ Composition <sup>7</sup>	15
Figure 3-1:	DC Sputterer Configuration <sup>27</sup>	20
Figure 3-2:	RF Sputterer Configuration <sup>27</sup>	21
Figure 3-3:	Schematic of Potentials in RF Sputtering	23
Figure 3-4:	Illustration of Bias Sputtering	24
Figure 4-1:	Target Schematic	29
Figure 4-2:	Plots of Ar Content and $K_u$ vs. Substrate Bias <sup>29</sup>	31
Figure 5-1:	Exchange Constants (in erg/cm) for Various $(\text{Gd}_{1-x}\text{Co}_x)_{1-y}\text{Mo}_y$ Films <sup>7</sup>	38
Figure 6-1:	The Co/Gd Content Vs. Substrate Bias of Films Fabricated between 5/16/81 and 6/11/81	41
Figure 6-2:	The Co/Mo Content Vs. Substrate Bias of Films Fabricated between 5/16/81 and 6/11/81	42
Figure 6-3:	The Co/Gd Content Vs. Substrate Bias of Films Fabricated between 10/3/81 and 10/7/81	43
Figure 6-4:	The Co/Mo Content Vs. Substrate Bias of Films Fabricated between 10/3/81 and 10/7/81	44
Figure 6-5:	IBM Calibration of Co/Gd Content and Co/Mo Content Vs. Substrate Bias <sup>21</sup>	46
Figure 6-6:	Qualitative Demonstration of the Rise in Ar Content with Substrate Bias	47
Figure 6-7:	Film Thickness Vs. Duration of Sputter Etching	48
Figure 6-8:	Sample 61081B1 Exhibiting Stripwidth Variation [scale: $14.8\mu\text{m}/\text{cm}$ ]	50
Figure 6-9:	Sample 61181A1 Exhibiting a Bubble Raft [scale: $4.71\mu\text{m}/\text{cm}$ ]	51
Figure 6-10:	Sample 6881A1 [scale: $4.71\mu\text{m}/\text{cm}$ ]	52
Figure 6-11:	Sample 61081B1 [scale: $4.71\mu\text{m}/\text{cm}$ ]	53
Figure 6-12:	Sample 61181A1 [scale: $14.8\mu\text{m}/\text{cm}$ (left photo), $4.71\mu\text{m}/\text{cm}$ (right photo)]	54
Figure 6-13:	Sample 33181A1 [scale: $4.71\mu\text{m}/\text{cm}$ ]	55
Figure 6-14:	Sample 10781A2 [scale: $4.71\mu\text{m}/\text{cm}$ ]	56
Figure 6-15:	Magnetic Parameter Chart for Sample 33181A1	58

Figure 6-16:	Magnetic Parameter Chart for Sample 61081B1	59
Figure 6-17:	Magnetic Parameter Chart for Sample 61181A1	60
Figure 6-18:	Magnetic Parameter Chart for Sample 61181B1	61
Figure 6-19:	Magnetic Parameter Chart for Sample 10781A2	62

## LIST OF TABLES

Table 4-1:	Comparison of Ar Pressures Measured with a Perkin Elmer Thermistor Gauge and an MKS Capacitance Monometer	27
Table 6-1:	Compositional Analysis of Films for Various Sputtering Conditions	40
Table 6-2:	Table of Magnetic Data for Bubble Films	57



## ABSTRACT

This thesis presents the results of work done in the electrical engineering department of Carnegie-Mellon University. The research is in partial fulfillment of the requirements for a Master of Science degree. Films in the GdCoMoAr system were fabricated by RF sputtering and their magnetic parameters were determined using optical and graphical methods. Relationships between fabrication conditions and film composition have been determined for the CMU sputterer and the resulting values of magnetization, characteristic length, stripwidth, dominant sublattice at room temperature, quality factor, exchange constant, collapse field and uniaxial anisotropy constant were either measured or determined from static magnetic bubble parameter charts. Both fabrication and magnetic data are compared with previously published values where possible. Further modifications to the basic GdCo ferrimagnetic spin system are discussed and directions for future research are conjectured.

## INTRODUCTION

Amorphous gadolinium cobalt molybdenum argon (GdCoMoAr) thin films, have, in the past, been investigated as a possible magnetic bubble material. It was discovered by researchers at IBM that a GdCoAr system possessed sufficient uniaxial, perpendicular anisotropy so as to permit the formation of magnetic bubbles<sup>1</sup>. The ease with which compositional and thus magnetic parameter variation is induced makes these materials especially attractive to "alternative applications" that other materials cannot so easily address. For instance, in addition to its utilization as a bubble device storage layer, feasibility of this ferrimagnetic spin system from a magneto optic standpoint has been demonstrated<sup>2, 3, 4</sup>. This study represents the first step in the initiation of GdCoMoAr research here at Carnegie-Mellon University: the establishment of a fabrication procedure flexible enough to allow films of varying properties to be made.

Since the formation of magnetic bubbles is the property for which GdCoMoAr is highly touted, it is worthwhile to compare this material with the standard magnetic bubble material - garnet. Garnet is a single-crystal oxide grown on single-crystal nonmagnetic garnet substrates by the process of liquid phase epitaxy. From an economic standpoint, the necessity of using such substrates and the combined need for a number of expensive rare earth metals in both substrate and grown film push up the cost of garnets. GdCoMoAr, on the other hand, is an amorphous material sputtered onto either glass or silicon substrates. The cost of such commonplace substrates does not even approach that of gadolinium gallium garnet, the usual garnet substrate. The sputtering process is one which is well known in the semiconductor industry. Hence, it is a thoroughly studied, commonly available, rapid fabrication method. Liquid phase epitaxy, although used to grow such semiconductor crystals as GaAs, is a costly, time consuming process. From a physical point of view, GdCoMoAr systems offer other advantages: a temperature insensitivity in the submicron

bubble range and freedom from the equilibrium solubility requirements to which single-crystals are bound. The research presented herein defines the fabrication and characterization procedures related to GdCoMoAr thin films.

## CHAPTER 1

### BUBBLE MATERIAL PHYSICS

A suitable magnetic bubble material - usually in the form of a thin film - possesses magnetization perpendicular to the film surfaces. The magnetization vector,  $\mathbf{M}$ , is analogous to the polarization vector,  $\mathbf{P}$ , which arises from a distribution of electric dipoles. The divergence of the magnetization at the material's surfaces results in the formation of magnetic poles, and the resulting situation can be likened to the familiar parallel plate capacitor. When a material's magnetization vector lies along a certain axis in the minimum energy state, the material is said to exhibit anisotropy about that axis. In the case of bubble materials, this single "easy" axis is perpendicular to the film plane thus its anisotropy is designated uniaxial perpendicular anisotropy. The energy associated with uniaxial magnetic anisotropy is minimized when the magnetization coincides with the easy axis and is maximized for a  $90^\circ$  deviation from this easy axis. Directions where anisotropy energy is maximized are termed "hard" directions. The energy relationship for uniaxial anisotropy is translated into equation form below:

$$E_u = K_u \sin^2 \theta \quad (1.1)$$

$E_u$  uniaxial anisotropy energy density

$K_u$  uniaxial anisotropy constant

$\theta$  angle of magnetization with respect to the easy axis

Under conditions where no external fields are present, half the material has its magnetization pointed upward and half pointed downward; the material is in its lowest energy or demagnetized state and the net magnetic moment is zero. When viewed under a microscope in properly polarized light, a magnetic bubble material appears as a maze of light and dark stripes which are actually the magnetic domains. One observes such domains by the polar Kerr effect which is the magneto-optical technique used for highly reflective (i.e. metallic)

samples of perpendicular magnetization. When a sample is magnetized such that positive poles litter its reflecting surface, a plane polarized beam of light at  $0^\circ$  incidence emerges from the sample surface elliptically polarized<sup>5</sup>. Thus the situation can be seen as a rotation of the plane of polarization of the reflected beam by the magnetic domains; the polarized light is rotated in opposite directions by domains of opposite polarity. By adjusting the microscope's analyzer, the light and dark stripe pattern is generated.

Were it not for the presence of uniaxial anisotropy, the magnetization of a bubble film would be oriented in the plane of the film because it is here that the demagnetization energy is minimized. This is due to geometrical demagnetizing effects. In a magnetic solid without any other type of anisotropy, the magnetization tends to lie parallel to the longest dimension of that solid (shape anisotropy). A spherical magnetic solid, for example, has no preferred direction whereas a needle-like solid has shape anisotropy about its long axis. Any movement of the magnetization from this direction is opposed by demagnetizing fields which are proportional to the magnetization and whose strength depends on the sample's geometry. The energy density associated with demagnetization is expressed in the equation below:

$$E_D = - \frac{1}{2} H_D \cdot M \quad (1.2)$$

$E_D$  demagnetization energy density

$H_D$  demagnetizing field vector

It is therefore apparent that the uniaxial anisotropy competes with the shape anisotropy for the direction in which the magnetization will lie. This competition has given rise to a quantity called the quality factor for magnetic bubble films. For the magnetization of a bubble film to be oriented perpendicular to the film's surface, the anisotropy energy must exceed the demagnetization energy which is  $2\pi M_s^2 \sin^2 \theta$  for a bubble film (n.b. the angle  $\theta$  is identical to that of equation (1.1)). The quality factor<sup>6</sup>,  $Q$ , is defined below:

$$Q = E_U / E_D = K_U / 2\pi M_s^2 \quad (1.3)$$

Of course, films capable of sustaining bubbles must have a  $Q$  greater than one but in practice higher values are sought in devices for greater bubble stability.

In a magnetic material, adjacent electron spins tend to be aligned parallel or antiparallel to one another. This is a result of the quantum mechanical exchange interaction. The exchange energy associated with this interaction prevents abrupt changes in the orientations of adjacent spins. A suitable expression for the exchange energy in GdCoMoAr or other magnetic bubble films is given below:

$$E_x = A(d\theta/dx)^2 \quad (1.4)$$

$E_x$  exchange energy density

$A$  exchange constant

$\theta$  as shown in Figure 1-1

It was previously stated that the lowest energy configuration of a magnetic bubble film without any applied field is a serpentine maze of antiparallel magnetizations. The domain walls separating these regions of antiparallel magnetizations are called Bloch walls; an example of which appears in Figure 1-1. The magnetostatic or demagnetization energy of the system is reduced by these antiparallel domains in the following manner: the magnetic poles or charges littering the surfaces of a magnetic film of totally parallel magnetization would result in a high magnetostatic energy situation due to the separated, uncompensated charges. The presence of these serpentine domains puts poles of opposite polarity in close proximity on the surfaces thereby reducing energy. This reduction in demagnetization energy is reflected in the energy of the domain walls produced. The resulting wall energy may be expressed as

$$\sigma_w = 4(AK_u)^{1/2} \quad (1.5)$$

$\sigma_w$  wall energy density

The wall energy gives rise to a convenient parameter for bubble materials known as the characteristic length<sup>6</sup>. Knowledge of its value can yield information regarding the stable bubble diameter for a particular material: the stable diameter is around either eight or nine times the characteristic length depending on the film's thickness (eight times for bubble diameters equal to twice the thickness). Its relationship to wall energy is given below:

$$l = \sigma_w / 4\pi M_s^2 \quad (1.6)$$

$l$  characteristic length

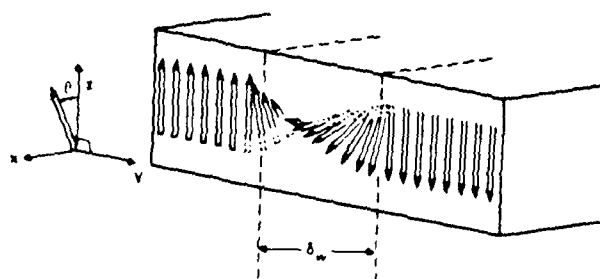


Figure 1-1: Electron Spins Within a Portion of a Bloch Wall<sup>7</sup>

The application of an external magnetic field also introduces an energy termed the magnetic field energy. The magnetic field energy density can be expressed as in the equation below:

$$E_H = -MH \quad (1.7)$$

$E_H$  magnetic field energy density

$H$  applied magnetic field vector

Thus all of the important energy terms contributing to the total energy of an amorphous bubble material have been defined. The various parameters associated with these energy terms will be cited quite frequently throughout the text of this treatise in connection with the specialized case of GdCoMoAr films.

The preceding discussion concerned magnetic bubble films without specific reference to the bubbles themselves. These will be treated briefly. Magnetic bubbles are created by applying a magnetic field perpendicular to the plane of the bubble film thereby perturbing the stripe domain energy configuration. Augmenting the applied bias field causes the stripes whose magnetization opposes the field to shrink thus increasing magnetostatic energy and decreasing wall energy. With adequately large bias fields, the stripes shrink into stable cylindrical magnetic domains whose magnetization opposes the applied magnetic field direction<sup>6</sup>; these domains are called bubbles. Their diameter is determined by minimizing the total energy consisting of magnetic field energy, demagnetizing field energy and domain wall energy. Figure 1-2 illustrates the process from the stripe domain configuration to the creation of stable bubbles.

As mentioned in the Introduction, the GdCo ferrimagnetic system is a material able to address unconventional applications. One such novel application lies in the area of thermomagnetic recording<sup>2, 3, 4</sup>; lasers can be used to read and write bubbles (data bits) into a material. It has been shown<sup>2</sup> that GdCo films having a compensation temperature (the temperature at which the magnitudes of the antiparallel Gd and Co magnetic moments become equal) in the immediate vicinity of room temperature will sustain bubbles in the absence of an applied bias field. Figure 1-3 illustrates the coercive force of a GdCo film with  $5^\circ\text{C} < T_{\text{comp}} < 10^\circ\text{C}$  as a function of temperature. The



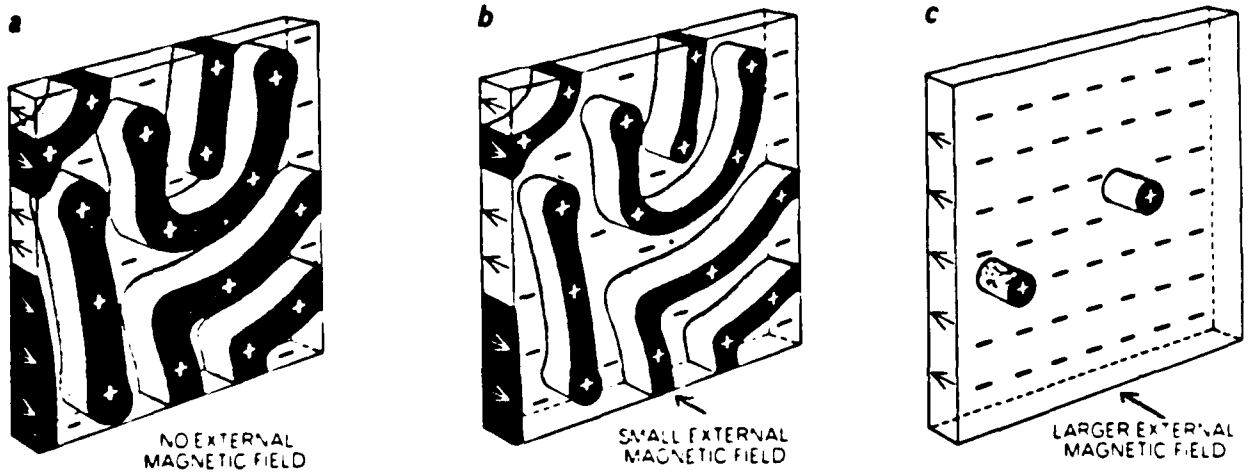


Figure 1-2: The Formation of Magnetic Bubbles Through the Application of a Magnetic Field to a Demagnetized Film<sup>8</sup>

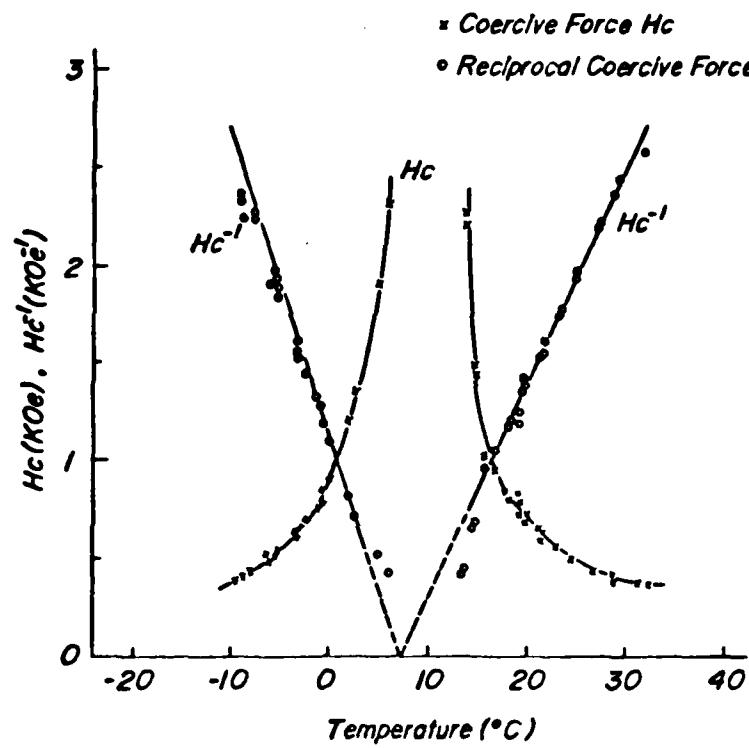


Figure 1-3: Coercive Force as a Function of Temperature for a GdCo Film<sup>3</sup>

coercive force or coercivity is half the width of a material's hysteresis loop (measured on the abscissa). In a physical sense, coercivity can be thought of as a field which pins the magnetization to a particular direction. The electronic spins will only reverse direction if an opposing field of greater magnitude than the coercive force is applied. The coercive force -  $H_c$  - goes to  $\infty$  at the compensation point thereby making the spins of a written bubble immovable. Nucleating bubbles (writing) is done by focussing the laser on a portion of the film thus raising the temperature of the irradiated area enough to significantly decrease the coercive force (moving to the right of  $T_{comp}$  in Figure 1-3). After the laser is removed, the stray fields from the surrounding material - augmented by a small applied field because of the material's low magnetization in the vicinity of its compensation temperature - induce an antiparallel magnetization in the cooling film - the bubble. The resulting bubble's diameter is a function of the laser's spot size and not of the magnetostatic, magnetic field and wall energy system minimization. A sufficient increase in  $H_c$  could also be brought about by the incorporation of oxygen, chromium or other additive into the GdCo spin system (to be discussed). Most magnetooptic research has centered on pure GdCo which has a larger Kerr angle than GdCoMo because Mo decreases the polar Kerr rotation<sup>9</sup>.

## CHAPTER 2

### BACKGROUND INFORMATION

#### 2.1 FILM STRUCTURE

The GdCoMoAr system is of interest in its amorphous thin film form - the fabrication of which will be discussed at length in a later section. The amorphous structure is desired for its advantageous magnetic properties; temperatures between 300°C and 750°C induce crystallization with higher temperatures attributed to thicker films and/or higher Gd content<sup>10, 11</sup>. The term "amorphous" usually defined as the absence of long range order at equilibrium can be misleading since a fine columnar microstructure perpendicular to the substrate has been observed in GdCoAr films<sup>12, 13</sup>. One group of researchers<sup>13</sup> has suggested that the Ar incorporated into the film during fabrication is responsible for the appropriate microstructure's growth by forming a boundary between adjacent columns. This hypothesis appears sound since GdCo films having an in-plane anisotropy develop a small perpendicular anisotropy when annealed in oxygen: fine channels of oxidized Gd delineated columns in annealed films<sup>14</sup>.

#### 2.2 FILM CONSTITUENTS

In order to understand the magnetic behavior of these films, it is important to grasp the role of each element in the material. Basically, the Gd and Co form a ferrimagnetic spin system of two sublattices. The exchange energy is minimized for antiparallel spin orientations of the 3d Co electrons and the 4f Gd electrons. It has been shown that this system complies with the Neel two-sublattice model<sup>15</sup> which predicts the variation of magnetization with temperature. The theory relates the exchange between similar (self-exchange) and dissimilar atoms to a molecular field which is proportional to the magnetization of its environment<sup>16</sup>. These proportionality constants are

determined from atomic separation distances and the quantum mechanical spin vectors of the magnetic atoms. In its simple form, this molecular field has the form shown below:

$$H_{Co} = - N_{Co,Co} M_{Co} + N_{Gd,Co} M_{Gd} \quad (2.1)$$

$$H_{Gd} = N_{Gd,Co} M_{Co} - N_{Gd,Gd} M_{Gd} \quad (2.2)$$

H molecular field of its subscript

N proportionality constant representing  
the exchange between its subscripts

M magnetization of its subscript

Whether determined theoretically or experimentally, the typical relationship between magnetization and temperature appears as in Figure 2-1. In this figure, the individual sublattice magnetizations are shown along with their combined behavior. The temperatures at which the total magnetization goes to zero are important to the designer of a magnetic bubble film: bubble devices are operated in the region where the Co sublattice moment dominates because it is here that the magnetization is most insensitive to temperature. The compensation point ( $T_{comp}$  in Figure 2-1) is that temperature at which the sublattice magnetizations cancel each other; the Curie point ( $T_C$  in Figure 2-1) is that temperature at which the thermal energy of the electrons exceeds the exchange between them resulting in a random arrangement of spins. Compositional variation allows the film designer to tailor Curie and compensation point placement. It is desirable from the standpoint of temperature insensitivity of bubble domains to tailor film compositions so as to yield optimal Curie and compensation point placement: the Curie point should be at least 150°C above room temperature, the difference between Curie and compensation points should be greater than 300°C to insure maximum flatness of the magnetization versus temperature curve, and the temperature midway between Curie and compensation points ( $T_m$ ) should be less than room temperature to maintain decreasing magnetization with temperature<sup>17</sup>. The latter point may require some clarification: if the magnetization increased with temperature then an increase in bias field would be necessary to stabilize bubbles, but the barium ferrite permanent magnets placed in the device package to produce this field have decreasing magnetization with temperature. Figure 2-2 illustrates these critical temperatures as a function of composition.

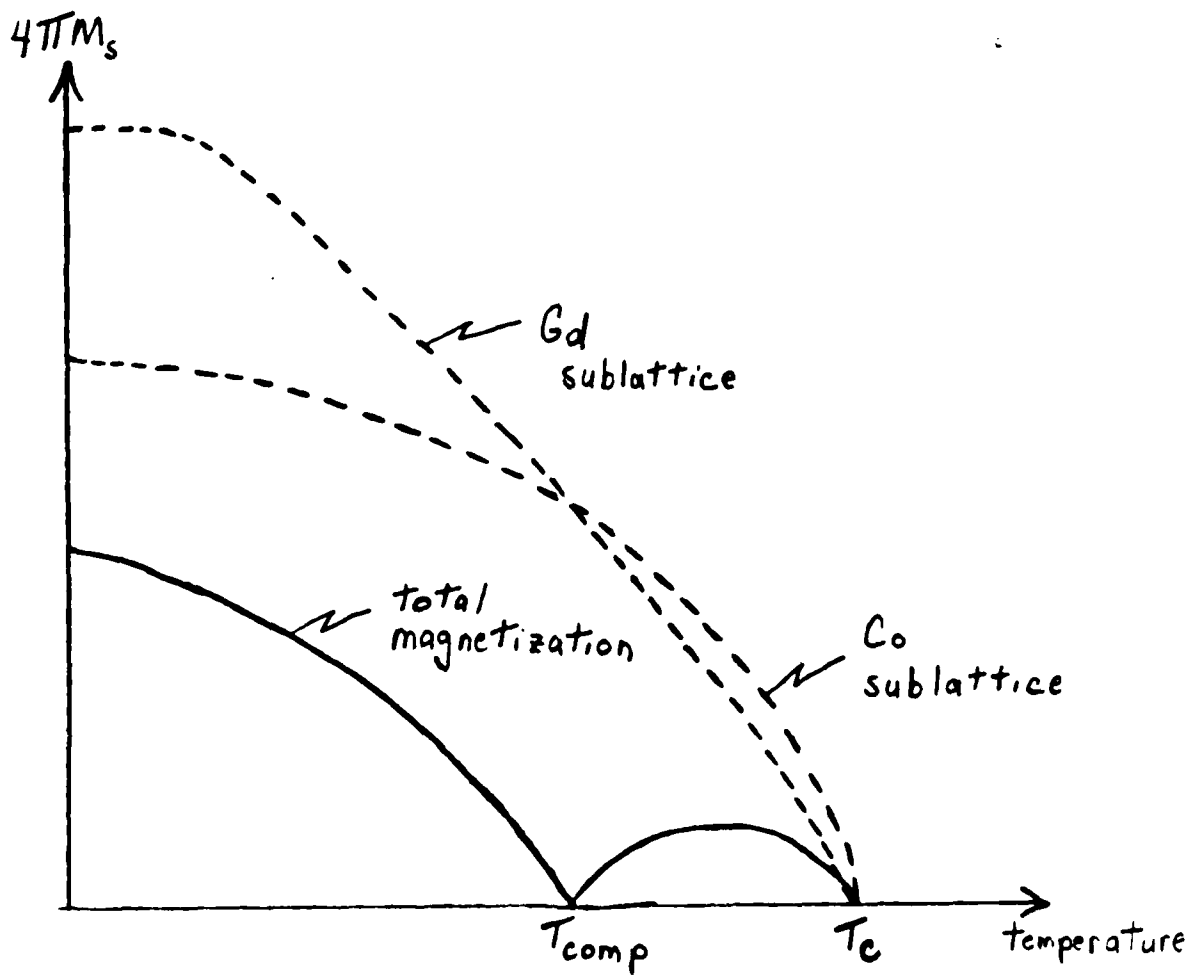


Figure 2-1: Typical Relationship Between Magnetization and Temperature for GdCoMoAr Films

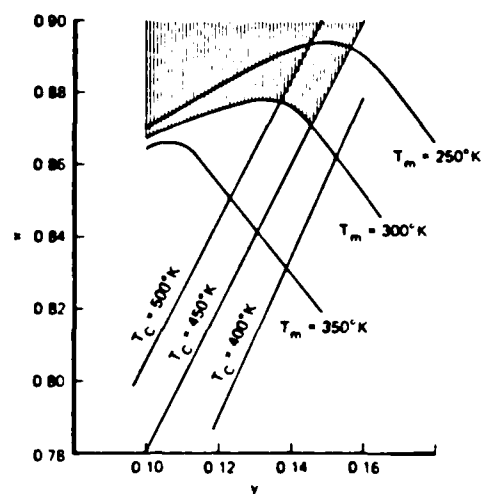


Figure 2-2: Critical Temperatures as a Function of  $(\text{Gd}_{1-x}\text{Co}_x)\text{Mo}_{1-y}$  Composition<sup>7</sup>

Temperature stability of the highly coercive GdCo films used for thermomagnetic recording applications has been found to be excellent. It has been reported<sup>2</sup> that bits written into these coercive films were stable at temperatures between -40°C and 60°C. This is due to a continuous or abrupt compositional change within the film which contains the room temperature compensation point composition. Such films also maintain written data in the presence of opposing fields in excess of 350 Oersteds (Oe)<sup>2</sup>.

In Figure 2-2, the presence of Mo is clearly seen to affect a bubble material's temperature characteristics. Mo, a nonmagnetic constituent of the system, reduces the film's overall magnetization in the temperature region where the Co moment dominates. Bozorth<sup>18</sup> gives data showing the Co moment is reduced at the rather rapid rate of  $6.5\mu_B$  ( $\mu_B$  is the Bohr magneton) per fraction of Mo atom. Such a rapid quench rate defines Mo as a spin dilutant of Co<sup>19</sup>; spin dilution involves the transfer of electrons from Mo to the 3d band of Co thereby lowering its moment<sup>15</sup>. The exchange constant, which depends on the individual atomic moments also decreases thereby lowering the Curie point<sup>20</sup>. The presence of the diluted Co also effectively increases the Gd content of the film thus causing the compensation temperature to rise.

The other non-magnetic constituent of the film - Ar - is incorporated as an inevitable by-product of the fabrication process. During sputtering, a negative bias is applied to the substrate to induce perpendicular anisotropy (discussed in previous subsection) by capturing ionized Ar during film formation. The Ar trapped within the film acts as an alloy dilutant: alloy dilution is merely the displacement of magnetic atoms by non-magnetic atoms thereby lowering magnetization<sup>19</sup>; it has been found that Ar decreases magnetization by 13.5% for every 5 atomic percent (at.%) of Ar in the film<sup>17</sup>. The increase in Ar content initiated by increasing the substrate bias does not appreciably affect the Curie or compensation temperatures<sup>17</sup>.



### 2.3 POTENTIAL FILM ADDITIVES

Aside from Mo, other elements could possibly be added to the GdCoMoAr system to "fine tune" the magnetic properties. Oxygen could be mixed with the Ar sputtering gas causing the sputtered Gd to form  $Gd_2O_3$  thus reducing the Gd content, lowering the compensation temperature and raising the Curie point. It has been found that films fabricated with oxygen had coercivities higher than films experiencing no oxygen contamination<sup>21, 22</sup>.

The other elements which are known to influence the Co moment include chromium (Cr), gold (Au) and copper (Cu); each of these will be treated briefly. Films of the GdCoCr system have been fabricated and Cr has been found to behave in a way similar to Mo. Sensitivity of the coercive force of GdCoCr to oxygen incorporation is much greater than GdCoMo: films sputtered at base pressures below  $10^{-8}$  torr (little  $O_2$  contamination) exhibited coercivities around 1 Oersted while those made around  $10^6$  torr (3-13 at.%  $O_2$  contamination) had coercivities rise to 10 Oe<sup>17</sup>. GdCoAu films demonstrate that Au is an alloy diluent of Co much the same as Ar. Au maintains a high magnetization and anisotropy by slowly lowering the Co moment while preserving temperature characteristics similar to Mo<sup>23, 24</sup>. Cu appears to be midway between spin and alloy dilution as seen by its effect on the Co moment. In GdCoCu films, a change in the Co to Cu ratio of -48% - with constant Gd concentration - reduces magnetization by 25% and increases the compensation temperature by 35%<sup>25</sup>. With the exception of Cr, all the aforementioned additives cause the anisotropy of their respective GdCo system to severely deteriorate as a result of high temperature annealing. Anisotropy changes occur in GdCoMo and GdCoCr after high temperature annealing but these changes are minimal. Typically, films experience temperatures between 200°C and 300°C during processing into devices. Decreased anisotropy results in a decreased quality factor. Therefore it is this high temperature sensitivity which makes films in the GdCoCu and GdCoAu systems inferior to those of GdCoMo; the GdCoCr system's susceptibility to high coercive forces causes it to be undesirable for bubble memory applications.

## CHAPTER 3

### THE SPUTTERING PROCESS

#### 3.1 ADVANTAGES OF SPUTTERING

Films in the GdCoMoAr system are typically deposited by sputtering although the literature also contains data for evaporated films. Therefore, before proceeding with a description of the actual sputtering process, it would be useful to outline some of the advantages of sputter deposition<sup>26</sup>:

- Film thickness is controllable by suitable adjustment of sputtering voltages and gas pressure.
- There are no difficulties with the ejection of larger agglomerates which often occurs in vacuum deposition.
- Unique properties of the sputtered materials can be brought forth through biasing of the substrate.
- Several materials can be deposited atop one another without breaking vacuum.
- Multi-component compounds can be created from single element sources without regard to vapor pressure disparities among the materials.

The main disadvantage to the sputtering process is that deposition rates tend to be relatively low. Yet, the advantages of sputtering films have earned it a place in a number of the procedures for semiconductor and magnetic bubble device processing.

### 3.2 AN OVERVIEW OF THE PROCESS

The simple schematic in Figure 3-1 shows the basic D.C. sputtering configuration. The material to be sputtered is attached to the target assembly which is in turn connected to the negative terminal of a D.C. power supply. A suitable substrate for the desired film is placed directly beneath the target. The sputtering chamber is evacuated to a predetermined pressure and then backfilled with an appropriate gas - usually an inert gas is used when no chemical reactions are sought. To begin the process, a low pressure electrical discharge (glow discharge) is ignited to induce ionization of the introduced gas (plasma). The negatively biased target is bombarded by positive ions from the plasma with energies in the 0.1 to 1.0 keV range<sup>27</sup>. Through an exchange of momentum, target atoms are knocked loose; some of which will fall onto the substrate to form the film. The discharge is sustained by the plasma electrons of energies in the 0.1 to 1.0 keV range<sup>27</sup> which ionize the sputtering gas. The sputtering apparatus just described is called diode since the negatively biased target forms a cathode of the electrical discharge.

D.C. methods cannot be used to sputter nonconducting targets because of positive charge accumulation on the target surface due to ion bombardment. The difficulty can be overcome by using radio frequency (RF) sputtering - the type used to fabricate GdCoMoAr at CMU. A schematic of an RF diode sputterer is shown in Figure 3-2. In this configuration, the electrodes reverse anode/cathode roles at times during each half cycle. The discharge is operated at a frequency (13.560 MHz) that is sufficiently high so that significant charge accumulation does not occur when an electrode is cathodic. Maisel<sup>26</sup> gives an account of the plasma's behavior during sputtering. At the MHz operating frequencies, the massive ions' low mobility makes them move much more slowly than the electrons. As the electron cloud approaches one electrode, the other electrode is left with a predominance of positive ions in its vicinity which takes up the applied electrode voltage and a situation similar to the D.C. case occurs. Due to the capacitive nature of the electrode placement, the total current (ions + electrons) to a given electrode must be zero. However, since electronic mobility exceeds the ionic, the electron cloud need approach a given electrode for a very short time during each half cycle to balance the ion current. Thus, in steady state, both electrodes develop a D.C. bias relative to the plasma potential (set equal to zero in most analyses) such that the

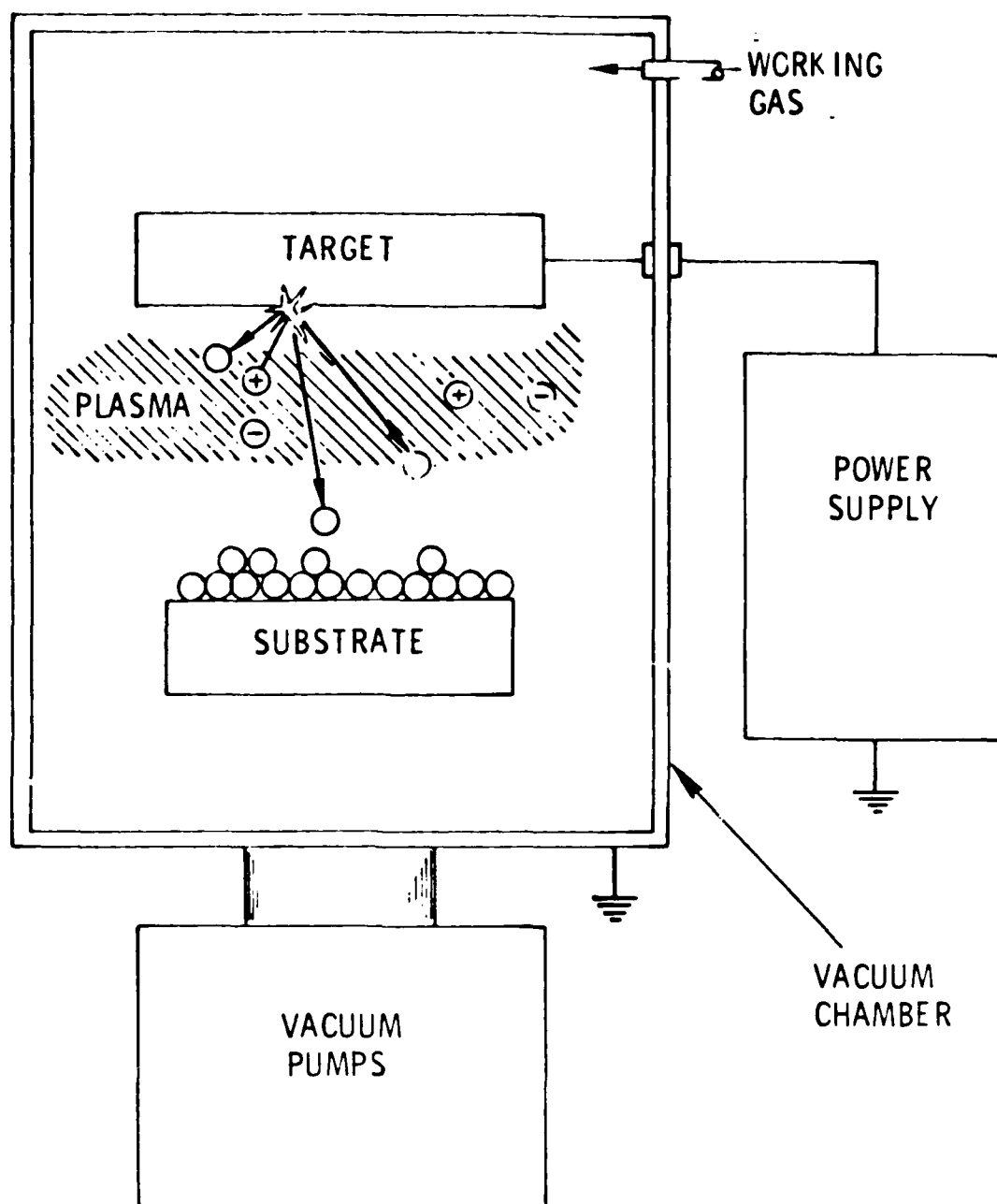


Figure 3-1: DC Sputter Configuration<sup>27</sup>

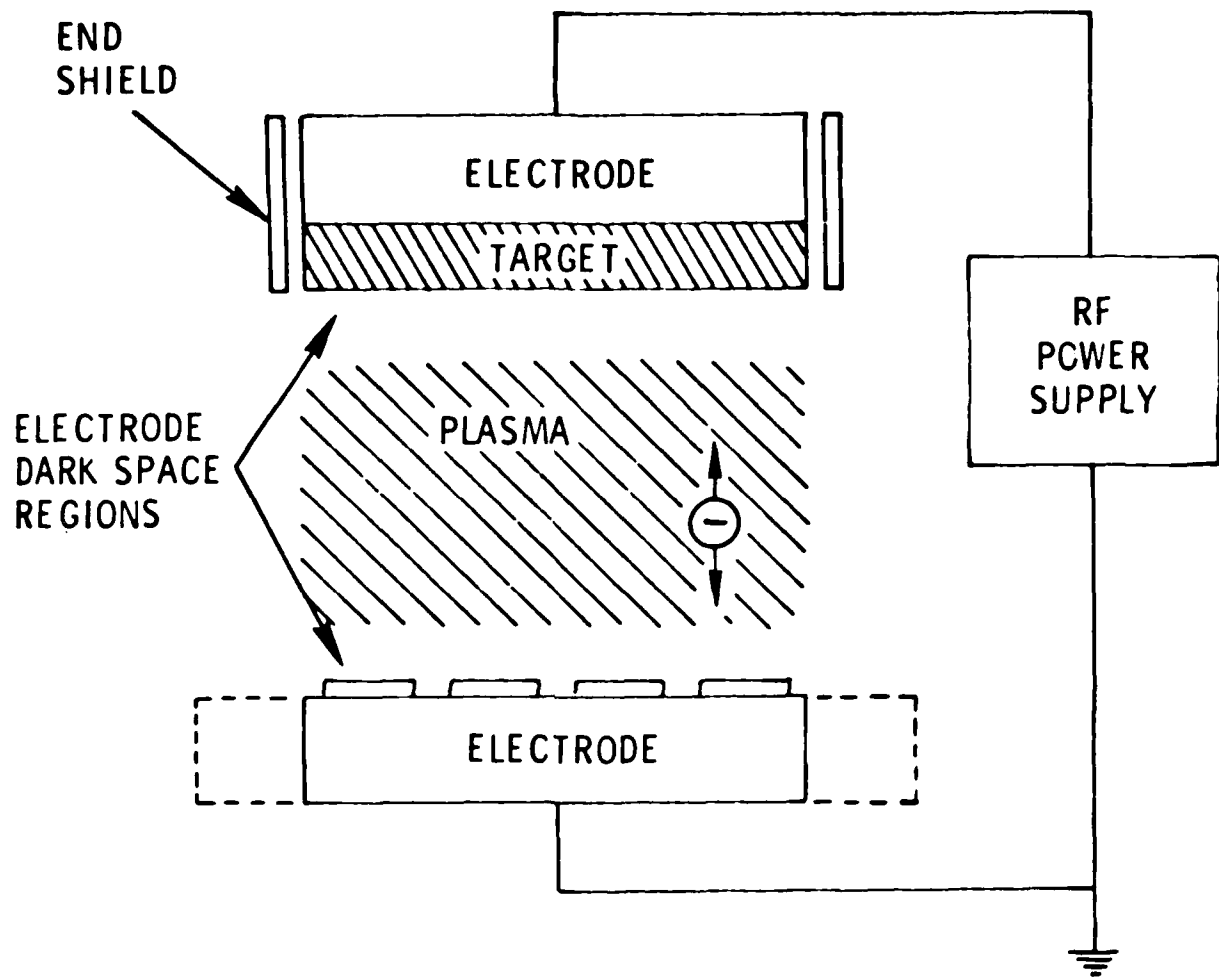


Figure 3-2: RF Sputterer Configuration<sup>27</sup>

electrodes approach or exceed the plasma potential for very short periods. This is shown in Figure 3-3. From this diagram, it can be seen that the maintenance of negative DC potentials at both target and substrate, which nearly equal their respective RF potential amplitudes, relative to the plasma implies continual sputtering at both electrodes.

For many applications, a substrate potential equal to that of the plasma is sought so that the composition of the deposited film will not differ from that of the target due to film resputtering: target elements having the highest sputtering yields - the number of target atoms ejected per incident ion - will be resputtered off the substrate in the greatest numbers. If compositional changes in the film are sought through resputtering, a small bias is applied to the substrate and the process is termed bias sputtering. Figure 3-4 illustrates the bias sputtering process. For bias sputtering, an impedance is added to the substrate electrode circuit so that the potential of this electrode can be controlled. The structure of the deposited film is also changed both by the ion bombardment damage and the incorporation of Ar into the films. Damage to a film by ion bombardment results from the kinetic energy of the incident Ar ions which alters the film's microstructure from that of a film sputtered with no substrate bias. Ar incorporation results from the trapping of the sputtering gas by the layers of depositing target atoms. At very high substrate biases, resputtering can occur at rates sufficient to release this trapped Ar.

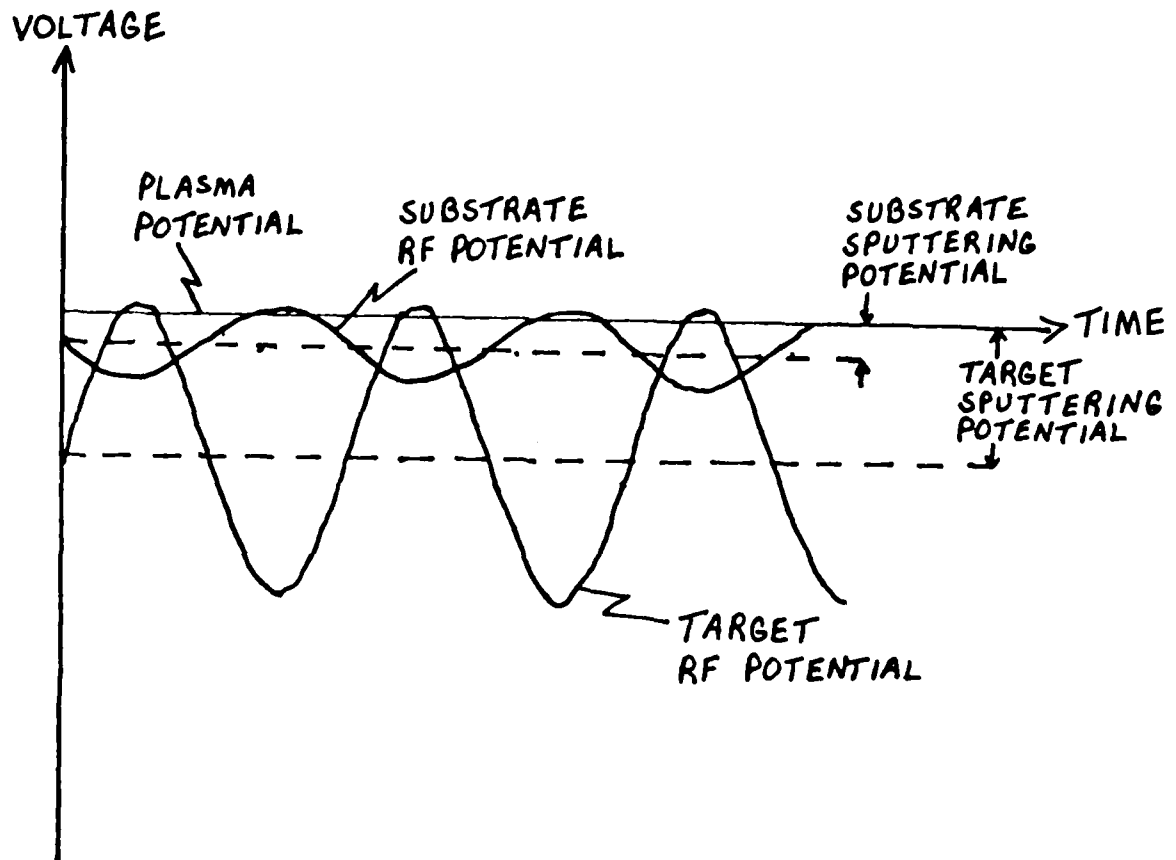


Figure 3-3: Schematic of Potentials in RF Sputtering

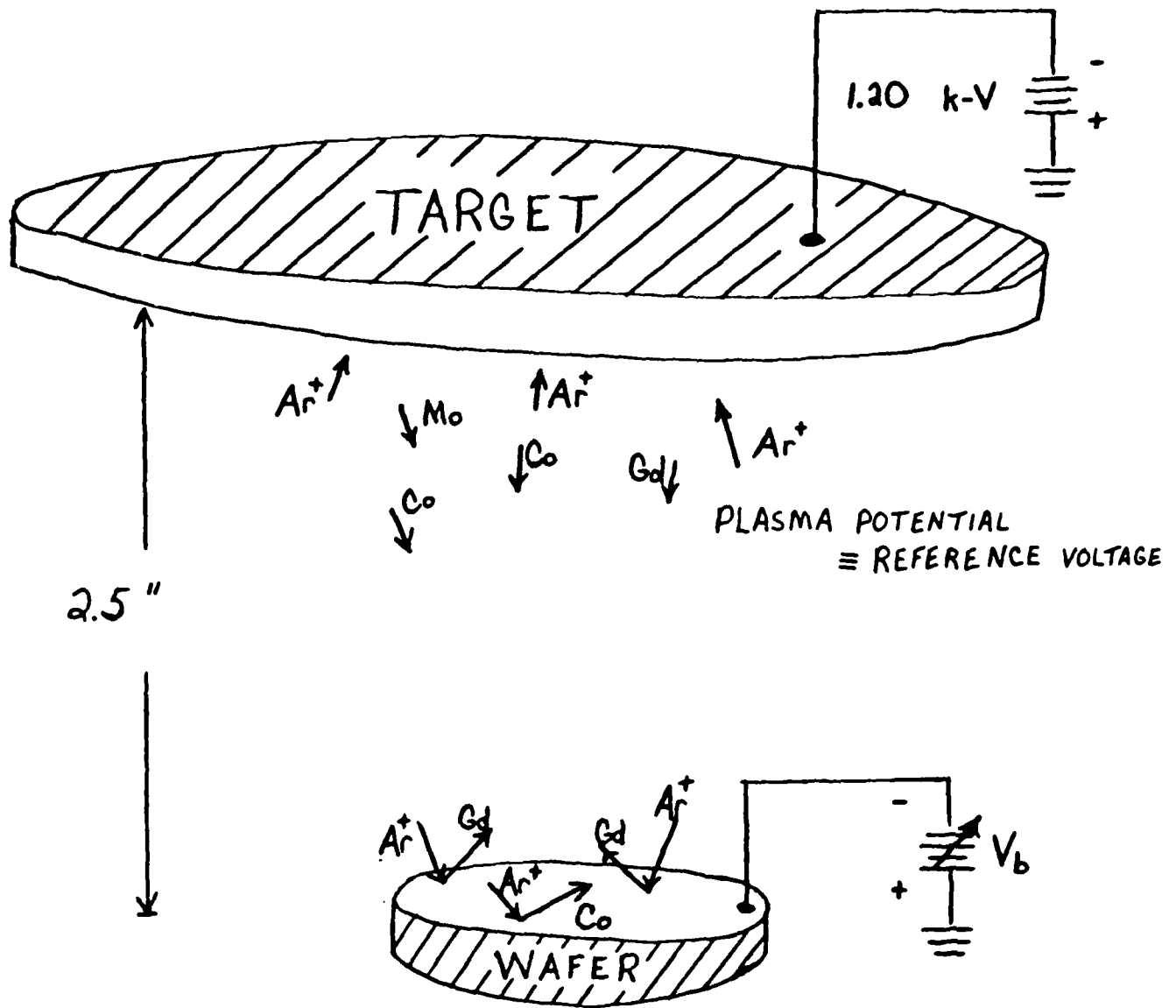


Figure 3-4: Illustration of Bias Sputtering



## CHAPTER 4

### SPUTTERING THE AMORPHOUS FILMS

#### 4.1 FABRICATION FACILITIES

The GdCoMoAr films fabricated at CMU were sputtered on a Perkin Elmer 2400J RF diode sputterer with a capacity of three six inch targets. The system is not equipped with a load lock option and must be pressurized to atmosphere to insert substrates and/or remove films. A roughing pump is used to initially lower the pressure in the sputtering chamber after which an Air Products cryogenic high vacuum pump lowers the chamber to pressures on the order of  $10^{-7}$  torr. Cooling for the target and substrate table during sputtering is provided by filtered, city tap water with a flow rate as high as 2 liters/minute; the temperature of this water and thus the degree of cooling is dependent on the season. Ar is the only sputtering gas used and its purity is rated at 99.999%.

The mechanism by which low base pressures are attained is the cryogenic pump. This system is akin to a refrigerator and uses helium under high pressure to maintain temperatures as low as 15K within the pump. Upon exposure to the interior of the sputter's bell jar, gases are frozen in the cold regions of the pump. Repeated pumpdowns during the normal routine of sputtering result in temperature increases within the pump as gases build up; the temperature of the cryogenic pump may be read from a gauge on the pump's exterior. The temperature will rise during sputtering as the introduced Ar is removed but consistent readings of temperature over 18K with no Ar in the system have been found to lengthen pumpdown times. Also, high cryogenic pump temperatures could cause unwanted impurities in sputtered films: the high temperatures produced during the sputtering process release absorbed gases from the sputterer's interior and only a cryopump in good operating condition can mitigate contamination of films. A regeneration

procedure involving the return of the cryopump to room temperature effectively restores the pump to peak operating performance.

As previously stated the roughing pump, a mechanical pump which utilizes special oil for its operation, initially lowers the system's pressure before the chamber's exposure to the cryopump. The crossover pressure between these pumps is an important consideration. A high crossover pressure - between .150 and .200 torr - imparts a greater load on the cryopump thus lessening the time between regenerations. On the other hand, a low crossover pressure - between 0.040 and 0.050 torr - could induce a backfill of roughing pump oil or the oil's more volatile components into the sputtering chamber if a xylene valve is not present between chamber and pump<sup>28</sup> (the CMU system has no such valve). The films described in this thesis were fabricated using high crossover pressures in light of the danger of film contamination.

The desired magnetic properties of GdCoMoAr are dependent on its amorphous structure. The high temperatures encountered by the films during bias sputtering create the potential for crystallization if adequate substrate cooling is not provided. Beneath the surface of the table on which the substrate rests is a water well connected in series with similar wells behind each target. Water into the system passes through a special filter before reaching these wells. This filter must be kept very clean for maximum throughput especially in the warmer months since no heat exchanger is present to cool the incoming water. In addition, since the water connects serially, the flow rate can be seriously altered if detritus, which builds up over long periods of time in the water wells, lodges in the lines. Substrate cooling will be discussed further on in this chapter.

Recently, Jim Fury, a member of the technical staff at the General Electric Research and Development Center in Schenectady, New York, and the author used an MKS Baratron capacitance monometer to measure Ar pressures within the sputtering chamber. The monometer readings were compared with those of the Perkin Elmer thermistor gauge present on the system. The results of this comparison are shown in Table 4-1. The salient lack of correspondence between the devices and the fairly large spread of thermistor readings at lower pressures should serve to caution those sputtering films sensitive to Ar pressure as the monometer's high accuracy contributes to its wide use as a

Perkin Elmer Thermistor ( $\mu\text{m Hg}$ )	MKS Capacitance Monometer ( $\mu\text{m Hg}$ )
1	$4.04 \pm 0.06$
2	$5.11 \pm 0.91$
3	$6.51 \pm 0.84$
4	$7.92 \pm 1.10$
5	$9.38 \pm 0.88$
6	$10.9 \pm 1.1$
7	$12.5 \pm 0.8$
8	$13.9 \pm 0.9$
9	$15.2 \pm 0.9$
10	$16.1 \pm 0.3$
20	$29.5 \pm 0.5$
25	$36.2 \pm 0.1$
30	$42.8 \pm 0.7$
35	$50.0 \pm 0.8$

Table 4-1: Comparison of Ar Pressures Measured with a Perkin Elmer Thermistor Gauge and an MKS Capacitance Monometer

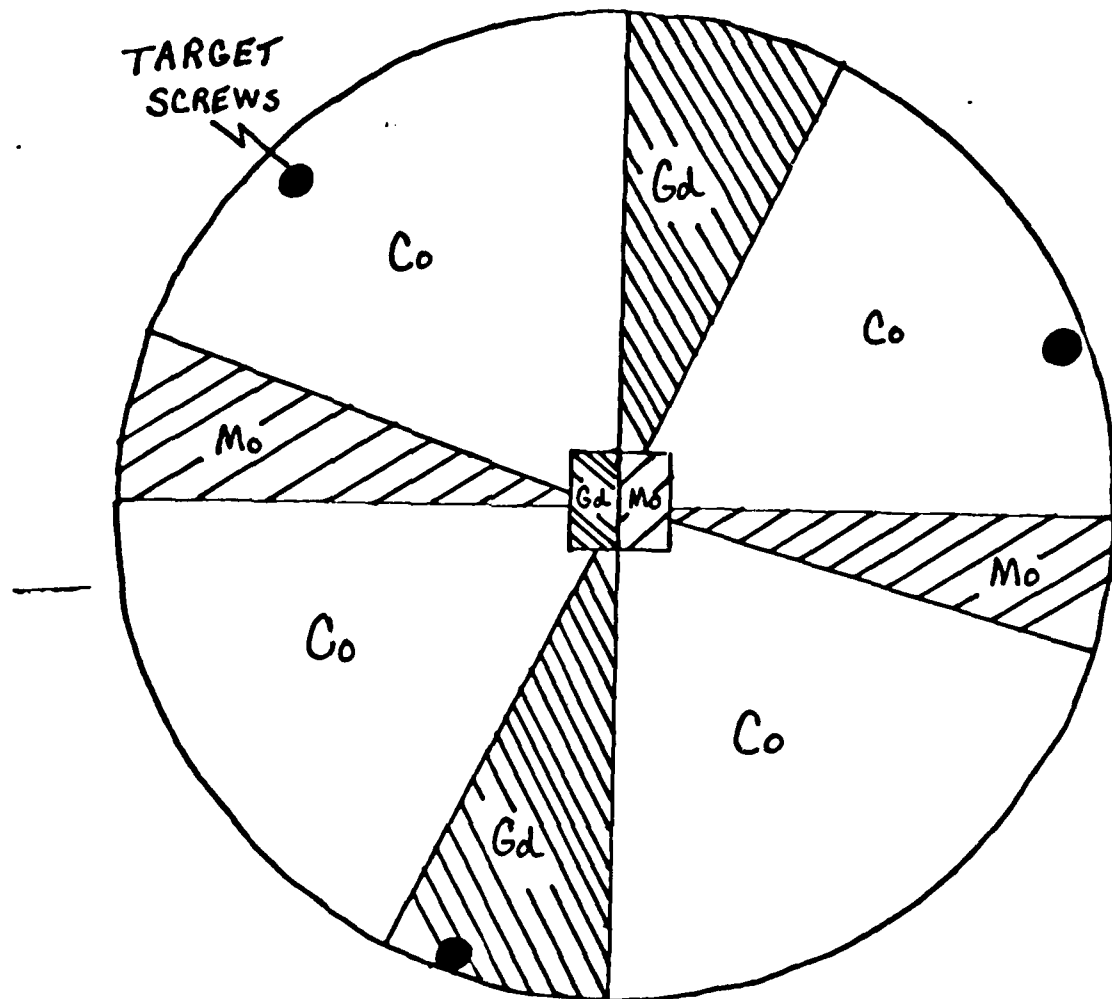
standard. In the remainder of this thesis, Ar pressures quoted in experimental results are uncorrected and represent the Perkin Elmer thermistor gauge reading.

#### 4.2 TARGET FABRICATION

The sputtering targets used for the films described herein were composites of foils of the individual elements attached to a Cu backing plate which is in turn screwed to the sputterer's target assembly. This arrangement was chosen to facilitate changing target composition - a parameter which is initially difficult to determine.

The circular Cu backing plate was 5.876 inches in diameter and 1/8 inch thick. The elemental foils were each 0.01 inches thick. Co strips measuring 6 inches by 1 inch were first laid over the backing plate completely covering it. Atop the Co, two right triangular sections each of Gd and Mo, cut with "tin snips", were attached. To fasten these foils, Epoxy Technology's Epo-Tek 3021 dual component, thermally conducting, silver epoxy was used. The two layers were laid down separately. Heat is required to cure this epoxy and a temperature of roughly 125°C has proved to be adequate. After applying one layer of the target, a piece of Al is clamped down over the assembly and placed in an appropriate oven for one hour. Two cautions are in order: the curing epoxy emits gaseous acetic acid among other things thus requiring that the oven be ventilated to curtail pressure buildup; after removing the target from the oven, allow it to cool completely before unclamping the Al sheet since the epoxy does not harden until cool. Upon completion of the foil attachment process, the excess material may be removed with a band saw and the screw holes punched out. A schematic of the completed target is shown in Figure 4-1. This figure shows that the tips of the Gd and Mo triangles have been truncated and replaced by a square whose area equals the area of the lost materials. By doing so, the problem of curing epoxy being squeezed out from beneath the "hard-to-glue" tips is circumvented.

To insure the integrity of the epoxy under high sputtering temperatures, Dow Corning high vacuum grease is applied between the backing plate and target assembly for intimate thermal contact. The grease is easily removed with isopropyl alcohol (ipa). Before sputtering any films, the target epoxy must be



APPROXIMATE COMPONENT SURFACE AREA :

Co  $\Rightarrow$  58%

Gd  $\Rightarrow$  26%

Mo  $\Rightarrow$  16%

Figure 4-1: Target Schematic

completely outgassed by presputtering. An RF power of 300W and an Ar pressure of 0.03 torr for 4 hours has worked very well in this regard.

#### 4.3 GdCoMoAr FILM FABRICATION

The optimal multicomponent film would possess a homogeneous composition throughout its volume. A target configuration such as that shown in Figure 4-1 will not yield such a film unless the substrate is subject to complex rotation during sputtering. Since such a feature is unavailable on the Perkin Elmer 2400J, other methods to partially homogenize composition were employed: the target-to-substrate distance was stretched to its limit and high Ar pressures were used. A large target-to-substrate distance should result in sputtered atoms undergoing more collisions with gas ions prior to their reaching the substrate thus homogenizing the film; high sputtering gas pressures increase the chances for such collisions to occur. These high Ar pressures also tend to increase anisotropy ( $K_U$ ) dramatically in GdCoMoAr<sup>21</sup>. As seen in Figure 4-2, maximum  $K_U$  - and thus  $Q$  - is achieved at the point of greatest Ar incorporation. Three plots made at Ar pressures of 10 millitorr (mtorr), 25 mtorr and 50 mtorr are shown. It is evident from these graphs that the lowest Ar pressure studied results in an anisotropy peak at a higher bias voltage than the other pressures. Since substrate heating is a function of bias voltage, these low sputtering pressures are undesirable. The 25 mtorr and 50 mtorr plots show  $K_U$  peaks at nearly equivalent substrate biases with a greater peak height at 50 mtorr. Since the difference in peak height is small, consideration of the efficacy of very high Ar pressures can be given. Such pressures will lessen the time between cryopump regenerations hence unnecessarily increasing sputterer downtime. In light of this fact, the pressure of 30 mtorr was chosen as the exclusive value to be used: it was close to the highest commonly used pressure on the system and published composition data at 30 mtorr simplified cross-checking with the literature. It should be mentioned that the monotonic decreases in Ar content are caused by enhanced substrate resputtering at the highest biases.

The fact that the target is screwed into the system's assembly introduces the problem of impurity introduction from these screws. To prevent contamination, an Al aperture was installed between target and substrate. The aperture, a disk with a 3.25 inch hole cut out of its center, is electrically

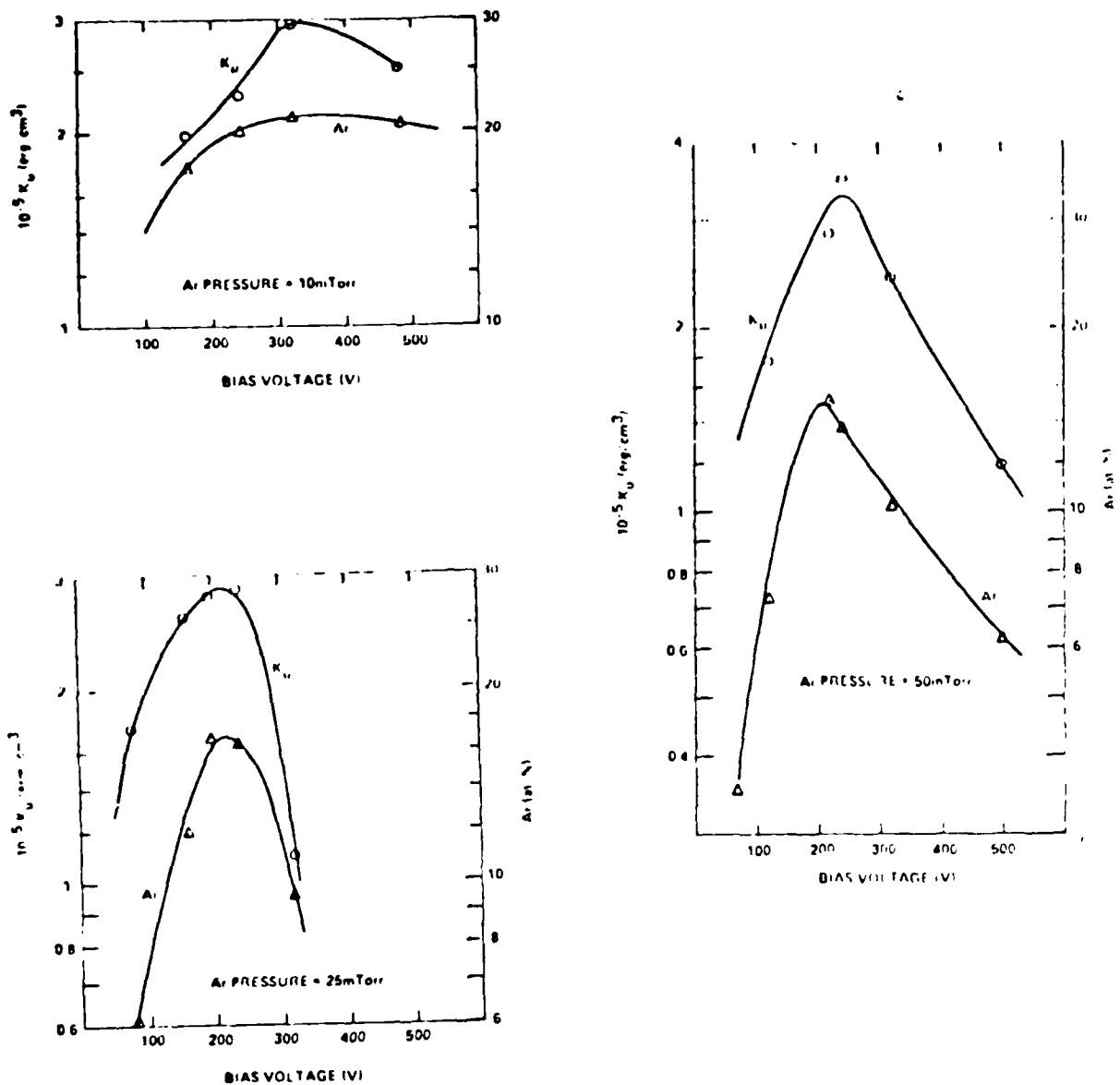


Figure 4-2: Plots of Ar Content and  $K_u$  vs. Substrate Bias<sup>29</sup>

connected to the sputtering chamber thereby precluding Al sputtering. However, significant accumulation of sputtered material and its array of unspattered oxides do cause contamination through the adsorption of water vapor as demonstrated by unusually long pumpdown times when apertures go uncleaned.

The base pressure at which sputtering is started will affect the overall properties of the deposited film. As stated in section 2.3, oxygen contamination is augmented at high base pressures. Since no study of film characteristics as a function of base pressure was sought, most films were fabricated at base pressures around  $6.0 \times 10^{-7}$  torr.

As mentioned in the previous section, substrate heating during deposition is detrimental to the amorphous structure as well as the magnetic properties of GdCoMoAr. Though one is unable to vastly improve substrate cooling beyond revamping the sputterer's cooling system, the establishment of intimate thermal contact between substrate and substrate table improves the efficiency of a system's cooling capability. The application of a thin layer of gallium (Ga) to the back of the substrate has proved to be an effective thermal link<sup>21</sup>. A melting point of approximately 30°C allows the Ga to be spread with a metal spatula and to be removed - after heating 60 seconds at 125°C - with an ipa-soaked cotton swab. The Ga is spread in a circular area concentric to the round substrates leaving a 0.25 inch annulus between Ga and wafer edge to prevent contamination of the film during fabrication.

Dow Corning 0211 cover glasses were the exclusive substrate used for the films described herein. The choice of this glass was based on several considerations: availability, optical purity (an implication of surface cleanliness), dielectric nature (for optimum field absorption during magnetic parameter measurement) and track record as GdCoMoAr substrates<sup>20</sup>. The cleaning procedure for these substrates involves their immersion in a heated surfactant solution such as Micro soap or Joy dishwashing liquid, subjection to heated ultrasonic cleaning for 5 minutes and a plasma ashing with purified air at 250W and 1 torr. The plasma asher is a system which uses an ionized gas to polymerize hydrocarbons whose presence is harmful to the sputtered film.

The fabrication of pure films implies cleanliness of both target and substrate



AD-A131 706

A PROGRAM OF RESEARCH ON MICROFABRICATION TECHNIQUES  
FOR VLSI MAGNETIC DEVICES(U) CARNEGIE-MELLON UNIV  
PITTSBURGH PA M H KRYDER ET AL. 01 OCT 82

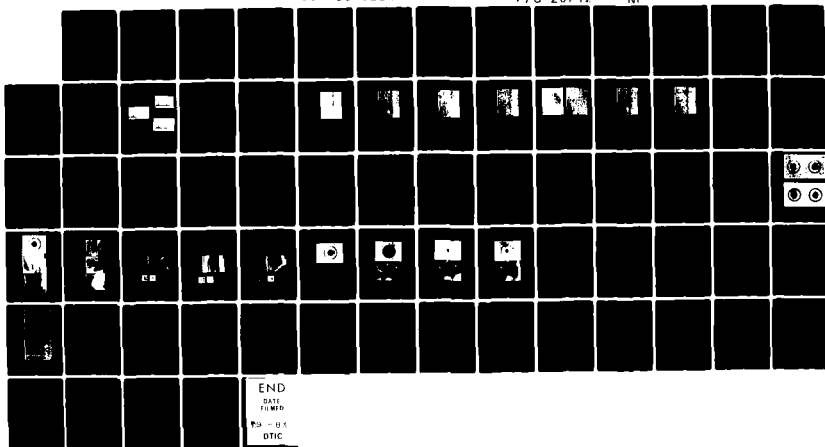
3/3

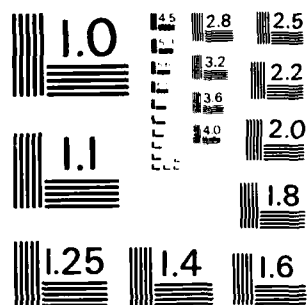
UNCLASSIFIED

AFOSR-TR-83-0685 AFOSR-80-0284

F/G 20/12

NI





MICROCOPY RESOLUTION TEST CHART  
NATIONAL BUREAU OF STANDARDS-1963-A

table. Repeated exposure to atmosphere causes surface oxidation of target materials; Gd is by far the most reactive in this respect. Such oxides are removed immediately prior to sputtering a film by presputtering the target with the intended substrate and table across the chamber from the target position. It has been found that an RF power of 300 W and Ar pressure of 30 mtorr for 30 minutes works well. Usage of the sputterer by others depositing other materials necessitates the cleaning of the substrate table to avoid contamination. Impurities mentioned in section 2.3 such as Au and Cr are commonly sputtered in the CMU system and could prove troublesome when sputtered off the table during bias sputtering. Therefore, at the outset of a block of runs, the table should be sputter etched at 500 W and 10 mtorr for one hour. The color of the Ar plasma can serve as a direct indication of target or table cleanliness. Blue is the characteristic color of the Ar plasma with the presence of a blue plasma being an implication of the absence of significant amounts of impurity gases. The color, red, indicates the presence of oxygen in the plasma and is the initial color during presputtering.

The tendency for these materials, Gd in particular, to develop oxides while attached to the target carries over to the films. These oxides manifest themselves as a cloudy magnetooptic image of the microscopic stripdomain configuration or, in the worst case, as white discolorations over the film's surface. Usually discoloration can be traced to in-system contamination such as exposed epoxy but surface oxidation sufficient to destroy the magnetooptic view is normal under atmospheric conditions. The application of an  $\text{SiO}_2$  overcoat to films prior to their exposure to atmosphere has been found adequate to curtail this phenomenon. An RF power of 150 W at 10 mtorr Ar for 5 minutes produces an approximately 0.21 micron ( $\mu\text{m}$ ) overcoat. To optimize the magnetooptic effect, it is desirable that the overcoat's thickness correspond to  $\frac{1}{4}$  of the wavelength of the light used to observe the stripdomains.

## CHAPTER 5

### CHARACTERIZING THE AMORPHOUS FILM

#### 5.1 DETERMINATION OF FILM COMPOSITION

Electron microprobe techniques were the exclusive means by which compositional analysis was performed. The author did not personally do the measurements rather the analysis was carried out at the General Electric Research and Development Center. In brief, the electron microprobe operates by exciting inner electrons of the sample atoms with a high energy electron beam. These excited electrons emit characteristic x-rays which are analyzed to determine the type of atom from which they came. Results are in the form of weight percents which are easily converted into atomic percents. Throughout this thesis, all compositions are given in atomic percentages.

#### 5.2 THICKNESS MEASUREMENT

Knowledge of a sputtered magnetic material's thickness is crucial to a proper understanding of its magnetic properties. This parameter was determined through the use of a Dektak stylus device which measures the height of an etched step. The precision of a thickness measurement is dependent on the steepness of the etched step. In practice, either "holes" are etched in small portions of the film or hillocks are etched out; the choice is up to the discretion of the experimenter. In any case, thicknesses herein were measured by placing the Dektak's stylus atop the film and allowing it to drop off the step. The resultant step height is recorded on a strip chart.

Etching the particular step is accomplished by masking portions of the film to be saved and dropping the film in a solution to which the film is susceptible and the substrate inert. The principal masking material has been a black wax which is dissolvable in and reconstitutable from trichlorethylene

(TCE). Normally, a small chunk is mixed with sufficient TCE to yield a workable solution and a thin layer spread over the film. After the TCE has completely evaporated, the sample can be inserted into the etchant. The wax is easily removed by a TCE dip. Photoresist (1350J) can also be used as a masking material: it is spun onto the sample, the blunt edge of a single-edged razor blade is dragged across areas where holes are desired, the sample is baked at 125°C for ten minutes and the sample is etched. Photoresist is removed by immersion in acetone. The author has shied away from this procedure because of the necessary extended heating of the sample.

The etchant used throughout the course of experimental work has been a 1:3 solution of nitric acid ( $\text{HNO}_3$ ) and water. The reaction takes place approximately 45 seconds after immersion and, coupled with a black wax mask, yields nice steps. Should one wish to determine the thickness of an  $\text{SiO}_2$  overcoated film, the oxide must be removed from the sample's surface (n.b. insertion of an overcoated film into the etchant solution provides valuable insight into the condition of the  $\text{SiO}_2$  film). The standard oxide etchant, hydrofluoric acid (HF), is both dangerous and harmful to the glass substrate. In lieu of this, a 3% solution by weight of ammonium bifluoride and water has been found most effective. The soaking of a slip of 0211 glass in this solution over a twelve hour period has produced no discernable change in its weight or appearance<sup>28</sup>.

### 5.3 MAGNETIC MEASUREMENTS

#### 5.3.1 DETERMINATION OF MAGNETIZATION, CHARACTERISTIC LENGTH AND DOMINANT SUBLATTICE

Fowles and Copeland<sup>30</sup> developed a rapid method for determining the magnetization and characteristic length of a magnetic bubble film and it is this method that is used here, exclusively. Film thickness, bubble collapse field and domain period of a straight domain configuration are the only parameters needed. Observation of stripes and bubbles was done on a Leitz Orthoplan polarizing microscope with TV camera, monitor, magnetic field coils (parallel and perpendicular fields) and still camera attachment. A variety of lenses are available but pictures appearing in this treatise were made with either 50X or

100X lenses. The straight domain configurations mentioned are generated by applying an alternating perpendicular field for short periods. The domain period ( $P_o$ ) is merely the total width of a light and dark stripe pair. The bubble collapse field ( $H_{coll}$ ) measurement requires that bubbles be nucleated in the film and this is easily accomplished. The application of an in-plane field to a demagnetized film (i.e. in a hard direction) will cause the stripdomains to form a bubble lattice<sup>31</sup>. The magneto-optics laboratory possesses a device which applies a high in-plane field pulse to the film (this device works by capacitive discharge). Bubble lattice generation by this method does not require a pulsed field, only a field of sufficient magnitude. It has been noted that this device does not have sufficient power to generate such a lattice in high magnetization GdCoMoAr films. Instead, a straight domain configuration is formed. In such cases, the film should be placed in an x- or y-oriented in-plane field within the microscope's coils where a higher in-plane field is attainable. The microscope set-up includes apparatus for obtaining quantitative field measurements. Appropriate tables containing values of  $l/h$  and  $H_{coll}/4\pi M_s$  for various values of  $P_o/h$  give the sought after results<sup>30</sup>.

Knowledge of dominant sublattice magnetization and thus whether  $T_{comp}$  is above or below room temperature can be determined optically. A film of known dominant sublattice is saturated in a perpendicular field with a note made of its color (light or dark), the microscope's polarizer setting and the orientation of the film (film side up or down). Other films viewed at the same polarizer setting and orientation which have the same dominant sublattice display the same color as the reference since the dominant sublattice moment follows the applied field direction. The other color is noted for dissimilar dominant sublattices.  $Co$  is solely responsible for rotation of the light's plane of polarization due to its significantly larger Kerr angle<sup>4</sup>.

### 5.3.2 DETERMINATION OF THE UNIAXIAL ANISOTROPY CONSTANT

The static magnetic bubble parameter chart<sup>17</sup> (to be seen in the next chapter) is the exclusive method used for determining a value of the uniaxial anisotropy constant. In using this graphical aid, the values of  $4\pi M_s$  and  $l$  were measured; the value of  $A$  was estimated; and the value for  $Q$  and  $K_u$  were read off the chart. As seen in Figure 5-1, it is not unreasonable to assume an exchange

constant between  $2.0 \times 10^{-7}$  and  $4.0 \times 10^{-7}$  erg/cm for GdCoMo bubble films, thus making use of the parameter chart convenient. Ar is assumed to have a negligible effect on the exchange constant and is not considered in Figure 5-1. The presence of other impurities in the author's films allows only reasonable estimates of A to be made from the known values of  $4\pi M_s$  and I with Figure 5-1 used merely as a guide. Therefore, the values obtained for  $K_u$  should be regarded as estimates of the true value. The completed charts for several samples are given in the following chapter.

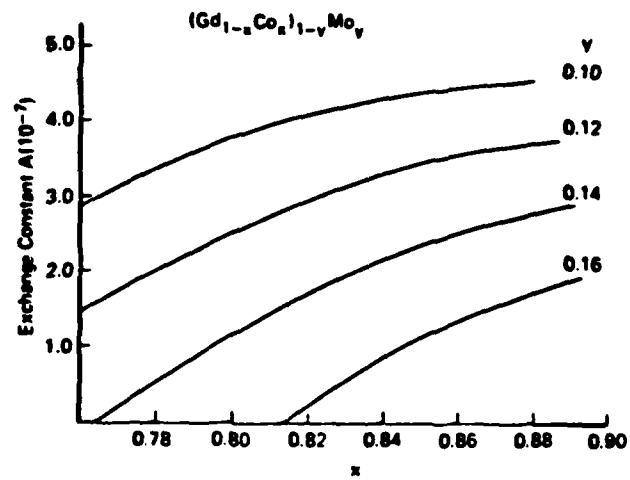


Figure 5-1: Exchange Constants (in erg/cm) for Various  $(Gd_{1-x}Co_x)_{1-y}Mo_y$  Films<sup>7</sup>



## CHAPTER 6

### RESULTS AND DISCUSSION

#### 6.1 COMPOSITION DATA

Herein is presented the results of microprobe analysis on various films made for this study. The films, their sputtering conditions and compositions are listed in Table 6-1. An explanation of the cataloging procedure is in order: the first group of numbers represents the date on which the particular film was made, the letter merely separates films made the same day, the number following a letter represents the target configuration used to fabricate a set of films and the presence of an asterisk (\*) signifies that the sample was overcoated prior to its removal from vacuum. Compositional data is not listed for overcoated films because these were originally intended for ferromagnetic resonance experiments and are duplicates of microprobed films.

It is correct to assume that those films made before July 1981 contain concentrations of Cu. This is due to the fact that the original target configuration (#1) did not occlude the Cu backing plate completely. At that time, it was believed that the presence of the aperture would prevent Cu contamination. Although the aperture did stop most of the Cu from reaching the film, there is strong evidence for the supposition that the heat in the vicinity of the target during sputtering is sufficient to cause some Cu evaporation off the "dirty" aperture and into the film. Complete coverage of the target and regular maintenance of the aperture eliminated contamination problems. For the purposes of compositional analysis, the quantity of Cu present in a film was equally divided among the desired constituents. The reasoning behind such a move is the assumption that each atom of Cu displaces an atom of Gd, Co and Mo thus the ratios of the latter elements are preserved. The Co/Gd and Co/Mo versus substrate bias are shown for two sets of films in Figures 6-1, 6-2, 6-3 and 6-4. It is evident that the Co/Gd

sample	substrate bias (V)	deposition time (min)	average % Co	average % Gd	average % Mo	average % impurities
51681A1	0	60	57.39	17.83	11.21	13.57 (Cu)
51681B1	20	60	58.80	17.90	11.41	11.89 (Cu)
51781A1	80	60	67.01	12.84	13.19	6.95 (Cu)
51781B1	50	60	65.27	13.47	12.40	8.85 (Cu)
33181A1	20	60	66.75	16.04	16.01	1.21 (Cu)
6981B1	100	60	70.36	12.80	13.45	3.39 (Cu)
61081A1	130	60	70.22	12.05	16.64	1.11 (Cu)
61081B1	10	60	61.05	18.50	10.71	9.74 (Cu)
61181A1	15	60	60.36	19.19	10.83	9.62 (Cu)
6781A1*	50	60				
6781B1*	80	60				
6881A1*	20	60				
6881B1*	100	60				
6981A1*	130	60				
61081C1*	10	60				
61181B1*	15	60				
10381A2	0	60	62.10	22.73	14.74	
10481A2	10	60	63.07	21.73	15.20	
10481B2	15	60	62.72	21.46	15.83	
10581A2	20	60	63.23	22.13	14.63	
10581B2	30	60	64.14	19.91	15.96	
10681A2	40	60	65.70	18.31	16.00	
10681B2	60	60	64.80	17.16	18.03	
10781A2	80	60	66.73	14.34	18.94	

Table 6-1: Compositional Analysis of Films for Various Sputtering Conditions

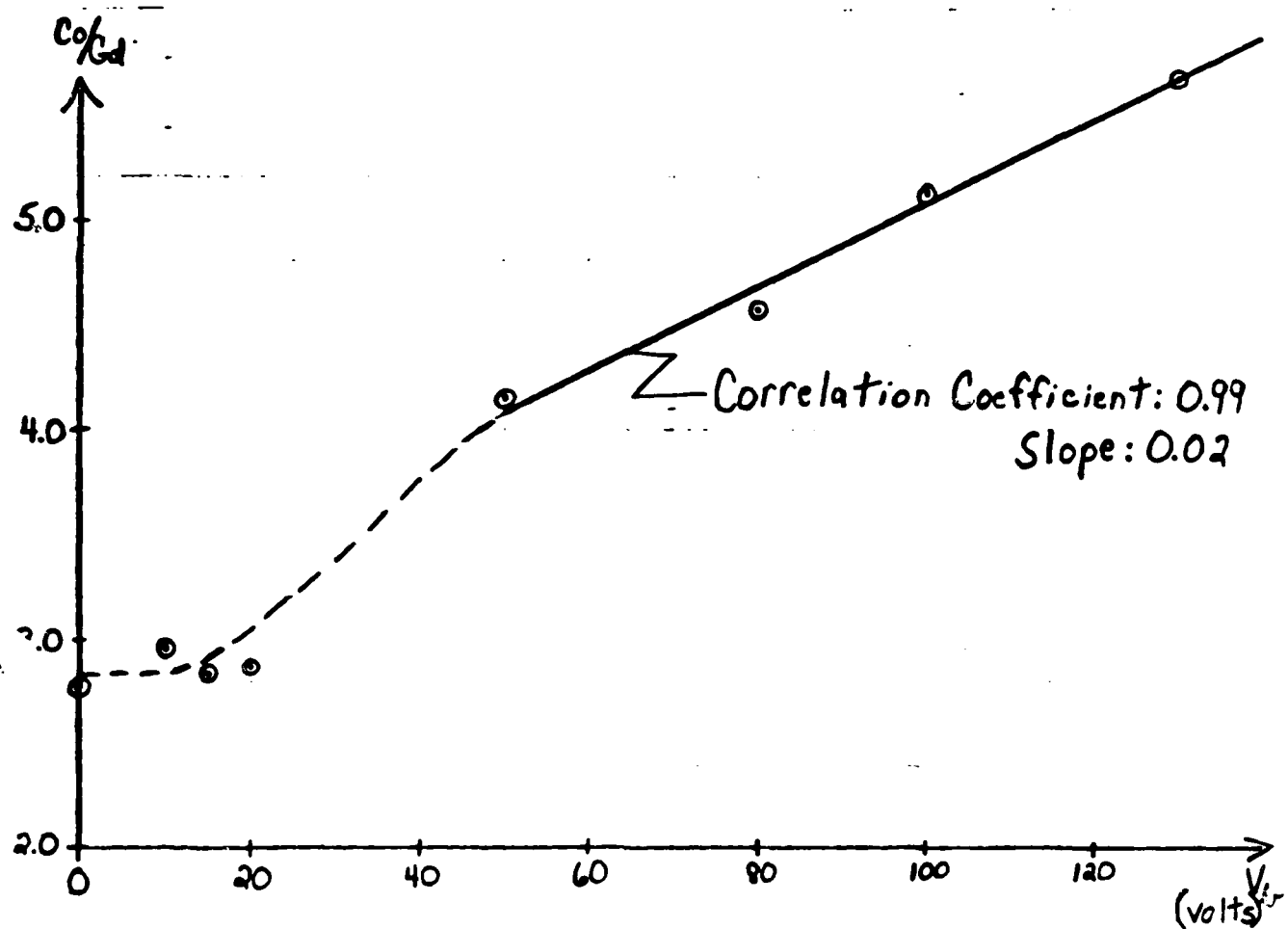


Figure 6-1: The Co/Gd Content Vs. Substrate Bias of Films Fabricated between 5/16/81 and 6/11/81

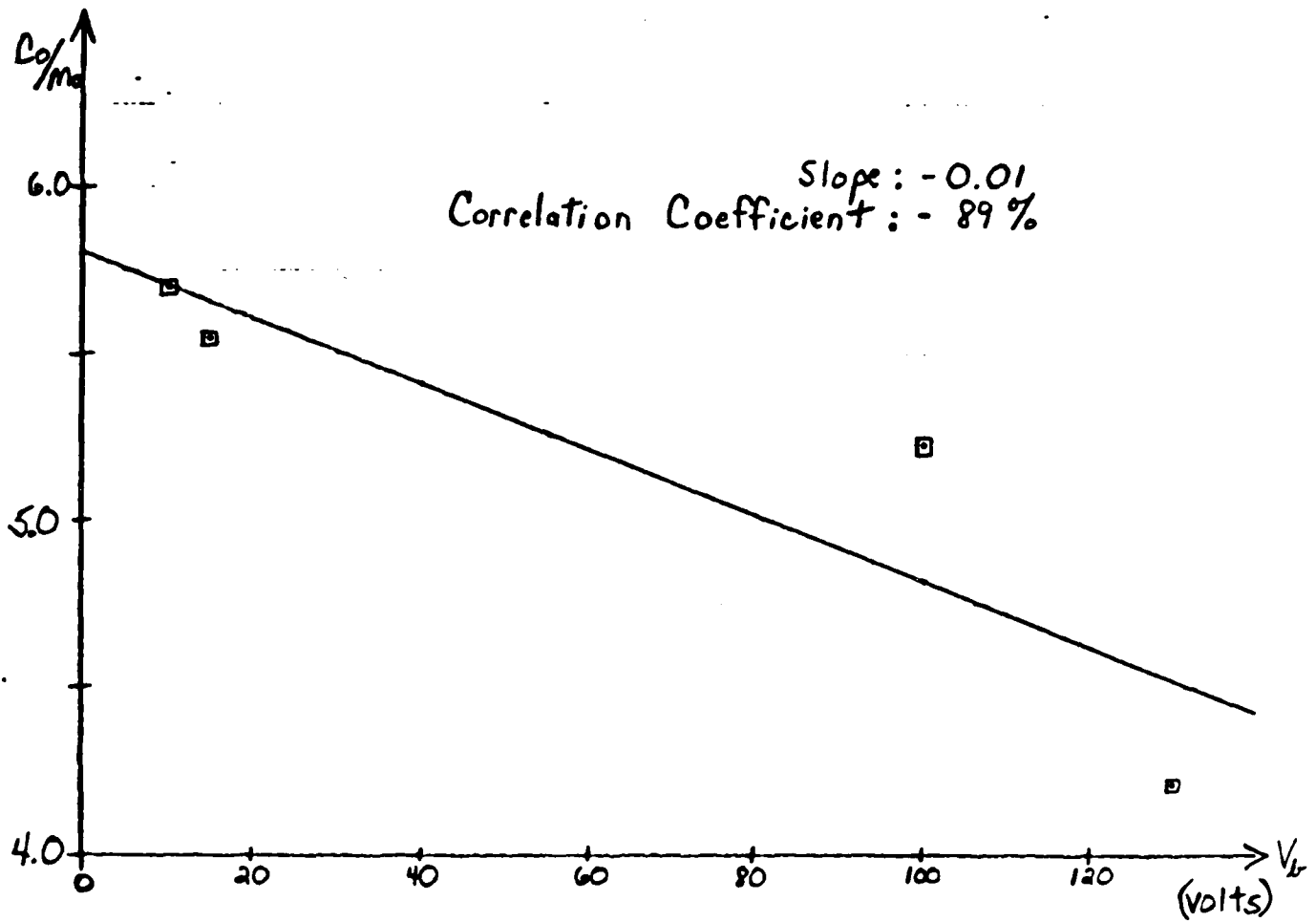


Figure 6-2: The Co/Mo Content Vs. Substrate Bias of Films Fabricated between 5/16/81 and 6/11/81

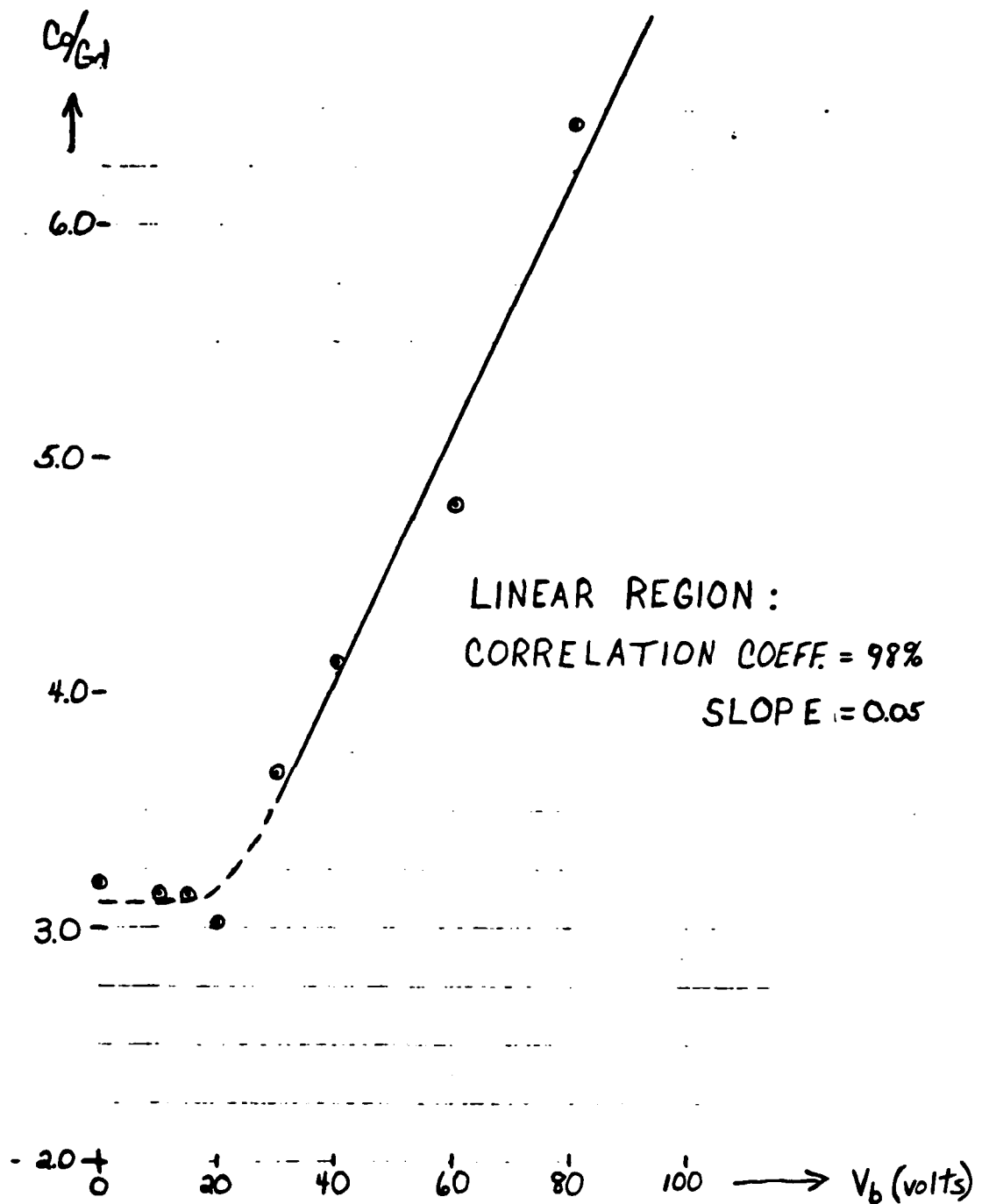


Figure 6-3: The Co/Gd Content Vs. Substrate Bias of Films Fabricated between 10/3/81 and 10/7/81

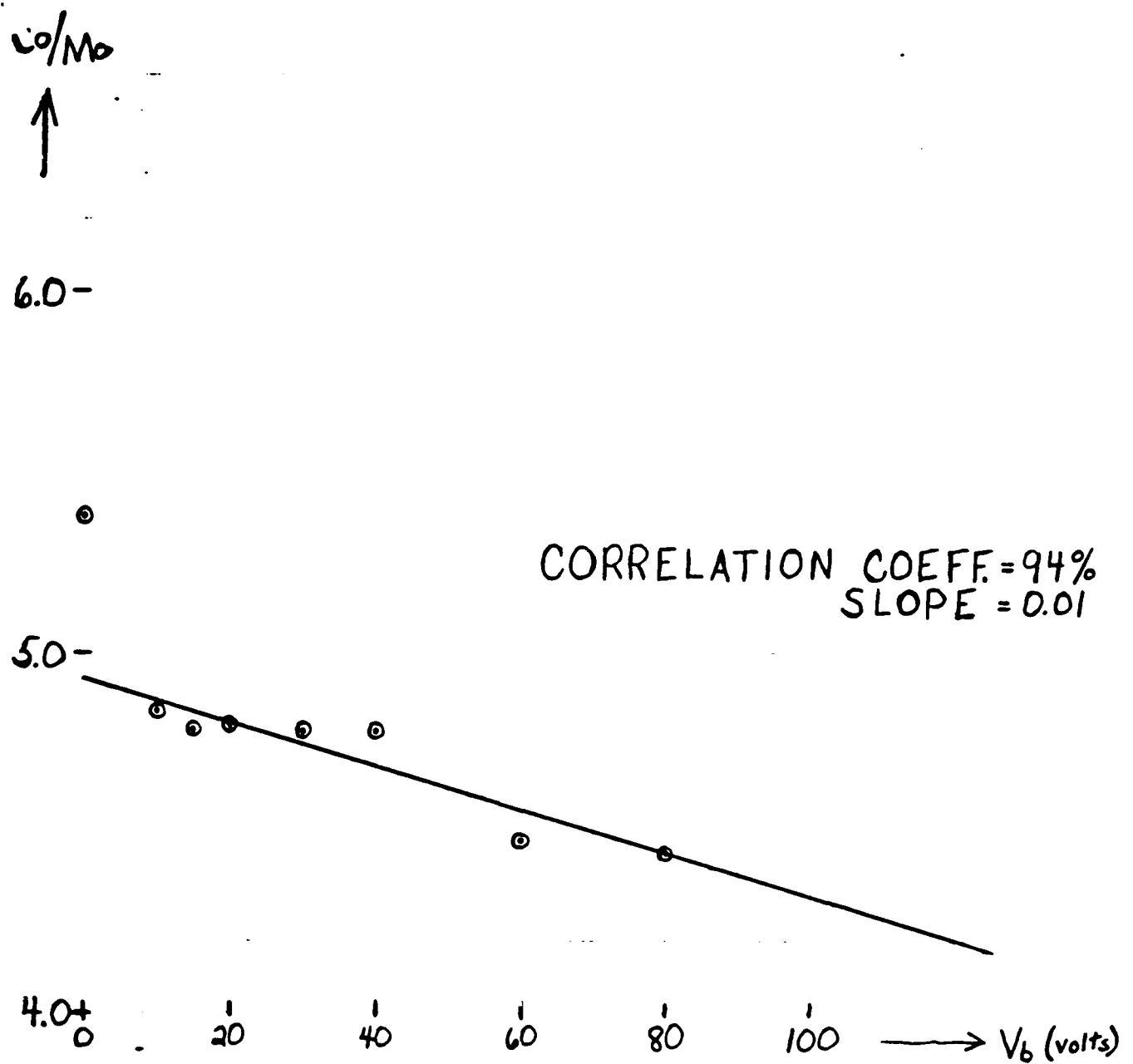


Figure 6-4: The Co/Mo Content Vs. Substrate Bias of Films Fabricated between 10/3/81 and 10/7/81

content exhibits a linear relationship to substrate bias for biases above 30 or 40 V. This is extremely convenient for the film maker in light of the compositional variation with cooling water temperature (the reason why films at very high biases are scarce). An indication of compositional change with cooling water temperature is apparent in the change of slope (however slight) between like plots. The fact that the changes are so slight points to the success of the Ga backing used on the substrates. Similar plots made by IBM researchers in calibrating their equipment are shown in Figure 6-5. A comparison of their plots with those of the author demonstrates that the fabrication procedures outlined heretofore have been a complete success. It should be noted however that the dotted portions of Figures 6-1 and 6-3 are modeled after the IBM curves. This region is actually of little concern to the magnetic bubble researcher because, as previously mentioned, uniaxial anisotropy increases with substrate bias and, normally, biases greater than 40 V will be used.

Measurement of Ar content of listed films is not available due to the lack of a proper Ar microprobe standard (a material containing a known amount of Ar). In lieu of this, a qualitative determination of the rise of Ar content with substrate bias was obtained. Figure 6-6 shows the readout from a mass analyzer hooked up to the General Electric microprobe. The amount of Ar is seen to rise with substrate bias, with little or no Ar at 20 V. This is to be expected if one observes the curves presented by IBM in Figure 6-5. Now that the CMU ion implanter is operational, a standard can be made by implanting a film with a known dose of Ar and quantitative measurements can be done.

## 6.2. SPUTTER ETCH RATE CALIBRATION

During the course of film making, it will probably become necessary to sputter etch oxide layers off uncoated films for the purposes of characterization. This rate has been calibrated using an RF power of 300 W and an Ar pressure of 10 mtorr. The results appear in Figure 6-7. A removal rate of 0.031  $\mu\text{m}$  per minute was found for the sputtering conditions stated. One should use this calibration only as a guide since the rate will vary with substrate temperature. In cases where the author sputter etched films, the thicknesses were always remeasured for maximum accuracy. The calibration of sputter etch rate has been valuable in that knowing the rate of film erosion prevented the loss of irreplaceable samples.

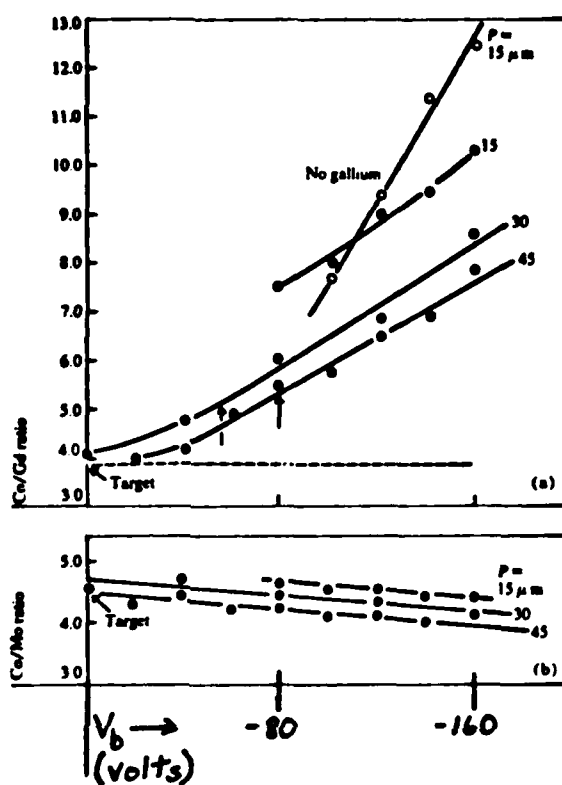


Figure 6-5: IBM Calibration of Co/Gd Content and Co/Mo Content Vs. Substrate Bias<sup>21</sup>



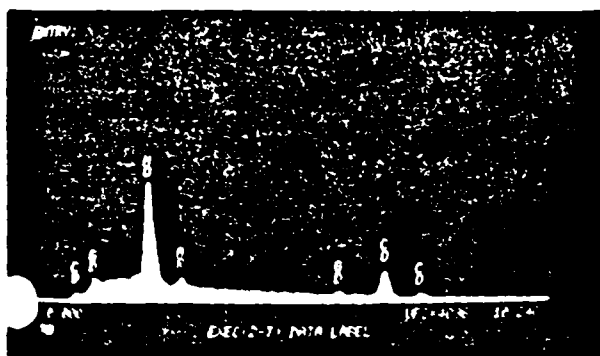
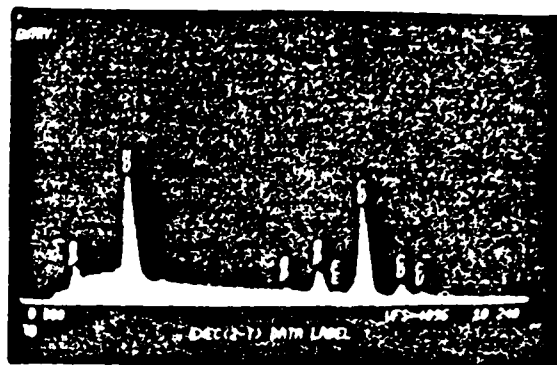
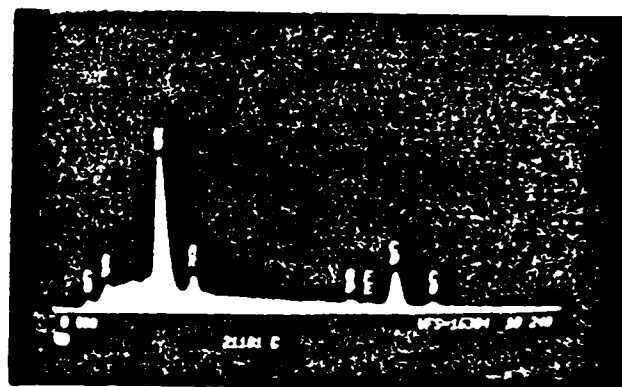
$V_b = -40V$ 

 $V_b = -20V$ 

 $V_b = -80V$ 


Figure 6-6: Qualitative Demonstration of the Rise in Ar Content with Substrate Bias

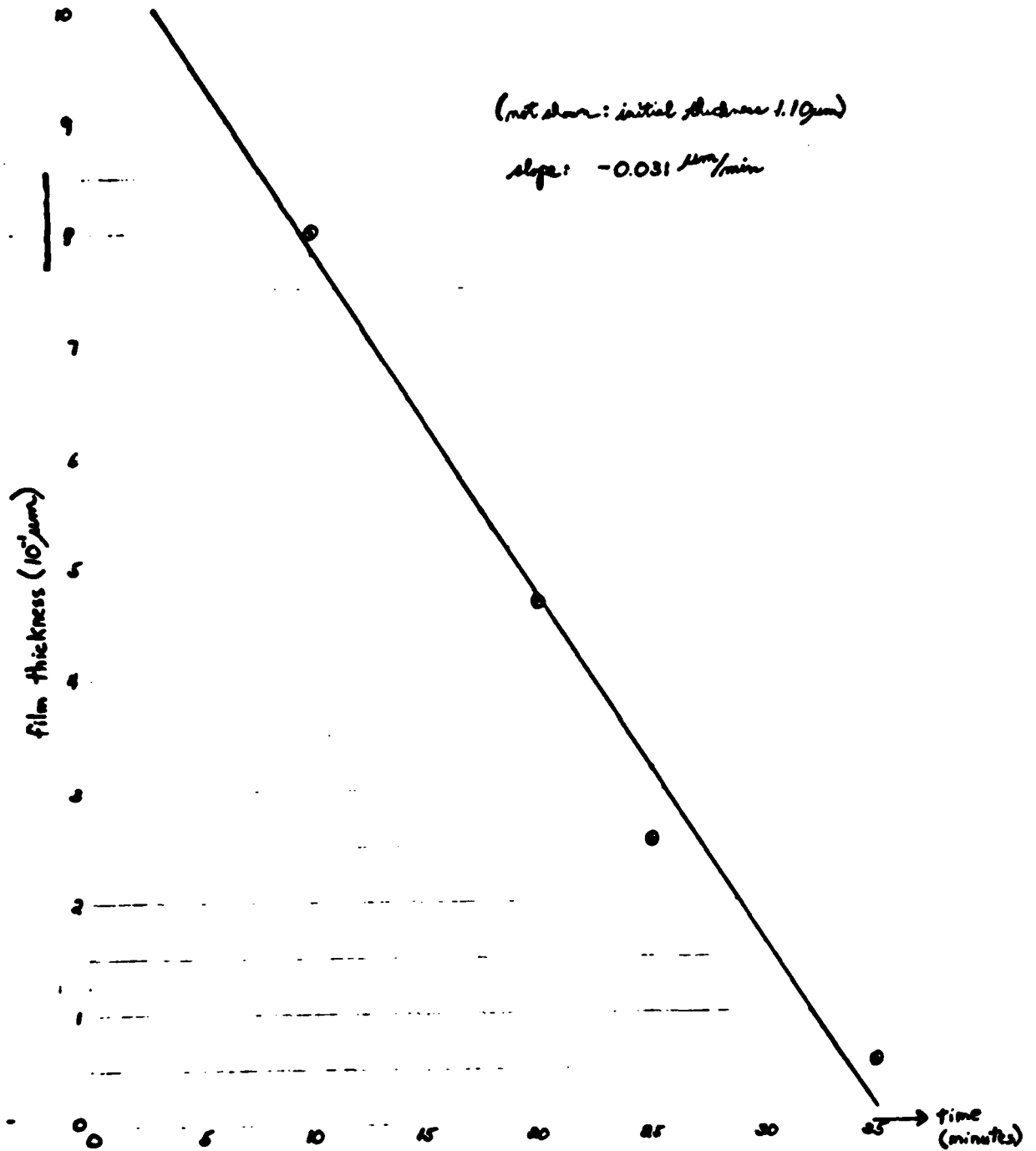


Figure 6-7: Film Thickness Vs. Duration of Sputter Etching

### 6.3 MAGNETIZATION, CHARACTERISTIC LENGTH AND ANISOTROPY DATA

Optical analysis is crucial to the acquisition of magnetization and characteristic length data. Stripwidths are easily obtained from photographs or directly off the TV monitor. Photographs taken of various samples appear in Figures 6-8 through 6-14. Three of these photographs deserve special mention. Figure 6-8 is a dramatic exhibition of compositional variation over the surface of a film. The photograph was taken about mid-radius on the sample listed. Figure 6-9 shows the raft of bubbles cited in the previous chapter. It is from such a configuration that the bubble collapse field is measured. Figure 6-10 shows a stripe configuration typical of films having  $T_{\text{comp}}$  near room temperature (the temperature at which all photographs were taken). Irregular stripe patterns such as Figure 6-10 are visual indications of the high coercivities shown by films near compensation temperature. The remaining photographs show films in order of increasing Co content and decreasing Gd and Mo contents (i.e. increasing substrate bias). Since the Co:Gd ratio increases much faster than the Co:Mo ratio, the trend of decreasing stripwidth from Figure 6-11 to 6-14 is expected. The fuzziness exhibited by some of the photographs is attributable to an oxide layer atop the uncoated sample which formed during the hour long period between their exposure to atmosphere and the photographic procedure. Differences in overall appearance are caused by the fact that some were photographed with a 50X lense on our old microscope and the others with a 100X lense on our new scope.

As mentioned in the previous chapter,  $4\pi M_s$  and  $I$  evaluations were performed using optical methods while  $K_u$  was determined from the static bubble parameter charts using an approximated  $A$ . These values are compiled in Table 6-2 along with the corresponding thicknesses, stripwidths, bubble collapse fields, quality factors and dominant sublattices at room temperature. The determination of the anisotropy constants for the samples listed in Table 6-2 appear in Figures 6-15 through 6-19.

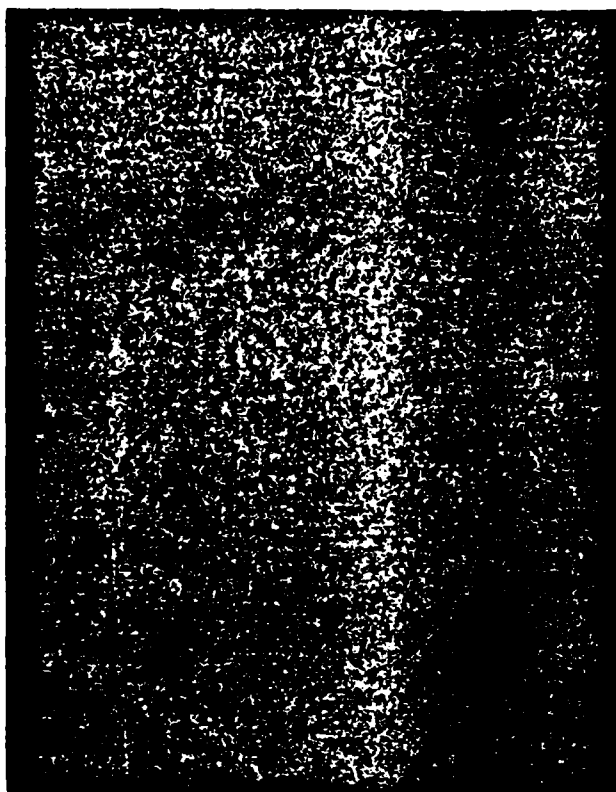


Figure 6-8: Sample 61081B1 Exhibiting Stripwidth Variation [scale:  $14.8\mu\text{m}/\text{cm}$ ]



Figure 6-9: Sample 611B1A1 Exhibiting a Bubble Raft [scale:  $4.71\mu\text{m}/\text{cm}$ ]



Figure 6-10: Sample 6881A1 [scale:  $4.71\mu\text{m}/\text{cm}$ ]

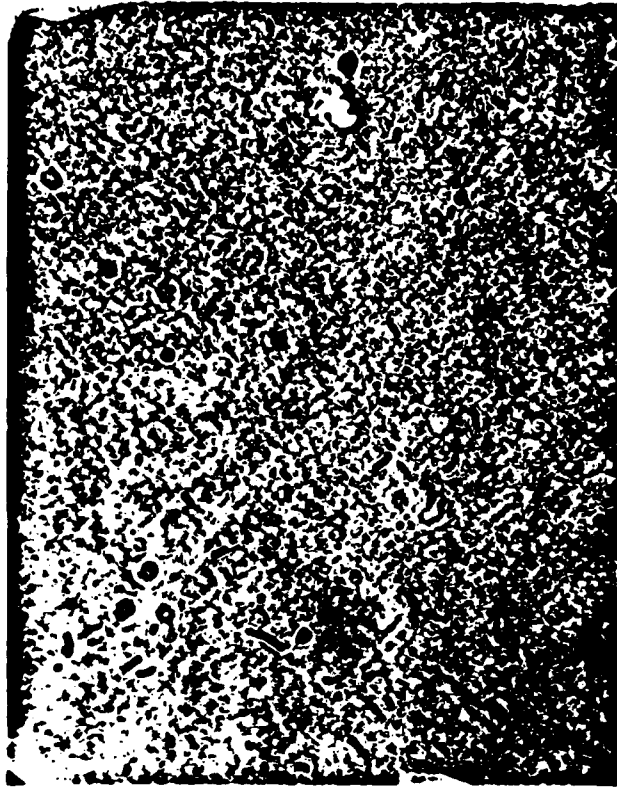


Figure 6-11: Sample 61081B1 [scale:  $4.71\mu\text{m}/\text{cm}$ ]

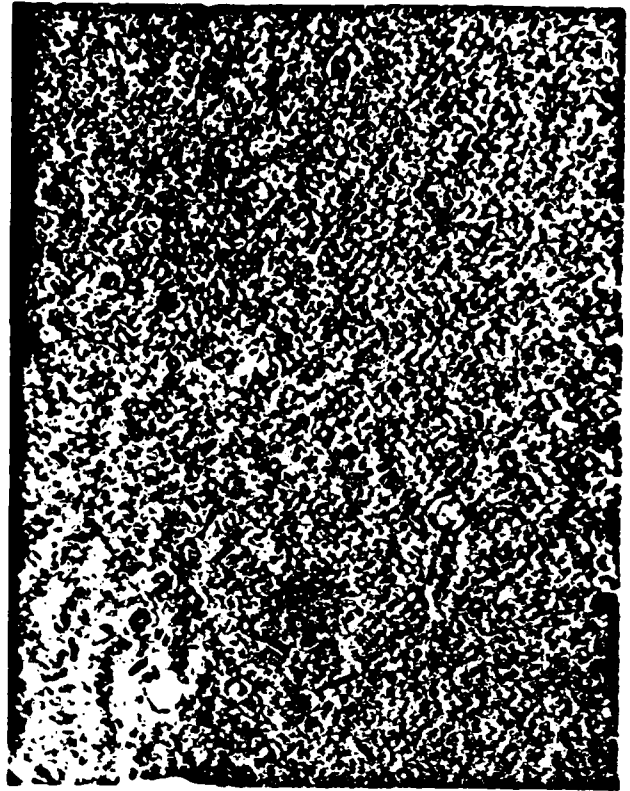
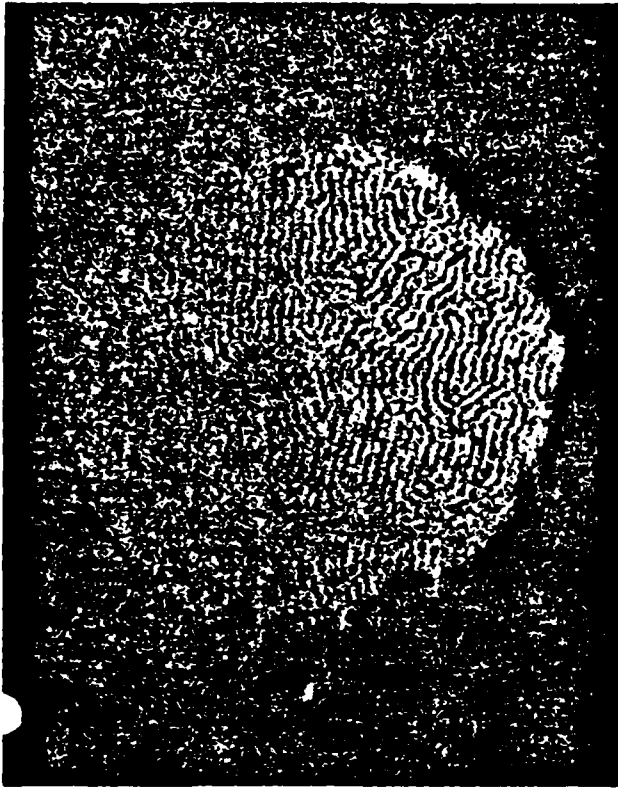


Figure 6-12: Sample 611B1A1 [scale:  $14.8\mu\text{m}/\text{cm}$  (left photo  
 $4.71\mu\text{m}/\text{cm}$  (right photo))]



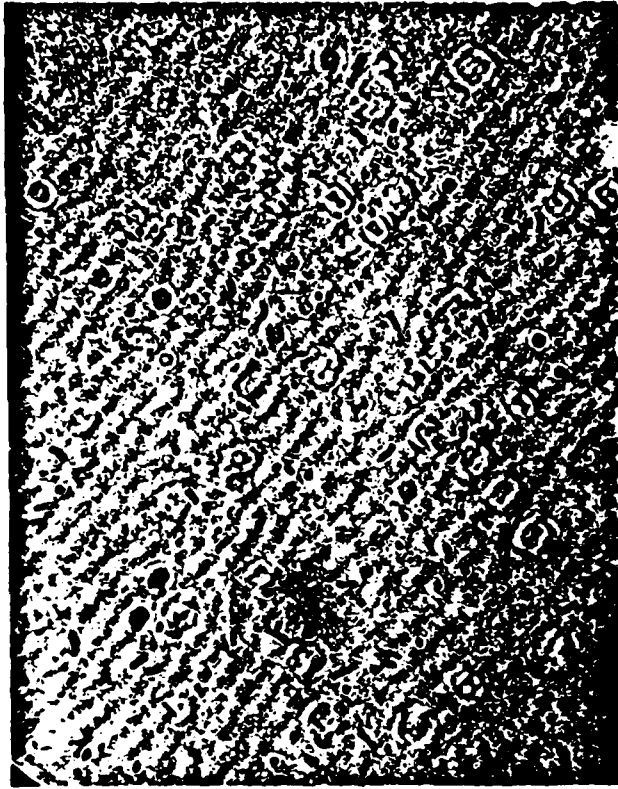


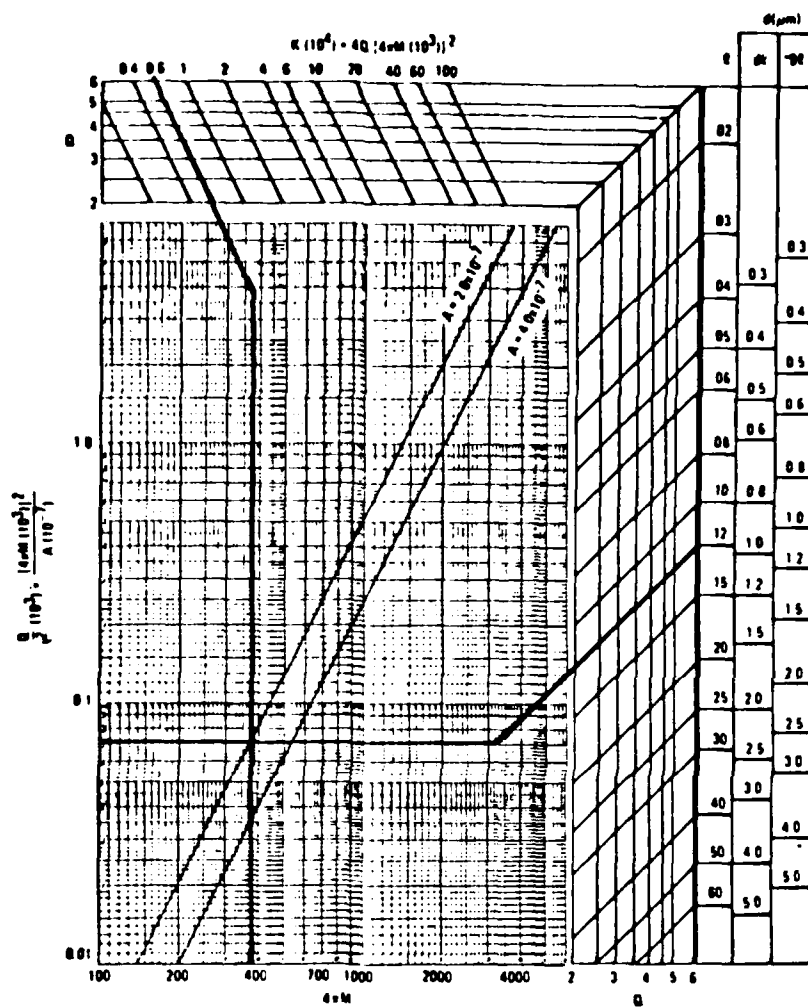
Figure 6-13: Sample 33181A1 [scale:  $4.71\mu\text{m}/\text{cm}$ ]



Figure 6-14: Sample 10781A2 [scale:  $4.71\mu\text{m}/\text{cm}$ ]

sample	thickness ( $\mu\text{m}$ )	stripwidth ( $\mu\text{m}$ )	$H_{\text{coll}}$ (Oe)	$4\pi M_s$ (G)	$l$ ( $\mu\text{m}$ )	$Q$	$A$ ( $10^{-7} \text{ erg/cm}$ )	$K_u$ ( $10^4 \text{ erg/cm}^3$ )	$T_{\text{comp}} \leq 300\text{K}$
33181A1	1.17	1.11	198	371	0.12	1.10	2.0	0.6	>
61081B1	1.46	1.96	129	304	0.25	1.38	4.0	0.5	>
61181A1	1.44	2.00	151	364	0.25	2.06	4.0	1.3	>
61181B1	1.34	1.49	323	659	0.18	3.24	4.0	6	>
10781A2	0.75	0.71	333	617	0.08	1.28	2.0	2	>
10681B2									<
6881A1									>

Table 6-2: Table of Magnetic Data for Bubble Films



**Figure 6-15: Magnetic Parameter Chart for Sample 33181A1**

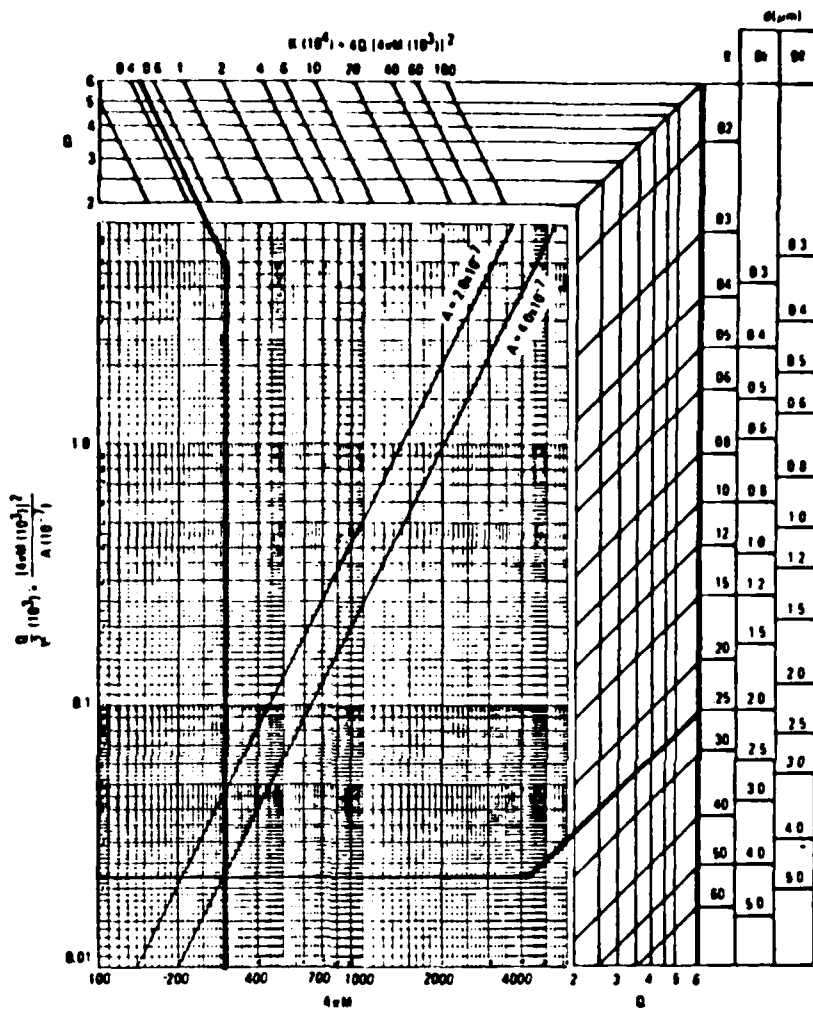


**Figure 6-16: Magnetic Parameter Chart for Sample 61081B1**

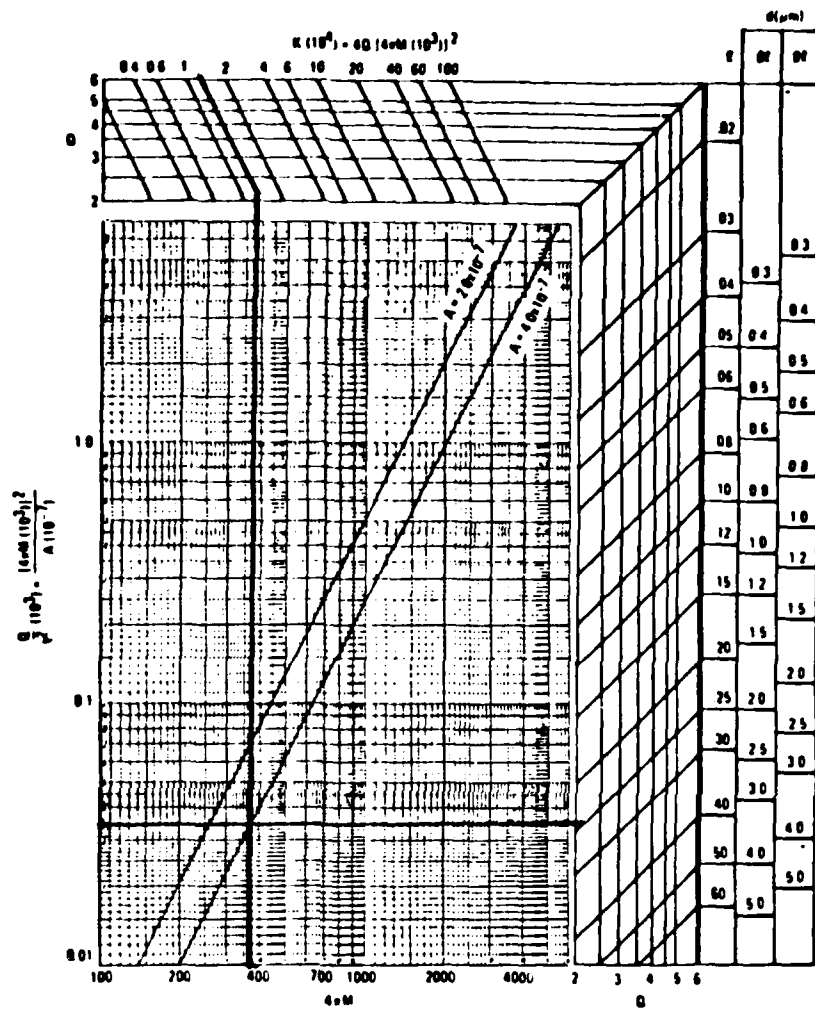


Figure 6-17: Magnetic Parameter Chart for Sample 611B1A1

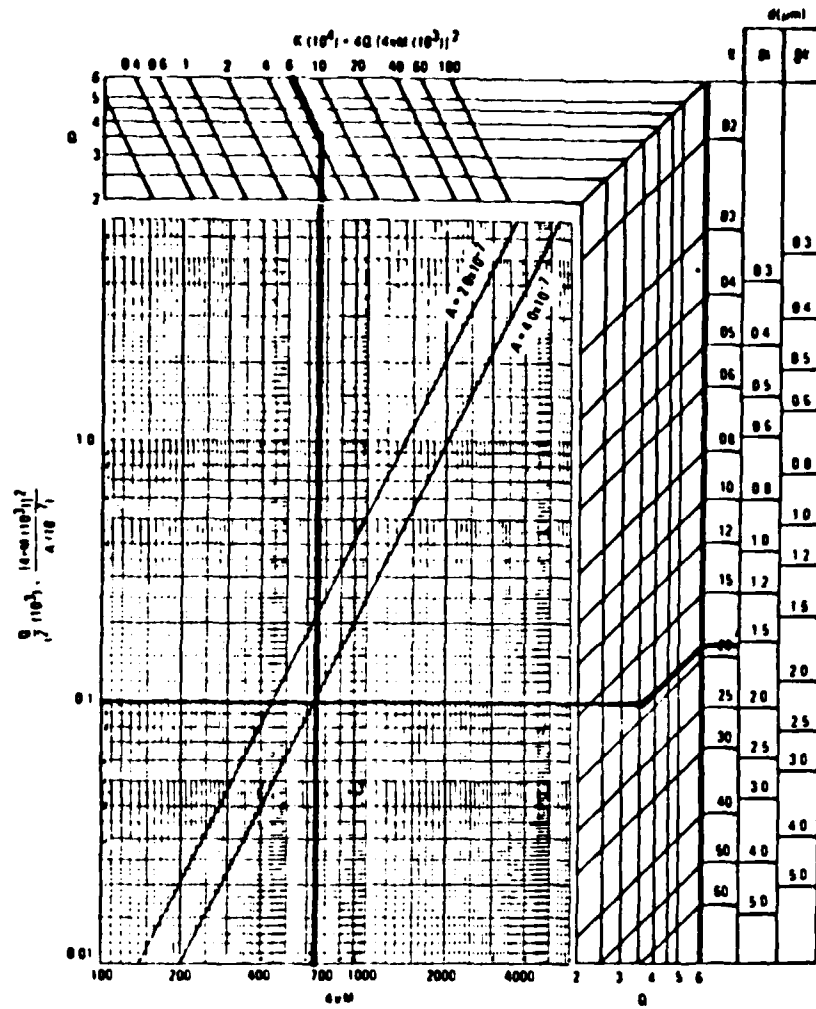


Figure 6-18: Magnetic Parameter Chart for Sample 61181B1

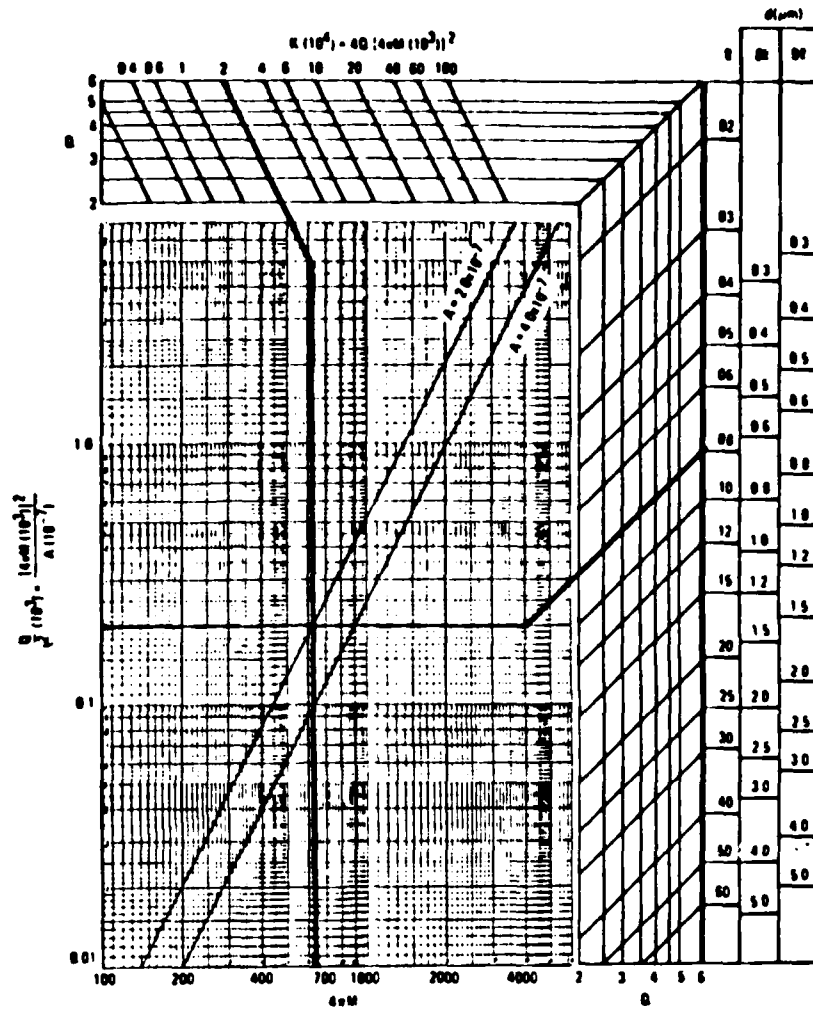


Figure 6-19: Magnetic Parameter Chart for Sample 10781A2



## CONCLUSION

Since this thesis concentrates on the basics of GdCoMoAr fabrication and research, future study of this spin system at CMU will be free to concentrate on new applications. It has been shown that GdCoMoAr thin films can be RF sputtered with relationships between composition and fabrication conditions similar to those shown in previously published papers. Although it will be necessary to investigate the magnetic parameters of this spin system in greater detail, the difficulty of determining a proper target composition and sputtering truly magnetic thin films is virtually eliminated.

At various points in the text, literature concerning thermomagnetic recording applications for GdCoAr films is cited. This is an exciting, new area for amorphous, magnetic films which CMU research will investigate and to which much of the work contained herein is readily transferrable. Already, GdCoAr films have been successfully made using the results obtained from GdCoMoAr study. In addition, the augmented polar Kerr rotation of GdCoAr makes optical observation and characterization much easier than for films containing Mo. The fabrication conditions developed for GdCoMoAr are also applicable to other amorphous materials which are prepared by RF sputtering such as TbFe, GdFe or other spin systems.

## ACKNOWLEDGEMENTS

The author would like to thank General Electric Research and Development for their generous support of this research: in particular, the author thanks Messers W. Meiklejohn and R. Skoda for their aid throughout the course of research; Mr. J. Fury for sharing his extensive knowledge of RF sputtering; and Messers M. McConnell and N. Lewis for their electron microprobe measurements. The author also thanks the members of the applied magnetism group and E.E. staff for their unfailing help: in particular, the author thanks Doug Saunders for his help with the polarizing microscope; Chris Bowman for making the fabrication of GdCoMoAr films far easier; and Frank Reid for his aid in fabricating GdCoAr films. The author especially thanks Dr. Kryder for his excellent guidance throughout this work and his paradigmatic patience with the author.

## References

1. P. Chaudhari, J.J. Cuomo and R.J. Gambino, "Amorphous Materials for Micrometer and Submicrometer Bubble Domain Technology," *IBM Journal of Research and Development*, Vol. 17, No. 1, January 1973, pp. 66-68.
2. Y. Togami, "Stability of Small Bits Written in Amorphous GdCo Thin Films," *Applied Physics Letters*, Vol. 32, No. 10, May 1978, pp. 673-675.
3. Y. Togami, U.S. Patent 4,293,621,.
4. P. Chaudhari, J.J. Cuomo and R.J. Gambino, "Amorphous Metallic Films for Magneto optic Applications," *Applied Physics Letters*, Vol. 22, No. 7, April 1973, pp. 337-339.
5. R. Carey and E. Isaac, *Magnetic Domains and Techniques for Their Observation*, Academic Press, 1967.
6. A.A. Thiele, "The Theory of Cylindrical Magnetic Domains," *Bell System Technical Journal*, Vol. 48, No. 10, December 1969, pp. 3287-3335.
7. A.H. Eschenfelder, *Magnetic Bubble Technology*, Springer-Verlag, Springer Series in Solid-State Sciences, Vol. 14, 1980.
8. A.H. Bobeck and H.E.D. Scovil, "Magnetic Bubbles," *Scientific American*, Vol. 224, No. 6, June 1971, pp. 78-90.
9. B.E. Argyle, R.J. Gambino and K.Y. Ahn, "Polar Kerr Rotation and Sublattice Magnetization in GdCoMo Bubble Films," *Proceedings of the Twenty-first Annual Conference on Magnetism and Magnetic Materials*, J.J. Becker, G.H. Lander and J.J. Rhyne, ed., American Institute of Physics, 1975, pp. 564-566.
10. J.J. Cuomo, "private communication," .
11. S.R. Herd, "Phase Separation as a Source of Perpendicular Anisotropy in Amorphous GdCo," *Journal of Applied Physics*, Vol. 49, No. 3, March 1978, pp. 1744-1746.
12. H.J. Leamy and A.G. Dirks, "Microstructure and Magnetism in Amorphous Rare-Earth-Transition Metal Thin Films - II - Magnetic Anisotropy," *Journal of Applied Physics*, Vol. 50, No. 4, April 1979, pp. 2871-2882.
13. T. Kusuda, S. Honda and M. Ohkoshi, "Perpendicular Anisotropy of Bias-Sputtered GdCo Film," *Journal of Applied Physics*, Vol. 53, No. 3, March 1982, pp. 2338-2340.
14. H.C. Bourne, Jr., R.B. Goldfarb, W.L. Wilson, Jr. and R. Zwingman, "Effects of D.C. Bias on the Fabrication of Amorphous GdCo RF Sputtered Films," *IEEE Transactions on Magnetics*, Vol. MAG-11, No. 5, September 1975, pp. 1332-1334.
15. R. Hasegawa, "Temperature and Compositional Dependence of Magnetic

Bubble Properties of Amorphous GdCoMo Films," *Journal of Applied Physics*, Vol. 46, No. 12, December 1975, pp. 5263-5267.

16. S. Chikazumi, *Physics of Magnetism*, Kreiger, 1964.
17. A.H. Eschenfelder, "Amorphous Films for Bubbles," in *Ferromagnetic Materials*, E.P. Wohlfarth, ed., North-Holland, 1980, pp. 345-380, ch. 6.
18. R.M. Bozorth, *Ferromagnetism*, D. Van Nostrand Co., 1951.
19. P. Chaudhari, C.H. Bajorek and M.H. Kryder, "Amorphous Gd-Co Alloys for Magnetic Bubble Applications," unpublished
20. P. Chaudhari and D.C. Cronmeyer, "The Temperature Dependence of the Uniaxial Anisotropy of  $Gd_{1-x}Co_xMo_y$  Amorphous Alloy Films on Glass Substrates," *Proceedings of the Twenty-first Annual Conference on Magnetism and Magnetic Materials*, J.J. Becker, G.H. Lander and J.J. Rhyne, ed., American Institute of Physics, 1975, pp. 113-114.
21. C.H. Bajorek and R.J. Kobliska, "Amorphous Materials for Micrometer and Submicrometer Bubble Domain Technology," *IBM Journal of Research and Development*, Vol. 20, No. 3, May 1976, pp. 271-281.
22. A. Brunsh and J. Schneider, "Perpendicular Magnetic Anisotropy in Evaporated Amorphous GdCo Films," *Journal of Applied Physics*, Vol. 48, No. 6, June 1977, pp. 2641-2643.
23. R. Hasegawa, B.E. Argyle and L.J. Tao, "Temperature Dependence of Magnetization in Amorphous GdCoMo Films," *Proceedings of the Twentieth Annual Conference on Magnetism and Magnetic Materials*, C.D. Graham, Jr., G.H. Lander and J.J. Rhyne, ed., American Institute of Physics, 1974, pp. 110-112.
24. R. Hasegawa, R.J. Gambino and R. Ruf, "Magnetic Properties of Amorphous GdCoAu Films," *Applied Physics Letters*, Vol. 27, No. 9, November 1975, pp. 512-513.
25. V.J. Minkiewicz, P.A. Albert, R.L. Potter and C.R. Guarnieri, "Magnetic Properties of Sputter Deposited GdCoCu Amorphous Bubble Films," *Proceedings of the Twenty-first Annual Conference on Magnetism and Magnetic Materials*, J.J. Becker, G.H. Lander and J.J. Rhyne, ed., American Institute of Physics, 1975, pp. 107-108.
26. L.M. Maissel, "Application of Sputtering to the Deposition of Films," in *Handbook of Thin Film Technology*, L. Maissel and R. Glang, ed., McGraw-Hill, 1970, pp. 1-44, ch. 4.
27. John A. Thornton American Vacuum Society, *Coating Deposition by Sputtering*, 1978, Vacuum Science and Technology Short Course offered by AVS Education Committee
28. J. Fury, "private communication,"
29. C.T. Burilla, W.R. Bekebrede and M. Kestigian, "Influence of Inert Gas

Incorporation on Uniaxial Anisotropy of Sputtered GdCo Thin Films," *Journal of Applied Physics*, Vol. 49, No. 3, March 1978, pp. 1750-1752.

30. D.C. Fowles and J.A. Copeland, "Rapid Method for Determining the Magnetization and Intrinsic Length of Magnetic Bubble Materials," *Proceedings of the Seventeenth Annual Conference on Magnetism and Magnetic Materials*, C.D. Graham, Jr. and J.J. Rhyne, ed., American Institute of Physics, 1971, pp. 240-243.
31. J. Kaczer and R. Gemperle, "Remanent Structure on Magnetoplumbite," *Czechoslovakian Journal of Physics*, Vol. B10, No. 8, August 1960, pp. 614,624a.

## DIRECT OBSERVATION OF HEAVILY ION IMPLANTED LAYERS IN GARNET

### INTRODUCTION

Irradiation produces numerous atomic collisions within a material, resulting in a spectrum of atomic displacements. In the case of ion implantation, not only interstitials and vacancies but also cascades of displacements are produced, since implanted ions have large energy. When irradiation dose increases, a build-up of defects and their interaction occur in the material. In some cases, a crystalline material containing a large density of defects can be transformed into an amorphous material.

Our previous investigations of ion implanted garnet described in last year's Progress Report (10/1/81) with 60 keV deuterium to a dosage of  $0.95 \times 10^{14}/\text{cm}^2$ , using the techniques of electron microscopy, showed that no change occurs in structure and that strain distortions at ion-implanted boundaries can be observed.

During this past year, the structure change of ion implanted garnet with increasing implantation dosage was investigated. Amorphization of garnet crystals was observed with 60 keV deuterium to a dosage of  $3.0 \times 10^{16}/\text{cm}^2$  and 110 keV oxygen to a dosage of  $5.7 \times 10^{14}/\text{cm}^2$ . In order to study profiles of implanted oxygen and deuterium layers, a cross-sectional TEM technique was developed. Preparation procedures of cross sectional samples, irradiation profiles and amorphization of garnet with oxygen and deuterium implantation and annealing behavior of amorphous garnet are described below.

### SAMPLE PREPARATION

The samples were implanted at room temperature with 60 keV deuterium ions at doses of  $1.0 \times 10^{16}$  to  $5.0 \times 10^{16}/\text{cm}^2$  and 110 keV oxygen ions at doses of  $1.9 \times 10^{14}$  to  $9.5 \times 10^{14}/\text{cm}^2$ . Two types of garnet samples were examined by electron microscopy. One type is for the observation normal to the implanted surface. For this purpose the garnet was thinned from the back side so that the LPE layer was preserved. These techniques were described in the previous progress report (10/1/81).

The other technique is for the observation of the cross section - i.e., normal to the implanted surface. The samples were prepared as follows: After ion implantation, two pieces of garnet were bonded with modified epoxy resin Araldite 502 and Hardener HY 956 with implanted surfaces in contact with each other. The bonded couples were then mounted in a simple stainless steel clamp under a moderate pressure, which could be adjusted via four tightening screws, and cured at  $60^\circ\text{C}$  for five hours.

Thin slices, approximately 0.5mm in thickness, were cut by a diamond saw. These slices were subsequently mechanically polished to a thickness of  $50\mu\text{m}$ , attached to

one-hole mesh (hole radius of 1mm) and ion milled with 6 keV argon ions to produce samples transparent to an incident electron beam.

#### STRUCTURAL CHANGE DURING ION IMPLANTATION

The structural changes detected by electron diffraction as a function of the dose of oxygen and deuterium ions are shown in Fig. 1. In Fig. 1 (a) the sample was implanted with  $1.0 \times 10^{16}$  deuterium/cm<sup>2</sup> and  $1.9 \times 10^{14}$  oxygen/cm<sup>2</sup>. Discrete diffraction spots and faint halo rings are observed, indicating that a small amount of amorphous material has been produced in a predominantly crystalline matrix. After ion implantation of  $2.0 \times 10^{16}$  deuterium/cm<sup>2</sup> and  $3.8 \times 10^{14}$  oxygen/cm<sup>2</sup>, halo rings become stronger and diffraction spots become weaker, as shown in Fig. 1 (b), indicating an increase in the degree of amorphization with increasing implantation dose. When the garnet was implanted with more than  $3 \times 10^{16}$  deuterium/cm<sup>2</sup> and  $5.7 \times 10^{14}$  oxygen/cm<sup>2</sup>, no spots were observed and only halo rings and a few Debye rings, which indicate the existence of small crystallites, were observed, as shown in Figs. 1 (c) and (d).

A bright-field, dark-field image and corresponding electron diffraction pattern for a specimen implanted with  $5 \times 10^{16}$  D<sub>2</sub>/cm<sup>2</sup> and  $9.5 \times 10^{14}$  O<sup>+</sup>/cm<sup>2</sup> are pictured in Figs. 2(a), (b) and (c) respectively. No discernible structural details are visible in the bright-field image but the existence of small crystallites (approximately 5 nm in diameter) can be observed in the dark field image corresponding to the Debye rings pictured in Fig. 1(d). The diffraction conditions for the dark-field image correspond to the circled spot in Fig. 2(c).

Cross sectional electron microscopy of ion implanted garnet showed that damage formed in some distinct bands as can be seen in Fig. 3, 4, 5 and 6. The interface between LPE and GGG can also be observed in each micrograph.

Figure 3 shows the cross sectional transmission electron micrographs of garnet films implanted with different doses of deuterium only. No change was observed with the implantation of  $1.5 \times 10^{16}$  deuterium/cm<sup>2</sup> (Fig. 3 (a)). With increasing dosage, however, an observable band was formed, as can be seen in Figs. 3 (b) and (c). The dosage of deuterium is  $3.0 \times 10^{16}$ /cm<sup>2</sup> and  $4.5 \times 10^{16}$ /cm<sup>2</sup>, respectively. The edge of the band is estimated to be 0.45  $\mu$ m from the surface of the garnet, and it can be considered to represent the penetration depth of deuterium. The crystalline nature of the band of the damaged layer was investigated by a selected area electron diffraction technique. No evidence could be found of Debye ring or halo ring associated with polycrystal structure or amorphous structure. For this reason, it is concluded that the band profile is caused by the difference of strain between the implanted and un-implanted region. The interface between the parent GGG and LPE layer can also be clearly observed.

Ion implantation with oxygen and deuterium changes the structure drastically. Figures 4, 5 and 6 show cross sectional transmission electron micrographs of garnet with

different doses of oxygen and deuterium. After the dose of  $1.5 \times 10^{16}$  deuterium/cm<sup>2</sup> and  $2.85 \times 10^{14}$  oxygen/cm<sup>2</sup> a narrow band of 1500 Å appeared as can be seen at the top of Fig. 4. For the investigation of this band, a micro-micro diffraction technique was used, in which a diffraction pattern from an area less than 100 Å can be obtained. Micro-micro diffraction patterns inserted in Fig. 4 show that the band consists of a crystalline part and an amorphous part, since in the diffraction from the band, both halo rings and spots are observed. No evidence could be found of the existence of small crystallites. Below this thin band the material is completely crystalline, as indicated by the corresponding electron diffraction pattern.

The formation of an amorphous layer on the surface was observed at doses of  $3.0 \times 10^{16}$  deuterium/cm<sup>2</sup> and  $5.75 \times 10^{14}$  oxygen/cm<sup>2</sup> (Fig. 5) and  $4.5 \times 10^{16}$  deuterium/cm<sup>2</sup> and  $8.6 \times 10^{14}$  oxygen/cm<sup>2</sup> (Fig. 6). Diffraction from the amorphous layer is shown in these figures. The thickness of both amorphous layers was about 1800 Å. There is also no evidence of the existence of small crystallites between the amorphous layer and crystalline substrate.

#### CRYSTALLIZATION PROCESS OF AMORPHOUS GARNET

The amorphous structure formed by ion implantation with  $4.0 \times 10^{16}$  deuterium/cm<sup>2</sup> and  $7.6 \times 10^{14}$  oxygen/cm<sup>2</sup> shown in Fig. 7 was studied as a function of temperature. Electron microscope observation was done normal to the ion implanted surface. No significant change in the structure was observed for annealing temperatures below 150°C. By annealing at 200°C for 30 minutes, however, small crystallites appear in the amorphous structure. Figure 8 shows the bright-field electron micrograph and corresponding diffraction pattern. In the diffraction pattern, some spots which indicate the existence of crystallites can be seen. When the sample was annealed at 200°C for 1 hour, growth of a single crystal was observed from the inner part of the film. The arrow in Fig. 9 shows thickness extinction contours which were not found after the previous annealing. Contours are only observed in the single crystal. As the amorphous layer existed only on the surface of the garnet, the growth of a single crystal can be considered to be epitaxial growth from the single crystal region of the inner part. When the annealing temperature was increased up to 250°C, no change was observed as shown in Fig. 10.

#### DISCUSSION OF RESULTS

Cross sectional transmission electron microscopy clearly shows the formation kinetics of an amorphous layer on the surface of garnet. At low dosage ( $< 0.5 \times 10^{16}$  deuterium/cm<sup>2</sup> and  $0.95 \times 10^{14}$  oxygen/cm<sup>2</sup>) no change was observed without strain profiles at ion implanted boundaries. As the implantation dose increases ( $< 1.0 \times 10^{16}$  deuterium/cm<sup>2</sup> and  $1.9 \times 10^{14}$  oxygen/cm<sup>2</sup>), isolated amorphous regions are directly formed, which can be seen in Figs. 2 (a) and 5. White and black spots in the band of Fig. 5 may come from both amorphous regions and crystal regions. These



isolated amorphous regions increase and finally a continual amorphous layer is formed by further ion implantation. The critical dosage of amorphization is below  $3 \times 10^{16}$  deuterium/cm<sup>2</sup> and  $5.7 \times 10^{14}$  oxygen/cm<sup>2</sup>.

No evidence of small crystallite formation was observed by cross sectional transmission electron microscopy. However, by the observation from the surface normal to the ion bombardment direction, small crystallites were observed. The Debye rings in Figs. 1 (c) and (d), and dark field image in Fig. 2 (b) show the evidence for this. These facts lead to the conclusion that small crystallites exist only in the very thin surface region. The surface receives a relatively small amount of damage, even after heavy ion implantation, since implanted ions do not exist in the shallow surface layer. Recovery of damage may occur easily in this shallow surface.

Oxygen implantation plays a dominant role for the crystalline to amorphous transformation, since no drastic change was observed to be caused by deuterium implantation. Two types of amorphization processes by ion implantation have been proposed (J. Bourgoin, Solid State Communications, 34, (1980) 25). One type is amorphization with heavy ion implantation where the concentration of defects in the cascade can be large enough to induce the transformation, and isolated amorphous regions are directly formed. The other type is amorphization with light ions where the critical concentration of defects is reached only after several ions have come to rest at the same region. In this case, an abrupt transformation of an implanted layer is expected. In our experiment, the former type of amorphization process has been observed. It is due to the fact that oxygen atoms are relatively heavy.

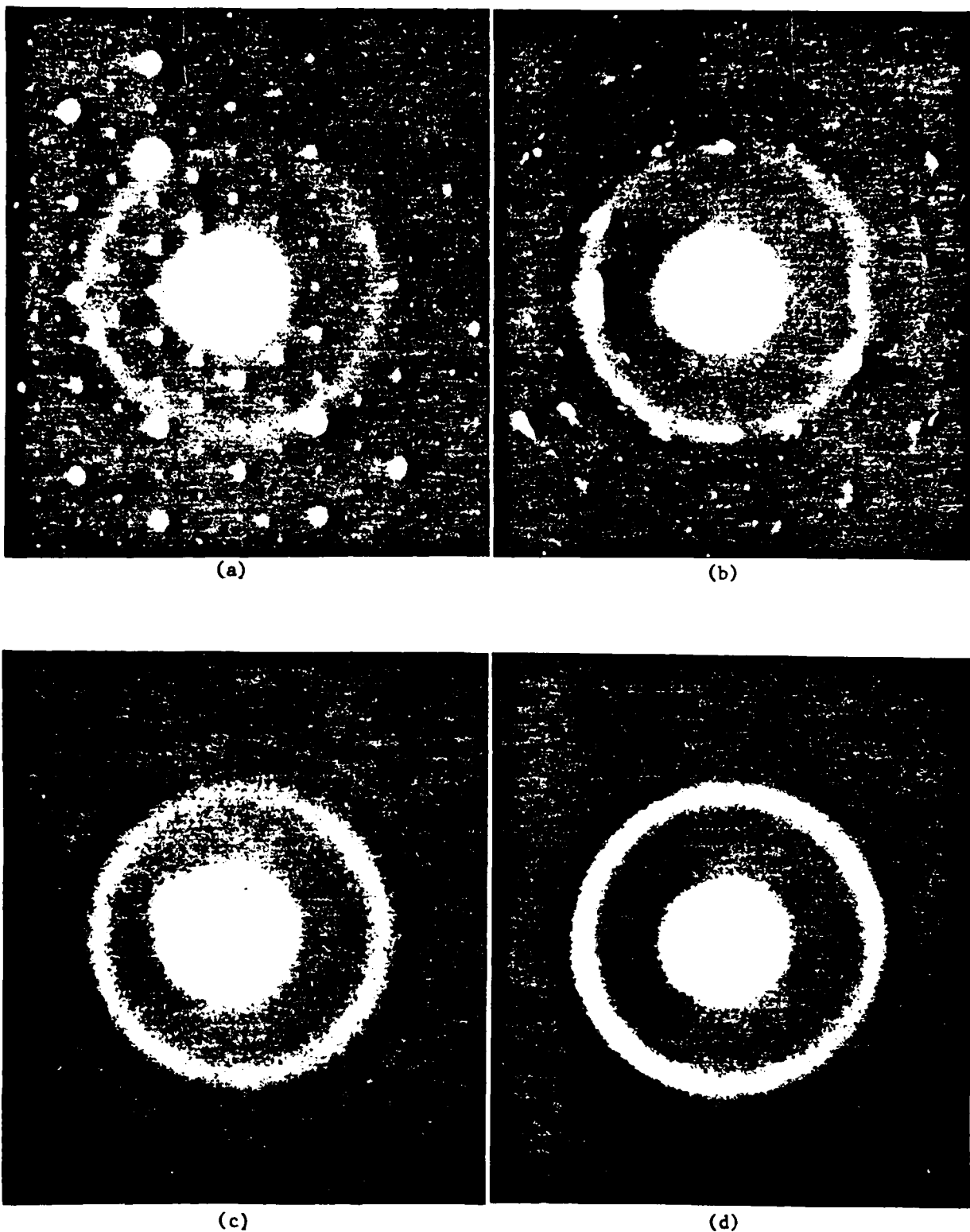
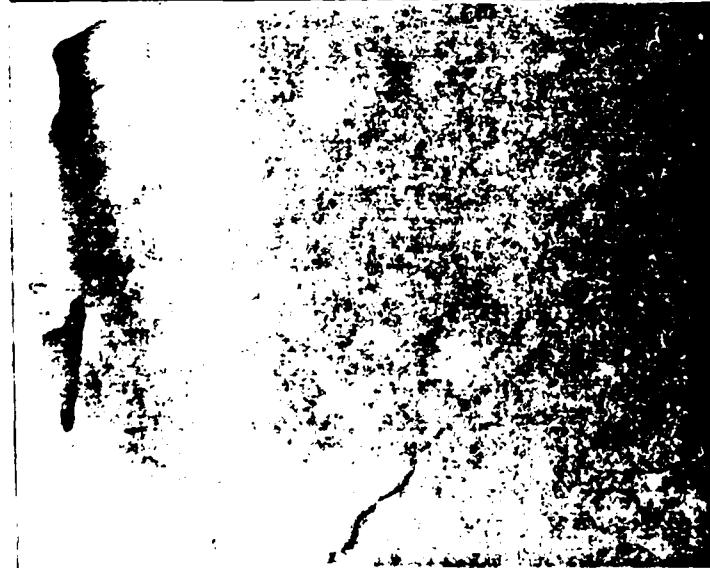
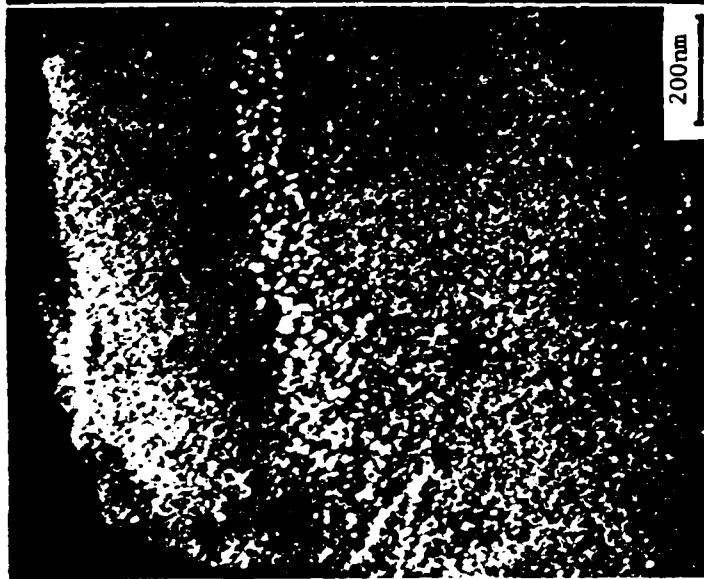


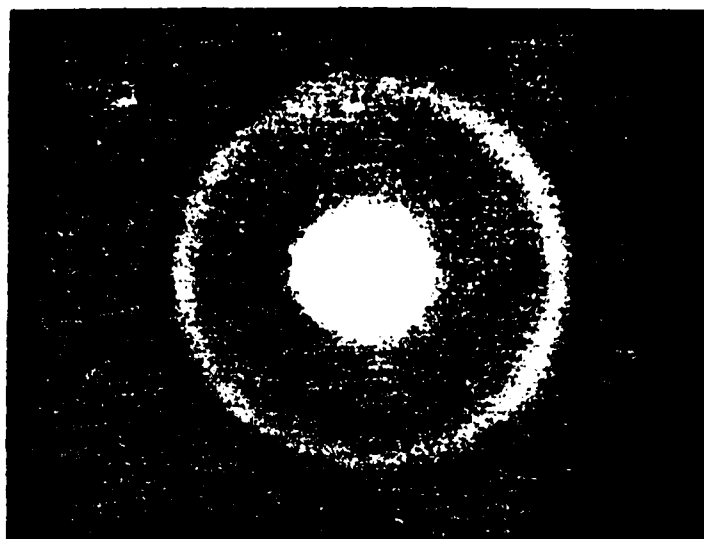
Fig. 1 Electron diffraction patterns of garnet implanted at room temperature with different doses of oxygen and deuterium ions: a)  $1.0 \times 10^6$  deuterium and  $1.9 \times 10^{14}$  oxygen, b)  $2.0 \times 10^{16}$  deuterium and  $3.8 \times 10^{14}$  oxygen, c)  $3 \times 10^{16}$  deuterium and  $5.7 \times 10^{14}$  oxygen, d)  $4 \times 10^{16}$  deuterium and  $7.6 \times 10^{14}$  oxygen.



(a)



(b)



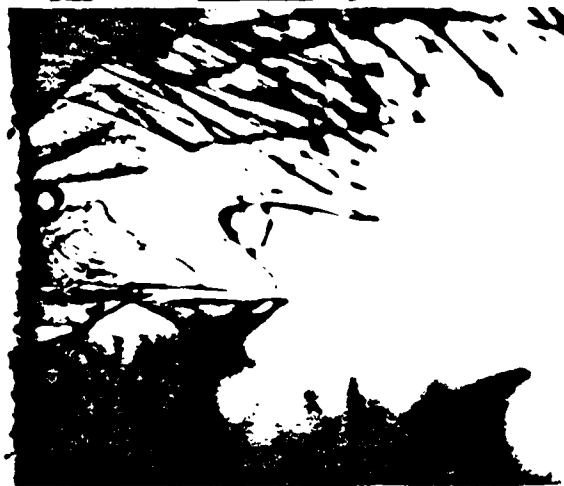
(c)

Fig. 2 a) Bright field electron micrograph and b) dark field electron micrograph and c) corresponding diffraction pattern of garnet implanted with  $5 \times 10^{16}$  deuterium and  $9.5 \times 10^{14}$  oxygen. The circle in c) shows the diffracting condition used to form the image of b).

Ions



(a)



(b)



(c)

LPE

GG:

Fig. 3 Cross sectional transmission electron micrograph of deuterium implanted garnets:

a)  $1.5 \times 10^{16}/\text{cm}^2$  b)  $3.0 \times 10^{16}/\text{cm}^2$  c)  $4.5 \times 10^{16}/\text{cm}^2$ .

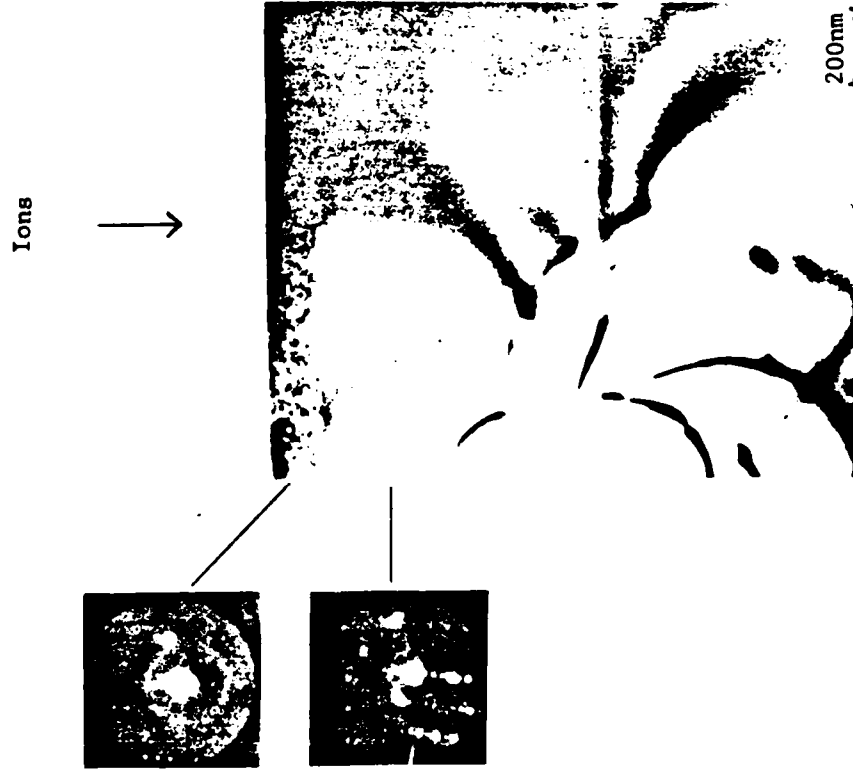


Fig. 4 Cross sectional transmission electron micrograph and diffraction patterns of garnet implanted with  $1.5 \times 10^{16}$  deuterium/cm<sup>2</sup> and  $2.85 \times 10^{14}$  oxygen/cm<sup>2</sup>.

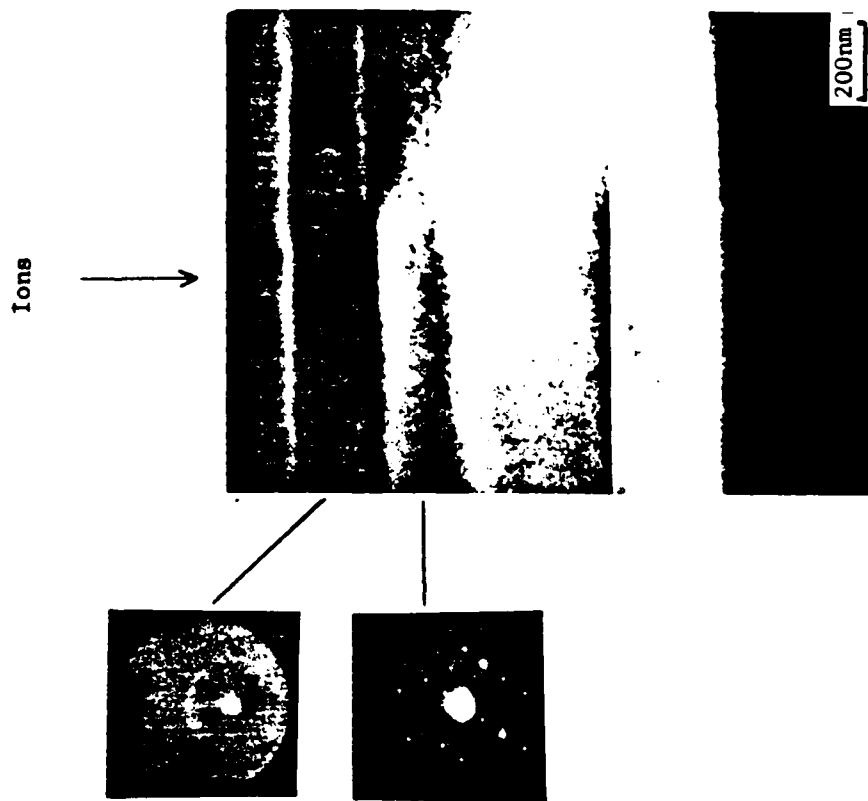


Fig. 5 Cross sectional transmission electron micrograph and diffraction patterns of garnet implanted with  $3.0 \times 10^{16}$  deuterium/cm<sup>2</sup> and  $5.7 \times 10^{14}$  oxygen/cm<sup>2</sup>.

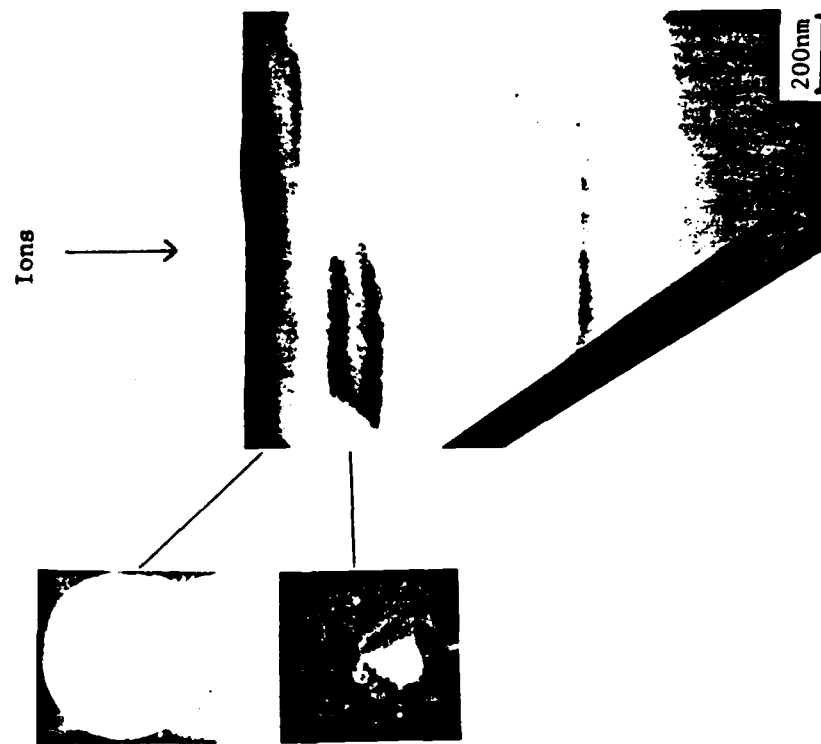


Fig. 6 Cross sectional transmission electron micrograph and diffraction patterns of garnet implanted with  $4.5 \times 10^{16}$  deuterium/cm<sup>2</sup> and  $8.5 \times 10^{14}$  oxygen/cm<sup>2</sup>.

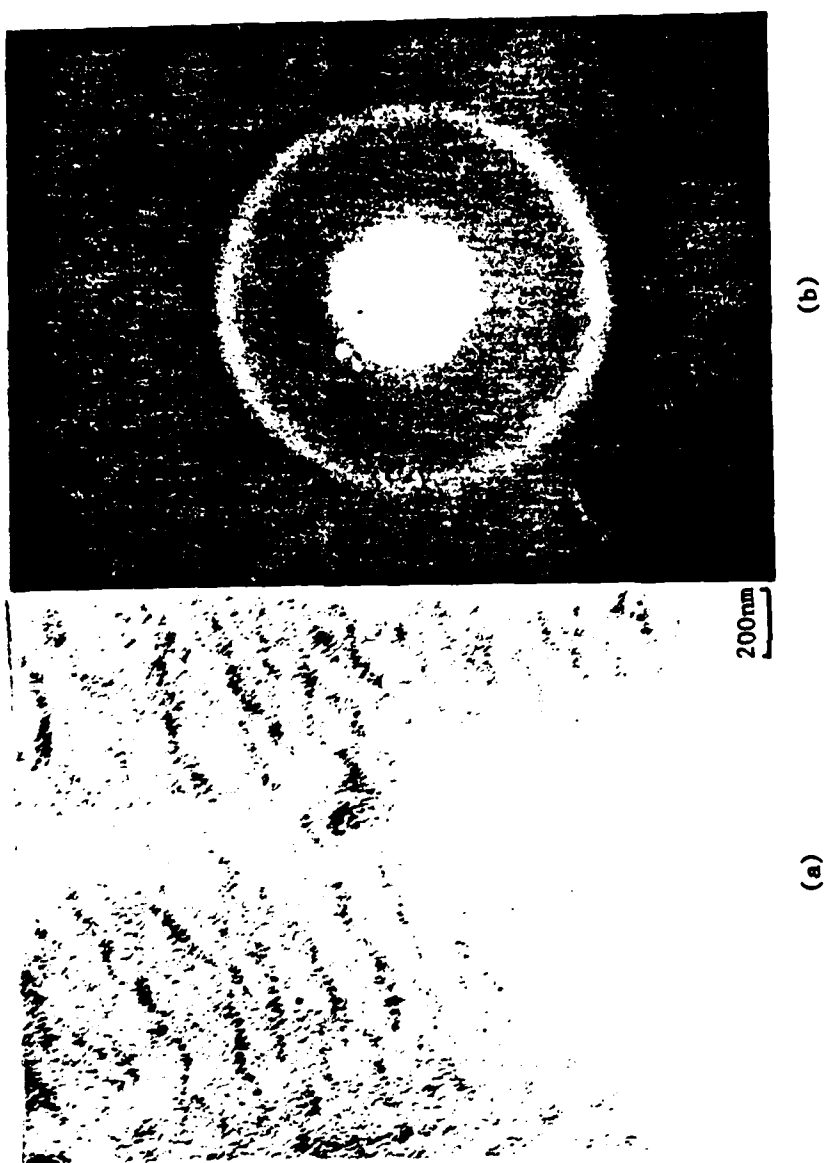


Fig. 7 Amorphous garnet made by ion implantation with  $4.0 \times 10^{16}$  deuterium/cm<sup>2</sup> and  $7.6 \times 10^{14}$  oxygen/cm<sup>2</sup>.



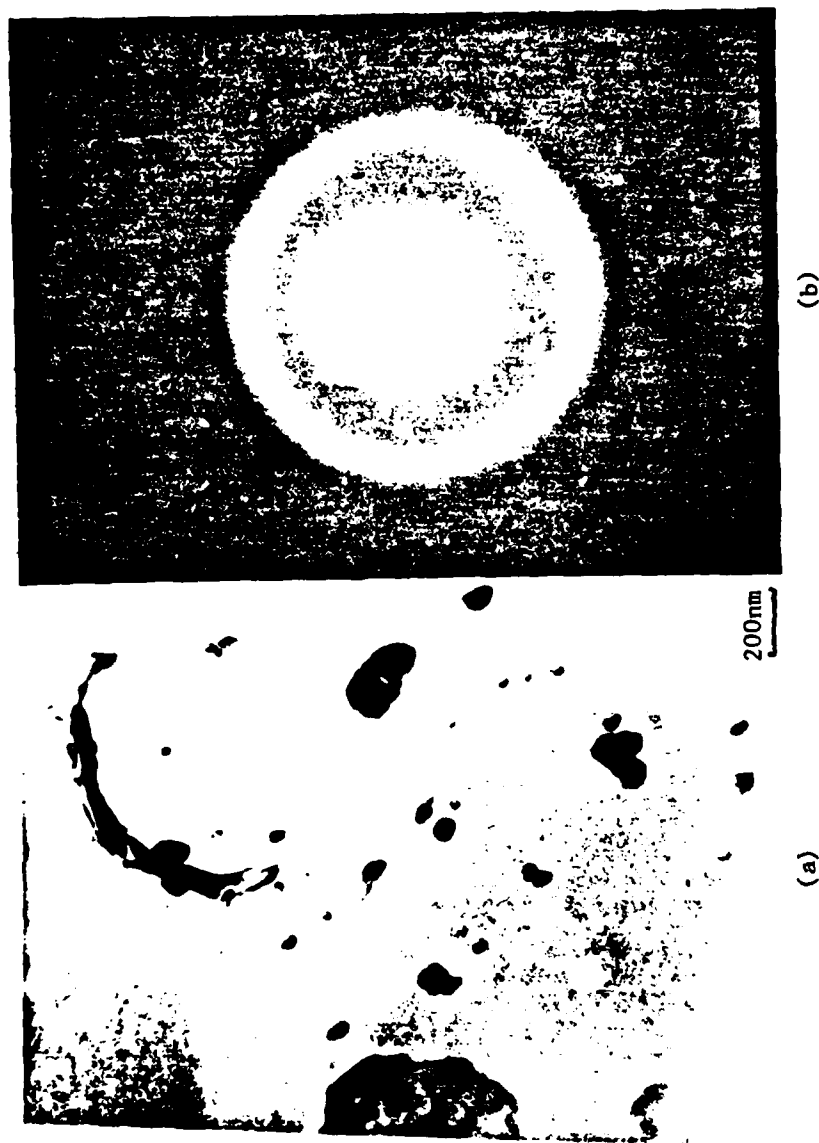
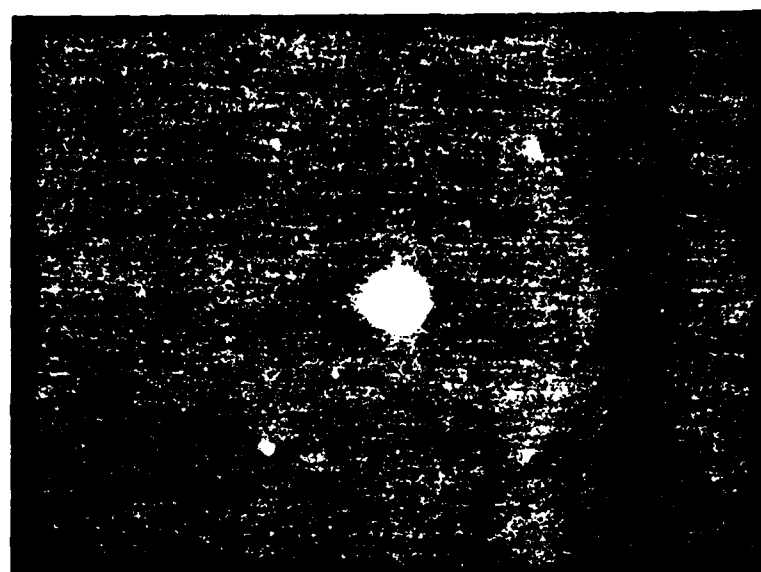


Fig. 8 Amorphous garnet after annealing at 200°C for 30 min.

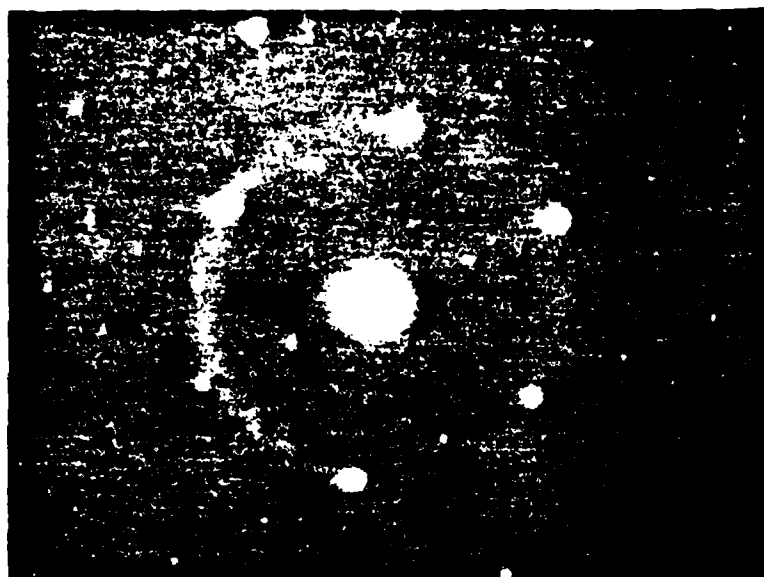


(b)



(a)

Fig. 9 Amorphous garnet after annealing at 200°C for 1 hour. An arrow indicates thickness extinction contours.



(b)



(a)

Fig. 10 Amorphous garnet after annealing at 250°C for 30 min.

# Fabrication of Contiguous Disk Magnetic Bubble Devices

## Introduction

Progress has been made in the following areas of device fabrication during the past year.

- Fabrication and testing of contiguous disk devices for  $1\mu\text{m}$  bubbles on single layer garnet films
- Redesign of the sample holder for the electroplating apparatus to improve plating reliability
- Direct writing of bubble propagation patterns on garnet wafers by electron beam
- Design of full function bubble memory chips for various bubble diameters

Also, a Karl-Suss contact aligner with a deep UV illumination system as well as a near UV system and a capability of  $0.1\mu\text{m}$  alignment has been installed and is being tested using various photoresists to determine achievable resolutions and optimum process conditions.

In the following sections, the work done in the above mentioned research areas will be described in detail and future research directions will be given .

## Device fabrication and testing

Propagation pattern devices for  $1\mu\text{m}$  magnetic bubbles were fabricated on a single layer garnet film with material characteristics shown in Table I. Their device structure and processing steps are identical to those described in detail in the last progress report except ion implantation conditions. Instead of triple implantation of Helium, double implantation of Deuterium and Oxygen was used to define propagation patterns. The deuterium implantation gives a deep penetration into the garnets at low energy levels and the linearly proportional damage levels with respect to ion dosages like Hydrogen implantation. Moreover, since Deuterium is twice as heavy as Hydrogen, it increases damage levels by factor of two at the same ion dosage, reducing implantation time by half compared with the Hydrogen implantation. The Deuterium implantation determines the ion implantation depth and the Oxygen implantation makes the damage profile uniform throughout the depth. The implantation conditions were 68 Kev,  $5 \cdot 10^{15}/\text{cm}^2$  for Deuterium and 180 Kev,  $0.95 \cdot 10^{14}/\text{cm}^2$  for Oxygen. The implantation depth was calculated to be  $0.4\mu\text{m}$ .

The gold ion implantation masks for  $1\mu\text{m}$  bubble devices are shown in Fig.1 and Fig. 2. Fig.3 and

Fig.4 show the bias margins of "the contiguous diamond shaped device" (Fig.1) and "the contiguous arrow shaped device" (Fig.2), respectively. Both devices have good propagation margins(13%-15%). Further measurements of other device characteristics will follow.

### Electroplating of gold

We have had problems in controlling the thickness of the plated gold which is used as the ion implantaion mask for some time. But, as long as the thickness of the plated gold was thicker than the minimum thickness required for stopping the implanted ions and thinner than the thickness of the photoresist used to define the implantation patterns, precise control of the thickness of the gold was not necessary. For example, devices described in the previous section required  $0.7\mu\text{m}$  of gold to stop the implanted ions. Since the photoresist thickness used was  $1.7\mu\text{m}$ , plated gold with any thickness between  $0.7\mu\text{m}$  and  $1.7\mu\text{m}$  was adequate as the implantation mask. As the bubble size becomes smaller, so does the minimum feature size of the photoresist patterns, which in turn requires thinner resist coatings. Generally, better photolithographic patterns will be obtained if one uses the minimum thickness of the photoresist required. Thus, we wish to control the thickness of the plated gold precisely.

The gold plating apparatus was described in the last report(10/1/81).It uses an alligator clip as a sample holder. When a sample is electroplated, the holder is also electroplated. Since the size of the plated area of the devices is negligible compared with that of the holder, the plating rate is determined by the surface area of the holder. One problem was that the plating rate of the device (so, the plating rate of the holder) was not constant. The other was that the plated surface was not shiny, but dull, indicating large grain size or impurities in the gold. The plating rate changed from one plating to another sometimes dramatically(up to 3 times). The reason was thought to be due to the change of the size of the surface area of the holder. Depending on the grain size of the plated gold, the size of the surface area of the holder can change substantially. Also particles in the air can adsorb on the surface of the holder and effectively reduce the size of the surface area of the holder considerably, especially when the holder is left in the air for a long time between electroplatings. Another important factor was that gold did not adhere very well to the holder. So, after few platings, the plated gold started to peel off the holder, changing the size of the surface area of the holder. Acid was used to remove the remaining gold on the holder, but it also attacked the holder itself. So, we decided to use stainless steel to make a new holder. The holder was sputter-deposited with Mo to enhance adherence of gold to stainless steel. A schematic diagram of the holder is shown in Fig.5. Shiny plated gold was obtained by using less plating current density ( $3\text{ mA/cm}^2$ ) than previously believed optimum ( $5\text{ mA/cm}^2$ ). When the plating bath (BDT 510) was initially purchased, the latter current density gave

shiny gold plating. It is not clear at this point why less plating current density is required after the bath is used for a while.

The plating rate with the new sample holder was  $2400 \text{ \AA}/\text{cm}^2/\text{min}$  ( $\pm 5\%$ ) at  $3 \text{ mA}/\text{cm}^2$  current density.

### Direct writing of patterns on wafers

Direct writing of submicron bubble propagation patterns on garnet wafers by electron beam was attempted. This was done before we obtained the submicron resolution Karl-Suss mask aligner previously mentioned. The resolution obtained by then existing aligner was not satisfactory for submicron bubble devices. Various propagation patterns for  $1 \text{ }\mu\text{m}$  and  $0.5 \text{ }\mu\text{m}$  bubbles including those shown in Fig.1 and Fig.2 were written on two garnet wafers with single layer epitaxial films using a Cambridge electron beam pattern generator at the National Research and Resource Facilities for Submicron Structures. PMMA positive resist was used since it gives better resolution for submicron features than other electron beam resists. The thickness of the resist was chosen as  $5,600 \text{ \AA}$  which is slightly thicker than the minimum thickness of the gold implantation mask. Because the electroplated gold faithfully follows the <sup>ours</sup>contour of the photoresist pattern vertically as well as laterally, careful consideration was given to obtain perpendicular resist profile with respect to the wafer surface. While too high electron beam dosage results in undercutting of the resist pattern, too low dosage gives uppercutting after development. Several dosages near  $80 \text{ }\mu\text{Coulomb}$  were tried and development time varied from 3 min. to 5 min. using MIBK developer (1 Methyl IsoButyl Keton:3 Isopropyl Alcohol).

Unfortunately, the final electroplated bubble propagation patterns were less than satisfactory. It seems ~~that~~ that the PMMA resist was not completely removed from the wafer surface in certain areas of the patterns, leaving some residue behind which prevented gold plating from taking place. If direct writing is needed in the future again, refinement of electron beam exposure and resist development conditions will be necessary using dummy wafers and a scanning electron microscope.

### Design of full function memory chips

The design of full function bubble memory chips for  $0.5 \text{ }\mu\text{m}$ ,  $1 \text{ }\mu\text{m}$  and  $2 \text{ }\mu\text{m}$  bubbles has been completed. The computer layout of memory chips is shown in Fig.6. A bubble generator is shown at the upper left corner of the layout. Bubbles propagate from the generator along the major track and are transferred into the minor loops located at the center of the layout. Bubbles stored in the minor loops are transferred out through the read gate and propagate to the right to be detected at the detector shown on the right end of the layout. The layouts of the chips for various bubble diameters are designed to be identical except the scale factors to facilitate the study of the scaling rules of the

devices. Also, a new replicate transfer-out gate utilizing bubble-bubble interaction has been designed.

### **Future research**

The masks for the full function bubble memory chips will be fabricated at the National Research and Resource Facilities for Submicron Structures at Cornell University. Then the devices will be made using those masks in the deep U.V. Karl-Suss mask aligner here at CMU. Tests will follow to optimize single layer garnet film growth conditions, ion implantation conditions, metal overlay fabrication techniques and overall device performances. Various factors determining bias margins for propagation patterns will be studied in detail including partial relief of stress at implanted boundaries of the devices. Previous studies did not include this contribution and its effect might be more critical for submicron structures. The ability to fabricate fully functional chips will allow us to study device functions such as transfer, generation, annihilation and detection of bubbles. These functions for submicron devices and the scaling rules for the devices will be studied as well as unforeseen problems that may be encountered during the course of the study.

TABLE I

Room Temperature Properties of the LPE Layer for Sample 68

Composition	$(Y_{.8}Sm_{.3}Tm_{1.3}Gd_{.6})(Fe_{4.6}Al_{.2}Ga_{.2})O_{12}$
Thickness, $h$ ( $\mu m$ )	1.47 $\mu m$
Stripewidth, $W_s$ ( $\mu m$ )	1.18 $\mu m$
Bubble Collapse Field, $H_o$ ( Oe )	401 Oe
Material Parameter, $l$ ( $\mu m$ )	1.12 $\mu m$
Saturation Magnetization, $4\pi M$ (G)	684 G
Quality Factor, $Q$	~2.2



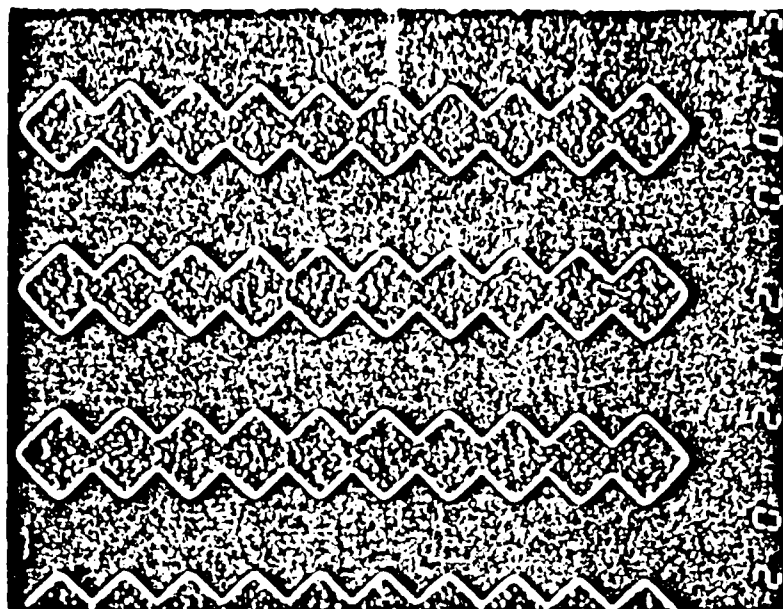


Fig. 1 : Scanning Electron Micrograph of the gold ion implantation masks of the 'Contiguous Diamond Shaped Devices' for 1  $\mu\text{m}$   
Bubbles Period: 5  $\mu\text{m}$

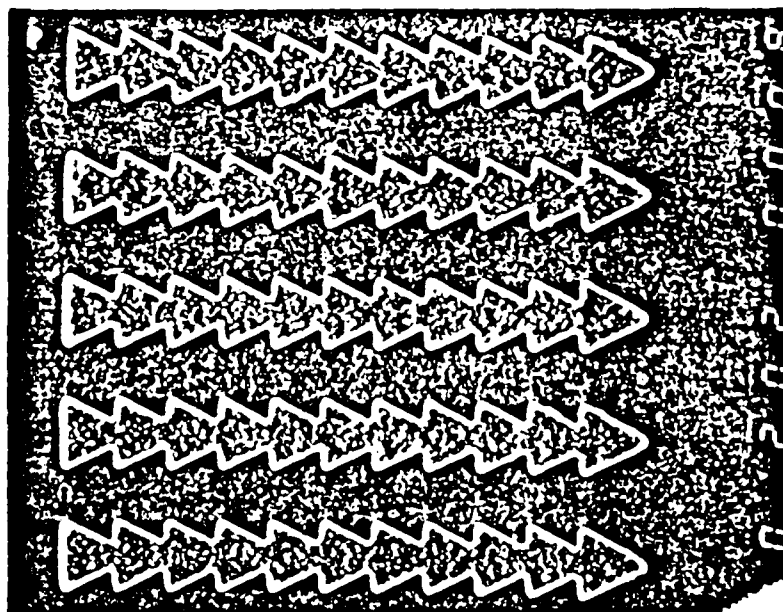


Fig. 2 : Scanning Electron Micrograph of the gold ion implantation masks of the 'Contiguous Arrow Shaped Devices' for 1  $\mu\text{m}$   
Bubbles Period: 4  $\mu\text{m}$

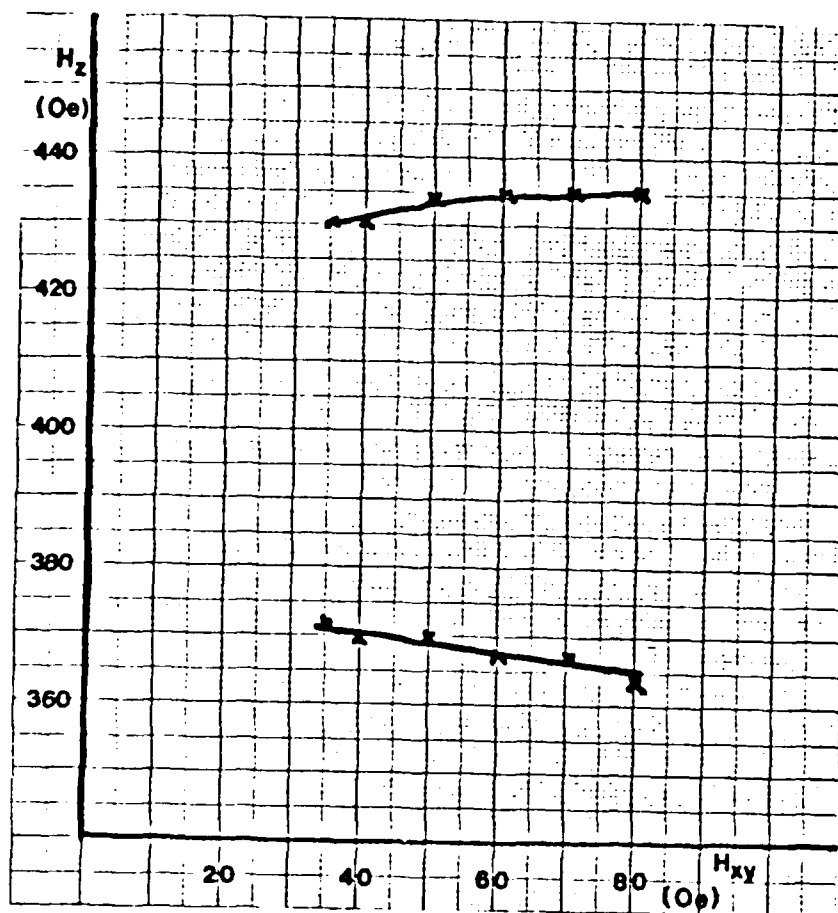


Fig. 3: Bias Margin of the 'Contiguous Diamond Shaped Device' for  
 1  $\mu$ m Bubbles      Period 6  $\mu$ m      Good Track

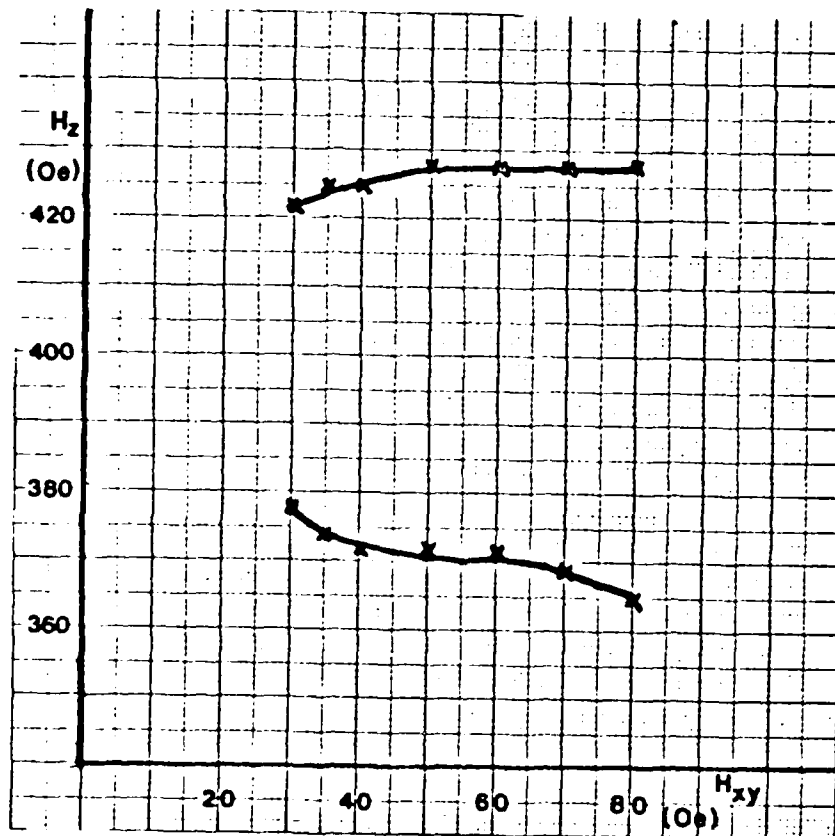


Fig. 4: Bias Margin of the 'Contiguous Arrow Shaped Device' for  
 1 μm Bubbles      Period: 5 μm      Good Track

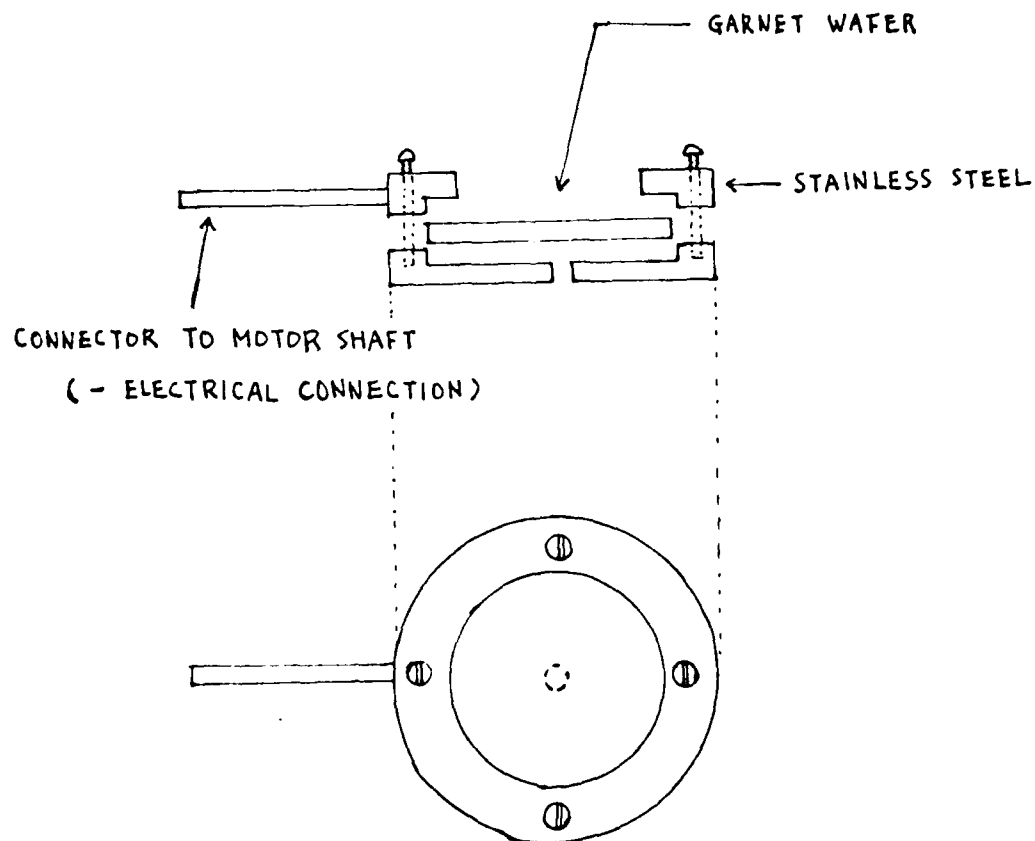


Fig. 5 Schematic diagram of new sample holder for the electroplating apparatus


The image is a technical drawing of a rectangular structure, oriented vertically. It features a grid pattern on the right side, which could represent a wall or a container. The drawing includes various structural details, such as lines indicating the edges and internal components. The overall appearance is that of a schematic or architectural plan.

## CURRENT ACCESSED-ION IMPLANTED DEVICES

### Introduction

In the progress report of 10/1/81, a current-accessed ion-implanted bubble device structure was described that circulated bubbles around unimplanted discs through the use of currents in an overlying perforated conducting sheet. In this device, a potential well due to current flow in the aperture sheet in conjunction with an attractive charged wall act upon the bubble domain. This new device structure requires less drive than a conventional current access device and as a result dissipates less power. In the past several months, work has been done designing propagation patterns that are based on the structure described above. In this report, in addition to a brief review of the hybrid structure and a discussion of some experimental results obtained, portions of a chip layout of propagation patterns are shown and described and a scheme for reducing power dissipation is presented.

### THE CURRENT-ACCESSED ION-IMPLANTED DEVICE STRUCTURE

The  device structure is depicted in Fig. 1. It consists of a planar current sheet with a circular aperture; the area under the sheet has been ion-implanted while in the aperture the magnetization remains normal to the film plane. Thus, except for the current sheet, the device looks just like a basic contiguous disc propagation structure.

Current flow through the sheet has two effects. First, the in-plane magnetic field component produces charged walls at the positions shown in the figure. At these same positions, potential wells due to the normal magnetic field component are created. Note that rotating the current will rotate the charged walls and potential wells simultaneously, which are in phase with each other.

In the figure a bubble is coupled to an attractive charged wall and this is also the position where the bias field is minimized, enhancing bubble stability at this position even further.

The potential well strength that a bubble experiences may be quantitatively determined by measuring the field needed to collapse a bubble,  $H_0$ , as a function of the drive field, or, as in the case of current access devices, the drive current. In Fig. 2 is given the data found when the collapse fields of a bubble on an 8  $\mu\text{m}$  aperture current access device and an 8  $\mu\text{m}$  hybrid structure were measured. Note that  $dH_0/dJ$  is less for the hybrid structure and nonlinearly hysteretic, but the magnitude of the collapse field and hence the potential well of the hybrid structure is deeper for practical drive current densities.

Another bubble device figure-of-merit, and one that is pertinent for propagation structures is the bias field of circulation. In order to ascertain this a bubble is circulated around an aperture at constant drive current magnitude and the bias fields at which the bubble stripes out and collapses are measured. The better the device, the larger the range of bias field obtained. In addition, one would also like the minimum drive current required for propagation to be as low as possible. The bias field margins for circulation of a bubble around a 6  $\mu\text{m}$  current access aperture and a 6  $\mu\text{m}$  hybrid device are seen in Fig. 3. Note that the hybrid structure has significantly better margins, and in particular, the minimum drive current of the hybrid device is roughly one half that of the conventional current access device. Since the power dissipation per unit device area is proportional to the square of the drive

current, the hybrid device needs roughly one quarter the power of the conventional structure.

### **Current Work**

#### **Mask Layout and Chip Design**

Presently, mask design and layout is being done on the Computer Science Department VLSI/VAX System and mask writing is scheduled for the week of Dec. 6, 1982 at the National Submicron Facility in Ithaca, NY. Typical designs for 1  $\mu\text{m}$  bubbles are seen in Fig. 4. The discs are apertures in an otherwise continuous conducting sheet and the gray areas are ion-implanted regions. The white areas within the propagation patterns and under the apertures are unimplanted. By using two overlapping conducting sheets and a pair of bipolar current supplies that are 90 degrees out of phase, a rotating current field, analogous to the rotating in-plane drive of field access devices, will act upon the bubbles *and the charged walls coupled to them*. An added advantage of using two conducting sheets with orthogonal currents is that the phase difference between currents may be varied and its effect upon propagation noted. Pattern periods range from 3.3 to 5.6 microns and propagation directions vary from 0 to 90 degrees with respect to current flow direction. By varying the propagation angle the effects of the crystalline anisotropy on this type of structure will be studied.

#### **Minimizing Power Consumption**

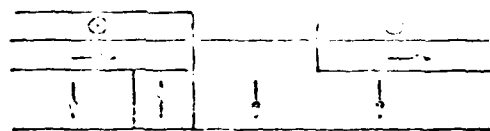
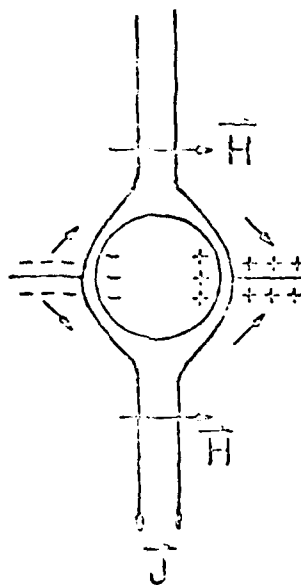
The hybrid structure has been shown to reduce the minimum drive current needed for circulation as compared to the conventional current accessed device. A further reduction in drive current is possible through the use of a



ground plane under the chip as depicted in Fig. 5. The in-plane fields produced by the conductors add between the conducting sheet and the ground plane, reducing the required current density by a factor of two. In addition, the perpendicular magnetic field components at the conductor edges will cancel, minimizing edge effects and thus allowing greater utilization of chip area with a concomitant increase in density.

### **Field Calculation**

A project currently being undertaken within the magnetics group is the creation of a user-interactive, graphics-oriented program in which current and magnetic field distributions can be calculated and displayed for an arbitrary distribution of apertures. The program is based upon the Finite Element Method and will be an invaluable tool in the design of current accessed devices.



G. G. G.

Figure 1: Hybrid device structure.

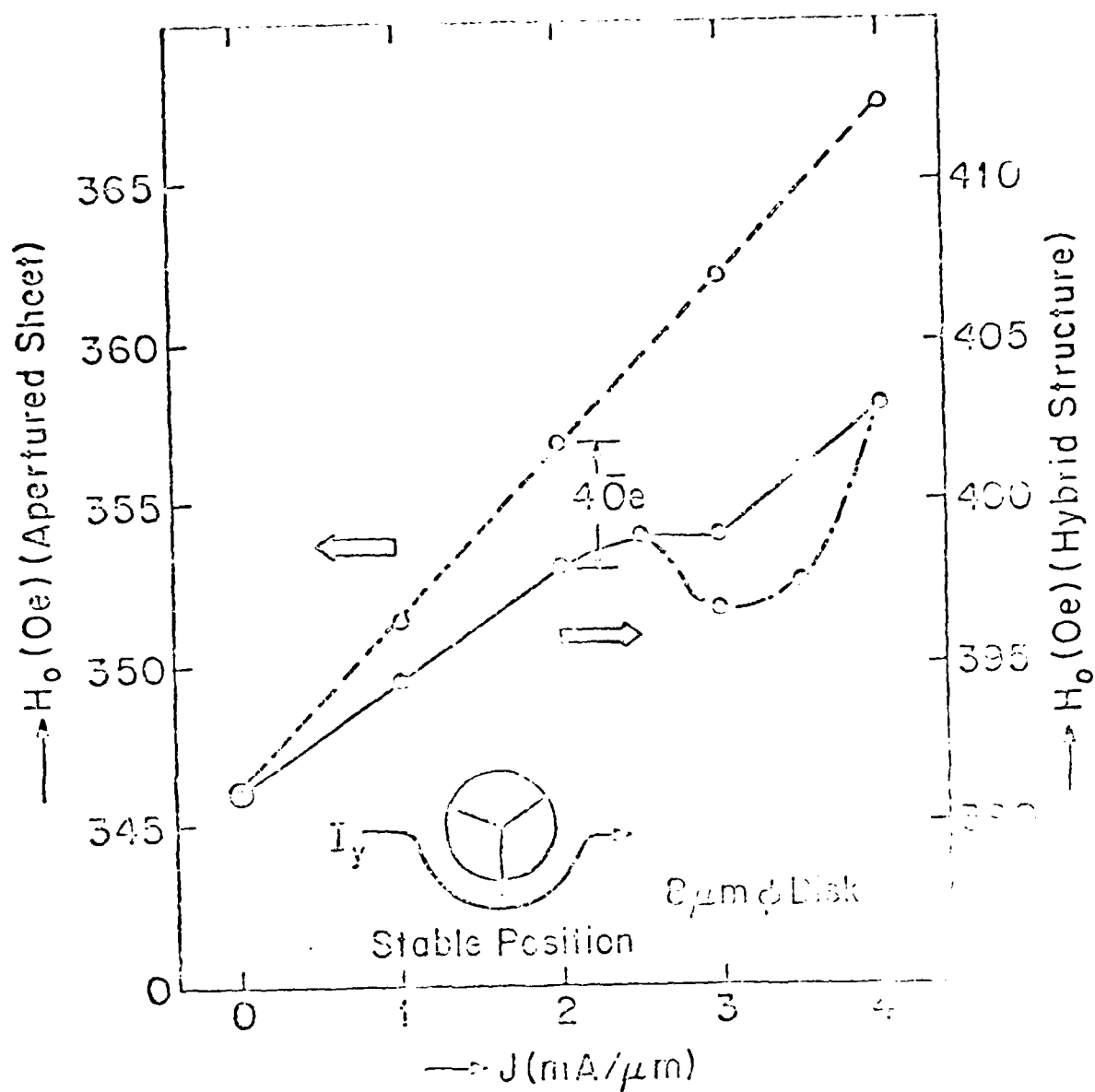


Figure 2: Collapse field of hybrid and current access device.

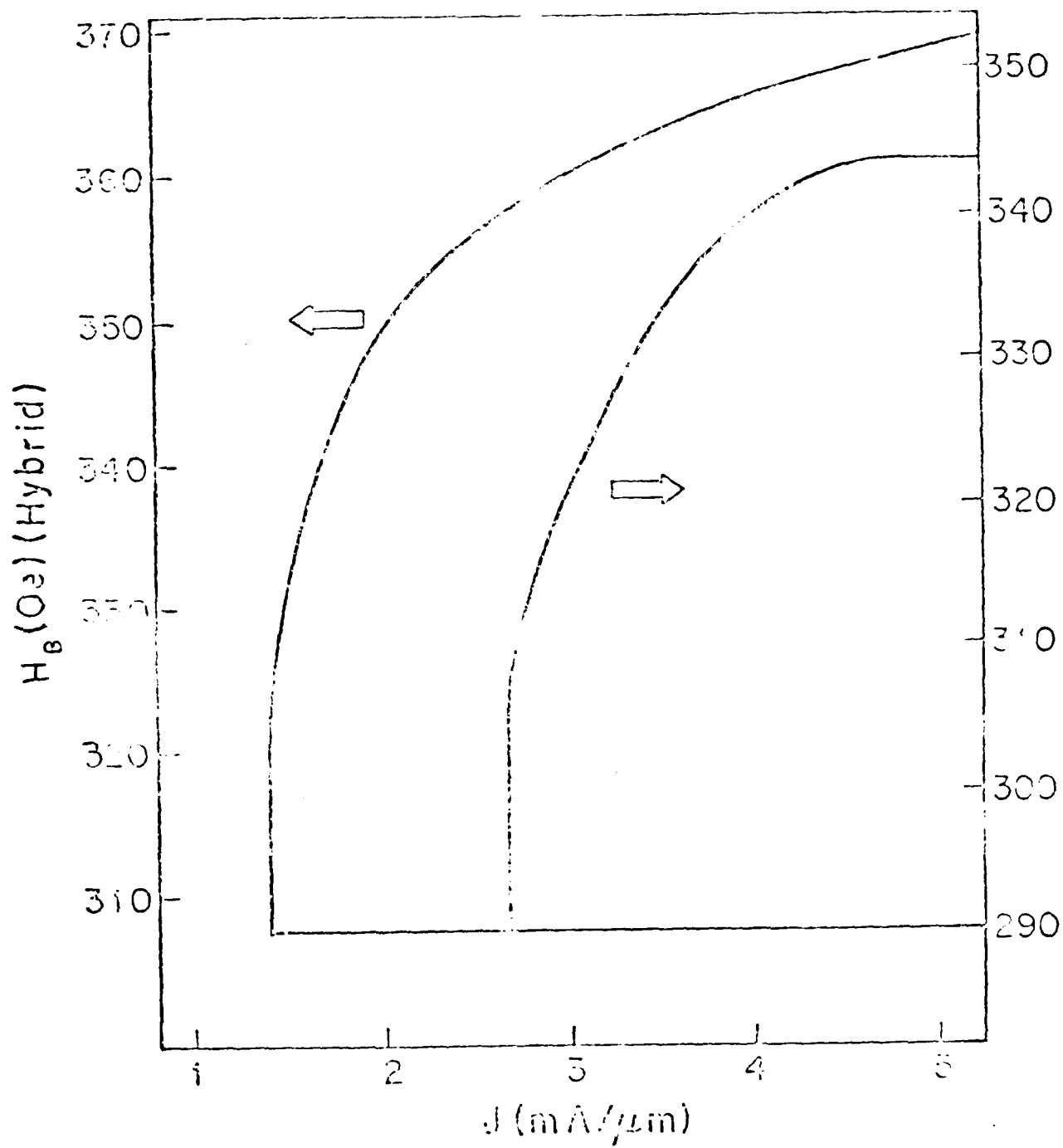
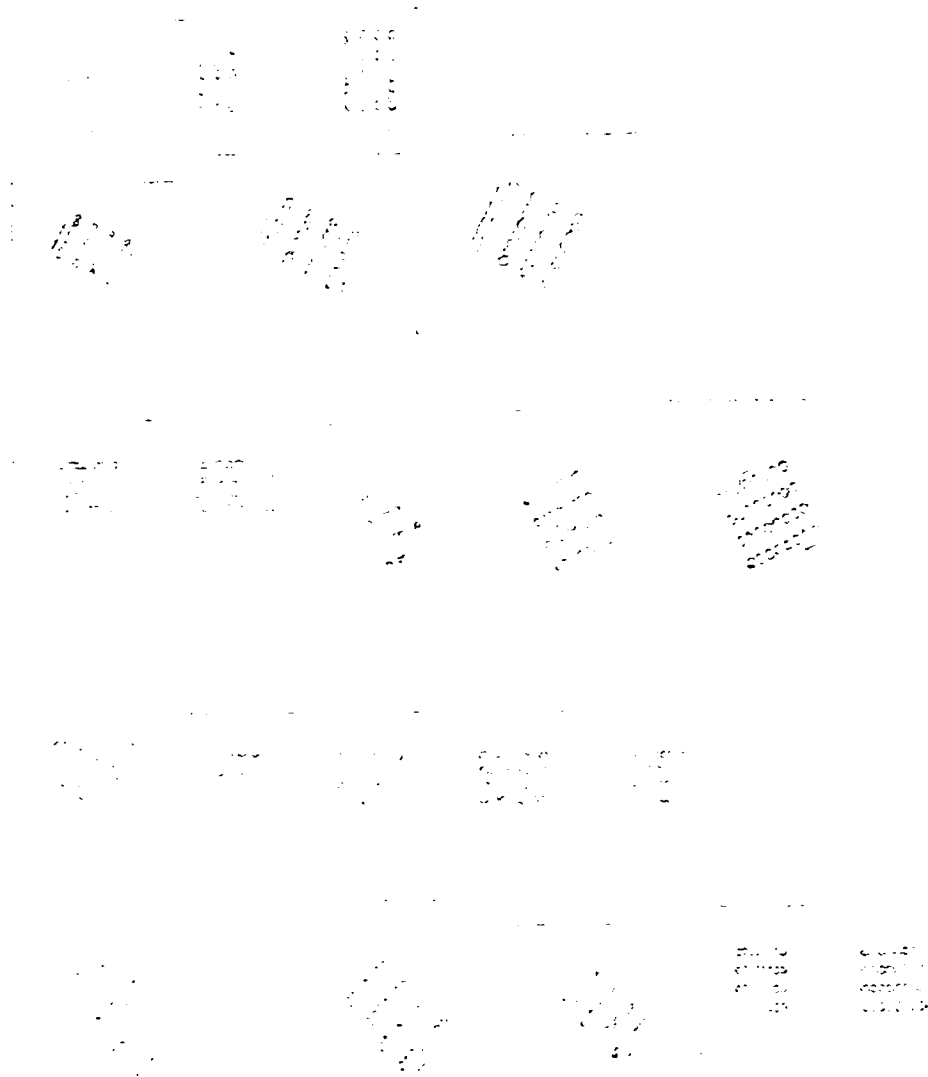


Figure 3: Bias margins of hybrid and current access devices.



**Figure 4:** Typical hybrid device propagation patterns.

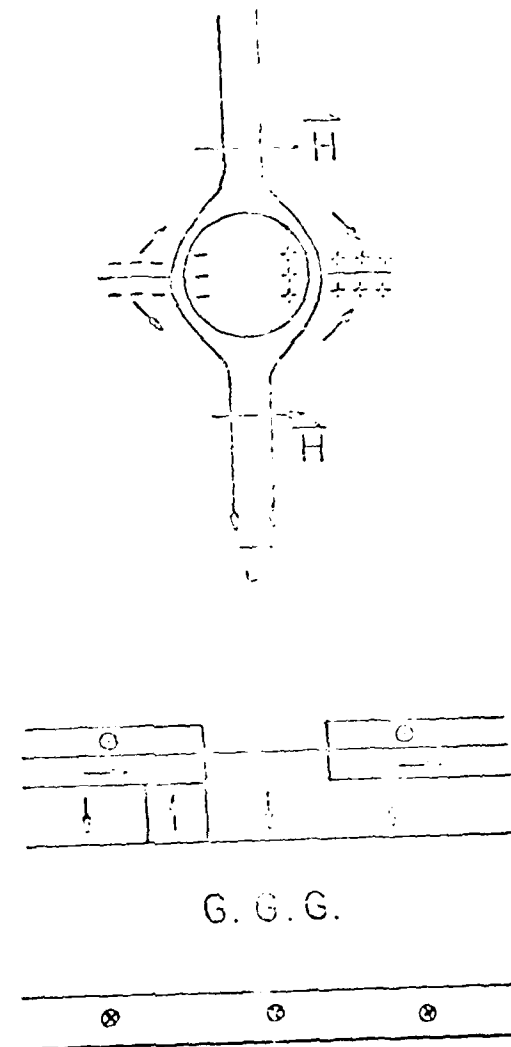


Figure 5: Hybrid device structure with ground plane.

## List of Figures

<b>Figure 1:</b> Hybrid device structure.	4
<b>Figure 2:</b> Collapse field of hybrid and current access device.	5
<b>Figure 3:</b> Bias margins of hybrid and current access devices.	6
<b>Figure 4:</b> Typical hybrid device propagation patterns.	7
<b>Figure 5:</b> Hybrid device structure with ground plane.	8

X. Wang, C. S. Krafft, M. H. Kryder

## ABSTRACT

We report here on improvements to standard techniques for the measurement of the effective uniaxial anisotropy field  $H_{KE} = H_K - 4\pi M_s$ , the magnetocrystalline anisotropy field  $H_1$ , and the magnetostriction coefficient  $\lambda_{111}$ . Measurements were made on full wafer garnets in a wideband resonance spectrometer with a nonresonant microstrip transmission line. Advantages of this technique include higher sensitivity than a previously reported microstrip structure [1], no problems with coupled resonances in  $\lambda_{111}$  measurements, as was reported by Vella-Coleiro [2] with a shorted waveguide, and ability to measure  $H_1$  on full wafer garnets, in contrast to use of a resonant cavity [3] which requires dicing the wafer into small chips. In the  $H_1$  calculation, the deviation of the magnetization from the applied field direction is considered. Accuracy of  $H_1$  is better than  $\pm 10$  Oe. A graphical method for determining  $H_1$  is presented. Results on different material compositions which support 1  $\mu\text{m}$  and 0.5  $\mu\text{m}$  diameter bubbles are reported.

## INTRODUCTION

The effective uniaxial anisotropy field  $H_{KE} = H_K - 4\pi M_s$ , magnetocrystalline anisotropy field  $H_1$ , and magnetostriction coefficient  $\lambda_{111}$ , are important parameters in material design of ion-implantable garnets for magnetic bubble devices. We report here on improvements which were made to previously reported measurement techniques [1, 2, 3, 4], and give results for 1  $\mu\text{m}$  and 0.5  $\mu\text{m}$  diameter bubble compositions. The microstrip transmission line structure, reported by Meyers et al. [1], was improved upon, enabling us to measure thinner films. The use of the microstrip in a transmission spectrometer eliminates the problem with coupled resonance inherent in the reflection type spectrometer. Thus we can calculate  $\lambda_{111}$  from resonant field shift measurement at one substrate thickness, typically 0.41 mm, instead of measuring resonant field shift at several thicknesses and extrapolating to zero substrate thickness [2].  $H_1$  is calculated using method similar to that reported by Makino et al. [4]. A graphical method for determining  $H_1$  from four resonance field measurements is presented.

## APPARATUS

We used a standard microwave spectrometer with a wide band non-resonant transmission stripline. The block diagram for this apparatus is shown schematically in Fig. 1.

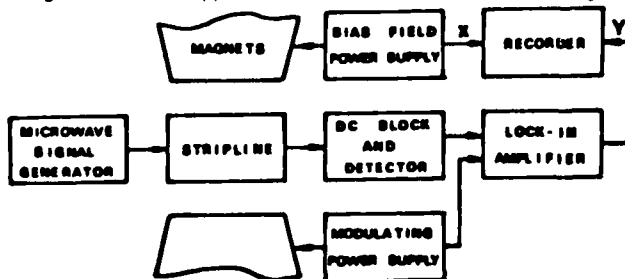


Fig. 1: Experimental Apparatus

Manuscript received 8/11/82

This work was supported by the Air Force Office of Scientific Research, under grant AFOSR 80-0284, and by the National Science Foundation under grant number ECS-7912677.

The authors are with Carnegie-Mellon University, Pittsburgh, Pennsylvania 15213.

The bias power supply is used to scan the external field, and the modulating power supply to modulate the external field. Phase-sensitive detection with a lock-in amplifier is used. An inner/outer DC block between the stripline and the detector helps to reduce modulating field pick-up, resulting in a significant increase in the signal to noise ratio. The y-axis input to the recorder is proportional to the derivative of the ferromagnetic resonance absorption of the film, while the x-axis input is proportional to the external field. The resonance field is the external field corresponding to the zero-cross point of the resonance curve. The frequency is held constant for each curve.

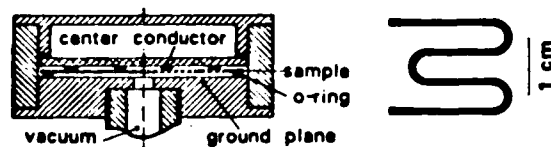


Fig. 2: Microbox Structure and Serpentine Conductor

Figure 2 shows the microbox structure used for the measurement of  $\lambda_{111}$ .  $H_1$  and  $H_{KE}$  were measured in a similar structure, without vacuum attachment. A heater was placed in the lid of the microbox for measurement of the temperature dependence of anisotropy field. The sample is placed between the ground plane and the center conductor so that the GGG acts as the dielectric substrate. A serpentine conductor, shown in Fig. 2, is used to increase the coupling between the sample and the microwave field by making the transmission path longer than that obtained with a straight conductor line.

The net perpendicular anisotropy field  $H_E = H_K - 4\pi M_s - 2/3 H_1$ , and the gyromagnetic ratio  $\gamma$ , may be obtained from the frequency dependence of normal resonance fields; whereas  $H_1$ ,  $H_{KE} = H_K - 4\pi M_s$ , and  $\gamma$  may be determined from angular dependence of resonance fields at one microwave frequency. For such measurements, the whole microbox is rotated about the  $[110]$  axis of the garnet wafer. With the microstrip there is no problem with detuning as this structure is non-resonant and the sample does not move with respect to the microwave field. We made measurements in a high Q resonant cavity and found that after rotating the sample the cavity had to be retuned. Use of lower frequencies lowers resonance field, improving field measurement accuracy. The sensitivity of our apparatus is comparable with that of the conventional resonant cavity. Sensitivity may be further increased by using a narrower conductor line or a larger wafer. Although the microstrip structure is theoretically wide band, we operated in region from 4 to 7 GHz due to decreased signal at higher frequencies. This is still more convenient than using different size resonant cavities to measure frequency dependent parameters.

To measure the magnetostriction constant, a reduced pressure is applied to one side of the wafer. A polystyrene o-ring is used to support the wafer and form a vacuum seal. The inner radius of the o-ring is used in the calculation, which is presented in the next section. The wafer is mechanically polished to a thickness of 0.41 mm to remove the back film and to create a larger resonance field shift for the same applied pressure. The pressure is adjustable while the sample is in the magnet gap, simplifying  $\lambda_{111}$  measurement. The strain could be applied such that the film was either in compression or in tension by turning the wafer over.

## THEORY

The equilibrium condition to determine the magnetization angle  $\theta$  is given by [4]:

1/3



$$-2H \sin(\beta - \theta) + H_{KE} \sin 2\theta + H_1 (-7/24 \sin 4\theta) \quad (1)$$

$$-1/12 \sin 2\theta + \sqrt{2}/3 (3 \sin^2 \theta - 4 \sin^4 \theta) = 0$$

where  $H$  is the external field applied in the  $(\bar{1}10)$  plane,  $M_s$  is the magnetic moment, and  $\beta$  is the external field angle as shown in Fig. 3. The resonance condition is given by [4]:

$$(\omega/\gamma)^2 = \{H \cos(\beta - \theta) + H_{KE} \cos 2\theta + H_1 (\sqrt{2}/6 \sin 2\theta \quad (2)$$

$$(3 - 8 \sin^2 \theta) - 7/12 \cos 4\theta - 1/12 \cos 2\theta\}$$

$$(H(\sin \beta / \sin \theta) - (3/4)\sqrt{2} H_1 \sin 2\theta)$$

where  $\omega$  is the microwave frequency, and  $H$  is the resonant field. Solution of Eqs.(1) and (2) gives the relationship between microwave frequency, applied field angle and resonance field. With the applied field  $H_N$  in the  $[111]$  direction normal to the film plane Eq.(2) reduces to

$$\omega/\gamma = H_N + H_{KE} - 2/3 H_1 \quad (3)$$

With the applied field  $H_P$  in the  $[11\bar{2}]$  direction, coplanar with the film, Eq.(2) reduces to

$$(\omega/\gamma)^2 = H_P(H_P - H_{KE} - 1/2 H_1) \quad (4)$$

At other applied field angles, Eq.(1) and Eq.(2) must be solved to determine the magnetization angle  $\theta$ .

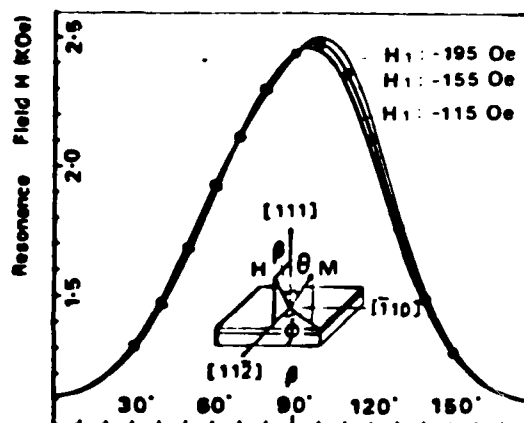


Fig. 3: Fitting of Experimental  $H_1$  Data

The magnetostriction coefficient is calculated from the resonance field shift due to an applied stress from the following equation [5]

$$\delta H_{111} = 1.5(\lambda_{111}/M_s) \sigma \quad (5)$$

where  $\sigma$  is the applied stress in the LPE film. The radial and tangential stress in the outermost layer of the GGG substrate,  $\sigma_r$  and  $\sigma_t$ , are calculated using formulae developed by Timoshenko [6] and used by Vella-Coleiro [2]. Averaging the stress by integration over the serpentine conductor pattern yields

$$(\sigma_r + \sigma_t)_{avg} = 75[(2+2\nu)(0.5136) + (1-\nu)]a^2q/T^2 \quad (6)$$

$$= 1.526a^2q/T^2$$

where  $\nu$  is Poisson's ratio,  $T$  is the thickness of the GGG substrate,  $a$  is the inner radius of the supporting o-ring, and  $q$  is the applied pressure. Assuming that the GGG substrate and the LPE film have the same Young's modulus and Poisson's ratio, the stress in the LPE film will be the same as that given by Eq.(6). Solving for the magnetostriction coefficient, we obtain

$$\lambda_{111} = 4\nu M_s T^2 \delta H_{111} / 28.76a^2q \quad (7)$$

#### CALCULATION

A program was developed to calculate  $H_1$  given the

experimentally measured resonance fields. This program searches for a minimum mean square deviation of  $\omega/\gamma$  in a method similar to that employed by Makino, et al. [4]. The first step involves solving Eq.(1) for  $\theta$  and Eq.(2) for  $(\omega/\gamma)$  at all applied field angles measured for a trial value of  $H_1$  and taking average  $\omega/\gamma$  and mean square deviation.  $H_{KE}$  is determined from  $H_P$  and  $H_N$  and the trial value of  $H_1$ . Incrementing  $H_1$  by 5 Oe, the process is repeated until a minimum in the mean square deviation of  $(\omega/\gamma)$  is found.

#### EXPERIMENTAL RESULTS

Figure 3 shows the fitting of experimental resonance field data to theoretical  $H_1$  curves. The middle curve represents  $H_1$  equal to -155 Oe. Adjacent curves represent  $\pm 40$  Oe variation in  $H_1$ . In Fig. 4, the deviation of the magnetization angle from the applied field angle,  $\beta - \theta$ , is plotted against the applied field angle  $\beta$ . For accurate determination of  $H_1$  it is important to consider angular deviation in resonance field calculation. The value for  $H_1$  is determined from minimum in mean square error versus  $H_1$ , which is plotted in Fig. 5. For a more rapid determination of  $H_1$ , we found that resonance data taken at applied fields of  $0^\circ$ ,  $70^\circ$ ,  $90^\circ$ , and  $110^\circ$  provided  $H_1$  to an accuracy of 10%. The choice of angles,  $70^\circ$  and its supplement  $110^\circ$ , was based upon difference in resonance field at supplementary angles versus applied field angle plot, shown in Fig. 6. The maximum difference occurs near  $70^\circ$ . We

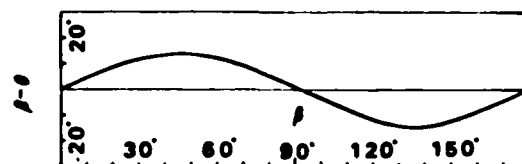


Fig. 4: Deviation of Magnetization Angle from Applied Field

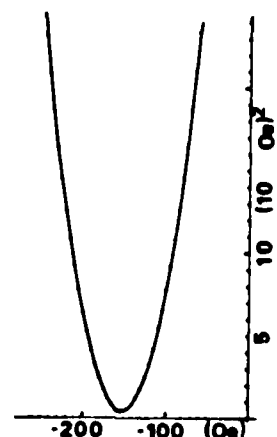


Fig. 5: Mean Square Error of  $\omega/\gamma$  Versus  $H_1$

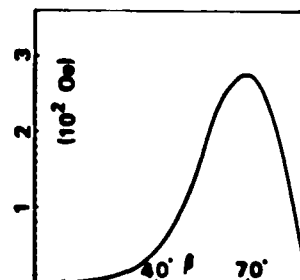


Fig. 6: Difference in Resonance Fields at  $\beta$  and  $180^\circ - \beta$

have developed a graphical method for determining  $H_1$  from the resonance fields at  $0^\circ$ ,  $70^\circ$ ,  $90^\circ$ , and  $110^\circ$  applied field angles.  $H_{KE}$  was determined from Eqs.(3) and (4) for given  $H_1$ . Equating Eqs.(2) and (3) to remove  $(\omega/\gamma)$ , and normalizing it and Eq.(1) to  $H_N$ , we solved for  $H/H_N$  and corresponding  $\theta$  for given  $\beta$ .  $H_1/H_N$  is plotted versus  $\Delta H/H_N = (H_{110} - H_{70})/H_N$  in Fig. 7 for given  $H_p/H_N$ .

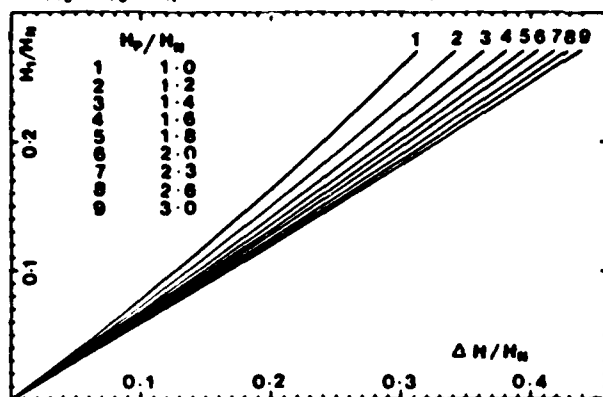


Fig. 7: Determination of  $H_1$  from 4 Resonance Fields

For magnetostriction measurement, we obtained the same magnitude shift in resonance field for the film in compression as in tension, as shown in Fig. 8. Furthermore, by doubling the pressure, we doubled the resonance field shift. Thus, the normal resonance field shift is attributed solely to the strain, and not to any other factors. The resonance field shift for a 635 mm Hg pressure is 90 Oe for the  $1\mu\text{m}$  garnet, film 2, and 50 Oe for the  $0.5\mu\text{m}$  garnet, film 5. On film 2,  $\lambda_{111}$  was determined to be  $-3.3 \times 10^{-6}$ . On film 5,  $\lambda_{111}$  is  $-3.8 \times 10^{-6}$ . Higher  $\lambda_{111}$  for film 5 is due to higher iron and samarium content.

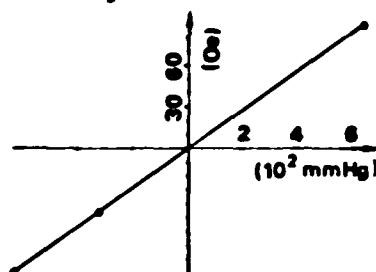


Fig. 8: Resonance Shift Versus Applied Pressure

Film compositions are given in Table I. Film parameters given in Table II include film thickness  $t$ , characteristic length  $l$ ,  $4\pi M_s$ ,  $H_{KE}$ , and  $H_1$ . Results of temperature dependence of  $H_{KE}$  and  $H_1$  measurements are given in Table III. The temperature dependence of  $H_1$  and  $H_{KE}$  is attributed to a decrease in the exchange effects with increasing temperature. This leads to a decrease in crystal dependent magnetic properties.

Table I: Film Compositions

Film	Composition
1,2	$\text{Y}_{0.9}\text{Sm}_{0.20}\text{TM}_{1.3}\text{Gd}_{0.80}\text{Fe}_{4.65}\text{Ga}_{0.35}\text{O}_{12}$
3	$\text{Y}_{0.9}\text{Sm}_{0.35}\text{TM}_{1.2}\text{Gd}_{0.55}\text{Fe}_{4.65}\text{Al}_{0.18}\text{Ga}_{0.17}\text{O}_{12}$
4	$\text{Y}_{0.91}\text{Sm}_{0.71}\text{TM}_{1.12}\text{Gd}_{0.26}\text{Fe}_{4.8}\text{Al}_{0.2}\text{O}_{12}$
5	$\text{Y}_{0.88}\text{Sm}_{0.89}\text{TM}_{1.09}\text{Gd}_{0.25}\text{Lu}_{0.09}\text{Fe}_{4.8}\text{Al}_{0.2}\text{O}_{12}$
6,7	$\text{Y}_{0.82}\text{Sm}_{0.65}\text{TM}_{1.02}\text{Gd}_{0.24}\text{Lu}_{0.27}\text{Fe}_{4.8}\text{Al}_{0.2}\text{O}_{12}$

Table II: Film Parameters

Film	$t$	$l$	$4\pi M_s$	$H_{KE}$	$H_1$
1	0.90 ( $\mu\text{m}$ )	0.11 ( $\mu\text{m}$ )	633 (G)	502 (Oe)	-160 (Oe)
2	1.26	0.14	636	960	-155
3	0.85	0.11	774	782	-155
4	0.73	0.06	1390	461	-125
5	0.5	0.06	1345	600	-115
6	0.70	0.06	1292	684	-115
7	0.75	0.06	1382	611	-125

Table III: Temperature Dependence of  $H_1$  and  $H_{KE}$

Film	Temp.	$H_1$	$H_{KE}$	$4\pi M$
3	27( $^\circ\text{C}$ )	-155 (Oe)	782 (Oe)	774 (G)
	95	-95	426	715
6	25	-115	684	1292
	94	-65	339	1073
7	25	-125	611	1382
	95	-80	300	1164

## DISCUSSION AND CONCLUSION

The accuracy of  $H_{KE}$  is typically  $\pm 20$  Oe, as determined by comparison of  $H_{KE}$  determined by angular and frequency dependence of resonance field. Uncertainty in resonance field is predominant source of error. Uncertainty in  $H_1$ , determined by minimum in mean square error of  $(\omega/\gamma)$  is  $\pm 10$  Oe, as shown in Fig. 5. Largest source of error is uncertainty in  $4\pi M_s$ , which is  $\pm 5\%$ .  $4\pi M_s$  was determined from collapse field, film thickness, and zero-field stripwidth measurements [7]. Reproducibility of  $H_1$  is better than 10 Oe. The resonance field shift for magnetostriction measurement is determined to within  $\pm 6$  Oe. This is the resolution of the field measurement. The absolute accuracy of  $\lambda_{111}$  is  $\pm 10\%$ , the relative accuracy is  $\pm 5\%$ .

Films 1, 2 and 3 are nominal  $1\mu\text{m}$  diameter bubble materials. Films 4-7 are nominal  $0.5\mu\text{m}$  diameter bubble materials. Film growth is described elsewhere [8]. Film compositions are estimated assuming unity segregation coefficients for the rare earths. The difference in  $H_1$  for  $1\mu\text{m}$  and  $0.5\mu\text{m}$  film compositions is attributed predominantly to difference in  $4\pi M_s$ , but also to difference in rare-earth content. Films 6 and 7 were grown from the same melt at different growth temperatures.

The techniques described here are suitable for the routine measurement of  $H_1$ ,  $H_{KE}$ , and their temperature coefficients on as-grown full wafer garnets.  $\lambda_{111}$  is measured on mechanically thinned substrates. The high sensitivity, attributed to the use of a serpentine conductor, placement of sample between conductor and ground plane, and use of an inner/outer DC block, enables us to make measurements on films as thin as  $0.3\mu\text{m}$ .

## ACKNOWLEDGEMENTS

The authors would like to thank Prof. J. O. Artman for use of his FMR equipment.

## REFERENCES

1. E.C. Meyers, S.-Y. Bi, S.H. Charap, and J.O. Artman, J. Appl. Phys., **53**, 2099,(1982)
2. G. P. Vella-Coleiro, Rev. Sci. Instrum., **50**, 8, 1130,(1979)
3. L.C. Hsia, P.E. Wigen, R.L. Bergner, and R.D. Henry, IEEE Trans. on Magn., **MAG-17**, 2559,(1981)
4. H. Makino, Y. Hidaka, Mat. Res. Bull., **16**, 957,(1981)
5. G. F. Dionne, J. Appl. Phys., **41**, 2264,(1970)
6. S. Timoshenko, S. Woinowsky-Krieger, *Theory of Plates and Shells*, McGraw-Hill, New York, (1959).
7. D. C. Fowles, J. A. Copeland, AIP Conf. Proc., **5**, 240,(1972)
8. C. S. Krafft, X. Wang, M. H. Kryder, Paper No.CB-07, presented this conference

**DA  
FILM**